

Developments and Applications of Quantum Chemistry: From Novel Electronic Structure Methods to Conjugated Optoelectronic Materials

by

Andrew William Prentice

*A thesis presented for the degree of
Doctor of Philosophy*



Heriot-Watt University
Institute of Chemical Sciences
November 2019

*The copyright of this thesis is owned by the author. Any
quotation from this thesis or use of any of the
information contained in it must acknowledge this thesis
as the source of the quotation information.*

Research Thesis Submission

Please note this form should be bound into the submitted thesis.

Name:	Andrew William Prentice		
School:	EPS		
Version: <small>(i.e. First, Resubmission, Final)</small>	Final	Degree Sought:	PhD

Declaration

In accordance with the appropriate regulations I hereby submit my thesis and I declare that:

1. The thesis embodies the results of my own work and has been composed by myself
2. Where appropriate, I have made acknowledgement of the work of others
3. The thesis is the correct version for submission and is the same version as any electronic versions submitted*.
4. My thesis for the award referred to, deposited in the Heriot-Watt University Library, should be made available for loan or photocopying and be available via the Institutional Repository, subject to such conditions as the Librarian may require
5. I understand that as a student of the University I am required to abide by the Regulations of the University and to conform to its discipline.
6. I confirm that the thesis has been verified against plagiarism via an approved plagiarism detection application e.g. Turnitin.

ONLY for submissions including published works

Please note you are only required to complete the Inclusion of Published Works Form (page 2) if your thesis contains published works)

7. Where the thesis contains published outputs under Regulation 6 (9.1.2) or Regulation 43 (9) these are accompanied by a critical review which accurately describes my contribution to the research and, for multi-author outputs, a signed declaration indicating the contribution of each author (complete)
8. Inclusion of published outputs under Regulation 6 (9.1.2) or Regulation 43 (9) shall not constitute plagiarism.

* Please note that it is the responsibility of the candidate to ensure that the correct version of the thesis is submitted.

Signature of Candidate:	Andrew William Prentice	Date:	17/04/2020
-------------------------	-------------------------	-------	------------

Submission

Submitted By <i>(name in capitals)</i> :	ANDREW WILLIAM PRENTICE
Signature of Individual Submitting:	Andrew William Prentice
Date Submitted:	17/04/2020

For Completion in the Student Service Centre (SSC)

Limited Access	Requested	Yes	No	Approved	Yes	No
E-thesis Submitted <i>(mandatory for final theses)</i>						
Received in the SSC by <i>(name in capitals)</i> :				Date:		

Abstract

The work contained within this thesis encompasses a variety of different techniques to describe chemical systems of varying complexity, ranging from geometrically simple systems with an inherently correlated, and thus complex, electronic structure and vice versa. The stochastic technique of Monte-Carlo configuration interaction, which can generate properties of full configuration interaction (FCI) quality despite vast reduction in wavefunction size, was locally modified to involve a more systematic configuration selection regime, termed systematic-MCCI. A comparison of both approaches was undertaken on Ne, H₂O, CO and Cr₂ due to varying electronic structure in these systems; for comparison FCI and a novel pruned-FCI alternative was also included. It shall be demonstrated that the stochastic MCCI approach produced near optimal wavefunctions when compared to these systematically generated wavefunctions, with a far reduced computational cost. We then switch our attention to the modelling of chemical reaction pathways, specifically those undergoing an intramolecular Diels-Alder (IMD-A) cycloaddition process, using the high-accuracy thermochemistry method, CBS-QB3. It was observed that incorporation of a nitro group into the IMD-A substrate resulted in more exergonic reactions and lower activation barriers, when compared to non-substituted substrates, attributed to the enhanced positive charge stabilisation in the cycloadduct. The nature of the important frontier molecular orbital (FMO) interaction was also found to completely reverse upon nitration. The substitution of the dieneophile was tolerated to a much better degree in nitro bearing systems due to the increased distances between the bond forming carbons in the transition state. However, this nitration effect was not observed in highly polarity mismatched substrates. We also investigate if structure-energy correlations are present in a set of hetero IMD-A substrates, between the bond length contraction upon going from the transition state to the cycloadduct and the overall reaction free energy change and the retro IMD-A barrier. However, as will be discussed for the substrates of interest herein we observe very little correlation. In addition we explored the structure-energy correlation for the aforementioned nitro and non-nitrated IMD-A reactions but similar findings were observed. A density functional theory (DFT) study is then undertaken for a range of organic π -conjugated materials. We explore the ionisation potential of these materials with a comparison to recent experimental findings. As shall be discussed we observe good agreement

with experiment, within 100 meV of the uncertainty range, for the computationally cheap approach of a single oligomer contained within an implicit solvent model when there is no known stacking within the polymer environment. However, if the thin film environment exhibits a degree of ordering this simple approach breaks down and more sophisticated models must be implemented. The thesis concludes with a molecular dynamics (MD) study of two simple π -organic conjugated materials using a recently parameterised force-field. The configurational landscape attained from the MD simulations are then explored with electronic structure methods and a brief statistical analysis undertaken.

Dedication

For my mother Hazel, sister Pamela and grandparents Elizabeth and Hugh, without your love, support, and copious supply of food and tea this journey would not have been possible.

I would also like to extend this dedication to Hugh and Janet for all their support not only in regards to this academic process but throughout my life.

Acknowledgements

Firstly, I would like to thank Professor Martin Paterson for not only providing the opportunity to undertake a Ph.D. but for making it such a worthwhile experience. His support, guidance and patience throughout has made the journey as pleasant as possible, and for that I am truly grateful.

I would also like to thank Dr. Jeremy Coe for not only the highly beneficial discussions regarding MCCI but for the flawless upkeep of HPC2/HPC6, allowing us to have a Ph.D. to complete. The rest of the Paterson group past and present: Clément, Nell, Thomas, Freda, Lisa and Paul - it has been a pleasure!

I would also like to thank Professor Ian Galbraith and Dr. Jack Wildman for all the help and tremendously useful discussions regarding the organic π -conjugated portion of this work. Without your help this work would not have been possible.

I also extend a thank you to Dr. Andrew McLean for not only our recent collaborative work but for opening my eyes to the truly wonderful field of computational chemistry.

List of Publications

Contained Within Thesis

Published

1. T.Y. Cowie, M. Veguillas, R.L. Rae, M. Rougé, J.M. Żurek, A.W. Prentice, M.J. Paterson, M.W.P. Bebbington, “Intramolecular Nitrofurane Diels-Alder Reactions: Extremely Substituent-Tolerant Cycloadditions via Asynchronous Transition States”, *J. Org. Chem.*, **2017**, 82, 13, 6656–6670.
2. A. W. Prentice, J.P. Coe, M. J. Paterson, “A Systematic Construction of Configuration Interaction Wavefunctions in the Complete CI Space”, *J. Chem. Phys.*, **2019**, 151, 16, 164112.

Submitted

1. S. E. Challinger, A.W. Prentice, I.D. Baikie, I. Galbraith, M.J. Paterson, G.A. Turnbull, I.D.W. Samuel, “Determining the Ionisation Energy of Conjugated Polymer Films Using Ambient Pressure Photoemission”, *J. Phys. Chem. Lett.* *In Submission*.

In Preparation

1. A.W. Prentice, J. Wildman, I. Galbraith, M.J. Paterson, “Quantum Mechanical Analyses of Molecular Dynamics of π -conjugated Materials”, *In Preparation*.

Omitted From Thesis

Published

1. J.M. Tobin, T.J.D. McCabe, A.W. Prentice, S. Holzer, G.O. Lloyd, M.J. Paterson, V. Arrighi, P.A.G. Cormack, F. Vilela, “Polymer-Supported Photosensitizers for Oxidative Organic Transformations in Flow and under Visible Light Irradiation”, *ACS Catal.*, **2017**, 7, 7, 4602–4612.

-
2. J. S. Foster, A. W. Prentice, R. S. Forgan, M. J. Paterson, G. O. Lloyd, “Targetable Mechanical Properties by Switching between Self-Sorting and co assembly with In Situ Formed Tripodal Ketoenamine Supramolecular Hydrogels”, *Chem. Nano. Mat.*, **2018**, 4, 853.

In Preparation

1. A. J. McLean, A.W. Prentice and M.J. Paterson, “Single Molecule to the Solid State: A Study on the Optical Properties of Methylene Blue Dimers”, *In Preparation*.

Contents

1	General Background of Computational Chemistry	1
1.1	Abstract	1
1.2	Introduction	2
1.3	<i>Ab-initio</i> and Density Based Approaches	3
1.4	High-Accuracy Composite Methods	5
1.5	Molecular Dynamics	6
1.6	Thesis Overview	7
1.7	References	9
2	Theoretical Background	12
2.1	Abstract	12
2.2	Quantum Mechanics	13
2.2.1	Schrödinger Equation and the Wavefunction	13
2.2.2	Molecular Hamiltonian	16
2.2.3	Adiabatic and Born-Oppenheimer Approximation	17
2.3	Hartree-Fock Theory	22
2.3.1	Restricted and Unrestricted Hartree-Fock Theory	28
2.3.2	Koopmans' Theorem	31
2.4	Basis Sets	32
2.5	Electron Correlation	35
2.6	Post Hartree-Fock Techniques	37
2.6.1	Configuration Interaction	37
2.6.2	Monte-Carlo Configuration Interaction	42
2.6.3	Many-Body Perturbation Theory	43

2.6.4	Coupled-Cluster Theory	46
2.6.5	Multi-Configurational Self-Consistent Field	47
2.6.6	Multi-Reference Configuration Interaction	49
2.7	Density Functional Theory	50
2.7.1	Kohn-Sham Density Functional Theory	52
2.7.2	Local Density Approximation	54
2.7.3	Generalised Gradient Approximation	54
2.7.4	Hybrid Methods	55
2.8	Time-Dependent DFT	57
2.9	Geometry Optimisation and Frequencies	59
2.10	Transition State Theory and Thermodynamic Quantities	61
2.11	Implicit Solvent Models	64
2.12	Quantum Chemical Composite Methods	67
2.13	Molecular-Dynamics	68
2.13.1	Force-fields	69
2.13.2	Integration Methods	72
2.13.3	Simulation Overview	73
2.14	References	74
3	A Systematic Construction of Configuration Interaction Wavefunc-	
	tions in the Complete CI Space	80
3.1	Abstract	80
3.2	Introduction	81
3.3	Computational Methodology	86
3.3.1	Full Configuration Interaction	86
3.3.2	Monte-Carlo Configuration Interaction	86
3.3.3	Systematic-Monte Carlo Configuration Interaction	89
3.3.4	Pruned-Full Configuration Interaction	91
3.4	Results and Discussion	91
3.4.1	Neon	91
3.4.2	H ₂ O	104

3.4.3	Carbon Monoxide	111
3.4.4	Chromium Dimer	113
3.5	Conclusion and Future Work	115
3.6	References	118
4	Investigating a Series of Intramolecular Diels-Alder Reactions <i>via</i>	
	High-Accuracy Thermochemical Analyses	120
4.1	Abstract	120
4.2	Introduction	121
4.3	Computational Details	125
4.3.1	Furan and Nitrofurane Dienes	125
4.3.2	Carbonyl Dienes and Dienophiles	126
4.4	Results and Discussion	127
4.4.1	Furan and Nitrofurane Dienes	127
4.4.2	Structure-Energy Correlations	134
4.5	Conclusion	142
4.6	References	142
5	Ionisation Potential of Organic π-Conjugated Materials: A Com-	
	parison Between Experiment and Theory	146
5.1	Abstract	146
5.2	Introduction	147
5.3	Photoemission Spectroscopy	152
5.4	Computational Details	152
5.5	Results and Discussion	153
5.5.1	Experimental Data	153
5.5.2	Initial DFT Benchmarking	155
5.5.3	Material Comparison	160
5.5.4	Ionisation Potential as a Function of F6 Oligomer Length . . .	161
5.5.5	Excited State Analysis	162
5.5.6	Crystalline Materials	164

5.6	Conclusion	169
5.7	References	169
6	Quantum Mechanical Analyses of Molecular Dynamics of π-conjugated Materials	174
6.1	Abstract	174
6.2	Introduction	175
6.3	Computational Details	178
6.3.1	Molecular Dynamics Simulation	178
6.3.2	Molecular Dynamics Post Processing	178
6.3.3	Electronic Structure Computations	181
6.4	Results and Discussion	181
6.4.1	Auto-Correlation and Sampling Protocol	181
6.4.2	Self Consistent Field Energy	183
6.4.3	Vertical Ionisation Potential	187
6.4.4	Optical Transition Gap	190
6.4.5	Magnitude of the Dipole Moment	192
6.5	Conclusion	194
6.6	References	195
7	Conclusions and Future Work	199
7.1	Conclusions and Future Work	200

Chapter 1

General Background of Computational Chemistry

1.1 Abstract

The following Chapter begins with a brief outline of the ever evolving field of computational chemistry, and how the need for a new rule-set governing atomic phenomena was of great importance due to deviations with established classical models. As exact wavefunctions are only available for a limited number of systems we explore the need to develop approximate methods, both ab-initio and electron density based in nature, that can provide properties of comparable quality to these exact theories despite vast reduction of the computational expense. The application of computational techniques in modelling various processes such as the thermo-chemical and kinetic reaction pathways, via composite methods that aim for chemical accuracy are then explored. The technique of molecular dynamics is then introduced with the Chapter terminating with a brief overview of what follows within the thesis.

1.2 Introduction

The last 150 years have been pivotal in developing our understanding of chemical phenomena on an atomic level, for example, through discovery of sub-atomic particles and the wave-particle behaviour of electrons and light [1]. Initially, the need for a new framework to describe phenomena occurring on this atomic level was a result of the poor agreement between the Rayleigh-Jeans law and that observed experimentally for the emission spectra of a blackbody in thermal equilibrium with the surrounding environment, termed the ultraviolet catastrophe. This discrepancy was especially substantial for smaller wavelengths (λ), corresponding to higher frequencies (ν), with the classical theory predicting that as $\lambda \rightarrow 0$ the spectral radiance would tend towards infinity which would be impossible, and thus highlighted a major flaw in classical models. It was Planck who provided the link between theory and experiment by making the assumption that matter could only absorb or emit electro-magnetic radiation at discrete energies (E), a so called quanta of energy, satisfying the following equation [1]:

$$E = h\nu \tag{1.1}$$

where h is Planck's constant and is equal to a value of $6.626 \cdots \times 10^{-34}$ J s, which highlights the relative scale that is being dealt with. However, the importance of this finding was not realised until Einstein's interpretation of the photoelectric effect [2, 3], which will be discussed briefly in Section 5.3 as it forms the underlying principles of photoemission spectroscopy, in which he proposed that light propagating through space consists of a stream of photons each with an energy given by equation 1.1. These initial findings gave rise to the realm of quantum mechanics (QM), deviating from the classical framework pioneered by Isaac Newton in the late 17th century. In the years which followed the field was heavily built upon through findings from Rutherford and Bohr, on establishing the atomic model, de Broglie, on the aforementioned wave-particle duality, Heisenberg, in matrix mechanics and Schrödinger, for his postulated Schrödinger equation, which have all been indispensable [1] to the

current state of field.

The application of QM allows one to accurately describe atomic and molecular systems, at this nanoscopic level, and potential chemistries they might undertake through determination of a central quantity known as the wavefunction, which encodes everything pertaining to the system of interest. The establishment of computational systems, and their constant evolution, has allowed these descriptions to become increasingly accurate, and to be routinely applied to a plethora of species, differing in both size and composition, for numerous chemical properties. The field of computational chemistry has become an indispensable tool to research scientists, not only being used as a method of comparison in its own right, but in tandem with experimental data.

1.3 *Ab-initio* and Density Based Approaches

Herein, we work within the framework of the Born-Oppenheimer approximation (BOA) [4] and exclude non-relativistic effects. This simplification allows one to compute a potential energy surface (PES) upon which nuclei move when subject to an external potential generated by the electrons, we will explore this approximation in greater depth within Section 2.2.3. The BOA gives rise to various fundamental concepts such as bond lengths, bond and dihedral angles, and through a process known as geometry optimisation one can ultimately determine energetically favourable nuclear arrangements. Despite operating within this frozen nuclei approach exact wavefunctions are only available for the smallest of chemical systems due to the rapidly increasing scaling factor as the number of basis functions and electrons increase. This has led to the development of various approximated methods, which stem from the Hartree-Fock (HF) solution and tend towards the exact full configuration interaction (FCI) solution [5].

In order to attain the FCI wavefunction for say a small hydrocarbon such as methane (CH_4), within a 6-31G(d) one-electron basis, diagonalisation of an $M \times M$ matrix where $M = 1.9 \times 10^{19}$ and represents the total number of different configurations, $\binom{68}{8}$, must be performed. The matrix dimensionality will be reduced when

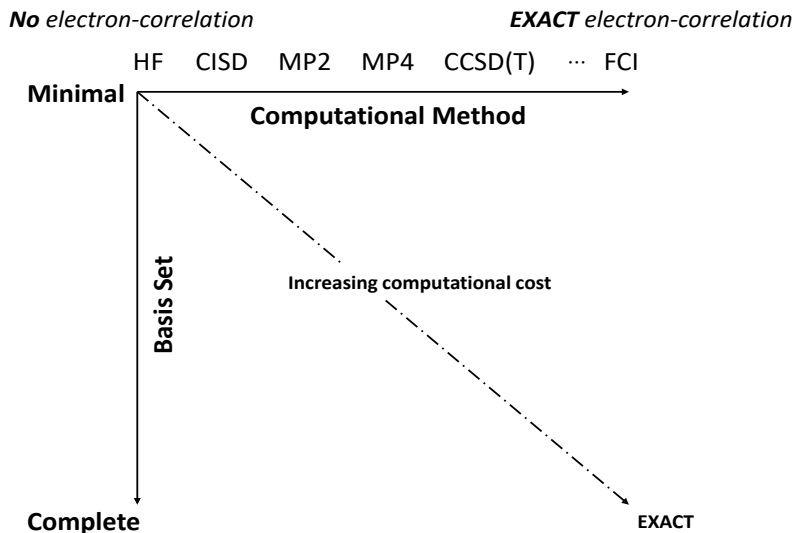


Figure 1.1: *Pople's diagram which highlights the relationship between various computational methods of increasing complexity and basis sets, the upper and lower limits of each has also been included. The graph is not drawn to scale.*

spatial and spin symmetry of the wavefunction is taken into consideration, however, this still highlights the unviable nature of this method for practically all systems, and hence the need for these approximated methods. These approximate *ab-initio* methods may consider only a portion of the configurational space in either an ordered approach, such as truncated configuration interaction (CI), multi-reference (MR)CI, complete active space self consistent field (CASSCF) [6] and truncated coupled cluster (CC) [7–9], or in a stochastic regime such as Monte-Carlo CI (MCCI) [10–12]. In conjunction to the above methods there are also those that utilise perturbation theory (PT), known as Møller-Plesset PT (MPPT) [13]. The applicability of these methods is not solely down to the computational cost but also the MR nature of the system to be described. The methods of truncated CI and CC, for example CISD and CCSD where up to double electron excitations relative to the HF wavefunction are considered, and MPPT, are known to provide accurate descriptions when the HF wavefunction dominates and thus only contains small contributions from all other configurations. These systems are commonly known as single reference systems, and the aforementioned techniques can routinely be applied to systems that contain tens of atoms [5]. However, as the contribution of the HF wavefunction depletes, particularly important as geometries deviate from their equilibrium arrangement

and configurations approach degeneracy, these methods do not give an accurate description, and thus methods such as MRCI, CASSCF and MCCI must be employed instead. These MR methods can become computationally intractable, once again due to the sheer number of configurations that must be considered, and also are less black box than single reference methods, especially in CASSCF as one must define an active-space that must be chemically relevant to the problem at hand.

The methods outlined above build upon the HF wavefunction, however, of increasing popularity are those which utilise the electronic density due to the favourable trade-off between accuracy and computational expense, termed density functional theory (DFT) [14, 15]. These methods are inherently single-reference and scale similarly to HF despite a generally drastic increase in the accuracy of such a calculation. The density based approaches rely heavily on the approximations used to determine the specific exchange-correlation functional ($E_{xc}[\rho]$), if this potential was known DFT would be an exact theory. Furthermore, as the true nature of $E_{xc}[\rho]$ is unknown one cannot systematically improve each functional, leading to the copious number of functionals that can be found in any electronic structure theory software package such as Gaussian 16 [16] or MOLPRO [17, 18]. It is therefore the role of the computational chemist to ensure that the level of theory employed, whether that be within the context of wavefunction or DFT, is adequate to describe the problem at hand whilst still remaining in the realms of feasibility.

1.4 High-Accuracy Composite Methods

In standard transition state theory, a reaction proceeds from energetically favourable reactants to products, *via* a higher energy transition state (TS) along the reaction coordinate [5]. These stationary points on the PES can be a minimum along all nuclear vibrational modes, generating a local minimum structure, global if the entire surface is known and this arrangement provides the lowest energy, or a maximum along the vibrational mode corresponding to the reaction coordinate and minima along all others. Therefore, high accuracy geometries and corresponding energies are of great importance to ensure that reaction energetics are sufficiently described.

This has led to the development of QM composite techniques, such as Gaussian- m theories ($m = 2, 3$ or 4) [5, 19] or complete basis set (CBS) methods [20, 21], which perform a series of optimisation and single-point energy computations at varying levels of theory, and ultimately aim for chemical accuracy. It is common to provide these reaction energetics in terms of thermodynamic quantities *via* enthalpic and entropic corrections to electronic, vibrational, rotational and translational energy levels. This is commonly achieved by invoking the ideal gas rigid rotor harmonic oscillator (IGRRHO) approximation to the aforementioned energy levels and omitting all contributions from excited electronic states.

1.5 Molecular Dynamics

The methods outlined above all rely on accurate determination of the electronic structure for the system of interest. However, methods also exist in which the atomic framework is not sub-divided into the constituent electronic and nuclei segments but instead atoms are handled as point particles, with the potential energy attained *via* force-fields. These methods are termed molecular mechanical and represent the remaining half of computational chemistry, with the other being quantum mechanical in nature. These methods have gained popularity primarily in the biological community as they can readily handle proteins or systems with thousands of atoms, far larger than the aforementioned *ab-initio* or density based approaches. Within these methods the specific force-field implemented is of central importance as they are used to determine the potential energy, which is given relative to a natural set of parameters [5]. Therefore one must ensure that the force-field contains all the terms necessary to describe the system. A technique that relies on a force-field, that is of interest within the context of this thesis, is molecular dynamics (MD). This approach uses Newton’s equation of motion to investigate the evolution of a chemical system in various different environments, such as immersing in solvent, allowing one to explore the configurational landscape of a protein or molecule under these conditions, and other properties that may change throughout a dynamical chemical system. From the potential energy one can determine the force on all the

atoms, which subsequently can be used to generate the trajectories of the atoms *via* numerical integration of Newton’s second law of motion, this process is repeated until the simulation has reached its end point.

1.6 Thesis Overview

A brief outline of each chapter within this thesis follows. In Chapter 2 the underlying principles of theoretical and computational chemistry are explored in considerable detail. We initially consider various *ab-initio* wavefunction methods before switching to a density based approach. The process of geometry optimisation, validation of resulting conformations and also computation of thermochemical properties are also outlined. The chapter concludes with a brief overview of MD.

In Chapter 3 we consider an approximate wavefunction based method known as MCCI, initially developed in 1995 by Greer [10]. This method takes advantage of the sparseness inherent to the Hamiltonian matrix and has been shown to generate extremely compact wavefunctions of FCI quality. MCCI has been readily applied to the determination of ground state PESs [22], excitation energies [23] complicated transition metal systems [24] and has been recently extended to include spin-orbit coupling [25]. However, to the best of our knowledge the optimality of these stochastically generated wavefunctions has never been explored. To explore this we employ a modification to the established algorithm allowing for a more systematic consideration of the configurational space and compare against this existing model [26]. We initially benchmark this novel model on a single neon atom before investigating the PES corresponding to the double hydrogen dissociation in H₂O, the first *A*₁ excited state in CO and a particularly challenging point of the chromium dimer PES. These systems were chosen due to the varying complexity in the electronic structure.

In Chapter 4 we investigate two different classes of intramolecular Diels-Alder (IMD-A) reactions *via* high accuracy thermochemical CBS-QB3 computations. It has been outlined previously that the addition of a halogen species into the aromatic diene led to more rapid reactions, contrary to simple chemical intuition, and their reactivity could not be explained solely through frontier molecular orbital (FMO)

interactions [27–30]. In the first part we explore incorporation of an extremely electron withdrawing nitro group at position 5 of the furan ring in conjunction with di-methylation of the dienophile. We explore these reactions not only in terms of thermodynamic and kinetic energetics but also of the nature and subsequent energy gap of the FMOs, to investigate if they undergo a normal or inverse electron demand process. The asynchronicity of the distance between the σ bond forming carbon atoms was also explored. In the second part of this study we investigate a structure energy-correlation that is known to exist in IMD-A substrates in which two σ bonds are formed between the same types of atoms [31]. We extend this to hetero IMD-A molecules in which one σ bond is formed between two carbon atoms with the other between a carbon and oxygen atom. The overall thermodynamic and kinetic energetics are also provided for these hetero IMD-A reactions.

In Chapter 5 we undertake a comparison of the ionisation potential attained from experimental and theoretical techniques for a range of π -conjugated materials that have use as electron donors in organic optoelectronics. As a result of the large system sizes we are limited to a DFT based approach. We begin with an initial benchmarking study of both the functional and basis set, and note the importance of including an implicit solvent model to simulate the organic thin film environment. The simple computational model is then altered to observe the effect of stacking on the approximated ionisation potential, which would be observed within highly ordered materials.

In Chapter 6 we turn our attention to the configurational landscape attained *via* MD simulations for two organic π -conjugated systems. Within the simulations a recently parameterised force-field for these materials was employed [32]. The configurational landscape was then explored using DFT to explore various properties such as the electronic energy, ionisation potential, optical gap and magnitude of the dipole moment for these two π -conjugated materials at varying backbone lengths. A brief statistical analysis of the aforementioned configurational landscape was then undertaken.

1.7 References

- [1] P. Atkins, R. Friedman, *Molecular Quantum Mechanics*, Oxford University Press Inc., New York, USA, **1997**.
- [2] A. Einstein, *Annalen der Physik* **1905**, *322*, 132–148.
- [3] A. Beck, *Volume 2: The Swiss Years: Writings, 1900-1909 (English translation supplement)*, Princeton University Press, Princeton, New Jersey, **1989**.
- [4] M. Born, J. Oppenheimer, *Annalen der Physik* **1927**, *84*, 457–484.
- [5] F. Jensen, *Introduction to Computational Chemistry*, John Wiley & Sons Ltd., West Sussex, England, **1999**.
- [6] P. A. Malmqvist, A. Rendell, B. O. Roos, *The Journal of Physical Chemistry* **1990**, *94*, 5477–5482.
- [7] J. A. Pople, R. Krishnan, H. B. Schlegel, J. S. Binkley, *International Journal of Quantum Chemistry* **1978**, *14*, 545–560.
- [8] R. J. Bartlett, *The Journal of Physical Chemistry* **1989**, *93*, 1697–1708.
- [9] I. Shavitt, R. J. Bartlett, *Many-Body Methods in Chemistry and Physics: MBPT and Coupled-Cluster Theory*, Cambridge University Press, **2009**.
- [10] J. C. Greer, *The Journal of Chemical Physics* **1995**, *103*, 1821–1828.
- [11] J. Greer, *Journal of Computational Physics* **1998**, *146*, 181–202.
- [12] L. Tong, M. Nolan, T. Cheng, J. Greer, *Computer Physics Communications* **2000**, *131*, 142–163.
- [13] C. Møller, M. S. Plesset, *Physical Review* **1934**, *46*, 618–622.
- [14] P. Hohenberg, W. Kohn, *Physical Review* **1964**, *136*, B864–B871.
- [15] W. Kohn, L. J. Sham, *Physical Review* **1965**, *140*, A1133–A1138.

- [16] M. J. Frisch, G. W. Trucks, H. B. Schlegel, G. E. Scuseria, M. A. Robb, J. R. Cheeseman, G. Scalmani, V. Barone, G. A. Petersson, H. Nakatsuji, X. Li, M. Caricato, A. V. Marenich, J. Bloino, B. G. Janesko, R. Gomperts, B. Mennucci, H. P. Hratchian, J. V. Ortiz, A. F. Izmaylov, J. L. Sonnenberg, D. Williams-Young, F. Ding, F. Lipparini, F. Egidi, J. Goings, B. Peng, A. Petrone, T. Henderson, D. Ranasinghe, V. G. Zakrzewski, J. Gao, N. Rega, G. Zheng, W. Liang, M. Hada, M. Ehara, K. Toyota, R. Fukuda, J. Hasegawa, M. Ishida, T. Nakajima, Y. Honda, O. Kitao, H. Nakai, T. Vreven, K. Throssell, J. A. Montgomery, Jr., J. E. Peralta, F. Ogliaro, M. J. Bearpark, J. J. Heyd, E. N. Brothers, K. N. Kudin, V. N. Staroverov, T. A. Keith, R. Kobayashi, J. Normand, K. Raghavachari, A. P. Rendell, J. C. Burant, S. S. Iyengar, J. Tomasi, M. Cossi, J. M. Millam, M. Klene, C. Adamo, R. Cammi, J. W. Ochterski, R. L. Martin, K. Morokuma, O. Farkas, J. B. Foresman, D. J. Fox, *Gaussian 09 Revision D.01*, Gaussian Inc. Wallingford CT, **2016**.
- [17] H.-J. Werner, P. J. Knowles, G. Knizia, F. R. Manby, M. Schötz, *Wiley Interdisciplinary Reviews: Computational Molecular Science* **2012**, *2*, 242–253.
- [18] H.-J. Werner, P. J. Knowles, G. Knizia, F. R. Manby, M. Schütz, P. Celani, W. Györffy, D. Kats, T. Korona, R. Lindh, A. Mitrushenkov, G. Rauhut, K. R. Shamasundar, T. B. Adler, R. D. Amos, S. J. Bennie, A. Bernhardsson, A. Berning, D. L. Cooper, M. J. O. Deegan, A. J. Dobbyn, F. Eckert, E. Goll, C. Hampel, A. Hesselmann, G. Hetzer, T. Hrenar, G. Jansen, C. Köppl, S. J. R. Lee, Y. Liu, A. W. Lloyd, Q. Ma, R. A. Mata, A. J. May, S. J. McNicholas, W. Meyer, T. F. Miller III, M. E. Mura, A. Nicklass, D. P. O'Neill, P. Palmieri, D. Peng, K. Pflüger, R. Pitzer, M. Reiher, T. Shiozaki, H. Stoll, A. J. Stone, R. Tarroni, T. Thorsteinsson, M. Wang, M. Welborn, *MOLPRO, version 2019.2, a package of ab initio programs*, **2019**.
- [19] C. W. Bauschlicher, H. Partridge, *The Journal of Chemical Physics* **1995**, *103*, 1788–1791.
- [20] J. A. Montgomery, M. J. Frisch, J. W. Ochterski, G. A. Petersson, *The Journal of Chemical Physics* **2000**, *112*, 6532–6542.

- [21] J. W. Ochterski, G. A. Petersson, J. A. Montgomery, *The Journal of Chemical Physics* **1996**, *104*, 2598–2619.
- [22] J. P. Coe, D. J. Taylor, M. J. Paterson, *The Journal of Chemical Physics* **2012**, *137*, 194111.
- [23] W. Györfy, R. J. Bartlett, J. C. Greer, *The Journal of Chemical Physics* **2008**, *129*, 064103.
- [24] J. Coe, P. Murphy, M. Paterson, *Chemical Physics Letters* **2014**, *604*, 46–52.
- [25] P. Murphy, J. P. Coe, M. J. Paterson, *Journal of Computational Chemistry* **2018**, *39*, 319–327.
- [26] A. Prentice, J. Coe, M. Paterson, *Journal of Chemical Physics* **2019**, *151*.
- [27] A. Padwa, K. R. Crawford, C. S. Straub, S. N. Pieniazek, K. N. Houk, *The Journal of Organic Chemistry* **2006**, *71*, 5432–5439.
- [28] K. R. Crawford, S. K. Bur, C. S. Straub, A. Padwa, *Organic Letters* **2003**, *5*, 3337–3340.
- [29] S. N. Pieniazek, K. N. Houk, *Angewandte Chemie International Edition* **2006**, *45*, 1442–1445.
- [30] R. L. Rae, J. M. Zurek, M. J. Paterson, M. W. P. Bebbington, *Organic and Biomolecular Chemistry* **2013**, *11*, 7946–7952.
- [31] J. M. Zurek, R. L. Rae, M. J. Paterson, M. W. P. Bebbington, *Molecules* **2014**, *19*, 15535–15545.
- [32] J. Wildman, P. Repiscak, M. J. Paterson, I. Galbraith, *Journal of Chemical Theory and Computation* **2016**, *12*, 3813–3824.

Chapter 2

Theoretical Background

2.1 Abstract

In this chapter a review of the main techniques used within computational chemistry, and the approximations, if any, that underpin them are explored in detail. The published texts of Jensen [1], Cramer [2] and, Szabo and Ostlund [3] provide excellent reviews of the field of computational chemistry.

2.2 Quantum Mechanics

2.2.1 Schrödinger Equation and the Wavefunction

As outlined in Section 1.2, the need for a set of rules governing physical phenomena at the atomic level was of widespread interest due to observed deviations with established classical models. This led to the development of quantum mechanics (QM), which fundamentally relies on the time-dependent Schrödinger equation (TDSE), providing a direct link between the system's energy and evolution. The TDSE is shown in equation 2.1 for a single particle system in three dimensional space, where Φ_n , the wavefunction, contains all possible information regarding the n^{th} state of the particle and \vec{r}_1 represents an arbitrary positional vector. Also contained within the TDSE is the Laplacian operator (∇^2), a second order partial differential operator, the mass of the specific particle (m) and the fundamental constants i and \hbar , which are the imaginary unit and the reduced Planck's constant respectively.

$$i\hbar \frac{\partial}{\partial t} \Phi_n(\vec{r}_1, t) = -\frac{\hbar^2}{2m} \nabla^2 \Phi_n(\vec{r}_1, t) + V(\vec{r}_1) \Phi_n(\vec{r}_1, t) \quad (2.1)$$

If the potential energy of the system does not contain an explicit time dependency, as is true above, the wavefunction can be constructed as the product of two distinct functions, one solely dependent on spatial coordinates [$\Psi_n(\vec{r}_1)$], the other on time [$\tau_n(t)$].

$$\Phi_n(\vec{r}_1, t) = \Psi_n(\vec{r}_1) \tau_n(t) \quad (2.2)$$

Through substitution of this trial solution into equation 2.1, and some basic algebraic manipulation, we arrive at the following equality between the two independent variables.

$$\frac{i\hbar}{\tau_n(t)} \frac{d}{dt} \tau_n(t) = -\frac{\hbar^2}{2m \Psi_n(\vec{r}_1)} \nabla^2 \Psi_n(\vec{r}_1) + V(\vec{r}_1) \quad (2.3)$$

For equation 2.3 to hold true for all possible values of \vec{r}_1 and t then each side must equal the same constant, which we will denote E_n and allow to represent the total energy of the n^{th} state of the system based upon the presence of kinetic and potential energy terms in the spatially dependant segment [4]. It is at this point

we arrive at the time-independent Schrödinger equation (TISE), as outlined below, where $\hat{\mathcal{H}}$ is the total energy operator commonly referred to as the Hamiltonian of the system.

$$\left[-\frac{\hbar^2}{2m} \nabla^2 + V(\vec{r}_1) \right] \Psi_n(\vec{r}_1) = \hat{\mathcal{H}} \Psi_n(\vec{r}_1) = E_n \Psi_n(\vec{r}_1) \quad (2.4)$$

The time-dependent segment, and the subsequent wavefunction, has the form of equation 2.5 and 2.6, respectively.

$$\frac{d}{dt} \tau_n(t) = \frac{-iE_n}{\hbar} \tau_n(t) \quad (2.5)$$

$$\Phi_n(\vec{r}_1, t) = \Psi_n(\vec{r}_1) e^{\frac{-iE_n t}{\hbar}} \quad (2.6)$$

The wavefunction is said to represent stationary states of the system as Born's statistical interpretation and the resulting expectation value of some quantum mechanical operator^{†1}, say $\hat{\mathcal{H}}$, contains no explicit time dependency as outlined in equation 2.7 and 2.8 respectively [5] where we have made use of Dirac's bra-ket notation.

$$\Phi_n^*(\vec{r}_1, t) \Phi_n(\vec{r}_1, t) d\vec{r}_1 = \Psi_n^*(\vec{r}_1) \Psi_n(\vec{r}_1) d\vec{r}_1 = |\Psi_n(\vec{r}_1)|^2 d\vec{r}_1 \quad (2.7)$$

$$\frac{\langle \Phi_n(\vec{r}_1, t) | \hat{\mathcal{H}} | \Phi_n(\vec{r}_1, t) \rangle}{\langle \Phi_n(\vec{r}_1, t) | \Phi_n(\vec{r}_1, t) \rangle} = \frac{\int_{-\infty}^{+\infty} \Psi_n^*(\vec{r}_1) \hat{\mathcal{H}} \Psi_n(\vec{r}_1) d\vec{r}_1}{\int_{-\infty}^{+\infty} \Psi_n^*(\vec{r}_1) \Psi_n(\vec{r}_1) d\vec{r}_1} = E_n \quad (2.8)$$

Born's interpretation of the wavefunction gives rise to the probabilistic nature that the particle will occupy the infinitesimal volume element $d\vec{r}_1$ centred on \vec{r}_1 . As the particle exists, and therefore must be located somewhere, integrating the

^{†1}Q.M. operators representing classical observables are both linear and hermitian, satisfying the respective equations:

- $\hat{\Omega}(c f(x) + d g(x)) = c \hat{\Omega} f(x) + d \hat{\Omega} g(x)$: for some arbitrary functions of x , scalars and operator,
- $\langle \Psi_m(x) | \hat{\Omega} | \Psi_n(x) \rangle = \langle \Psi_n(x) | \hat{\Omega} | \Psi_m(x) \rangle^*$.

probability density over all space must satisfy the equality outlined in equation 2.9 [5], resulting in normalised wavefunctions.

$$\int_{-\infty}^{+\infty} |\Psi_n(\vec{r}_1)|^2 d\vec{r}_1 = 1 \quad (2.9)$$

If we wish to explore the expectation value in greater depth it is necessary to introduce some key properties relating to the eigenfunctions of quantum mechanical observables; it should also be noted that the subsequent eigenvalues are real numbers i.e. $E_n \in \mathbb{R}$. The entire set of eigenfunctions form an orthonormal basis^{†2} in which any general function (Θ), within the same dimensionality, can be expressed as a linear combination of these functions as highlighted in equation 2.10 [4]:

$$\Theta(\vec{r}_1) = \sum_n^{\infty} c_n \Psi_n(\vec{r}_1) \quad (2.10)$$

where c_n is the expansion coefficient of the relevant basis function. The importance of this finding can be highlighted if we once again compute the expectation value but now implementing a constraint that $\Theta(\vec{r}_1)$ is not a known eigenfunction of the Hamiltonian.

$$\frac{\langle \Theta(\vec{r}_1) | \hat{\mathcal{H}} | \Theta(\vec{r}_1) \rangle}{\langle \Theta(\vec{r}_1) | \Theta(\vec{r}_1) \rangle} = \sum_{n,m}^{\infty} c_n^* c_m E_m \delta_{nm} = \sum_n^{\infty} |c_n|^2 E_n \quad (2.11)$$

This now expresses the expectation value as a sum of eigenvalues, each weighted by a factor corresponding to the absolute square of the appropriate expansion coefficient; prior normalisation of $\Theta(\vec{r}_1)$ has been assumed thus the denominator equals unity. If one represents the lowest-lying eigenvalue by E_0 , such that $E_n \geq E_0$, and rewrites equation 2.11 as follows:

$$\left[\underbrace{\left(1 - \sum_{n \neq 0}^{\infty} |c_n|^2 \right)}_{|c_0|^2} E_0 + \sum_{n \neq 0}^{\infty} |c_n|^2 E_n \right] = E_0 + \sum_{n \neq 0}^{\infty} |c_n|^2 (E_n - E_0) \quad (2.12)$$

it can easily be observed that the energy of some arbitrary function will never be

^{†2} $\langle \Psi_m(\vec{r}_1) | \Psi_n(\vec{r}_1) \rangle = \delta_{mn} = \delta_{nm} = 1$, iff $m = n$ else 0.

lower than the true energy, as the R.H.S. summation term will always be positive thus only ever increasing the energy. Herein, E_0 and E_n will be referred to as the ground and n^{th} excited state energy, respectively. The same notation will be used in regards to the wavefunction. This finding is universally known as the variational principle and is of utmost importance as one will never generate a lower energy than the true energy of the system for a suitable approximate wavefunction^{†3}.

$$\langle \Theta(\vec{r}_1) | \hat{\mathcal{H}} | \Theta(\vec{r}_1) \rangle \geq E_0 \quad (2.13)$$

It is evident that for this equality to hold the general function must be the exact ground state wavefunction i.e. $c_0 = 1$ and $\Theta(\vec{r}_1) = \Psi_0(\vec{r}_1)$.

As will be explored in the following sections for practically all chemical systems of interest one must approximate the wavefunction, and in turn the energy. The variational principle thus provides a tool to judge the quality of the approximations, with any improvements lowering the energy with the caveat that this will remain upper bound to the exact energy.

2.2.2 Molecular Hamiltonian

In order to delve deeper into the nature of Ψ we turn our attention back to the non-relativistic Hamiltonian operator, which is shown below for a chemical system containing Y nuclei and N electrons:

$$\hat{\mathcal{H}} = \left(- \sum_A^Y \frac{\hbar^2}{2m_A} \nabla_A^2 - \sum_i^N \frac{\hbar^2}{2m_e} \nabla_i^2 \right) + \frac{e^2}{4\pi\epsilon_0} \left(\sum_{B>A}^Y \frac{Z_A Z_B}{r_{AB}} + \sum_{j>i}^N \frac{1}{r_{ij}} - \sum_A^Y \sum_i^N \frac{Z_A}{r_{Ai}} \right) \quad (2.14)$$

where A and B run over all nuclei, i and j over all electrons, m_A and Z_A denote the mass and atomic number of nucleus A, respectively, and r_{ij} denotes the distance between electron i and j . Also present are various constants such as m_e , the mass of an electron, $-e$ the charge of said electron, ϵ_0 the vacuum permittivity and finally

^{†3} Must be suitable in a Q.M. sense: single valued, square-integrable and continuous (except for points at which the potential energy is infinite).

\hbar . The terms enclosed within the first parenthesis relate to the particle's kinetic energy with the latter containing both repulsive, electron-electron and nuclei-nuclei interactions, and attractive, electron-nuclei, potential energy terms. It is convenient to express $\hat{\mathcal{H}}$ in terms of internal coordinates, with the reference point taken to be the nuclei centre of mass system, the reason for this will become apparent in the text which follows [1]. This incorporates an additional term into $\hat{\mathcal{H}}$, known as the mass-polarisation, such that equation 2.14 becomes:

$$\hat{\mathcal{H}} = (\hat{T}_N + \hat{T}_e) + (\hat{V}_{NN} + \hat{V}_{ee} + \hat{V}_{Ne}) - \frac{1}{2M_{tot}} \left(\sum_i^N \nabla_i \right)^2 \quad (2.15)$$

where the kinetic and potential energy terms are represented by their respective operators and M_{tot} is combined mass of all nuclei present. As we are dealing with particles at the molecular level it is convenient to employ appropriate microscopic units, termed atomic units. The application of these units simplify $\hat{\mathcal{H}}$ as the associated mass and charge of each particle is defined as a multiple of m_e and e respectively. The value of \hbar and $4\pi\epsilon_0$ is also set equal to 1, and the unit of energy and distance now become a Hartree and Bohr respectively [3]. As per the TISE, mathematical operation of $\hat{\mathcal{H}}$ on Ψ provides the total energy-wavefunction eigenpair, however, this current formulation is only solvable for at most a two-particle system (i.e. a single hydrogen atom). Therefore, to proceed one must invoke approximations to simplify $\hat{\mathcal{H}}$ which will be outlined in the succeeding Section.

2.2.3 Adiabatic and Born-Oppenheimer Approximation

If we initially decompose $\hat{\mathcal{H}}$ into an electronic ($\hat{\mathcal{H}}^{elec.}$) and nuclear ($\hat{\mathcal{H}}^{nuc.}$) component, Ψ then becomes a product of an electronic ($\Psi^{elec.}$) and nuclear ($\Psi^{nuc.}$) wavefunction.

$$\hat{\mathcal{H}} = \hat{\mathcal{H}}^{elec.} + \hat{\mathcal{H}}^{nuc.} \quad (2.16)$$

$$\Psi = \Psi^{elec.} \Psi^{nuc.} \quad (2.17)$$

The $\hat{\mathcal{H}}^{elec.}$ and $\hat{\mathcal{H}}^{nuc.}$ operators have the following form:

$$\hat{\mathcal{H}}^{elec.} = \hat{T}_e + \hat{V}_{ee} + \hat{V}_{Ne} + \hat{V}_{NN} - \frac{1}{2M_{tot}} \left(\sum_i^N \nabla_i \right)^2 \quad (2.18)$$

$$\hat{\mathcal{H}}^{nucl.} = \hat{T}_N \quad (2.19)$$

where it should be noticed that the electronic term is dependent solely on the set of nuclear positions with no regards to their corresponding momenta. As a result of this the electronic wavefunction contains an explicit dependence on the set of electronic coordinates (\vec{r}_i) whilst depending parametrically on the nuclear framework (\vec{R}_A). The electronic Schrödinger equation has been given in equation 2.20 where the eigenpair now pertains to the electronic energy and wavefunction of state k respectively.

$$\hat{\mathcal{H}}^{elec.} \Psi_k^{elec.}(\vec{r}_i; \vec{R}_A) = E_k^{elec.}(\vec{R}_A) \Psi_k^{elec.}(\vec{r}_i; \vec{R}_A) \quad (2.20)$$

If all solutions to equation 2.20 are available one could expand the true wavefunction as a linear combination of the complete orthonormal set of eigenfunctions for $\hat{\mathcal{H}}^{elec.}$, with the expansion coefficients having a dependence on the nuclear coordinates [6], this has been highlighted in equation 2.21.

$$\Psi(\vec{r}_i, \vec{R}_A) = \sum_{k=1}^{\infty} \mathcal{X}_k(\vec{R}_A) \Psi_k^{elec.}(\vec{r}_i; \vec{R}_A) \quad (2.21)$$

$$\sum_{k=1}^{\infty} \hat{\mathcal{H}} \mathcal{X}_k(\vec{R}_A) \Psi_k^{elec.}(\vec{r}_i; \vec{R}_A) = E \sum_{k=1}^{\infty} \mathcal{X}_k(\vec{R}_A) \Psi_k^{elec.}(\vec{r}_i; \vec{R}_A) \quad (2.22)$$

If one operates on this linear expansion with $\hat{\mathcal{H}}$, see equation 2.22, pre-multiplies by the complex conjugate of an arbitrary electronic state, say $\Psi_l^{elec.}(\vec{r}_i; \vec{R}_A)$, and subsequently integrates over all electron coordinates, the following equation is generated. Moreover, the mass-polarisation term has been omitted as the pre-factor, $M_{tot.}^{-1}$, ensures this term has a negligible contribution relative to the others, resulting

in an approximated energy.

$$\begin{aligned}
 & - \sum_A^Y \frac{1}{2m_A} \nabla_A^2 \left| \chi_l(\vec{R}_A) \right\rangle + E_l^{elec.}(\vec{R}_A) \left| \chi_l(\vec{R}_A) \right\rangle \\
 & + \sum_{k=1}^{\infty} \left[\left\langle \Psi_l(\vec{r}_i; \vec{R}_A) \right| - \sum_A^Y \frac{1}{m_A} \nabla_A \left| \Psi_k(\vec{r}_i; \vec{R}_A) \right\rangle \nabla_A \left| \chi_k(\vec{R}_A) \right\rangle \right. \\
 & \quad \left. + \left\langle \Psi_l(\vec{r}_i; \vec{R}_A) \right| - \sum_A^Y \frac{1}{2m_A} \nabla_A^2 \left| \Psi_k(\vec{r}_i; \vec{R}_A) \right\rangle \left| \chi_k(\vec{R}_A) \right\rangle \right] \\
 & = E^{tot.} \left| \chi_l(\vec{R}_A) \right\rangle; l = 1, 2, \dots, \infty \quad (2.23)
 \end{aligned}$$

The third and fourth terms, commonly referred to as the non-adiabatic elements, couple the different electronic states *via* nuclear momenta. Within the adiabatic approximation all off-diagonal elements, i.e. when $l \neq k$, are neglected as it is expected that electronic states are sufficiently separated such that this term would have an insignificant contribution. For most systems this difference in energy between electronic states would be larger than the thermal energy at reasonable temperatures (T), which is represented by the following:

$$E_n - E_0 \gg k_B T \quad (2.24)$$

where k_B is the Boltzmann constant, thus somewhat validating the consideration of a sole electronic state. If one makes a further simplification by removing the diagonal correction we arrive at a central concept in electronic structure theory, the Born-Oppenheimer approximation (BOA) [7]. This omission is based upon the m_A^{-1} pre-factor, as even a single proton weighs a factor of ~ 1800 more than that of an electron, therefore this term would essentially be swamped by $E_l^{elec.}(\vec{R}_A)$. As the energetic difference between electronic states decreases these aforementioned approximations start to break down, as we must consider more than one electronic state and cannot treat the motion of nuclei and electrons independently as they are coupled *via* equation 2.23. However, for the vast majority of chemical systems these approximations are valid and only lead to small errors [1]. The Schrödinger equation, within the framework of the BO approximation, now takes the form of

equation 2.25:

$$\left[-\sum_A^Y \frac{1}{2m_A} \nabla_A^2 + E_l^{elec.}(\vec{R}_A) \right] |\chi_l(\vec{R}_A)\rangle = E_l^{tot.} |\chi_l(\vec{R}_A)\rangle \quad (2.25)$$

in which the eigenfunctions pertain to rotational and vibrational energy levels of the nuclear network and $E_k^{tot.}$ represents the total energy within the BOA approximation. Through systematic variation of \vec{R}_A , essentially treating each nuclei as a fixed point charge, and solving equation 2.20 for each particular arrangement, a potential energy surface (PES) can be constructed for each electronic state of interest. A PES thus represents the movement of nuclei subject to the potential generated by $E_l^{elec.}(\vec{R}_A)$ [3]. An example PES for the internuclear separation (IS) of an arbitrary diatomic system is shown in Figure 2.1.

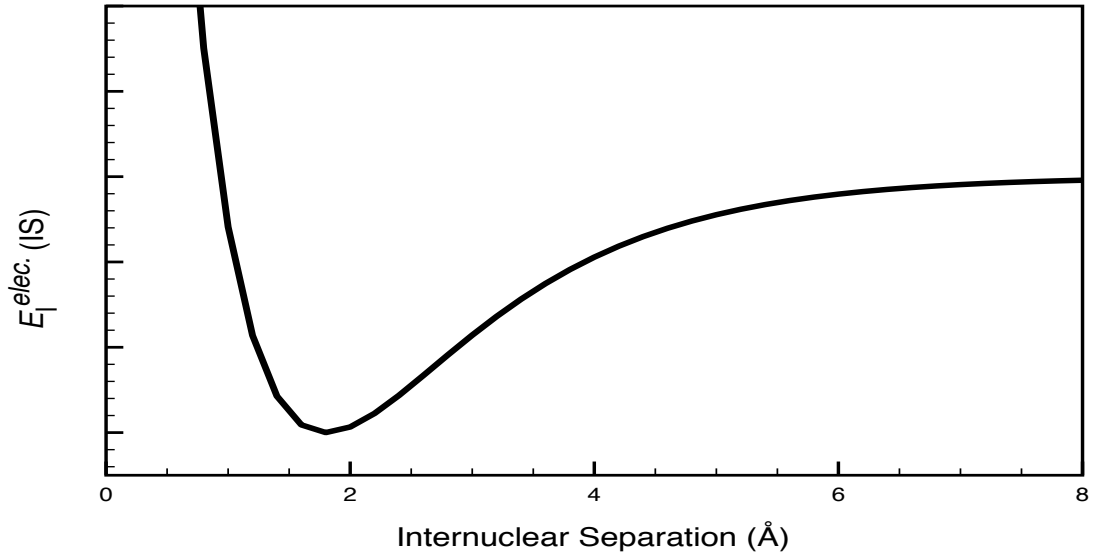


Figure 2.1: *Arbitrary PES for an example diatomic system. The scale of the y axis increases, however, specific values are arbitrary.*

From a PES surface one can locate various stationary points with respect to $E_l^{elec.}(\vec{R}_A)$ along all $3Y - 5$ and $3Y - 6$ internal coordinates, for linear and non-linear systems, respectively. The nature of these critical points along each coordinate allows classification of either minima, which are energetically favourable conformations, for example at the lowest energy separation ($IS_{eq.}$) in Figure 2.1 for which

$$\frac{d E_l^{elec.}(IS_{eq.})}{d IS_{eq.}} = 0; \frac{d^2 E_l^{elec.}(IS_{eq.})}{d IS_{eq.}^2} > 0 \quad (2.26)$$

or G^{th} order saddle points. For the specific case of $G = 1$ this is referred to as a transition state for which there is positive curvature along $3Y - 7$ coordinates with negative curvature along the remaining mode. These conformations are of great importance when modelling chemical species and reaction pathways as they allow determination of not only thermodynamic properties but also relevant activation barriers. This shall be further explored in Chapter 4 when we investigate the reaction pathways of various intramolecular Diels-Alder reactions.

However, despite operating within the context of electronic motion in a static nuclear potential, exact eigenfunctions of equation 2.20 would only be obtainable for one-electron systems, such as the H_2^+ or HeH^{2+} molecules, due to the presence of \hat{V}_{ee} . As all electron motion is coupled *via* coulomb repulsion, r_{ij}^{-1} , one cannot represent the true electronic wavefunction as a single product of single-variable functions, commonly termed the many-body problem within the chemical physics community. However, as a first approximation the wavefunction is represented as a combination of N one-electron functions, generating $N!$ individual terms to be precise, which subsequently reduces the many-electron repulsion to a single variable problem in which each electron is subject to the average field generated by the remaining $N - 1$ electrons [3]. If only a single-product of N one-electron functions was used this would be found to violate the anti-symmetry requirement and thus cannot be a suitable wavefunction to describe fermions. This approximation of the many-electron wavefunction as a single expression of N one-electron functions forms the basis of Hartree-Fock (HF) theory, which we will examine in greater depth below due to the widespread use in electronic structure theory as either, a starting point for post-HF algorithms or making additional approximations leading to semi-empirical methods. From herein, we shall remove the *elec.* superscript as this will be assumed and work within the realms of the aforementioned BO approximation, equating this energy to the exact energy of the system.

2.3 Hartree-Fock Theory

In order to fully describe an electron one must also specify a spin component, in addition to the three spatial coordinates, which can either be spin up $[\alpha(\omega)]$ or spin down $[\beta(\omega)]$, despite not being explicitly included in $\hat{\mathcal{H}}$. We now introduce the concept of a spin orbital $[\chi_j(\vec{\mathbf{x}}_i)]$, a wavefunction describing a single electron. Spin orbitals are composed of a spatial orbital (ψ_j) and a spin function (σ_j):

$$\chi_j(\vec{\mathbf{x}}_i) = \psi_j(\vec{r}_i)\sigma_j(\omega) \quad (2.27)$$

where $\vec{\mathbf{x}}_i$ incorporates the four degrees of freedom with respect to electron i . It can easily be observed that for every spatial function there are two spin functions, sharing the same spatial orbital but with opposing spins. It is also assumed that the spatial (spin) orbitals form an orthonormal set. Suppose we dissect $\hat{\mathcal{H}}$ into one and two-electron operators as per equation 2.28.

$$\hat{\mathcal{H}} = \sum_{i=1}^N \hat{h}_i + \sum_{j>i}^N \hat{g}_{ij} + \hat{V}_{NN} \quad (2.28)$$

$$\hat{h}_i = -\frac{1}{2}\nabla_i^2 - \sum_A^Y \frac{Z_A}{r_{Ai}} \quad (2.29)$$

$$\hat{g}_{ij} = r_{ij}^{-1} \quad (2.30)$$

If we initially disregard electron-electron repulsion the full Hamiltonian would just be a sum of one-electron operators, this approach is commonly referred to as the independent-electron approximation (IEA). A possible eigenfunction of this reduced Hamiltonian operator would be a product of spin orbitals, as highlighted in equation 2.31, where the indistinguishability of electrons has been removed as electron 1 occupies χ_i , electron 2 occupies χ_j and so on [3]. The corresponding eigenvalue would thus be a summation of the relevant orbital energies.

$$\Psi^{IEA}(\vec{\mathbf{x}}_1, \vec{\mathbf{x}}_2, \dots, \vec{\mathbf{x}}_N) = \chi_i(\vec{\mathbf{x}}_1) \chi_j(\vec{\mathbf{x}}_2) \dots \chi_N(\vec{\mathbf{x}}_N) \quad (2.31)$$

As one would expect neglecting the electronic interaction is a somewhat crude approximation, however, the resulting wavefunction also fails to satisfy the anti-symmetry principle rendering them redundant unless modifications are made. This requirement states that the wavefunction must change sign if the coordinates of two electrons are interchanged, see equation 2.32, subsequently prohibiting more than one electron occupying any spin orbital at a given time, this gives rise to the more generally known Pauli exclusion principle. This anti-symmetry constraint inherently introduces correlation, commonly referred to as exchange correlation, between electrons with parallel spin as the probability of them occupying the same spatial orbital is zero, which is not the case for electrons of opposing spin.

$$\pm \Psi(\vec{\mathbf{x}}_1, \vec{\mathbf{x}}_2, \dots, \vec{\mathbf{x}}_N) = \mp \Psi(\vec{\mathbf{x}}_2, \vec{\mathbf{x}}_1, \dots, \vec{\mathbf{x}}_N) \quad (2.32)$$

If we wish to satisfy this condition one can represent the many-electron anti-symmetric wavefunction by a single Slater determinant (SD), generating the Hartree-Fock wavefunction (Ψ^{HF}), as outlined in equation 2.33 for N electrons occupying N spin orbitals:

$$\Psi^{HF}(1, 2, \dots, N) = \frac{1}{\sqrt{N!}} \begin{vmatrix} \chi_i(1) & \chi_j(1) & \dots & \chi_N(1) \\ \chi_i(2) & \chi_j(2) & \dots & \chi_N(2) \\ \vdots & \vdots & \dots & \vdots \\ \chi_i(N) & \chi_j(N) & \dots & \chi_N(N) \end{vmatrix} = |\chi_i(1)\chi_j(2)\dots\chi_N(N)\rangle \quad (2.33)$$

with the pre-factor ensuring normalisation and 1 implying the set of four coordinates describing electron 1, i.e. $\chi_i(\vec{\mathbf{x}}_1) = \chi_i(1)$, etc. The shorthand notation, final term of equation 2.33, only explicitly states the main diagonal with the normalisation constant also implied. As stated earlier, representing the wavefunction in this fashion forms the basis of HF theory [1]. An expression for the energy of a SD can be attained

via application of Slater-Condon rules [3]:

$$E^{HF} = \sum_a^N \underbrace{\langle \chi_a(1) | \hat{h}(1) | \chi_a(1) \rangle}_{h_{aa}} + \sum_a^N \sum_{b>a}^N \langle \chi_a(1) \chi_b(2) | \hat{g}_{12} | \chi_a(1) \chi_b(2) \rangle + \hat{V}_{NN} \quad (2.34)$$

where the final bra-ket of equation 2.34 can be further decomposed into a coulomb and exchange integral as follows.

$$\langle \chi_a(1) \chi_b(2) | \hat{g}_{12} | \chi_a(1) \chi_b(2) \rangle - \langle \chi_a(1) \chi_b(2) | \hat{g}_{12} | \chi_b(1) \chi_a(2) \rangle = \mathcal{J}_{ab} - \mathcal{K}_{ab} \quad (2.35)$$

$$\mathcal{J}_{ab} = \int \int \rho_a(1) r_{12}^{-1} \rho_b(2) d\vec{r}_1 d\vec{r}_2 \quad (2.36)$$

$$\mathcal{K}_{ab} = \int \int \chi_a^*(1) \chi_b^*(2) r_{12}^{-1} \chi_b(1) \chi_a(2) d\vec{x}_1 d\vec{x}_2 \quad (2.37)$$

The coulomb term (\mathcal{J}_{ab}) has an easily understood classical interpretation as it represents the repulsion energy between two probabilistic electron densities described by $\rho_a(1)$ and $\rho_b(2)$, and integrated throughout all space. The exchange term (\mathcal{K}_{ab}) on the other hand is not so straightforward as it does not have a Newtonian counterpart, it is purely a quantum mechanical artefact arising from the aforementioned anti-symmetric requirement of the wavefunction. This attractive term is only found between spin orbitals which have parallel spin. As $\mathcal{J}_{aa} = \mathcal{K}_{aa}$ we can lift the summation restriction placed on the two-electron integral of equation 2.34, and such allow to run over all a and b , ensuring we pre-multiply by 2^{-1} . One may also wish to express the coulomb and exchange integrals by their respective operators acting on an occupied spin orbital:

$$\hat{\mathcal{J}}_b |\chi_a(1)\rangle = \left(\int \chi_b^*(2) \chi_b(2) r_{12}^{-1} d\vec{x}_2 \right) |\chi_a(1)\rangle = \left(\int \rho_b(2) r_{12}^{-1} d\vec{x}_2 \right) |\chi_a(1)\rangle \quad (2.38)$$

$$\hat{\mathcal{K}}_b |\chi_a(1)\rangle = \left(\int \chi_b^*(2) \chi_a(2) r_{12}^{-1} d\vec{x}_2 \right) |\chi_b(1)\rangle \quad (2.39)$$

where the only difference between the two is an interchange of the spin orbitals. As the true form of the N spin orbitals that constitute the HF wavefunction are

unknown, a trial or guess-wavefunction is generated. The resulting energy of which will never fall below the true value of the system as per the variation principle. Therefore, one can theoretically find the exact form of the HF wavefunction *via* minimisation of this trial energy with respect to the N spin orbitals, subject to the constraint that they retain their orthonormal relation. This constrained optimisation leads to the HF equation below:

$$\hat{f}(1) |\chi_a(1)\rangle = \left[\hat{h}(1) + \sum_b^N \left(\hat{\mathcal{J}}_b(1) - \hat{\mathcal{K}}_b(1) \right) \right] |\chi_a(1)\rangle = \varepsilon_a |\chi_a(1)\rangle; a = 1, 2, \dots, N \quad (2.40)$$

where $\hat{f}(1)$ is the one-electron Fock operator with the eigenvalue corresponding to the orbital energy of χ_a . As per equation 2.40, \hat{V}_{ee} has been reduced to a one-electron problem in which an electron occupying χ_a is subject to an electronic potential generated by the remaining $N-1$ electrons occupying $\{\chi_b\}$. Therefore we have shown that representing the wavefunction as an anti-symmetrised product of occupied spin orbitals treats the electronic repulsion in a mean-field fashion [3].

At this point it is customary to switch our attention from spin to spatial orbitals, through integration over the spin coordinate and using the orthonormal relations which follow.

$$\langle \alpha(\omega) | \alpha(\omega) \rangle = \langle \beta(\omega) | \beta(\omega) \rangle = 1 \quad (2.41)$$

$$\langle \beta(\omega) | \alpha(\omega) \rangle = \langle \alpha(\omega) | \beta(\omega) \rangle = 0 \quad (2.42)$$

In restricted closed-shell HF theory (RHF), each spatial orbital is occupied by two electrons of opposing spin, $\psi_i(j)$ and $\bar{\psi}_i(j+1)$, where the bar, or lack of, denotes spin down and up respectively. In terms of spatial orbitals the Fock operator and energy are given by equation 2.43 and 2.44:

$$\begin{aligned} \hat{f}(1) |\psi_j(1)\rangle &= \left[\hat{h}(1) + \sum_a^{N/2} \left(2 \hat{\mathcal{J}}_a(1) - \hat{\mathcal{K}}_a(1) \right) \right] |\psi_j(1)\rangle \\ &= \varepsilon_j |\psi_j(1)\rangle; j = 1, 2, \dots, \frac{N}{2} \end{aligned} \quad (2.43)$$

$$E^{HF} = 2 \sum_a^{N/2} h_{aa} + \sum_{a,b}^{N/2} \left(2 \mathcal{J}_{ab} - \mathcal{K}_{ab} \right) \quad (2.44)$$

where the integrals are over the spatial coordinates. As the coulomb and exchange operators in equation 2.43 involve summations over all occupied spatial orbitals, the Fock operator is therefore dependant on the eigenfunctions it generates. This adds a degree of complexity as the HF equations are non-linear and must be solved through an iterative self consistent-field (SCF) procedure [3], i.e. the set of orbitals used to construct the Fock-operator remain unchanged, albeit within a suitable tolerance threshold, throughout the cycle. A general overview of the SCF procedure is provided in Figure 2.2. As it stands the set of spatial orbitals $\{\psi_a\}$, that satisfy the above formulation of the Fock operator, represent the exact orbitals within the HF framework. However, to proceed in determining this occupied set of molecular orbitals (MOs) one subsequently expresses each as a linear combination of M fixed basis functions (ϕ_ν), thus removing the exactness of each MO as a finite basis is introduced.

$$\psi_i(1) = \sum_\nu^M c_{\nu i} \phi_\nu(1) \quad (2.45)$$

The true form of the basis functions will be explored in Section 2.4 but for now the above description will suffice. The unknown of interest is thus the expansion coefficient of each basis function for the relevant MO. Through substitution of equation 2.45 into 2.43, with further multiplication by ϕ_μ^* and integration over the space spanned by the basis set, one can generate the following:

$$\sum_\nu^M c_{\nu i} \langle \phi_\mu(1) | \hat{f}(1) | \phi_\nu(1) \rangle = \varepsilon_i \sum_\nu^M c_{\nu i} \langle \phi_\mu(1) | \phi_\nu(1) \rangle; \mu = 1, 2, \dots, M \quad (2.46)$$

or commonly expressed in terms of a Fock (**F**), overlap (**S**) and co-efficient (**C**) matrix, each of $M \times M$ dimensionality.

$$\sum_\nu^M F_{\mu\nu} C_{\nu i} = \varepsilon_i \sum_\nu^M S_{\mu\nu} C_{\nu i}; \mu = 1, 2, \dots, M \quad (2.47)$$

The **S** matrix arises as the basis functions need not form an orthogonal set, despite a need for resulting MOs to be. This representation of the MOs in an orthonormal

basis is generally known as Roothan-Hall scheme [8, 9]. The elements of the Fock

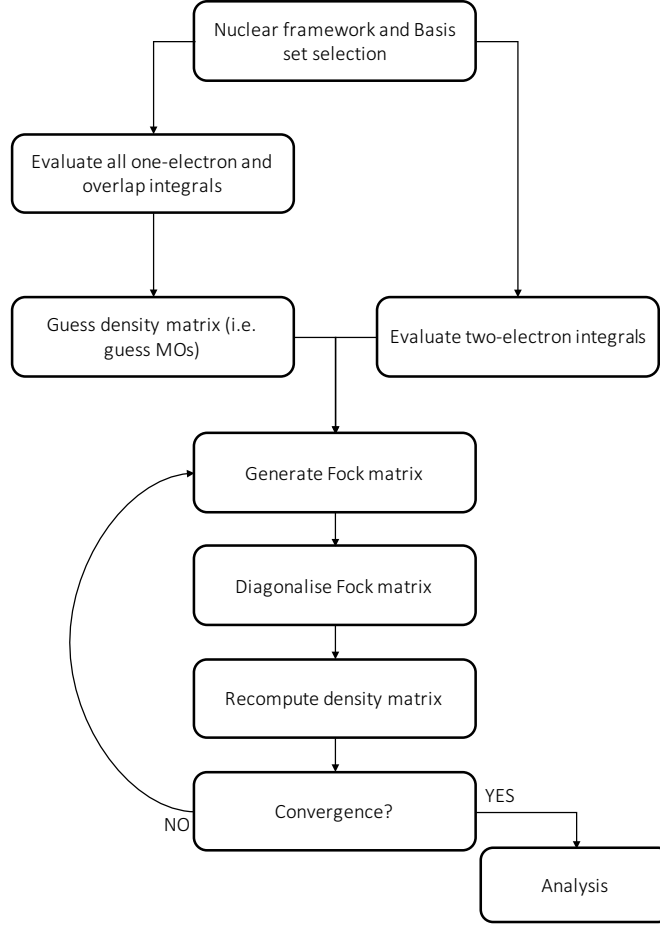


Figure 2.2: *General overview of an SCF procedure.*

operator within this basis representation have the following general form:

$$F_{\mu\nu} = \langle \phi_\mu(1) | \hat{h}(1) | \phi_\nu(1) \rangle + \sum_{\gamma}^M \sum_{\delta}^M D_{\gamma\delta} \langle \phi_\mu(1) \phi_\gamma(2) | \hat{g}_{12} | \phi_\nu(1) \phi_\delta(2) \rangle \quad (2.48)$$

where \mathbf{D} is a density matrix containing the unknown expansion coefficients of each basis function and is attained from the total charge density (ρ_{HF}) and using the MO expansion.

$$\rho_{HF} = 2 \sum_i^{N/2} |\psi_i(1)|^2 \quad (2.49)$$

$$\rho_{HF} = 2 \sum_i^{N/2} \sum_{\gamma}^M c_{\gamma i}^* \phi_{\gamma}^*(1) \sum_{\delta}^M c_{\delta i} \phi_{\delta}(1) = \sum_{\gamma\delta}^M \underbrace{\left[2 \sum_i^{N/2} c_{\gamma i}^* c_{\delta i} \right]}_{D_{\gamma\delta}} \phi_{\gamma}^*(1) \phi_{\delta}(1) \quad (2.50)$$

The one-electron terms are known as the core integrals, which involve both the

kinetic energy integrals ($T_{\mu\nu}$) and the attractive nuclei-electron potential ($V_{\mu\nu}^{nuc.}$), using the expansion for the one-electron operator as per equation 2.29. The two-electron component, which can be compactly written as $G_{\mu\nu}$, contains both the basis function density matrix and the set of all two-electron integrals.

$$F_{\mu\nu} = T_{\mu\nu} + V_{\mu\nu}^{nuc.} + G_{\mu\nu} \quad (2.51)$$

Also, in order to solve the Roothan-Hall equations in a standard matrix eigenvalue process the basis must be orthonormalised.

Therefore to summarise, within this regime a set of M eigenvectors and eigenvalues are obtained, each corresponding to a specific MO and energy, respectively. Of this set $\frac{N}{2}$ orbitals will be doubly occupied with the remaining, $M - \frac{N}{2}$, pertaining to virtual, or unoccupied, orbitals. The latter set also has no contribution to E^{HF} as the sum, for example that present in equation 2.44, is over all $\frac{N}{2}$ occupied orbitals only. As one increases the number of basis functions, towards the basis set limit, the limiting factor is thus evaluation of the vast amount of two-electron integrals with HF formally scaling as M^4 . However, approaches are available which can reduce this scaling factor such as integral screening, which omit integrals by introducing a cut-off threshold for the product of the density matrix elements with the two-electron integrals [1]. Thus within a SD approach this set of spatial orbitals correspond to an optimal set which minimises the energy.

2.3.1 Restricted and Unrestricted Hartree-Fock Theory

As outlined above two electrons of opposing spin share the same spatial component, resulting in doubly occupied MOs, which is normally termed as restricted-HF (RHF) theory. However, one may remove this restriction and allow the spatial orbitals containing α and β spin electrons to vary, this is known as unrestricted-HF (UHF). As the orbital flexibility has been increased the following relation will always hold.

$$E^{UHF} \leq E^{RHF} \quad (2.52)$$

For the majority of closed-shell systems, no unpaired electrons, around their equilibrium geometry RHF and UHF solutions are identical therefore the former approximation is valid, and is the common approach [1]. For systems containing an uneven number of α and β electrons, termed open-shell systems, one can once again employ a restricted or unrestricted treatment. As we are dealing with open-shell systems the restricted wavefunction is commonly termed restricted open-shell HF (ROHF) for which the doubly occupied orbitals are treated in an analogous fashion to that of RHF. However, if we consider an arbitrary system containing one extra β electron, resulting in a doublet spin state, this unpaired electron will interact differently with the remaining α and β orbitals, thus influencing the spatial distribution of the entire set. This spin polarisation effect is not modelled in a restricted regime only in the unrestricted counterpart.

The main benefits of RHF over UHF is the reduction of variational parameters, therefore reducing the computational expense, and the fact these are eigenfunctions of the total electron spin squared operator (\hat{S}^2), resulting in pure spin states. UHF wavefunctions suffer from a drawback known as spin-contamination in which higher-spin states are incorporated into the wavefunction [10], for a doublet this would correspond to a mixing of quartet, sextet, \dots , spin states, which have the effect of raising the energy through these nonphysical artefacts. However, on a single determinant level the energy lowering due to increasing number of variational parameters dominates and thus the relationship in equation 2.52 holds. If the spin contamination was found to dominate the UHF wavefunction would collapse to the restricted variant. The extent of spin-contamination increases with increasing spin polarisation and can be measured through comparison of the following:

$$\langle \Psi^{UHF} | \hat{S}^2 | \Psi^{UHF} \rangle = S_z(S_z + 1) + N_\beta - \sum_{i,j}^{occ.} \langle \psi_i | \bar{\psi}_j \rangle^2 \quad (2.53)$$

with the theoretical value of $S_z(S_z + 1)$, where $S_z = 0, \frac{1}{2}, 1, \frac{3}{2}$ for a singlet, doublet, triplet and quartet respectively. In equation 2.53, N_β is the number of electrons with β spin and the final term represents the spatial overlap between all pairs of α and β spin electrons with the summation over all occupied orbitals. This difference

must be small, it is common practice to limit this deviation to $< 10\%$, ensuring this unwanted consequence is kept to a minimum and the results are viable and meaningful. A similar methodology can be used for Kohn-Sham density functional theory [11, 12] which will be discussed in Section 2.7, a technique based upon the electron density at a point in space and not explicit approximation of the many-electron wavefunction. However, as a Kohn-Sham single determinant is introduced to determine the kinetic energy contribution to the energy the expectation value of \hat{S}^2 will be based upon a fully non-interacting system which must be remembered when using equation 2.53 [13]. The unrestricted variant of Kohn-Sham density functional theory is used in Chapter 5 and 6 when determining ionisation potentials, specifically to compute the energy of the ionised open-shell species.

Despite the aforementioned benefits RHF has its own major deficiencies, which become prevalent in systems for which the geometry deviates from the optimum arrangement. Suppose now we consider the ground state of molecular hydrogen for which we have two MOs, $|\sigma_g\rangle$ and $|\sigma_u\rangle$, pertaining to the in phase and out of phase overlap from the $1s$ orbitals, respectively. To illustrate this we use the distinction $1s_A$ and $1s_B$ to differentiate between the hydrogen atoms. As per equation 2.54, the Ψ^{RHF} contains equal amounts of covalent and ionic terms.

$$\Psi^{RHF} = \frac{1}{4} \underbrace{(1s_a(1)1s_a(2) + 1s_b(1)1s_b(2))}_{\text{ionic}} + \underbrace{(1s_a(1)1s_b(2) + 1s_b(1)1s_a(2))}_{\text{covalent}} \quad (2.54)$$

As the dissociation limit is reached the ionic contribution should be non-existent as bond cleavage would be homolytic, $\text{H}_2 \rightarrow 2 \times \text{H}^\bullet$. This is not the case in RHF as the ionic terms would still be present and contribute to 50 % of the wavefunction, therefore predicting energies that are too large. However, within an UHF approach, the ionic contribution can be nullified and therefore the correct dissociation products observed [1]. This subtly introduces a concept known as electron-correlation, which we will discuss in Section 2.5.

2.3.2 Koopmans' Theorem

As discussed previously the optimised RHF wavefunction contains a set of M optimised molecular orbitals, of which $\frac{N}{2}$ are doubly occupied and $M - \frac{N}{2}$ unoccupied. From Koopmans' theorem we can relate the negative energy of an occupied orbital to the exact energy required to remove an electron from the specific MO, thus giving a physical interpretation to these computed eigenvalues as they can be related to ionisation energies [14]. However, at the core of this relation is the frozen orbital approximation, as upon extraction of an electron from an N -electron SD to an $(N - 1)$ -electron SD the orbitals remain unchanged. To illustrate this consider we remove an electron from the occupied spin orbital χ_a , which is occupied in the N -electron SD and take the energy difference between the two [3].

$$E_N - E_{N-1} = h_{aa} + \sum_{i=1}^N (\mathcal{J}_{ia} - \mathcal{K}_{ia}) = \varepsilon_a \quad (2.55)$$

All the one-electron terms cancel except for that involving χ_a , with a similar finding for the two-electron terms. If one relates this to the highest occupied molecular orbital (HOMO) this would approximate the ionisation potential of the system. An analogous approach can be undertaken in regards to the electron affinity, however, this time it would pertain to the addition of an electron in an unoccupied orbital, generating an $(N + 1)$ -electron SD.

The frozen orbital approximation can be seen as a somewhat crude approach as the ionic systems would have their own optimal sets of MOs due to the varying electron density thus influencing the one and two-electron integrals between the system and that used as a reference. This discrepancy would become increasingly apparent as more electrons are removed, and thus the approximation to higher order ionisation potentials would be expected to be poorer. One may also question the validity of the electron-correlation deficient HF wavefunction in representing the true wavefunction, and therefore the inability to model phenomena for which we know electron-correlation is present.

2.4 Basis Sets

We now turn our attention to the nature of commonly employed basis sets in electronic structure theory methods. As per equation 2.45 the unknown orbitals are expanded in terms of M basis functions, leading to the aforementioned Roothan-Hall equations. These basis functions are commonly centered on the nuclei giving rise to the molecular orbital-linear combination of atomic orbitals (MO-LCAOs) model.

The first set of basis functions introduced were Slater-type orbitals (STOs) [15], having the form $e^{-\zeta r}$. These functions accurately describe the true nature of a $1s$ orbital, cusp at $r = 0$ and the exponential dependence on r as we move from the nucleus, however, are not used for molecular systems due to the time consuming nature of evaluating the electron integrals they generate. In order to overcome this Gaussian-type orbitals (GTOs) [16] are used, as the product of two Gaussian functions is in-fact a single Gaussian located between the two originals, thus greatly simplifying the one and two-electron integrals described above. A primitive-GTO (PGTO) has the following form:

$$\phi_{\zeta, l_x, l_y, l_z}^{PGTO}(x, y, z) = C x^{l_x} y^{l_y} z^{l_z} e^{-\zeta r^2} \quad (2.56)$$

where $r = \sqrt{x^2 + y^2 + z^2}$, ζ controls the width of each function, C is a normalisation constant and $l_x + l_y + l_z = 0, 1, 2, 3, 4$ for an s, p, d, f and g orbital respectively. Despite having computational benefits, a single PGTO fails to accurately model the behaviour at regions close to and far from the nuclei as no cusp observed at $r = 0$, for s orbitals, and the r^2 dependency ensures functions decrease too rapidly. Therefore a linear combination of fixed PGTOs, referred to as single contracted-GTO (CGTO), are taken to represent a STO, as this generates a better description at the aforementioned anomalous regions. The CGTO outlined in Figure 2.3 contained 3 PGTOs, for which we observe near identical description for $r \geq 1.2$ Bohr, the cusp is not modelled to the same degree and thus would require the addition of more PGTOs within the contraction.

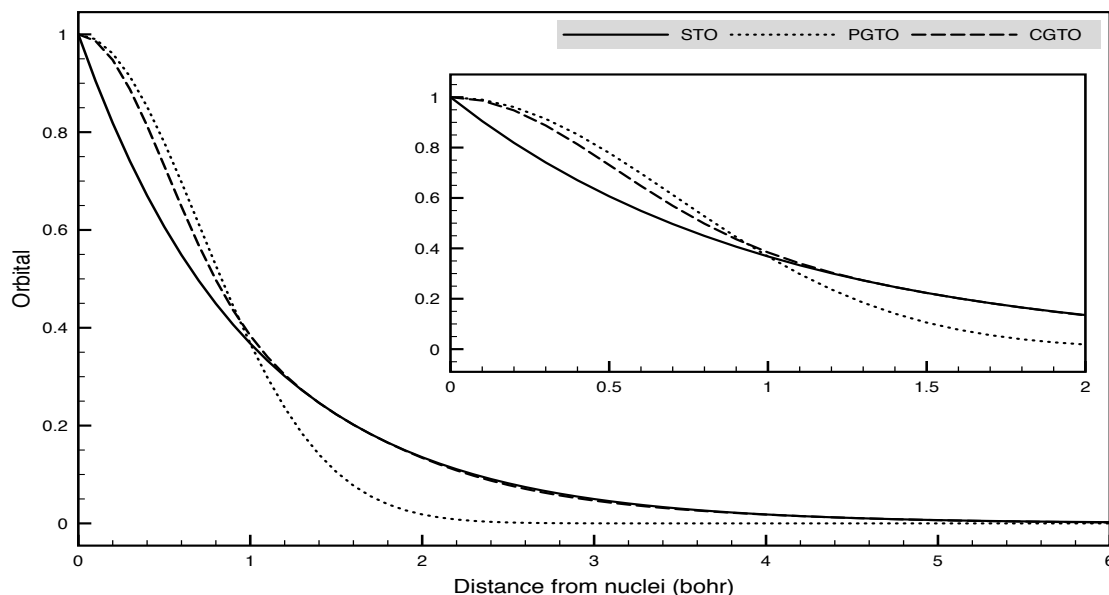


Figure 2.3: *Comparison of a generic STO, PGTO and CGTO 1s basis function.*

As electronic structure methods formally scale, at least, as M^4 , one must strike a balance between the number of basis functions, ensuring a level of accuracy, and being viable in a computational sense. One such approach to limit the number of variationally optimisable parameters is to represent each occupied orbital in the neutral atom(s) by a single CGTO containing v PGTOs, with v typically taking a value of 3 giving the STO-3G basis [17]. For 1st and 2nd row elements this would correspond to 1 (1s) and 5 (1s, 2s, 2p_x, 2p_y and 2p_z) basis functions respectively. It should be noted that 2p_{x,y,z} orbitals are still included for Lithium and Beryllium despite containing no electron in their neutral ground state. The coefficient and exponent of each individual PGTO within the CGTO is derived via fitting with the appropriate STO. It should also be noted within this basis set the exponents of each orbital relating to the same principal quantum number are the same.

An initial improvement upon this minimal approach is using two CGTO of varying exponents to describe each occupied orbital, known as a double- ζ basis set, triple- ζ and above would be formed in analogous fashion. Increasing the flexibility within each occupied orbital allows for a better description of the varying bonding network throughout the molecule. As electrons that are important in a chemical sense, such as those involved in bonding and photochemical events, reside in valence orbitals one would expect the subsequent core orbital(s), to be relatively well

described by their atomic counterpart as they would remain fairly unchanged even within the molecular environment. Therefore, it is common practice to treat the core orbitals as a single CGTO, containing more PGTOs than the valence orbitals, that have been pre-optimised by atomic calculations. Treating the valence and core orbitals with an uneven number of basis functions is known as a split-valence basis set.

The next improvement upon an n -tuple- ζ basis is the incorporation of higher angular momentum functions, most commonly of the valence orbital only. This increases the basis flexibility by allowing the orbitals shape to change, not just the size thus providing a more accurate description of the anisotropic electron density throughout the system, commonly termed angular correlation. For 1^{st} and 2^{nd} row elements this involves adding a set of p and d functions, with an exponent that is of the same order of magnitude as the most diffuse valence orbital.

A final basis set enhancement is the addition of diffuse functions, which are orbitals with exponents smaller, often by an order of magnitude, than the most diffuse valence orbital. These are essential when studying anionic systems, as the electronic density will spread further from the nuclei when compared to the neutral species for which the basis functions were optimised for. The two most common types of basis sets that have a widespread use in electronic structure theory are those of Pople and Dunning, a general overview of each follows.

We shall initially consider Pople style bases [18, 19] which are split-valence and have the form: p - qrs G, where p represents the number of PGTOs contained within the single CGTO describing a core orbital, qrs act in a similar fashion however pertain to the valence orbitals, of which are treated in a double (qr) or triple (qrs)- ζ framework. Therefore, a 6-311G basis [20] for a 2^{nd} row element would consist of 13 basis functions, $1s\ 2s\ 2s'\ 2s''\ 2p\ 2p'\ 2p''$ where ' indicates a more diffuse orbital. Once again, the exponent of each s - p shell is the same, as $\zeta_{2s} = \zeta_{2p}$, $\zeta_{2s'} = \zeta_{2p'}$ and $\zeta_{2s''} = \zeta_{2p''}$, albeit slightly hindering the molecular orbital flexibility but reducing the computational expense. This basis is commonly expressed in a PGTO \rightarrow CGTO contraction scheme i.e. $[11s\ 5p] \rightarrow [4s\ 3p]$. If one wishes to include orbitals of higher

angular momentum the following notation is used: $p - qrsG(t, u)$ where t and u relate to heavy atoms and hydrogen respectively. The diffuse valence orbitals are also added separately for heavy atoms and hydrogen through inclusion of $+$ and $++$ respectively. A 6-311+G(d,p) basis [20, 21] would therefore include a set of d and diffuse s - p orbitals on all heavy atoms, with added p functions on hydrogen in conjunction with the 13 functions outlined above.

Another class of basis sets are those of Dunning [22], which differ with regards to the pre-optimisation of each CGTO as this was via atomic electron correlated computations, and not by way of HF as is the case for Pople bases, the restriction of s - p shells sharing the same exponent has also been removed. These basis sets have the form: cc-pVXZ, where cc represents correlation-consistent, p is the addition of higher angular momentum orbitals and X represents the n-tuple- ζ of the valence orbitals. These basis sets are extremely balanced and converge to the complete basis limit as the value of X increases, as upon every increment one set of orbitals sharing the same and higher angular momentum are added. For 2^{nd} row elements, increasing the basis set from cc-pVDZ to cc-pVTZ [22] would result in over double the amount of available basis functions, $[3s\ 2p\ 1d]$ to $[4s\ 3p\ 2d\ 1f]$, respectively. The inclusion of diffuse functions for each angular momentum type is represented by aug, for example aug-cc-pVDZ [22, 23] would add $[1s\ 1p\ 1d]$ per 2^{nd} row atom. Therefore, appropriate selection of a basis set for the problem at hand is of utmost importance if meaningful results are to be obtained.

2.5 Electron Correlation

The accurate description of electron-electron interactions has long been the crux of electronic structure methods. Within HF theory the electron repulsion is approximated in a mean-field fashion thereby overestimating this interaction, when compared to reality as all electron motion should be instantaneously correlated, resulting in electrons encroaching on one another to a larger degree. Despite the inherent correlation of electrons with parallel spins, *via* the presence of exchange terms ensuring no two parallel spin electrons can occupy the same region of space,

resulting wavefunctions are termed uncorrelated as no analogous term for opposing spin electrons is present. This inability to sufficiently describe the true nature of the repulsion gives rise to the electron correlation energy ($E^{corr.}$), a negative value representing the difference between E^{RHF} and the true energy of the system (E^{Exact}).

$$E^{corr.} = E^{Exact.} - E^{RHF} \quad (2.57)$$

Herein, we will remove the RHF superscript as this it is assumed we are working with closed shell systems and will be explicitly stated otherwise. A single SD approach captures the vast majority of the energy for most chemical systems around their equilibrium geometries, with $E^{corr.}$ typically contributing $\sim 1\%$ to the total energy when a considerable basis set is used [3]. However, there are also cases in which $E^{corr.}$ has a dramatic effect on the energy and as such must be accounted for, such as at large internuclear separations in diatomic molecules. As $E^{corr.}$ varies throughout the PES, insufficient recovery can become problematic when providing reaction energetics, see Figure 2.5 for an example of this.

Electron correlation can be divided into two separate components, termed static and dynamic correlation, this is not a rigorous separation and the two are still somewhat intertwined. The former represents situations for which various electronic configurations become close to degeneracy, and as such the wavefunction would have a significant contribution from more than one configuration, thus representation by a single configuration would be a severe misrepresentation. This type of correlation is highly system dependent and is not always applicable. Dynamic correlation is a more universal type contribution and is related to the correlation of electron motion, for which many configurations are included with small expansion coefficients in the total wavefunction. A distinction between the two has been outlined below for a fictitious wavefunction:

$$|\Psi^{arb.}\rangle = 0.67 |\Psi^{HF}\rangle + 0.67 |\Psi^1\rangle + \sum_{k=2}^W c_k |\Psi^k\rangle \quad (2.58)$$

where W is large and $c_r |\Psi^r\rangle$ represents the contribution of each arbitrary config-

uration where $|\Psi^{HF}\rangle \neq |\Psi^r\rangle$. As can be seen for this system the two degenerate configurations contribute to 90 % of the total energy of the wavefunction, representing the static portion, with the remaining 10 % split over W configurations, thus representing the dynamic portion. In order to attain credible energies the approach should provide a balanced treatment of both static and dynamic correlation. We will now explore various post HF methods that use different underlying techniques in order to recover this correlation energy either exactly, or a significant portion.

2.6 Post Hartree-Fock Techniques

The methods discussed in the following section are commonly referred to as post HF methods as they build upon the converged HF wavefunction in one of two ways. One involves expanding the wavefunction as a linear combination of different SDs with the other being based on a perturbation to an already known problem.

2.6.1 Configuration Interaction

The simplest post HF method is that of configuration interaction (CI) theory [3, 24]. This method has the potential to recover both static and dynamic correlation by promoting electrons in occupied orbitals to those contained in the valence set, essentially representing the true wavefunction as a linear combination of all the potential N -electron determinants that can be formed from a given set of MOs. A generic CI wavefunction takes the following form:

$$|\Psi^{FCI}\rangle = c^{HF} |\Psi^{HF}\rangle + \sum_{a,r} c_a^r |\Psi_a^r\rangle + \sum_{a<b, r<s} c_{ab}^{rs} |\Psi_{ab}^{rs}\rangle + \sum_{a<b<c, r<s<t} c_{abc}^{rst} |\Psi_{abc}^{rst}\rangle + \dots \quad (2.59)$$

where a, b, c and r, s, t relate to the occupied and virtual orbitals, respectively. As all potential determinants can be formed *via* excitations from Ψ^{HF} , it is common to only indicate the MOs which are involved in the substitution. If we take the specific example $c_a^r |\Psi_a^r\rangle$ this would relate to a single excitation, for which an electron in the

occupied spin orbital, χ_a , is promoted to the virtual spin orbital, χ_r . If all N -tuple excitations are considered this is termed Full-CI theory, and would equate to the true wavefunction (Ψ^{FCI}) and energy (E^{FCI}) of the system, within the space spanned by the one-electron basis set^{†4} [25]. The number of potential SDs that can be generated, including Ψ^{HF} , is given by the binomial coefficient outlined in equation 2.60.

$$\text{Number of SDs} = \binom{2M}{N} = \frac{(2M)!}{N!(2M-N)!} \quad (2.60)$$

To illustrate the concept of FCI theory we shall once again consider molecular hydrogen, as described by the STO-3G minimal basis set, this would correspond to the six determinants shown in figure 2.4(b), with varying occupation of the bonding $|\sigma_g\rangle$ and anti-bonding $|\sigma_u\rangle$ MO. As $|\Psi^{HF}\rangle$ for this system is a closed-shell singlet, with overall g symmetry due to the double occupation of $|\sigma_g\rangle$, only configurations that retain this spatial and spin symmetry can contribute to $|\Psi^{FCI}\rangle$ [3]. This reduces $|\Psi^{FCI}\rangle$ to solely two terms, that represent the double occupation of $|\sigma_g\rangle$ and $|\sigma_u\rangle$, with the coefficients determined via a constrained variational optimisation procedure. It should be noted that the set of HF orbitals remain unchanged throughout this optimisation.

Currently, such FCI treatments are computationally intractable for all but the smallest of systems and basis sets due to the rapidly increasing dimensionality of the Hamiltonian matrix (\mathbf{H}^{FCI}), that must be diagonalised, as the number of basis functions increase. This technique formally scales as $M!$ in the large basis set limit, with an arbitrary \mathbf{H}^{FCI} outlined in 2.61 where S, D, T, ... represent all single, double, triple ... excitations respectively. To put this into context a FCI computation on H_2O , within a cc-pVDZ basis and the $1s$ MO of oxygen doubly occupied in all configurations, would require consideration of a $\sim (3 \times 10^7) \times (3 \times 10^7)$ matrix. This is an upper bound value as configurations would be removed due to the spin and spatial requirements outlined above. It should also be noted that the expectation value of $\hat{\mathcal{H}}$, for configurations that differ by the occupation of 3 spin orbitals gives 0,

^{†4}If a complete basis set is used then this would correspond to E , commonly termed Complete CI.

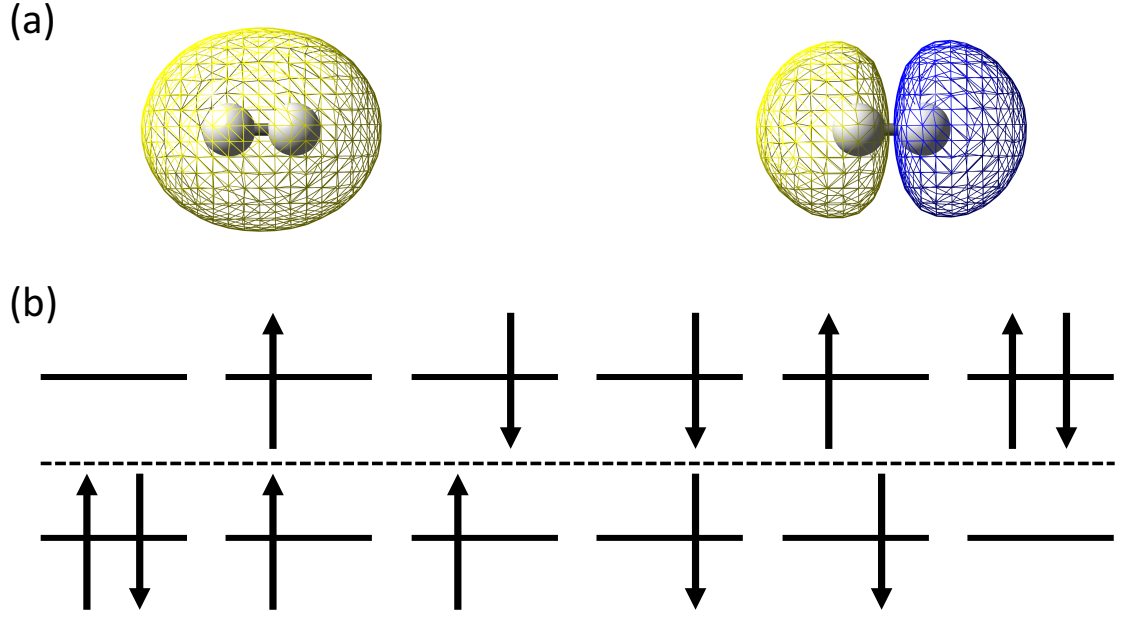


Figure 2.4: (a) $|\sigma_g\rangle$ and $|\sigma_u\rangle$ MO's respectively. (b) Six potential configurations for H_2 , highlight varying occupation of $|\sigma_g\rangle$ (lower) and $|\sigma_u\rangle$ (upper).

allowing further simplification of \mathbf{H}^{FCI} as many matrix elements involve these [3].

$$\begin{array}{c}
 \langle \Psi^{HF} | \\
 \langle S | \\
 \langle D | \\
 \langle T | \\
 \vdots
 \end{array}
 \begin{pmatrix}
 \langle \Psi^{HF} | \hat{\mathcal{H}} | \Psi^{HF} \rangle & 0 & \langle \Psi^{HF} | \hat{\mathcal{H}} | D \rangle & 0 & \dots \\
 \langle S | \hat{\mathcal{H}} | S \rangle & \langle S | \hat{\mathcal{H}} | D \rangle & \langle S | \hat{\mathcal{H}} | T \rangle & \dots & \\
 \langle D | \hat{\mathcal{H}} | D \rangle & \langle D | \hat{\mathcal{H}} | T \rangle & \dots & & \\
 \langle T | \hat{\mathcal{H}} | T \rangle & \dots & & & \\
 \vdots & \dots & & &
 \end{pmatrix}
 \quad (2.61)$$

As we build upon the converged $|\Psi^{HF}\rangle$, one can also omit the elements that involve mixing of this state and the entire set of singles, known as Brillouin's theorem. This is a result of the elements equalling an off diagonal element in the Fock matrix, that must be diagonalised if we are to obtain $|\Psi^{HF}\rangle$ [1]. Despite not interacting directly with $|\Psi^{HF}\rangle$ they still have a contribution, mixing with the set of double and triples.

It is not possible to predict the importance of each configuration prior to diagonalisation, however, of all new determinants it is usually doubly excited configurations which are found to have the largest impact. Therefore, it is a common approach

to limit the potential excitation space to differ at most by two MOs. This truncation method, formally known as CISD [24], significantly reduces the computational expense whilst still recovering a large portion of E^{corr} . This approach formally scales as M^6 . However, truncating the FCI space introduces another problem as the energies are no longer size-consistent, see equation 2.62. Consider a system containing two arbitrary atoms, $A + B$.

$$E_{IS \rightarrow \infty}^{CISD}(A + B) \neq E^{CISD}(A) + E^{CISD}(B) \quad (2.62)$$

For the above relation to hold, the energy of a system for which all individual nuclei are infinity separated, and thus non-interacting, should equal the sum of individual components. This is not the case for any truncated CI method, except when this treatment equates to FCI. If we once again relate this back to the aforementioned H_2 set-up, it can easily be observed, that CISD would equate to the exact energy within the one-electron basis. However, if we extend this to two H_2 molecules there would be a discrepancy between the energy of the fragments and the combined system. For the combined system a simultaneous double excitation of both individual H_2 molecules would never be reached within a CISD treatment as at most only two excitations can occur. This configuration would be present in the segmented approach, resulting in the aforementioned discrepancy between the two values. Therefore, as the system size increases the E^{CISD} energy would become less accurate. This inability to predict a linear scaling of the energy as the system size increases is sometimes referred to as a size-extensivity issue, however, this is predominately used for when there is an interaction, albeit very weak, between the separate units (i.e. ΔR of 4 Å) [1]. Outlined in Figure 2.5 below is the PES for a double hydrogen dissociation in H_2O , employing a cc-pVDZ basis, at the HF, CISD and FCI level of theory. The 1s orbital of oxygen was doubly occupied in all configurations.

As shown the inclusion of singles and doubles gives energies of FCI quality for O-H distances ≤ 2 Bohr, despite having a potential excitation space of only 0.03 % to that of FCI. However, above this separation the discrepancy between E^{FCI}

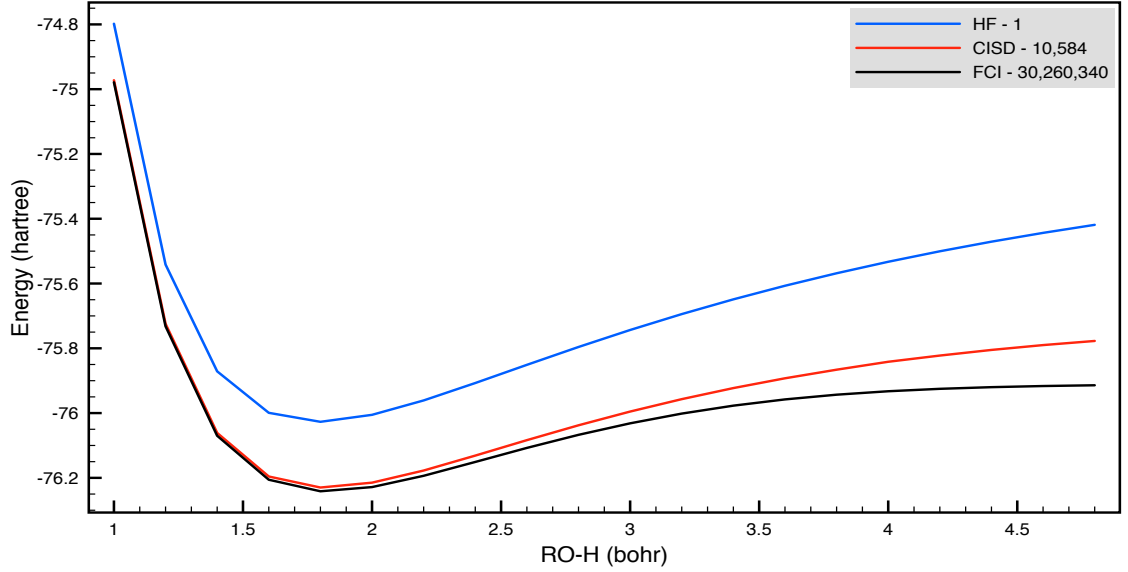


Figure 2.5: *PES for the double Hydrogen dissociation in H_2O , within a cc-pVDZ basis, for HF, CISD and FCI. The upper limit of SDs for each approach is located in the legend which has the following values: HF - 1, CISD - 10584 and FCI - 30260340. All computations were performed using Gaussian 09 [26].*

and E^{CISD} becomes apparent as higher order excitations become important to the wavefunction. One can also extend these methods to include triples and quadruples, resulting in CISDT and CISDTQ, respectively, which would capture more of $E^{corr.}$ but are far more computationally expensive. This example also highlights the complex nature of the electron correlation as one would expect the electron correlation to be more apparent at close internuclear distances, however, the opposite is observed as this discrepancy becomes more significant at larger distances. This can be owed to the decreasing single reference nature of the system and thus the inability to be represented by a single SD as would be the case in HF theory.

It should also be noted that one may also reduce the computational expense even further by using configuration state functions (CSFs). This representation reduces the number of optimisable parameters as each CSF is a symmetry-adapted linear combination of SDs, which is guaranteed to be an eigenfunction of \hat{S}_z and \hat{S}^2 [1]. Therefore, if an arbitrary wavefunction was composed of 3000 CSFs or 3000 SDs one would expect the former to provide the lower energy as this wavefunction would contain more than 3000 SDs. However, CSFs also have their shortcoming as one must initially generate the set of CSFs from the SDs and the elements of \mathbf{H}^{FCI} become inherently more complex, which may negate this speed up resulting from the

reduction of optimisable parameters. The use of SDs or CSFs in computations shall be explored in Chapter 3, see Section 3.4.1 and 3.4.2, for a novel and established post HF technique.

2.6.2 Monte-Carlo Configuration Interaction

A non traditional approach to capture electron correlation is that of Monte-Carlo configuration interaction (MCCI) [27–29], a stochastic approach initially developed by Greer in 1995, despite $|\Psi^{FCI}\rangle$ being entirely deterministic in nature. This technique involves iteratively building up a wavefunction through a random assortment of accessible single and double excitations from an ever increasing reference space, see Figure 2.6. This approach is based upon the sparsity of \mathbf{H}^{FCI} as many of the elements have little to no contribution on the resulting properties, therefore, in the grand scheme are not essential. This methodology has been successfully applied in the description of ground state PESs [30], dissociation energies [31], transition metal dimers [32], electronic excitation energies [33], multipole moments [34] and spin-orbit coupling [35] despite the vast reduction of configurations contained within the wavefunction when compared to FCI.

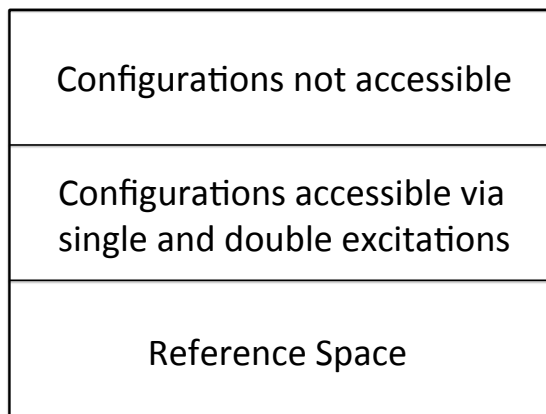


Figure 2.6: *Partitioning of the FCI space relative to the MCCI reference space, the size of each partition is not drawn to scale. Adapted from [36].*

Only a brief review of the method follows as an in-depth outline is given in Section 3.3.2, for clarity the MCCI algorithm running in serial is provided in Figure 2.7. From an initial reference space, once again the converged $|\Psi^{HF}\rangle$, a number of coupled configurations are generated, *via* random single and double excitations, and

subsequently appended to the aforementioned reference space. This augmentation process is known as branching the wavefunction. The coefficient of each configuration, when combined with the reference space, is computed *via* diagonalisation of \mathbf{H} within this reduced basis space. The configurations are then subject to a selection criterion governed by a user-defined threshold value (c_{min}). If any configurations are found to have a weighting less than c_{min} they are removed from the wavefunction, and the pruned wavefunction then forms the reference space for the next iteration. This process of branching, diagonalisation and pruning is repeated until convergence of both the energy and vector length is achieved. As the computation evolves the potential excitation space will increase and subsequently the partition that is unavailable will reduce. If the c_{min} parameter was set to 0 and the computation allowed to run indefinitely the results would equate to that of FCI. This method is of importance in Chapter 3 for which we undertake a detailed comparison to a locally modified MCCI algorithm, termed systematic-MCCI, which considers the entire excitation space as potential additions to the wavefunction. This allows us to explore the optimality of these stochastically generated wavefunctions, a comparison with FCI and a novel pruned-FCI alternative is also employed [37].

2.6.3 Many-Body Perturbation Theory

Another technique often employed for the recovery of E^{corr} , primarily a portion of the dynamic correlation, is many-body perturbation theory (MBPT). The underlying principle of this approach is that the exact system can be represented as a small perturbation to a problem for which solutions are known, either exactly or approximately [1]. One can therefore define the following:

$$\hat{\mathcal{H}} |\Psi\rangle = (\hat{\mathcal{H}}^{(0)} + \lambda \hat{\mathcal{H}}'') |\Psi\rangle = E |\Psi\rangle \quad (2.63)$$

$$\hat{\mathcal{H}}^{(0)} |\Psi_n^{(0)}\rangle = E_n^{(0)} |\Psi_n^{(0)}\rangle \quad (2.64)$$

where $\hat{\mathcal{H}}^{(0)}$ and $\hat{\mathcal{H}}''$ represent the unperturbed and perturbed Hamiltonian operator respectively. The strength of the perturbation is measured by the dimensionless

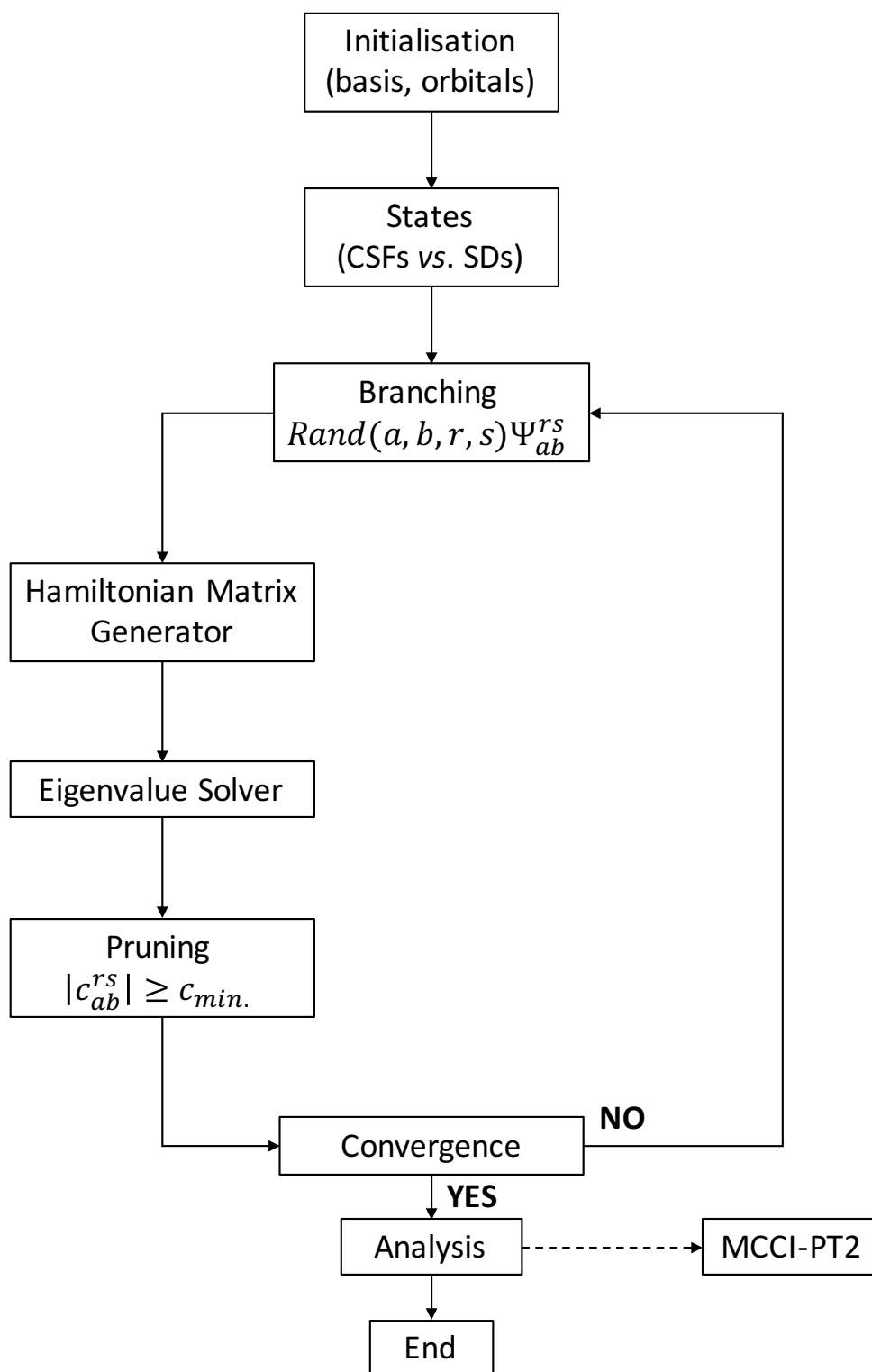


Figure 2.7: General overview of the MCCI algorithm, based on unpublished work by Martin J. Paterson with permission.

parameter (λ), for $\lambda = 0$, the total Hamiltonian would equate to the unperturbed system. Within the context of this thesis we shall only consider MBPT for which the unperturbed system is non degenerate. One can express the energy and wavefunction as a Taylor series of increasing powers of λ :

$$E = E_n^{(0)} + \lambda E_n^{(1)} + \lambda^2 E_n^{(2)} + \dots \quad (2.65)$$

$$|\Psi\rangle = |\Psi_n^{(0)}\rangle + \lambda |\Psi_n^{(1)}\rangle + \lambda^2 |\Psi_n^{(2)}\rangle + \dots \quad (2.66)$$

where the superscript denotes the order of correction to both the wavefunction and energy. The perturbed wavefunction is then taken to be intermediately normalised, $\langle \Psi | \Psi_n^{(0)} \rangle = 1$, leading to the zero-overlap, orthogonal, relation between the correction terms and the reference wavefunction. Inserting equation 2.65 and 2.66 into 2.63, subsequently collecting the same powers of λ generates the following:

$$\lambda^0 : \hat{\mathcal{H}}^{(0)} |\Psi_n^{(0)}\rangle = E_n^{(0)} |\Psi_n^{(0)}\rangle \quad (2.67)$$

$$\lambda^1 : \hat{\mathcal{H}}^{(0)} |\Psi_n^{(1)}\rangle + \hat{\mathcal{H}}'' |\Psi_n^{(0)}\rangle = E_n^{(0)} |\Psi_n^{(1)}\rangle + E_n^{(1)} |\Psi_n^{(0)}\rangle \quad (2.68)$$

$$\lambda^2 : \hat{\mathcal{H}}^{(0)} |\Psi_n^{(2)}\rangle + \hat{\mathcal{H}}'' |\Psi_n^{(1)}\rangle = E_n^{(0)} |\Psi_n^{(2)}\rangle + E_n^{(1)} |\Psi_n^{(1)}\rangle + E_n^{(2)} |\Psi_n^{(0)}\rangle \quad (2.69)$$

From this it can be shown that $E_n^{(2)}$ can be generated from the 1st order wavefunction. This finding can be represented more generally, as the $2w + 1$ energy correction can be attained from the w^{th} wavefunction, and is formally known as Wigner's $2w + 1$ rule [38].

As determination of $E^{corr.}$ is of interest a sensible starting point for the unperturbed Hamiltonian would be a sum over the Fock operators, where the perturbation would be a difference between the exact and mean-field electron repulsion. This choice of unperturbed operator gives rise to Møller-Plesset (MP) perturbation theory [39], which has the benefit of being size-extensive, however, is non-variational. As the premise of all perturbation theory is that the unperturbed eigenfunctions are very close to the exact counterparts, convergence issues can arise when the reference state gives a poor representation. It can be observed that $E_n^{(1)}$ is just $\langle \Psi_n^{(0)} | \hat{V}_{ij} | \Psi_n^{(0)} \rangle$, therefore, first-order MP theory (MP1) offers no advantage over HF. The 2nd order energy contribution is the first term that adds part of the electron-

correlation energy, as outlined below:

$$E_n^{(2)} = \langle \Psi_n^{(0)} | \hat{\mathcal{H}}^{(1)} | \Psi_n^{(1)} \rangle = \sum_{k \neq n} \frac{\langle \Psi_k^{(0)} | \hat{\mathcal{H}}^{(1)} | \Psi_n^{(0)} \rangle \langle \Psi_n^{(0)} | \hat{\mathcal{H}}^{(1)} | \Psi_k^{(0)} \rangle}{E_n^{(0)} - E_k^{(0)}} \quad (2.70)$$

where this term can only have contributions from the reference with the set of doubly-excited configurations. In most cases, MP2 accounts for ~ 80 to 90 % of E^{corr} , and formally scales as M^5 , giving significant improvement over HF whilst still maintaining a similar level of computational expense [1]. Increasing to MP3 and MP4 results in methods that now scale as M^6 and M^7 , with the former now needing knowledge of $|\Psi_n^{(2)}\rangle$ and typically captures ~ 95 % of E^{corr} .

2.6.4 Coupled-Cluster Theory

Another technique used to determine E^{corr} is that of coupled-cluster (CC) theory [40–42]. This formulation uses an exponential ansatz for the cluster operator (\hat{T}), which can be expressed as a Taylor series, and operates on $|\Psi^{HF}\rangle$:

$$|\Psi^{CC}\rangle = e^{\hat{T}} |\Psi^{HF}\rangle = (1 + \hat{T} + \frac{1}{2!}\hat{T}^2 + \frac{1}{3!}\hat{T}^3 + \dots) |\Psi^{HF}\rangle \quad (2.71)$$

where

$$\hat{T} = \hat{T}_1 + \hat{T}_2 + \hat{T}_3 + \dots + \hat{T}_x \quad (2.72)$$

and represents single, double, triple, \dots , N -tuple excitations. It is common to group the same excitation levels together resulting in equation 2.73.

$$e^{\hat{T}} = 1 + \hat{T}_1 + (\hat{T}_2 + \frac{1}{2}\hat{T}_1^2) + (\hat{T}_3 + \hat{T}_2 \hat{T}_1 + \frac{1}{6}\hat{T}_1^3) + (\hat{T}_4 + \hat{T}_3 \hat{T}_1 + \frac{1}{2}\hat{T}_2^2 \hat{T}_1^2 + \frac{1}{24}\hat{T}_1^4 + \dots) \quad (2.73)$$

If all N -tuple excitations are considered then $|\Psi^{CC}\rangle = |\Psi^{FCI}\rangle$, and too is only applicable to the smallest of systems and basis sets. Once again due to the computational demanding nature approximate approaches are also available *via* truncation of the cluster operator. From the alternative excitation grouping notation it can

be clearly observed for configurations generated by double excitations, and above, a mixture of connected and disconnected terms arise namely \hat{T}_2 and \hat{T}_1^2 respectively. If one truncates at this excitation level, giving rise to CCSD [43], such that $\hat{T} = \hat{T}_1 + \hat{T}_2$, higher terms still exist via these disconnected components, thus ensuring that truncated CC is size-consistent. If we relate this back to the H_2 system discussed previously, disconnected terms relating to triple and quadruple excitations would be present within CCSD, $\hat{T}_2 \hat{T}_1$, \hat{T}_1^3 , $\hat{T}_2 \hat{T}_2$ and \hat{T}_1^4 therefore recovering the terms that were found to be non-existent within a CISD wavefunction.

Table 2.1: *First three excitation levels for various truncated CC methods.*

Acronym	Truncation of \hat{T}	$e^{\hat{T}}$
CCS	\hat{T}_1	$1 + \hat{T}_1 + \frac{1}{2}\hat{T}_1^2 + \frac{1}{6}\hat{T}_1^3 + \dots$
CCSD	$\hat{T}_1 + \hat{T}_2$	$1 + \hat{T}_1 + (\hat{T}_2 + \frac{1}{2}\hat{T}_1^2) + (\hat{T}_2 \hat{T}_1 + \frac{1}{6}\hat{T}_1^3) + \dots$
CCSDT	$\hat{T}_1 + \hat{T}_2 + \hat{T}_3$	$1 + \hat{T}_1 + (\hat{T}_2 + \frac{1}{2}\hat{T}_1^2) + (\hat{T}_3 + \hat{T}_2 \hat{T}_1 + \frac{1}{6}\hat{T}_1^3) + \dots$

Despite not suffering from size-consistency issues, truncated CC methods are non-variational. The current standing of *ab-initio* computations equate CCSD(T) to the gold-standard [1]. This method deviates from CCSDT, as the connected triples are estimated *via* a perturbation theory approach. Despite not being used explicitly within this thesis CC and MPPT are contained within composite QM methods such as Gaussian-2(MP2) [44] and the complete basis set (CBS)-QB3 model [45], which will be discussed further in Section 2.12 due to the latter's importance in Chapter 4.

2.6.5 Multi-Configurational Self-Consistent Field

We now turn our attention to multi-configurational self-consistent field (MCSCF) techniques. These methods can be related back to CI theory in which not only the set of expansion coefficients are optimised, but also the set of corresponding MOs. As is to be expected, increasing the number of configurations leads to SCF

procedures that need more iterations to reach convergence, therefore it is uncommon for MCSCF wavefunctions to be larger than those of CI theories.

A widely utilised MCSCF technique is complete active space self-consistent field (CASSCF) [46]. This method has profound application when the $|\Psi^{HF}\rangle$ gives a qualitatively and quantitatively poor description of the true wavefunction, through primarily capturing the deficient static correlation. This approach involves preselecting a range of occupied and virtual MOs, known as the active space, and undertaking a FCI regime within this subspace. The MOs not contained within this subset are either doubly or non-occupied in all configurations, having occupation numbers of 2 and 0, respectively. The occupation number of orbitals within the active space should range between 0 and 2, however, if any values fall close to the outer limits it is indicative of a poor choice of orbital selection. The orbitals outwith the active space are therefore referred to as the inactive space. The nomenclature of CASSCF(N, M) is given relative to this active space, for which N electrons are distributed between M orbitals. The selection of the active space is extremely dependent on the problem at hand, and one should include all MOs that would be likely to have the biggest deviations and significance chemical relevance. As prior knowledge of the system, and problem at hand, is essential for meaningful results the technique is commonly referred to as non black box.

The active space can be further divided into three separate components, RAS1, RAS2 and RAS3, giving rise to the restricted active space self-consistent field (RASSCF) method [47], reducing the computational expense when compared to CASSCF as the number of available configurations has been lowered. The RAS2 partition is treated analogously to the active space in CASSCF, and contains the essential occupied and virtual orbitals to describe the main chemistry of the problem. The RAS1 and RAS3 space contain solely occupied or virtual orbitals, respectively. To generate additional configurations the RAS1 space is allowed to vary, for example, by allowing no more than two holes across the set of doubly occupied orbitals in each configuration. A similar approach is undertaken on RAS3 for which no more than two electrons can be promoted into this unoccupied space. A general overview

of the CASSCF and RASSCF partitions are outlined in Figure 2.8.

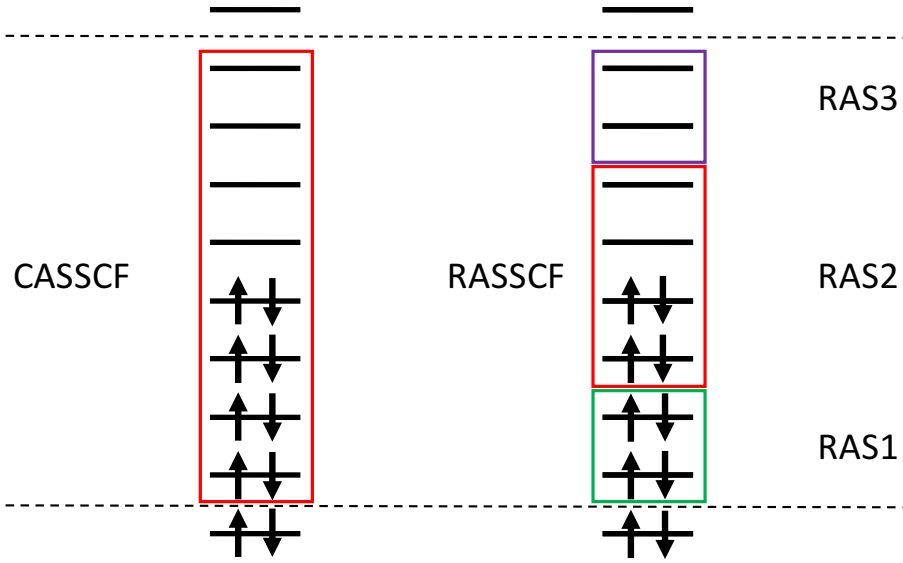


Figure 2.8: *General overview of the various partitions in CASSCF and RASSCF, the dashes lines separate the active and inactive space.*

This method is a fairly unbalanced approach to capture $E^{corr.}$, as dynamic correlation out with the active space is completely negated, in-conjunction with the coupling between electrons in the different spaces. Therefore, it is common to further account for this missing correlation through a perturbation approach, giving CASPT2.

2.6.6 Multi-Reference Configuration Interaction

In conventional single reference CI theory, all configurations are generated with respect to $|\Psi^{HF}\rangle$. It can be argued that MCCI is a multi-reference (MR) technique as a stochastic CI type regime is performed from the ever increasing reference space, and thus after the initial iteration we would have more configurations than just $|\Psi^{HF}\rangle$ to use as a starting point. All single reference methods build upon a single reference and can have significant problems when the HF orbitals give a qualitatively poor description. However, a MCSCF wavefunction may also be taken to form the reference space, and as such excitations can be performed on each of the contained configurations. This approach allows one to incorporate a level of dynamic correlation into the already static correlated $|\Psi^{MCSCF}\rangle$. Once again, it is common to truncate the method after single and double excitations giving MR-CISD, which still

suffers from the size-consistency issue discussed previously. Even within MR-CISD the excitation space can become too large to be handled, and as such various other approximations may be introduced. A common approach is to use perturbation theory to estimate the interaction between the excited configuration and the subsequent reference, omitting terms that fall below this interaction threshold, referred to as state-selected MCSCF [1]. However, as the interaction between configurations would vary upon change of the geometrical parameters, it can become problematic to compare energies at different points on the PES as some states may be present in one and not in the other.

2.7 Density Functional Theory

Density functional theory (DFT) is an alternative approach to the *ab-initio* wavefunction based methods outlined above. This method utilises the electronic density as opposed to explicitly using the many-body wavefunction. In traditional wavefunction techniques all $4N$ coordinates (the three spatial and one spin component of each electron) must be considered, in comparison to electronic density methods which require only 3 coordinates (i.e. x , y and z) irrespective of the total number of electrons present. Unlike the wavefunction, which is purely a mathematical construct, the density can be obtained from experimental techniques, such as x-ray diffraction, therefore having an analogous physical interpretation. The electron density for a chemical system at a particular point in space is given by the following equation [1]:

$$\rho(\vec{r}_1) = N \int |\Psi(1, 2, \dots, N)|^2 \partial\sigma_1 \partial\vec{x}_2 \dots \partial\vec{x}_N \quad (2.74)$$

with the integral taking effect over all spin variables and over all but one of the spatial coordinates. If we consider the electronic Hamiltonian operator, shown once again in equation 2.75 for reference and omitting the fixed \hat{V}_{NN} potential for the time being, it can be easily seen that this is dependent on the number of electrons and \hat{V}_{Ne} only, within the context of DFT we will refer to this external potential as

$\hat{V}_{ext.}$

$$\hat{\mathcal{H}} = - \sum_i^N \frac{1}{2} \nabla_i^2 + \sum_{j>i}^N r_{ij}^{-1} - \sum_A^Y \sum_i^N \frac{Z_A}{r_{Ai}} \quad (2.75)$$

These aforementioned quantities uniquely determine the Hamiltonian, as the kinetic energy and electron repulsion would be the same for any N -electron system irrespective of the accompanying nuclear framework. It was then Hohenberg and Kohn that proved, *via a reductio ad absurdum* process in their crucial 1964 paper [11], the one to one correspondence between $\hat{V}_{ext.}$ and $\rho(\vec{r})$ and as one can obtain the total number of electrons *via* integration of the latter:

$$\int \rho(\vec{r}) d\vec{r} = N \quad (2.76)$$

it is abundantly clear that the electronic density must be a unique fundamental property of system. This therefore ensures that the energy can be given as a functional of the density, see equation 2.77, where the universal functional $U[\rho(\vec{r})]$ has been introduced which incorporates all terms which would be the same for any N -electron system.

$$E[\rho(\vec{r})] = U[\rho(\vec{r})] + \int V_{ext}(\vec{r}) \rho(\vec{r}) d\vec{r} \quad (2.77)$$

The second finding by Hohenberg and Kohn also stated that this energy functional obeys the variational principle:

$$E[\rho'(\vec{r})] = \langle \Psi' | \hat{\mathcal{H}} | \Psi' \rangle > \langle \Psi | \hat{\mathcal{H}} | \Psi \rangle = E[\rho_0(\vec{r})] = E_0 \quad (2.78)$$

where ρ_0 represents the ground state electron density, which through theorem one, provides a unique ground state wavefunction with an eigenvalue corresponding to the ground state energy. Therefore an arbitrary density which is not equal to the ground state, ρ' , would give Ψ' , such that $\Psi \neq \Psi'$ and from the variation principle one knows that the energy obtained must be upper bound to E_0 . Therefore the exact ground state energy will only be at the minimum value when the exact ground state density is known, else the energy will be larger. This thereby allows one to minimise the density without having to fret about the consequences of dropping below the

true energy.

However, despite the known presence of this exact relationship between density and energy the functional connecting them is unknown, and as such must be approximated. The accurate approximation of this functional has been of central importance in modern DFT.

2.7.1 Kohn-Sham Density Functional Theory

As the Hohenberg-Kohn theorem only indicates the existence of such a mapping, approaches must be employed to analytically determine the nature of this unknown functional linking the electronic density and energy. One such approach was that developed by Kohn and Sham (KS-DFT) [12], building on the fact that a set of non-interacting particles, subject to an effective external potential, could be tailored to share the same density as the fully interacting system. The Hamiltonian for this fictitious system would thus be a summation of one electron operators, analogous to that outlined in the IEA model, see equation 2.29. The key concept of the Kohn-Sham (KS) approach is in the determination of the kinetic energy term, as this was found to be represented very poorly in earlier DFT approaches by Thomas and Fermi [48]. The exact kinetic energy for non-interacting electrons (T_{ni}) can be attained from a SD composed of N KS spin-orbitals (ϕ_i^{KS}).

$$T_{ni}[\rho] = \sum_{i=1}^N \langle \phi_i^{KS} | -\frac{1}{2} \nabla^2 | \phi_i^{KS} \rangle \quad (2.79)$$

As the KS orbitals provide the ground state density one could, in theory, obtain the exact energy if the universal function was known.

$$\rho_{exact}(\vec{r}) = \sum_i^N |\phi_i^{KS}(\vec{r})|^2 \quad (2.80)$$

As expected there would be a difference between the kinetic energy for a system of non-interacting and interacting particles (T_{true}). However, the discrepancy is minimal [1], and as such the non-interacting set-up provides a good representation of the real system. This small discrepancy between the kinetic energies is contained

within the exchange-correlation ($E_{xc}[\rho]$) term, with the total Kohn-Sham energy given as:

$$E_{DFT}[\rho] = T_{ni}[\rho] + E_{ne}[\rho] + J[\rho] + E_{xc}[\rho] \quad (2.81)$$

where $J[\rho]$ is the classical repulsive coulombic interaction, which must be corrected as this contains self-interaction between electrons. The $E_{xc}[\rho]$ is outlined in equation 2.82.

$$E_{xc}[\rho] = (T_{true}[\rho] - T_{ni}[\rho]) + (E_{ee}[\rho] - J[\rho]) \quad (2.82)$$

The exchange-correlation term essentially encompasses all the terms that cannot be computed exactly within KS-DFT, such as that described above and also those arising from the exchange requirement of fermions and explicit correlation effects. As KS-DFT also relies on MOs it has a computational expense similar to HF theory, despite providing more accurate results. The KS energy expression provided in equation 2.81 is then minimised with respect to the electron density, subject to the constraint that $\int \rho(\vec{r})d\vec{r} = N$ i.e. the number of electrons remain constant. This generates the following KS equations:

$$\left[\frac{1}{2} \nabla^2 + V_J(\vec{r}) + V_{ext}(\vec{r}) + V_{xc}(\vec{r}) \right] \phi_i^{KS}(\vec{r}) = \varepsilon_i \phi_i^{KS}(\vec{r}) \quad (2.83)$$

where $V_J(\vec{r})$ and $V_{xc}(\vec{r})$ have the following form of equation 2.84 and 2.85 respectively and ε is the KS orbital energy.

$$V_J(\vec{r}) = \frac{\partial J[\rho(\vec{r})]}{\partial \rho(\vec{r})} \quad (2.84)$$

$$V_{xc}(\vec{r}) = \frac{\partial E_{xc}[\rho]}{\partial \rho(\vec{r})} \quad (2.85)$$

If the true nature of E_{xc} was known this would correspond to the exact energy, therefore containing the exact electron repulsion. However, there is no guarantee that this will ever be known exactly or that it will require less computational resources as subjecting the system to a FCI treatment. Therefore, the difference between various KS-DFT methodologies is solely down to the different approximations used to determine E_{xc} . As like the Roothan-Hall scheme for HF theory, the

KS orbitals are expressed in a LCAOs fashion and the resulting matrix eigenvalue problem solved in a SCF regime.

Furthermore, E_{xc} is commonly divided into two components, one relating to the exchange term and the other to that of correlation:

$$E_{xc} = E_x[\rho] + E_c[\rho] = \int \rho(\vec{r}) \eta_x[\rho(\vec{r})] d\vec{r} + \int \rho(\vec{r}) \eta_c[\rho(\vec{r})] d\vec{r} \quad (2.86)$$

where η relates to corresponding energy per particle. A brief overview of various approximations to E_{xc} follows.

2.7.2 Local Density Approximation

The Local Density Approximation (LDA) is the simplest estimation in which the exchange-correlation energy is equated to that of a uniform electron gas sharing the same density at the point of interest [49]. This assumption applies relatively well for solid-state systems, however, on a molecular level this is a rather crude approximation as the electron density would vary significantly at various regions of the molecule.

2.7.3 Generalised Gradient Approximation

Following on from the LDA formalism we arrive at the generalised gradient approximation (GGA), commonly referred to as a non-local method. This subset of functionals lift the constraint of a uniform electron gas, as the functional is not only dependent on the density but also on the first derivative of said density. A vastly popular GGA exchange functional is that proposed by Becke (B) [50]. This involves the addition of a gradient corrector term, containing parameters derived via fitting to known atomic data, to η_x^{LDA} as shown in equation 2.87. Another example of a GGA functional that incorporates η_x^{LDA} is that proposed by Perdew and Wang (PW86) [51].

$$\eta_x^B = \eta_x^{LDA} + \Delta\eta_x^B \quad (2.87)$$

There are also exchange functionals that do not explicitly build upon η_x^{LDA} ,

such as that proposed by Becke and Roussel (BR) [52]. This GGA functional also deviates from the two outlined above as it not only contains derivatives, both 1st and 2nd order, of the total electronic density but also of the orbitals. This class of functionals are commonly referred to as meta-GGA due to the inclusion of higher order terms than solely the gradient of the electron density. However, despite the additional computational expense, the results are very similar to those obtained *via* equation 2.87.

Similar approaches have been undertaken for the correlation portion of E_{xc} . A common GGA correlation functional is that proposed by Lee, Yang and Parr (LYP) [53], a four variable functional parametrised with respect to data obtained for the helium atom. It is also possible to use a GGA functional which incorporates both exchange and correlation GGA terms, an example of this is the BLYP [50, 53] functional. Another GGA functional was that proposed by Perdew, Burke and Ernzerhof (PBE) which also contains both an exchange and correlation GGA segment [54, 55].

2.7.4 Hybrid Methods

As KS-DFT involves the generation of MOs it is a reasonable proposition to replace the exchange portion of E_{xc} with the exact value computed *via* HF theory, computing the challenging correlation energy with DFT. This arises from the fact that E_x is the dominant term in equation 2.86, when compared to E_c with respective values of -12.11 and -0.39 a.u. for a Neon atom, therefore accounting for the former is of far more importance [1]. This strict decoupling process does not work so well in practice due to the discrepancy between exchange and correlation terms within the framework of KS-DFT and *ab-initio* wavefunction methods.

However, hybrid methods have been developed which incorporate a portion of the HF exchange (E_x^{exact}). One of the most globally recognised hybrid exchange functionals is the Becke 3 (B3) parameter functional, which incorporates ~ 20 % of pure HF exchange and is used with the LYP correlation term, resulting in the B3LYP approximation [53, 56]. Another class of functionals that incorporate various amounts of HF exchange are that developed by Truhlar *et al.*, which are based upon

meta-GGA functionals. Examples of these functionals are M06 [57], M06-HF [58], M06-2X [57] and MN15 [59] which include 27, 100, 54 and 44 % of HF exchange, respectively, and have intended uses in describing various chemical systems and properties. At large distances exchange functionals can become very inaccurate due to the rapid decay of the non-Coulomb portion of the functional. This is of particular importance in systems which will involve very diffuse processes such as electron excitations to Rydberg states. Therefore methods which utilise long-range corrections have been developed such as CAM-B3LYP [60].

The plethora of available functionals are also commonly illustrated by a hypothetical Jacob’s ladder, see Figure 2.9. The rungs correspond to the varying approximations used when designing the exchange-correlation functional, with the level of sophistication and computational cost increasing as one goes up the ladder until chemical accuracy is achieved. As outlined the top rung corresponds to double-hybrid based functionals which incorporate both HF exchange and MP2 correlation, however, incorporation of the latter significantly limits the system size which can be studied essentially negating the main benefit of DFT.

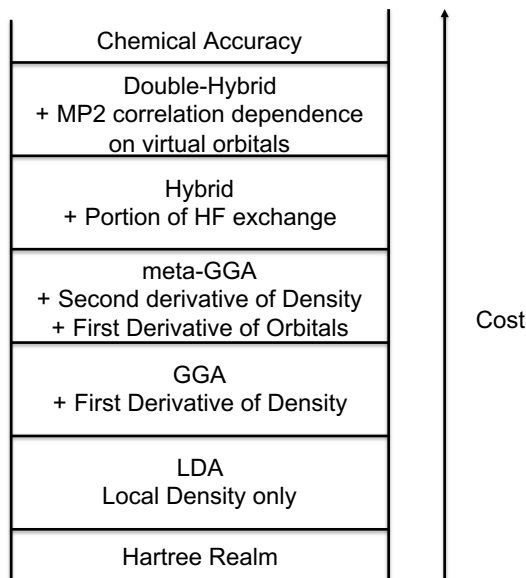


Figure 2.9: *Hypothetical Jacob’s Ladder. Adapted from [61].*

A crucial drawback with the current form of the aforementioned DFT functionals is the inability to model long range dispersive interactions. This attractive intermolecular electrostatic interaction is of great importance when two or more molecules exhibit hydrogen bonding or π - π interactions. For example many func-

tionals describe the interaction between two rare gas atoms as purely repulsive while others describe a weaker interaction, however, do not display the correct long-range behaviour. This is due to the local nature of the exchange correlation functional and thus if the two electron densities have no overlap this interaction will therefore not be considered. This shortcoming has led to the development of dispersion corrected DFT (DFT-D), which employs an atomic pair-wise potential, adding this quantity to the KS-DFT energy. In Section 5.5.6, we utilise the GD3BJ empirical correction [62] which makes use of Grimme’s dispersion, GD3 variant, and for short range behaviour uses Becke-Johnson (BJ) finite-damping. Another common DFT-D functional is B97-D [63].

It should be noted that increasing the sophistication of the exchange-correlation functional does not necessarily provide chemical properties that are closer to the true value. As a result of this it is imperative that for DFT methods an initial benchmarking of the exchange-correlation function is undertaken through comparison of the approximated property with a known standard to establish the best computational model. This is performed in Chapter 5 through a comparison of the theoretical and experimentally obtained ionisation potential for a range of exchange-correlation functionals belonging to different classes.

2.8 Time-Dependent DFT

The KS-DFT approach outlined above solely pertains to the ground state electronic structure of the system of interest. However, an extension to this method exists which allows exploration of the excited state landscape, known as time-dependent DFT (TD-DFT) [64]. This approach uses linear response theory, assuming a weak time dependent perturbation ($V_{pert.}$) to the unperturbed Hamiltonian (\hat{H}_0).

$$\hat{H}(t) = \hat{H}_0 + \hat{V}_{pert.}(t) \quad (2.88)$$

This time dependent perturbation is commonly taken as an oscillating electric field. The first-order response of the density matrix, equating to the ground state

stationary density, to this time dependent perturbation is generated which provides the vertical excitation energies. The electronic transitions are characterised by either one, or many, single-particle hole excitation/de-excitations of the relevant MOs, with the weightings relevant to the importance of each in describing the state specific perturbed density. Within a TD-DFT computation one can also attain, for each vertical excited state, the relevant oscillator strength (f). This quantity represents how probable an electronic transition is, states with large f are commonly referred to as bright states with $f = 0$ representing dark states which are inaccessible. An example of a dark state is a spin forbidden transition such as $S_0 \rightarrow T_1$. The term vertical is used as within the time scale of electronic excitation the nuclear framework will remain unchanged, analogous to the Born-Oppenheimer approximation covered previously. The most probable vibrational state occupied upon this transition will be that which gives the greatest overlap with the ground state vibrational wavefunction as per the Franck-Condon principle [4]. If one allows the geometry of the excited state to optimise, the concept of geometry optimisation will be explored in the following Section, the adiabatic $S_0 \rightarrow S_1$ transition energy can be obtained. The difference between a vertical and adiabatic excitation has been schematically shown in Figure 2.10.

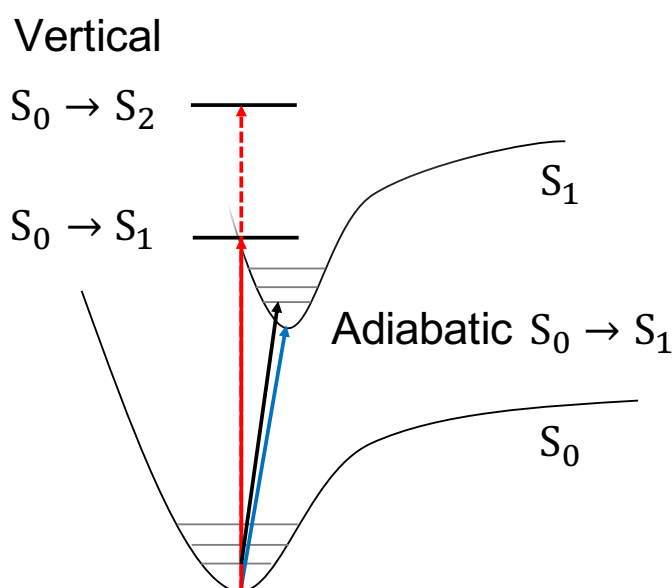


Figure 2.10: Arbitrary S_0 and S_1 PES highlighting a vertical (red) or adiabatic (blue) transition.

In the above Figure four different excitation processes have been outlined. The

red lines indicate a vertical excitation transition, with the solid and dashed representing an excitation from $S_0 \rightarrow S_1$ and $S_0 \rightarrow S_2$, respectively. These values can be obtained directly from a single TD-DFT computation on the relevant optimised ground state geometry. The blue transition involves an additional TD-DFT computation for which the nuclear arrangement is optimised for S_1 . The energetic difference between the optimised S_1 and S_0 provides the lower energy adiabatic $S_0 \rightarrow S_1$ transition. The final excitation process outlined, black line, involves a further frequency computation on both optimised structures to account for the zero point energy. The role of a frequency computation will be further developed in the following Section along with geometry optimisation. This gives a more realistic model of the excitation energy than the electronic energy difference as even at 0 K the molecules will possess vibration energy.

In order to provide a better comparison to experimental excited state data such as that attained via UV-Vis spectroscopy, one may simulate spectral broadening. This simulates various phenomena such as collision broadening, energy/time uncertainty principle and Doppler effects [65], through multiplication of each TD-DFT generated stick peak by a Gaussian or Lorentzian function. The spectral intensity from all transitions at a specific wavelength in a predetermined range can be obtained from the following:

$$I(\lambda) = \sum_i f_i e^{\left(-\frac{1}{2} \left(\frac{\lambda - \lambda_i}{\sigma}\right)^2\right)} \quad (2.89)$$

where f_i and λ_i is the oscillator strength and wavelength pertaining to excited state i , and σ is the width of the Gaussian. Within this thesis we utilise TD-DFT to compute the vertical excited states of a range of organic π -conjugated materials.

2.9 Geometry Optimisation and Frequencies

Up until this point we have solely described procedures involving the calculation of ground and excited states energies with varying degrees of accuracy, utilising both wavefunction and electron density approaches. However, geometry optimisations and determination of nuclear vibrations are other tools which are indispensable to

computational chemists. When used in conjunction these methods have the ability to predict, the former, and validate, the latter, chemically relevant conformations such as equilibrium geometries, transition states and conical intersections, and hence investigate potential chemistries molecules could undertake.

In regards to attaining equilibrium structures an initial guess of the nuclear framework is constructed, with the force along each of the internal coordinates computed via the negative first-order derivative of the potential energy. The atomic positions are then displaced in the direction of this stabilising force, and the potential energy and force once again calculated. This process is repeated until the forces and atomic displacements satisfy a set of convergence threshold values, generating the optimised geometry. At this arrangement the resultant forces will be approximately zero. From this optimised framework the local curvature along each mode is then computed, in order to classify the nature of stationary point, termed a frequency computation. This involves generation of a Hessian matrix ($\mathbf{H}_{ess.}$) which contains all the second order derivatives of the energy with respect to the nuclear Cartesian coordinates. An example $\mathbf{H}_{ess.}$ for an arbitrary system is shown in equation 2.90, where x_i and y_i represent the x and y coordinate of nuclei i and z_n is the z coordinate of the nuclei n .

$$\mathbf{H}_{ess.} = \begin{bmatrix} \frac{\partial^2 E}{\partial x_1^2} & \frac{\partial^2 E}{\partial x_1 \partial y_1} & \cdots & \frac{\partial^2 E}{\partial x_1 \partial z_n} \\ \frac{\partial^2 E}{\partial y_1 \partial x_1} & \frac{\partial^2 E}{\partial y_1^2} & \cdots & \frac{\partial^2 E}{\partial y_1 \partial z_n} \\ \vdots & \vdots & \ddots & \vdots \\ \frac{\partial^2 E}{\partial z_n \partial x_1} & \frac{\partial^2 E}{\partial z_n \partial y_1} & \cdots & \frac{\partial^2 E}{\partial z_n^2} \end{bmatrix} \quad (2.90)$$

Upon diagonalisation of $\mathbf{H}_{ess.}$ the eigenvalues and eigenvectors relate to the nuclei vibrational frequency and corresponding mode, respectively. If all eigenvalues are positive then the optimised structure has been validated as a minima. In comparison, if n negative eigenvalues are present then this structure would be classified as an n^{th} order saddle point which too have chemical importance, as outlined in the following Section. Moreover, frequency computations allow one to predict the

IR/Raman spectra of a specific molecular geometry and are needed when predicting thermochemical quantities.

2.10 Transition State Theory and Thermodynamic Quantities

As covered in the previous Section, structures corresponding to stationary points, for which the first derivative of the electronic energy with respect to nuclear displacement is zero, are important when modelling chemical pathways as they allow one to quantify not only overall energetics but also activation barriers and subsequent reaction rates. In transition state theory (TST) reactions proceed from the favourable conformations of reactants to that of the products, through a higher energy transition state [1], as shown in Figure 2.11 for an arbitrary system.

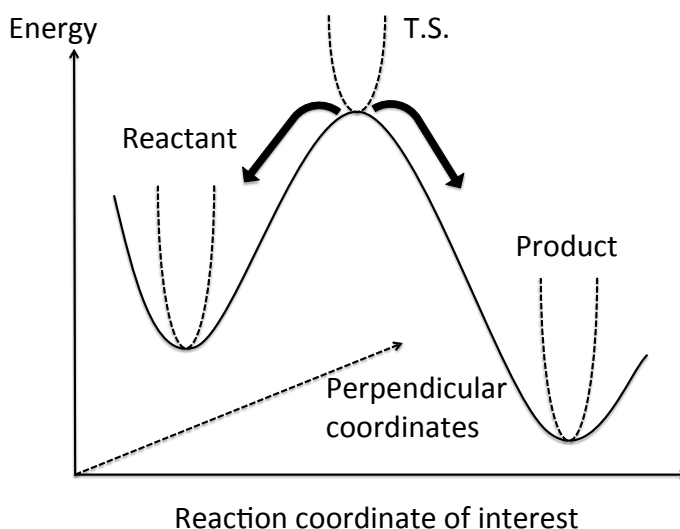


Figure 2.11: A generic reaction pathway highlighting important points on the PES.

The energetically favourable conformations of reactants and products have positive curvature along all $3Y - 6$ or $3Y - 5$ vibrational modes, classifying as either a local or global minima, with the transition state having positive curvature along $3n - 7$ modes and a maxima along the one remaining vibrational mode which pertains to the reaction coordinate. Assuming equilibria between the reactant and transition

state one can calculate a rate constant (k) [1]:

$$k = \frac{k_B T}{h} e^{-\Delta G_r^\ddagger / RT} \quad (2.91)$$

where ΔG_r^\ddagger relates to the free energy activation barrier as shown in equation 2.92. In order to validate that the transition state leads to the expected structures, and hence the correct reaction pathway is modelled, it is good practice to subject the transition structure to an intrinsic reaction coordinate (IRC) [66, 67] calculation, other methods such as QST2 and QST3 [68] are also available however these were not used within this thesis. The underlying premise of this algorithm is that the reaction pathway is followed downhill from the transition state in both the forward and reverse direction, this is relative to the directionality of the transition vector. Upon each displacement of the transition vector all other internal coordinates are optimised to ensure that the reaction pathway is of minimum energy. Therefore a connection can be made between reactants and products *via* an appropriate transition state. We utilise IRC computations in Chapter 4 to validate the reaction pathways under investigation.

When computing properties of reaction pathways it is also common to quote differences in thermodynamic quantities such as the enthalpy (ΔH) or Gibbs free energy (ΔG) which can be attained *via* corrections to the electronic energy. The overall free energy change and relevant activation barrier for a forward reaction can be computed from the following:

$$\Delta G_r(T) = \sum_{products} [E + G_{corr.}](T) - \sum_{reactants} [E + G_{corr.}](T) \quad (2.92)$$

$$\Delta G_r^\ddagger(T) = [E + G_{corr.}](T) - \sum_{reactants} [E + G_{corr.}](T) \quad (2.93)$$

where $G_{corr.}$ is the free energy correction and E is the electronic energy for the specific component within the reaction. Enthalpy changes would be computed in an analogous fashion, however, utilising the enthalpy correction. For all thermochemical studies contained within this thesis Gaussian09 and 16 was used [69], therefore we

will consider the specific implementation of these corrections within this software only.

The calculation of thermodynamic quantities relies on the partition function (q), which is shown below for a single molecule:

$$q = \sum_i^{\text{all levels}} g_i e^{-\frac{\epsilon_i}{k_B T}} \quad (2.94)$$

where the sum is over all translational, rotational, vibrational and electronic levels with g_i and ϵ_i the corresponding degeneracy and energy, respectively. The basic assumption is that the energy can be represented as a decoupled sum of contributions from these aforementioned states. This approximation is valid, however, can break down in analogous situations to that of the BO approximation, when one cannot decouple the vibrational and electronic state, and in specific cases regarding linear molecules when the rotational and vibrational states can mix [1]. The corresponding energy and partition function can thus be represented by the following equations, respectively.

$$\epsilon_{tot.} = \epsilon_{trans.} + \epsilon_{rot.} + \epsilon_{vib.} + \epsilon_{elec.} \quad (2.95)$$

$$q_{tot.} = q_{trans.} q_{rot.} q_{vib.} q_{elec.} \quad (2.96)$$

Within Gaussian an ideal gas system is assumed, with non-interacting particles [69]. The contributions from $q_{trans.}$ and $q_{rot.}$ are attained from the fundamental particle in a box and rigid-rotor approximations, respectively. The contribution from molecular vibrations are approximated, in the most basic scenario, by the harmonic oscillator. This vibrational correction to the enthalpy ($H_{vib.}$) and entropic ($S_{vib.}$) terms are thus:

$$H_{vib.} = R \sum_{i=1}^{3Y-6} \left(\frac{h\nu_i}{2k_B} + \frac{h\nu_i}{k_B} \frac{1}{e^{h\nu_i/k_B T} - 1} \right) \quad (2.97)$$

$$S_{vib.} = R \sum_{i=1}^{3Y-6} \left(\frac{h\nu_i}{k_B T} \frac{1}{e^{h\nu_i/k_B T} - 1} - \ln(1 - e^{-h\nu_i/k_B T}) \right) \quad (2.98)$$

where ν_i is the vibrational frequency of mode i , k_B is the Boltzmann constant and

T , the temperature. Upon further inspection of the vibrational enthalpy contribution we observe a temperature dependent and independent part. The temperature independent term is the zero point energy (ZPE), which accounts for the vibrational energy contained within the system at absolute zero, particles will never be at complete rest as a result of Heisenberg’s uncertainty principle. The temperature dependent terms account for molecules that occupy excited vibrational states. When modelling reaction pathways it should be noted that the upper limit of the summations will vary, as the transition state contains one imaginary vibrational mode which will be omitted from the term and the summation will be over the $3Y - 7$ real modes. In regards to the electronic contribution, the separation between the ground and first excited state is assumed to be far larger than $k_B T$, thereby making this state inaccessible and hence containing no additional electronic term. The contribution of each is combined to give the resulting corrections for both enthalpy and free energy.

2.11 Implicit Solvent Models

In many instances the solute environment may also be important and as such must be implemented within the computation as it may have an influence on the resultant properties. The treatment of solvation effects can be classified as either explicit, if they include specific solvent molecules, or implicit, which express the solvent as a continuous medium. One may also utilise a combination of the two approaches. For the former approach to sufficiently model the intermolecular interactions and behaviours one must use high accuracy *ab-initio* methods, which include a level of electron-correlation, however, as many solvent atoms are required this is not always a valid or readily available method at this moment of time [1]. The latter involves incorporating the solute into a suitable shaped cavity within the solvent environment, which is described by a uniform polarisable medium with a dielectric constant pertaining to the solvent of interest. The solvation free energy, which is the change in free energy associated with going from a vacuum to solvated environment

is given by the following:

$$\Delta G_{solv.} = \Delta G_{cavity} + \Delta G_{disp.} + \Delta G_{elec.} \quad (2.99)$$

where ΔG_{cavity} represents the energy required to generate the cavity within the reaction field, $\Delta G_{disp.}$ and $\Delta G_{elec.}$ are the dispersion and electrostatic interactions between the solute-solvent. As the solute electron density would polarise the continuum, with the solvent reorganising and subsequently re-polarising the solute until self-consistency is achieved the model is often referred to as a self-consistent reaction field (SCRF) model. The solute is placed within a cavity to simplify the computation, as the solute is excluded from the solvent and *vice versa*. The range of SCRF models available mainly differ in the following aspects:

- construction of the cavity both in terms of size and shape,
- how the intermolecular terms are approximated,
- description of the solute and the charge distribution,
- specific nature of the dielectric medium.

The earliest SCRF model was that developed by Onsager [70] in which the cavity takes a spherical shape and the central solute molecule is characterised solely by the dipole moment. These models were primarily used due to the computational ease of using spherical and ellipsoids shaped cavities, however, most chemical systems do not take this shape thus providing a poor representation. As the charge distribution is represented by the dipole moment this also causes problems when modelling symmetric systems as there would be no dipole moment. The default solvent model within Gaussian, and of relevance within this thesis, is the polarisable continuum model (PCM) [71]. This generates a molecular shaped cavity via a set of overlapping spheres centered on each of the nuclei in the solute. For each individual sphere the radius employed is commonly close to the van der Waals radius, $\sim 20\%$ larger, as provided in the universal force-field (UFF) [72]. The inaccessibility of solvent at specific points on the solute is common, therefore models such as the solvent acces-

sible surface have been developed, this has been outlined in Figure 2.12 [73]. These models essentially generate a surface by rolling a spherical probe solvent molecule, with a given radii, along the van der Waals generated surface with the centre of the probe at each pointing defining the surface. However, despite the marginal increase in accuracy the van der Waals surfaces are instead commonly employed due to the reduced computational expense.

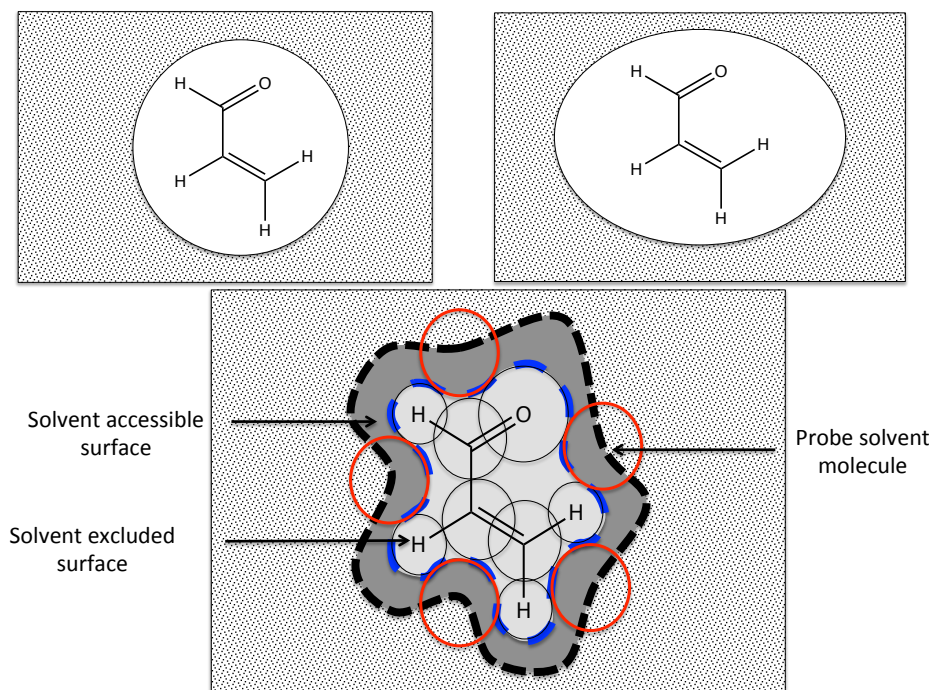


Figure 2.12: Various solvent models highlighting different cavity shapes, circular ellipsoid and molecular based respectively. For the molecular shaped cavity the solvent accessible and inaccessible region has been highlighted. Adapted from [73].

For the electrostatic interactions PCM models, such as DPCM [74], were based on the assumption that the solute electron density was contained completely within the cavity. However, this did not take into account the slow decay of the electron density as the distance from the nuclei is increased such as the 1s orbital decay of $e^{-\zeta r}$. Therefore, some of the charge would actually be located outside the cavity which would have been completely omitted within a DPCM approach. The default SCRF model within Gaussian is the integral equation formalism PCM (IEFPCM) [75–77], which was used heavily throughout Chapter 5 to simulate a polymer environment. This approach is found to cope well with the constraint to the electron density when compared to other PCM models [78].

2.12 Quantum Chemical Composite Methods

As expressed throughout, the majority of chemical reactions that are of interest contain molecules which are not feasible to computational investigation at the CCSD(T) level even when employing a moderately sized basis set. This limitation has given rise to a class of QM composite methods which aim to recover a significant amount of electron correlation, reaching chemical accuracy at points, *via* the combination of individual calculations. The level of theory for each individual calculation varies between each composite method, however, all are based on the following principle: the greater the electron correlation of the individual calculation the lower the basis set. The theoretical model used to obtain geometries and harmonic frequencies also deviates between these methods. The first suite of composite models we consider are the Gaussian- n theories, which assume the energy at each basis set is additive and also contain an empirical correction term [1]. The Gaussian-2 method is as follows:

- Geometry Optimisation & Frequency: HF/6-31G(d).
- Geometry: MP2/6-31G(d) used in subsequent calculations.
- Single point: MP2/6-311+G(3df,2p) also yields corresponding HF energy.
- Single point: QCISD(T)/6-311G(d,p) also yields MP2 and MP4 energy.
- Single point: MP4/6-311G(2df,p) and /6-311+G(d,p).
- Empirical correction: $-0.00481 N_{\alpha} - 0.00019 N_{\beta}$

where it is assumed that the number of alpha electrons (N_{α}) will always be equal or greater than that of N_{β} . The G-2 method has a mean absolute deviation (MAD) error of 1.1 kcal mol⁻¹ with respect to atomisation energies, ionisation potentials, electron and proton affinities of the G2-2 data set [79]. If one replaces the explicit MP4 energies with an estimated energy, obtained from the difference of the QCISD(T) and MP2 energies, this gives the G2(MP2) [44] method which has a MAD error of 1.5 kcal mol⁻¹. Another family of QM composite methods that are of interest are the complete basis set (CBS) models developed by Petersson and coworkers. These

methods differ from the Gaussian- n theories as basis set additivity is not assumed but instead an explicit extrapolation to the CBS limit is performed. A popular CBS model, particularly the CBS-QB3 extrapolation procedure [45], is outlined below

- Geometry Optimisation: B3LYP/6-311G(2d,d,p)
- Frequency: B3LYP/6-311G(2d,d,p)
- Single point and CBS extrapolation: UMP2/6-311+G(3d2f,2df,2p)
- Single point: MP4(SDQ)/6-31+G(d(f),p)
- Single point: CCSD(T)/6-31+G(d[‡])

where d[‡] represents the fact that the exponents of the d orbitals are from the triple- ζ , 6-311G(d), basis and therefore will be slightly different than the true exponent for that basis [1]. This CBS model was found to have a MAD of 1.1 kcal mol⁻¹ for the G2 test set. Once again several CBS methods are available with each having their own computational makeup, and thus varying cost. Examples of such methods are CBS-4 [45, 80], CBS-Q [80] and CBS-APNO [80] each with a corresponding MAD of 2.1, 1.0 and 0.5 kcal mol⁻¹ [1]. The most accurate method CBS method, CBS-APNO, requires an intense QCISD/6-311G(d,p) geometry optimisation thus limiting the systems this can be readily applied to. As these methods have extremely low errors they are prime candidates to compute reaction thermodynamic and kinetic quantities. Within the context of this thesis we use the CBS-QB3 method to model a variety of intramolecular furan Diels-Alder reactions due to the relatively cheap DFT optimisation procedure thus being applicable for our system size. The CBS-QB3 method has also been applied to very similar systems as the ones of interest herein, and performed well when compared against experimental findings [81].

2.13 Molecular-Dynamics

In the preceding text the overarching aim was to describe the electronic structure and how nuclei move when subjected to this external potential. However, one may wish to explore the structural dynamics of a particular molecular system, giving rise to

a method known as molecular dynamics (MD). Within this approach the electronic structure is not explicitly computed as molecules are described by their constituent atoms held together by chemical bonds. From an initial conformation and set of velocities the dynamic evolution of a system can be explored *via* numerically solving Newton’s second law of motion:

$$-\frac{dV(\vec{r})}{d\vec{r}} = m\frac{d^2\vec{r}}{dt^2} = \vec{F} = m\vec{a} \quad (2.100)$$

where \vec{r} denotes the collection of coordinates for the particles and $V(\vec{r})$ is the potential energy function at the specific arrangement, \vec{F} and \vec{a} relate to the force and acceleration vectors, respectively. In standard Cartesian coordinates the length of \vec{r} would equate to $3N$.

2.13.1 Force-fields

The potential energy of a system is generated by the force-field, a collection of parameters that have been derived from either QM computations or experimental findings. This computed potential is an extremely important factor in predicting the dynamics of a system, as the negative of the potential energy gradient is equal to \vec{F} , and it is therefore crucial that the specific force-field utilised includes parameters optimised for the system under analysis. These force-fields also rely on the fact that a vast amount of chemical systems share structurally similar segments, and as such a number of terms should be transferable across various molecular species. This idea is validated as C-H bonds vary by only 0.04 Å across various chemical systems, this variation reduces even further if the specific hybridisation is accounted for [1].

Force-fields are commonly subdivided into all atom (AA), united atom (UA) and course-grained (CG) potentials. Within the AA approach the force-field includes parameters for every type of atom, and normally all bonding environments (i.e. sp^3 , sp^2 and sp for the C atom), contained within the system. For UA groups specific atoms are grouped together as one interaction centre such as CH₃ or a methylene bridge (–CH₂–). This helps reduce the number of interactions within the system, thus allowing for larger atomic structures to be explored. For CG potentials these

interaction centres span even more atoms, providing an even cruder approximation of the atomic interactions. However, these are highly important when simulating large macro-molecules such as proteins due to the sheer amount of atoms.

The energy of a force-field is given by the sum of bonded and non-bonded terms, which in turn can be further decomposed, the former into bond-stretching ($E_{str.}$), angle-bending ($E_{bend.}$), torsion ($E_{tors.}$) and the latter involves van der Waals (E_{vdW}) and electrostatic terms ($E_{el.}$).

$$E_{FF} = E_{bonded} + E_{non-bonded} = E_{str.} + E_{bend.} + E_{tors.} + E_{vdW} + E_{el.} \quad (2.101)$$

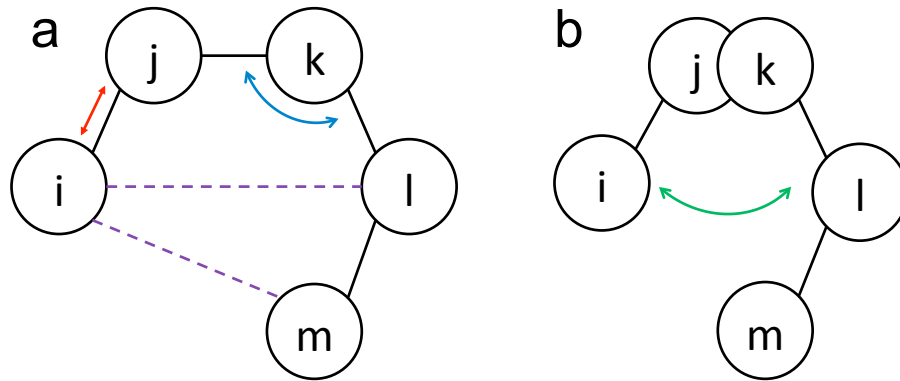


Figure 2.13: *Various bonding and non-bonded terms. The red, blue and green arrows represent a bond stretching, angle and torsion term respectively. The dashed purple lines represents the non-bonded interactions.*

The $E_{str.}$ and $E_{bend.}$ terms, as shown in equation 2.102, can be attained from a Taylor expansion around the relevant minimum energy strain-free bond length (r_0) and angle (θ_0), commonly truncating at second order terms. The terms k^{ab} and k^{abc} relate to the force constants. At large deviations these functions do not exude the correct limiting behaviour, convergence to the dissociation energy. However, for most simulations the important region is $\sim 10 \text{ kcal mol}^{-1}$ (40 kJ mol^{-1}) above the equilibrium arrangement therefore large deviations need not be modelled so accurately [1]. In regards to stretching, within this region a second order Taylor expansion (P2) is accurate to $\pm 0.1 \text{ \AA}$ from equilibrium, for a fourth-order expansion (P4) it is practically identical to the exact curve. For bending, P2 is accurate to about $\pm 30^\circ$ whilst P3, the third order truncation, gives exact quality energies up to $\pm 70^\circ$, see Figure 2.14.

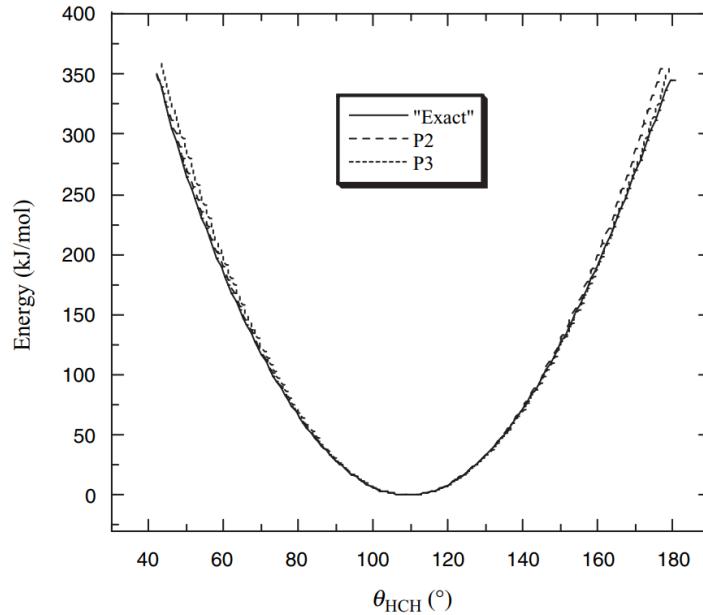


Figure 2.14: *The bending energy for CH_4 [1].*

The rotation around a bond has a far lower energy cost, for example going from staggered to eclipsed conformation of ethane has a barrier of only a few kcal mol^{-1} , when compared to the magnitude of stretching and bending. As large deviations are entirely possible the torsion energy is not approximated through a Taylor expansion. Instead this term is commonly approximated by the final term of equation 2.102, where n is the periodicity of the rotation.

$$\begin{aligned}
 E_{\text{bonded}} = & \sum_{A \neq B}^{\text{bonds}} k^{AB} (R^{AB} - R_0^{AB})^2 + \sum_{A \neq B \neq C}^{\text{angles}} k^{ABC} (\theta^{ABC} - \theta_0^{ABC})^2 \\
 & + \sum_{A \neq B \neq C \neq D}^{\text{torsion}} \sum_n k^{ABCD} (1 + \cos(n\phi_0^{ijkl})) \quad (2.102)
 \end{aligned}$$

We now turn our attention to non-bonded interactions which are modelled as a summation of pair wise interactions of atoms that are separated by at least two atoms, see equation 2.103. The first term is that of van der Waals (vdW) interactions which are commonly approximated by a Lennard-Jones potential. The vdW interactions are highly repulsive at short distances, as the term raised to the power 12 dominates, corresponding to the extreme repulsion between the two entities. At intermediate separations the instantaneous motion of electrons generates a temporary dipole, which in turn polarises the charge distribution of neighbouring molecules

or atoms therefore providing a slight attraction between the two. As the distance between the relevant species tends to ∞ this interaction goes to 0. This type of force is commonly referred to as an induced dipole-induced dipole. The final non-bonded term is that relating to the electrostatic interaction between the charged point particles with charge q_i and q_j and given by Coulomb's law. The partial charge of each atom is commonly obtained via fitting to the electrostatic potential as acquired from electronic structure theory.

$$E_{non-bonded} = \sum_{i>j}^{non-bonded} \left[\varepsilon_{ij} \left[\left(\frac{R_0}{R_{ij}} \right)^{12} - 2 \left(\frac{R_0}{R_{ij}} \right)^6 \right] + \frac{1}{4\pi\epsilon_0} \frac{q_i q_j}{R_{ij}} \right] \quad (2.103)$$

In high accuracy force-fields there may also be cross coupling terms between the three bonding interactions. The interpretation of this additional term is easily understood through consideration of a specific test case. If we consider H₂O the global optimum arrangement has an O–H distance of 0.958 Å and an H–O–H of 104.5°. If one compresses the angle to 90° this subsequently elongates the equilibrium O–H distance to 0.968 Å, determined via electronic structure computations. The opposite is true if the angle is allowed to widen. This lengthening can be attributed to the reduced distance between the H atoms as the angle is compressed, therefore leading to increased repulsion and a subsequent bond stretch to alleviate this. As this term was not included in the original force-field description coupling of the aforementioned angle–stretch would not be accounted for. One may also argue that cross linking terms should be present between the bonding and electrostatic terms, however, this is not common practice due to the increased computation expense [1].

2.13.2 Integration Methods

As the very essence of MD simulations are to investigate the time evolution of an initial system, through a series of minuscule time steps (Δt), one must explore the various methods used to propagate the system. The first integrator is the Verlet algorithm [82], which to third order relies on the following:

$$\vec{r}_i(t + \Delta t) = 2\vec{r}_i(t) - \vec{r}_i(t - \Delta t) + \vec{a}_i(\Delta t)^2 \quad (2.104)$$

where the positions at time t and $(t - \Delta t)$, and accelerations, are used to generate the atomic positions one time step after at a time of $t + \Delta t$. As one would expect a lower time step has a greater degree of accuracy, however, this comes at the cost of more iterations to reach a given time. As rotations and vibrations can occur on the order of 10 fs a common time step is usually one order of magnitude lower at 1 fs. Therefore, if a 10 ns run is desired this would require 1.0×10^7 individual time steps. A drawback of the Verlet algorithm is a result of explicit velocities not being considered which are very useful in controlling the temperature of the ensemble. This has been highlighted below:

$$\frac{1}{2}(3Y - N_c)k_B T = \frac{1}{2} \left\langle \sum_i^Y m_i \vec{v}_i^2 \right\rangle_{Fr} \quad (2.105)$$

where N_c represents the number of geometrical constraints and Fr is the specific frame i.e. the specific point sampled. If one wishes to deal with velocities directly they may use a leap-frog algorithm [83] which computes the positions and velocities at different times, separated by half the time step. This method has been shown to have better numerical accuracy, however, the positions and velocities are always out of synchronisation.

2.13.3 Simulation Overview

In order to begin these simulations one has to specify a number of input parameters, such as the atomic positions, initial velocities and the specific force-field used to generate the potential energy function. The initial set of coordinates may be taken from the x-ray crystal structure, as is the common in the case of proteins, or high accuracy QM methods, if the system is small enough to be handled by a geometry optimisation procedure. Initial velocities are generated *via* random selections from a Maxwell-Boltzmann distribution. In conjunction with the above parameters there are also various different ensembles that may be generated based upon the quantities that are held constant throughout the simulation. If the energy and volume remains constant, this generates an NVE ensemble. Within this approach no control on the temperature and pressure is implemented. It should be remembered that due

to the asynchronous nature of the leap-frog algorithm the kinetic and potential energy terms will pertain to slightly different arrangements. The total energy can be obtained from equation 2.106.

$$E_{tot.} = \sum_{i=1}^N \frac{1}{2} m_i \vec{v}_i^2 + V(\vec{r}) \quad (2.106)$$

In addition to an NVE ensemble one may also generate those of constant volume and temperature (NVT) or constant pressure and temperature (NPT). The temperature is normally controlled through scaling of the velocities, or coupling to a heat bath, with a pressure bath normally used to maintain a constant pressure [1]. After the system is equilibrated the simulation is ready to be undertaken and configurations extracted based upon a user-defined sampling interval. This technique of exploring the potential configurational space of a dynamic system is used in Chapter 6 on various organic π -conjugated material employing a recently parameterised force-field [84]. From the MD generated configurations we then subject them to a QM treatment to explore the electronic structure properties.

2.14 References

- [1] F. Jensen, *Introduction to Computational Chemistry*, John Wiley & Sons Ltd., West Sussex, England, **1999**.
- [2] C. J. Cramer, *Essentials of Computational chemistry: Theories and Models*, John Wiley & Sons Ltd., West Sussex, England, **2004**.
- [3] A. Szabo, N. S. Ostlund, *Modern Quantum Chemistry: Introduction to Advanced Electronic Structure Theory*, Dover Publications, New York, USA, **1996**.
- [4] P. Atkins, R. Friedman, *Molecular Quantum Mechanics*, Oxford University Press Inc., New York, USA, **1997**.
- [5] D. J. Griffiths, *Introduction to Quantum Mechanics*, Prentice Hall, New Jersey, USA, **1995**.

- [6] L. S. Cederbaum, *The Journal of Chemical Physics* **2013**, *138*, 224110.
- [7] M. Born, J. Oppenheimer, *Annalen der Physik* **1927**, *84*, 457–484.
- [8] C. J. Roothaan, *Reviews of Modern Physics* **1951**, *23*, 69.
- [9] C. J. Roothaan, *Reviews of Modern Physics* **1960**, *32*, 179–185.
- [10] T. Bally, W. T. Borden in *Reviews in Computational Chemistry*, John Wiley Sons, Ltd, **2007**, pp. 1–97.
- [11] P. Hohenberg, W. Kohn, *Physical Review* **1964**, *136*, B864–B871.
- [12] W. Kohn, L. J. Sham, *Physical Review* **1965**, *140*, A1133–A1138.
- [13] A. J. Cohen, D. J. Tozer, N. C. Handy, *The Journal of Chemical Physics* **2007**, *126*, 214104.
- [14] T. Koopmans, *Physica* **1933**, *1*, 104–113.
- [15] J. C. Slater, *Physical Review* **1930**, *36*, 57–64.
- [16] S. F. Boys, A. C. Egerton, *Proceedings of the Royal Society of London. Series A. Mathematical and Physical Sciences* **1950**, *200*, 542–554.
- [17] W. J. Hehre, R. F. Stewart, J. A. Pople, *The Journal of Chemical Physics* **1969**, *51*, 2657–2664.
- [18] R. Ditchfield, W. J. Hehre, J. A. Pople, *The Journal of Chemical Physics* **1971**, *54*, 724–728.
- [19] W. J. Hehre, R. Ditchfield, J. A. Pople, *The Journal of Chemical Physics* **1972**, *56*, 2257–2261.
- [20] R. Krishnan, J. S. Binkley, R. Seeger, J. A. Pople, *The Journal of Chemical Physics* **1980**, *72*.
- [21] T. Clark, J. Chandrasekhar, G. W. Spitznagel, P. V. R. Schleyer, *Journal of Computational Chemistry* **1983**, *4*.
- [22] T. H. Dunning, *The Journal of Chemical Physics* **1989**, *90*, 1007–1023.
- [23] R. A. Kendall, T. H. Dunning, R. J. Harrison, *The Journal of Chemical Physics* **1992**, *96*.

- [24] J. A. Pople, R. Seeger, R. Krishnan, *International Journal of Quantum Chemistry* **1977**, *12*, 149–163.
- [25] J. Foresman, A. Frisch, *Exploring Chemistry with Electronic Structure Methods*, 3rd ed., Gaussian, Inc.: Wallingford, CT, 2015, **2003**.
- [26] M. J. Frisch, G. W. Trucks, H. B. Schlegel, G. E. Scuseria, M. A. Robb, J. R. Cheeseman, G. Scalmani, V. Barone, G. A. Petersson, H. Nakatsuji, X. Li, M. Caricato, A. V. Marenich, J. Bloino, B. G. Janesko, R. Gomperts, B. Mennucci, H. P. Hratchian, J. V. Ortiz, A. F. Izmaylov, J. L. Sonnenberg, D. Williams-Young, F. Ding, F. Lipparini, F. Egidi, J. Goings, B. Peng, A. Petrone, T. Henderson, D. Ranasinghe, V. G. Zakrzewski, J. Gao, N. Rega, G. Zheng, W. Liang, M. Hada, M. Ehara, K. Toyota, R. Fukuda, J. Hasegawa, M. Ishida, T. Nakajima, Y. Honda, O. Kitao, H. Nakai, T. Vreven, K. Throssell, J. A. Montgomery, Jr., J. E. Peralta, F. Ogliaro, M. J. Bearpark, J. J. Heyd, E. N. Brothers, K. N. Kudin, V. N. Staroverov, T. A. Keith, R. Kobayashi, J. Normand, K. Raghavachari, A. P. Rendell, J. C. Burant, S. S. Iyengar, J. Tomasi, M. Cossi, J. M. Millam, M. Klene, C. Adamo, R. Cammi, J. W. Ochterski, R. L. Martin, K. Morokuma, O. Farkas, J. B. Foresman, D. J. Fox, *Gaussian 09 Revision D.01*, Gaussian Inc. Wallingford CT, **2016**.
- [27] J. C. Greer, *The Journal of Chemical Physics* **1995**, *103*, 1821–1828.
- [28] J. Greer, *Journal of Computational Physics* **1998**, *146*, 181–202.
- [29] L. Tong, M. Nolan, T. Cheng, J. Greer, *Computer Physics Communications* **2000**, *131*, 142–163.
- [30] J. P. Coe, D. J. Taylor, M. J. Paterson, *The Journal of Chemical Physics* **2012**, *137*, 194111.
- [31] J. C. Greer, *The Journal of Chemical Physics* **1995**, *103*, 7996–8003.
- [32] J. Coe, P. Murphy, M. Paterson, *Chemical Physics Letters* **2014**, *604*, 46–52.
- [33] W. Györfy, R. J. Bartlett, J. C. Greer, *The Journal of Chemical Physics* **2008**, *129*, 064103.

- [34] J. Coe, D. Taylor, M. Paterson, *Journal of Computational Chemistry* **2013**, *34*, 1083.
- [35] P. Murphy, J. P. Coe, M. J. Paterson, *Journal of Computational Chemistry* **2018**, *39*, 319–327.
- [36] N. M. da Silva Almeida, PhD thesis, Heriot-Watt University, **2016**.
- [37] A. Prentice, J. Coe, M. Paterson, *Journal of Chemical Physics* **2019**, *151*.
- [38] V. Kvasnička, V. Laurinc, S. Biskupič, *Molecular Physics* **1980**, *39*, 143–161.
- [39] C. Møller, M. S. Plesset, *Physical Review* **1934**, *46*, 618–622.
- [40] J. A. Pople, R. Krishnan, H. B. Schlegel, J. S. Binkley, *International Journal of Quantum Chemistry* **1978**, *14*, 545–560.
- [41] R. J. Bartlett, *The Journal of Physical Chemistry* **1989**, *93*, 1697–1708.
- [42] I. Shavitt, R. J. Bartlett, *Many-Body Methods in Chemistry and Physics: MBPT and Coupled-Cluster Theory*, Cambridge University Press, **2009**.
- [43] G. D. Purvis, R. J. Bartlett, *The Journal of Chemical Physics* **1982**, *76*, 1910–1918.
- [44] C. W. Bauschlicher, H. Partridge, *The Journal of Chemical Physics* **1995**, *103*, 1788–1791.
- [45] J. A. Montgomery, M. J. Frisch, J. W. Ochterski, G. A. Petersson, *The Journal of Chemical Physics* **2000**, *112*, 6532–6542.
- [46] B. O. Roos, P. R. Taylor, P. E. Sigbahn, *Chemical Physics* **1980**, *48*, 157–173.
- [47] P. A. Malmqvist, A. Rendell, B. O. Roos, *The Journal of Physical Chemistry* **1990**, *94*, 5477–5482.
- [48] E. H. Lieb, B. Simon, *Advances in Mathematics* **1977**, *23*, 22–116.
- [49] J. P. Perdew, Y. Wang, *Physical Review B* **1992**, *45*, 13244–13249.
- [50] A. D. Becke, *Physical Review A* **1988**, *38*, 3098–3100.
- [51] J. P. Perdew, *Physical Review B* **1986**, *33*, 8822–8824.
- [52] A. D. Becke, M. R. Roussel, *Physical Review A* **1989**, *39*, 3761–3767.

- [53] C. Lee, W. Yang, R. G. Parr, *Physical Review B* **1988**, *37*, 785–789.
- [54] J. P. Perdew, K. Burke, M. Ernzerhof, *Physical Review Letters* **1996**, *77*, 3865–3868.
- [55] J. P. Perdew, K. Burke, M. Ernzerhof, *Physical Review Letters* **1997**, *78*, 1396–1396.
- [56] A. D. Becke, *The Journal of Chemical Physics* **1993**, *98*, 1372–1377.
- [57] Y. Zhao, D. G. Truhlar, *Theoretical Chemistry Accounts* **2008**, *120*, 215–241.
- [58] Y. Zhao, D. G. Truhlar, *The Journal of Physical Chemistry A* **2006**, *110*, 13126–13130.
- [59] H. S. Yu, X. He, S. L. Li, D. G. Truhlar, *Chemical Science* **2016**, *7*, 5032–5051.
- [60] T. Yanai, D. P. Tew, N. C. Handy, *Chemical Physics Letters* **2004**, *393*, 51–57.
- [61] M. Jäger, L. Freitag, L. González, *Coordination Chemistry Reviews* **2015**, *304-305*, 146–165.
- [62] S. Grimme, S. Ehrlich, L. Goerigk, *Journal of Computational Chemistry* **2011**, *32*, 1456–1465.
- [63] S. Grimme, *Journal of Computational Chemistry* **2006**, *27*, 1787–1799.
- [64] E. Runge, E. K. U. Gross, *Physical Review Letters* **1984**, *52*, 997–1000.
- [65] J. M. Hollas, *Basic Atomic and Molecular Spectroscopy*, (Ed.: E. W. Abel), The Royal Society of Chemistry, **2002**, pp. X001–X004.
- [66] K. Fukui, *Accounts of Chemical Research* **1981**, *14*, 363–368.
- [67] H. P. Hratchian, H. B. Schlegel in *Theory and Applications of Computational Chemistry*, (Eds.: C. E. Dykstra, G. Frenking, K. S. Kim, G. E. Scuseria), Elsevier, Amsterdam, **2005**, pp. 195–249.
- [68] C. Peng, H. Bernhard Schlegel, *Israel Journal of Chemistry* **1993**, *33*, 449–454.
- [69] J. W. Ochterski, *Thermochemistry in Gaussian* **2000**.
- [70] L. Onsager, *Journal of the American Chemical Society* **1936**, *58*, 1486–1493.

- [71] M. Cossi, V. Barone, R. Cammi, J. Tomasi, *Chemical Physics Letters* **1996**, *255*, 327–335.
- [72] A. K. Rappe, C. J. Casewit, K. S. Colwell, W. A. Goddard, W. M. Skiff, *Journal of the American Chemical Society* **1992**, *114*, 10024–10035.
- [73] J. Tomasi, B. Mennucci, R. Cammi, *Chemical Reviews* **2005**, *105*, 2999–3094.
- [74] S. Miertus, E. Scrocco, J. Tomasi, *Chemical Physics* **1981**, *55*, 117–129.
- [75] E. Cancès, B. Mennucci, *Journal of Mathematical Chemistry* **1998**, *23*, 309–326.
- [76] E. Cancès, B. Mennucci, J. Tomasi, *The Journal of Chemical Physics* **1997**, *107*, 3032–3041.
- [77] B. Mennucci, E. Cancès, J. Tomasi, *The Journal of Physical Chemistry B* **1997**, *101*, 10506–10517.
- [78] R. E. Skyner, J. L. McDonagh, C. R. Groom, T. van Mourik, J. B. O. Mitchell, *Physical Chemistry Chemical Physics* **2015**, *17*, 6174–6191.
- [79] L. A. Curtiss, K. Raghavachari, G. W. Trucks, J. A. Pople, *The Journal of Chemical Physics* **1991**, *94*, 7221–7230.
- [80] J. W. Ochterski, G. A. Petersson, J. A. Montgomery, *The Journal of Chemical Physics* **1996**, *104*, 2598–2619.
- [81] R. L. Rae, J. M. Zurek, M. J. Paterson, M. W. P. Bebbington, *Organic and Biomolecular Chemistry* **2013**, *11*, 7946–7952.
- [82] L. Verlet, *Physical Review* **1967**, *159*, 98–103.
- [83] R. Hockney, S. Goel, J. Eastwood, *Journal of Computational Physics* **1974**, *14*, 148–158.
- [84] J. Wildman, P. Repiscak, M. J. Paterson, I. Galbraith, *Journal of Chemical Theory and Computation* **2016**, *12*, 3813–3824.

Chapter 3

A Systematic Construction of Configuration Interaction Wavefunctions in the Complete CI Space

3.1 Abstract

In this chapter we introduce a systematic alternative to Monte-Carlo configuration interaction (MCCI) termed systematic-MCCI (sMCCI). Within this approach the entire interacting space is reduced to smaller batches, subjecting only the most important configurations across all batches as potential additions to the wavefunction. We compare this method to MCCI and a novel pruned-FCI approach. For the ground state of neon, as described in the cc-pVTZ basis, we observe no apparent difference between the various methods, with all recovering 99 % of the correlation energy and generating wavefunctions of a very similar composition. We then consider the potential energy surface corresponding to the symmetric double-hydrogen dissociation of water within a cc-pVDZ basis. Once again MCCI performs comparable to the systematic approaches. Despite sMCCI having longer run times across the number of processors considered we do observe very good scalability. We then extend this comparison to the first A_1 excitation energy of carbon monoxide, once again within a cc-pVDZ basis, for which we are within 0.1 eV of the FCI transition energy for both MCCI methods despite vast reductions in the wavefunction size. Finally, we consider the chromium dimer, within a cc-pVTZ basis constraining double occupation of the 18 lowest orbitals in all configurations. For this system we find that sMCCI avoids becoming trapped in the same local minimum of configuration space as MCCI, however, repeated MCCI calculations with increasing number of processors can yield a lower energy. The calculations regarding Cr_2 were performed as part of collaborative work by Dr. Jeremy Coe of Heriot-Watt University.

3.2 Introduction

The accurate description of electron-electron interactions has long been the crux of electronic structure theories, assuming a frozen nuclear framework. The central wavefunction based approach, Hartree-Fock (HF) theory, overestimates this repulsive interaction as it is treated in a mean-field fashion leading to higher absolute energies and shorter predicted bond lengths. As outlined in Section 2.6.1 the full configuration interaction (FCI) wavefunction ($|\Psi^{FCI}\rangle$), and corresponding energy (E^{FCI}), are exact within the space spanned by the one-electron basis set. However, such a treatment is only computationally viable for all but the smallest of systems and/or basis sets. These restrictions can be attributed to the dramatic scaling of the potential excitation space, and subsequently the vast dimensionality of the Hamiltonian matrix (\mathbf{H}^{FCI}), as the number of basis functions (M) grows large. FCI computations formally scale factorially as both M and the number of electrons increase (n). At this moment in time the largest FCI wavefunction considered contains $\sim 10^{10}$ Slater determinants (SD) pertaining to the nitrogen molecule [1]. The potential energy surface (PES) of Be_2 using a cc-pV6Z has also been investigated at the FCI level with determinants containing $\sim 1.85 \times 10^8$ configurations [2].

As the $|\Psi^{FCI}\rangle$ is unattainable for the majority of chemical systems many techniques have been developed to approximate this quantity and therefore capture a significant portion of the correlation energy ($E^{corr.}$), see equation 2.57 provided in the earlier Chapter. These methods consider only a portion of the configurational space, significantly reducing the computational costs, and thus allow for the application of these methods to a greater range of chemical problems whilst still reaching a suitable level of accuracy, despite the vast reduction of variationally optimisable parameters. This is a valid approach due to the extreme sparsity of \mathbf{H}^{FCI} as many elements are equal to zero, due to the occupation of specific MOs, or have a negligible contribution to the wavefunction.

Elegant methods that build upon a single reference, such as configuration interaction singles and doubles (CISD), have known problems when bonds deviate sig-

nificantly from equilibrium arrangements as the single determinant approach breaks down, and thus can deviate quite substantially from FCI results. The development of multi-reference (MR) methods, such as complete active space self consistent field (CASSCF), attempt to recover this missing static correlation, from which subsequent MRCI or perturbative computations may be employed to recover the remaining dynamic portion. However, these methods can still suffer from similar problems to FCI and also require considerable knowledge of both the system of interest and the problem at hand, as the determination of an appropriate active space is crucial.

As many of the configurations contained within $|\Psi^{FCI}\rangle$ have small coefficients, and as such have negligible influence on resulting properties, there has been a recent surge in the development and use of approaches that iteratively build up the wavefunction through addition of configurations with a noticeable weighting (selected-CI). These methods have the ability to create very compact wavefunctions and can be applied to both single and multi-reference problems. A method that uses a stochastic approach to build the wavefunction is Monte-Carlo configuration interaction (MCCI) [3–5]. This involves randomly augmenting an initial trial vector through the addition of coupled configurations, maintaining their place in the resulting wavefunction only if their absolute coefficient is larger than a user defined parameter (c_{min}). An in-depth overview of this algorithm is provided in Section 3.3.2. MCCI has been successfully applied to the description of ground-state PESs for various chemical systems [6]. For example the surface corresponding to a single hydrogen dissociation in methane, MCCI has been shown to outperform UCCSD(T) [7] and CASPT2 [8] despite wavefunctions that only contain 1.6×10^{-2} % of the FCI space. MCCI has also been used in the prediction of electronic excitation energies [9] for various systems such as Ne, N₂ and H₂O. MCCI is found to perform extremely well, computing excitation energies with an accuracy comparable to that of the computationally intensive equation-of-motion (EOM) CCSDT methodology. When compared to FCI these excitation energies differ by a few tens of a meV, despite once again containing only a minuscule fraction of the potential configurational space. Transition metal dimers, such as Cr₂, Sc₂, Mo₂ and ScNi have also

been studied with MCCI [10], which pose difficulties due to the highly correlated nature of the wavefunction and sheer number of potential configurations that could be considered. The PES relating to the internuclear displacement of Cr_2 is outlined below for a cc-pVDZ and cc-pVTZ basis, with a varying c_{\min} .

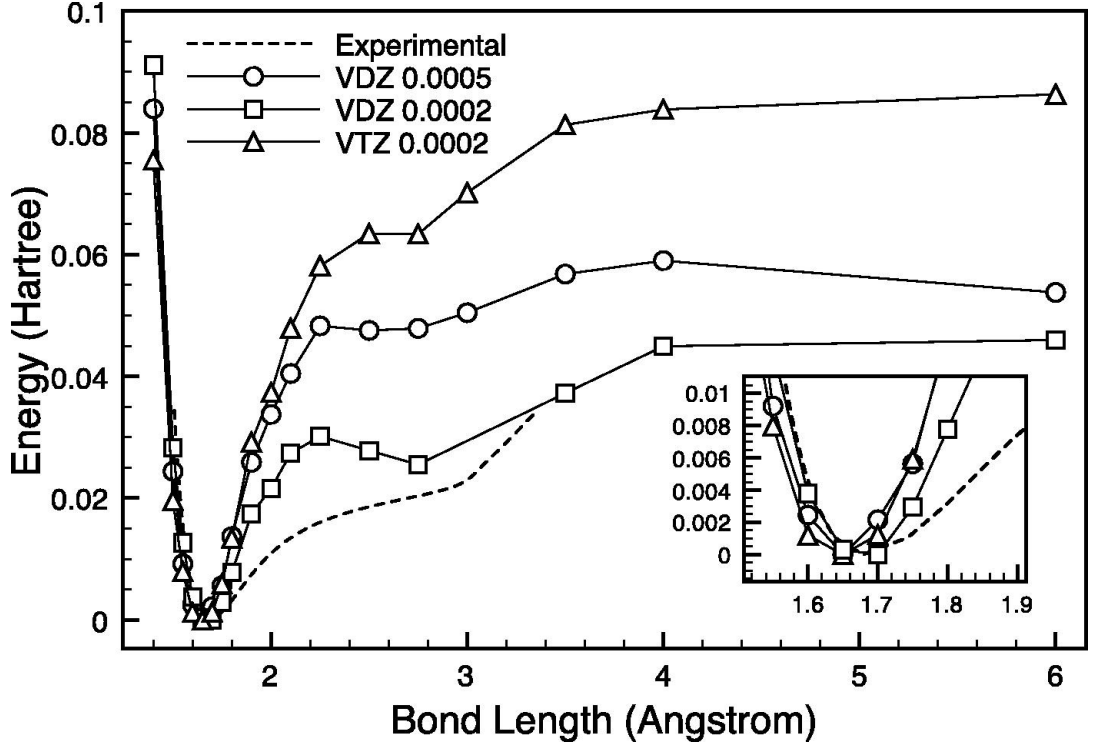


Figure 3.1: Energy as a function of Cr internuclear separation, all minima were shifted to zero. For cc-pVDZ a c_{\min} of 5×10^{-4} or 2×10^{-4} was used in the MCCI computations, in regards to the larger cc-pVTZ basis only the latter was employed, the lowest 18 orbitals were double occupied in all instances. Reprinted from [10].

At a $c_{\min.} = 2 \times 10^{-4}$ the dissociation energy for cc-pVDZ provides far better agreement than the cc-pVTZ counterpart, with respective values of 1.22 and 2.32 eV, to the experimental value of 1.53 ± 0.06 eV [11]. The cc-pVDZ and cc-pVTZ energies are also found to increase too rapidly at separations slightly larger than $R_{eq.}$, with the latter being the more dramatic of the two. This has been attributed to the increasing FCI space, with spaces of 10^{15} and 10^{18} CSFs respectively. As both converged wavefunctions contain 1.2×10^5 CSFs there is a greater chance that important CSFs can be missed for cc-pVTZ as a result of the increased excitation space and the stochastic selection process. The MCCI approach has also been extended to investigate excited PESs, including potential conical intersections, [12], spin-orbit coupling [13] and determine hyperpolarisabilities [14].

As stated above MCCI has the potential to generate highly compact wavefunctions with accuracy rivalling the most computationally demanding methods for systems containing at most a few heavy atoms. However, the optimal nature of resulting MCCI wavefunctions, has to the best of our knowledge, never been studied. This raises important ideas such as, can one obtain a lower energy with a wavefunction of similar size or can a smaller wavefunction give a similar energy? In order to propose possible answers to these questions one would have to employ a somewhat systematic approach to MCCI. This systematic approach would entail consideration of the entire single and double space (N_{sd}), not just a stochastic selection from this space. If one considers the N_{sd} as a single entity the method will quickly suffer from similar drawbacks as FCI, storage and diagonalisation of a matrix with a dimensionality that is not computationally feasible, when N_{sd} inevitably becomes large. A potential alternative to this would involve systematically checking all possible combinations of smaller subsets of N_{sd} , adding only the largest weighted configurations on each iteration and continuing within this iterative fashion. However, this approach would also be computationally intractable for virtually any system of interest. If we limit the potential addition on a single iteration to 30 configurations, from a N_{sd} containing 1000 configurations, one would have to perform $\binom{1000}{30}$ diagonalisations. This would be a serious underestimate as in most cases N_{sd} will be orders of magnitude larger, and one would also wish to add more than 30 configurations per cycle, which would only worsen the issue at hand. Therefore both systematic methods would be unfeasible for entirely different reasons, the former based upon the diagonalisation of a matrix with a large dimensionality, and the latter due to the sheer volume of diagonalisations of smaller configurational spaces.

Herein, we propose a new methodology, referred to as systematic-MCCI (sM-CCI), which considers N_{sd} , albeit not in every possible combination but in a computationally viable regime. This approach works through the randomly ordered N_{sd} space in batches (i_{batch}) to be added to the current set of configurations, adding only the largest weighted i_{add} configurations across all batches. As every configuration is only considered in one batch the number of diagonalisations per iteration

is $\simeq N_{sd}/i_{batch}$, which is drastically reduced when comparing to $\binom{N_{sd}}{i_{add}}$. As N_{sd} is randomly ordered within each iteration different combinations will be considered as the computation evolves. The independent nature of the batches also ensures that this algorithm can run efficiently across any number of processors hereby leading to a deal of scalability.

The MCCI methods outlined above iteratively build up the wavefunction, however, for comparative purposes it would be interesting to investigate an approach that does the opposite, essentially systematically deconstructing the exact wavefunction. From the normalised $|\Psi^{FCI}\rangle$ all configurations that have an absolute coefficient lower than c_{min} are discarded, and the energy computed in this reduced configurational space. We refer to this methodology as pruned-FCI (p-FCI). We acknowledge that this process can only be performed on the smallest of systems, as the FCI wavefunction must be available, and may seem counter intuitive, however, this merely serves to allow another way of investigate how optimal the MCCI wavefunctions are.

We therefore begin with an overview of the computational methods used within this study. An initial benchmarking study on a single neon atom using a cc-pVTZ basis is then performed to determine suitable i_{batch} and i_{add} parameters for sMCCI, as this is a relatively straightforward test case in terms of the ground state electronic structure. A comparison between sMCCI, MCCI and p-FCI is then explored in terms of accuracy and wavefunction composition. The scalability of the MCCI methods is also explored for various processor amounts ranging from 8 to 72, with a brief comparison between the use of SDs and CSFs performed. We then turn our attention to the PES corresponding to the double-hydrogen dissociation in H_2O , due to the varying degree of multi-reference character as the bond length is stretched. Next we compare the methods in approximating the first A_1 excitation energy of carbon monoxide using a cc-pVDZ basis. The study concludes with consideration of the chromium dimer at an internuclear separation of 2.75 Å, as this is a particularly challenging geometry.

3.3 Computational Methodology

3.3.1 Full Configuration Interaction

The FCI wavefunction can be expressed in terms of all potential excited determinants that can be generated from a set of k occupied and $M - k$ virtual orbitals. This is shown below

$$\begin{aligned} |\Psi^{FCI}\rangle = c^{HF} |\Psi^{HF}\rangle + \sum_{a,r}^{k,M-k} c_a^r |\Psi_a^r\rangle + \sum_{a<b,r<s}^{k,M-k} c_{ab}^{rs} |\Psi_{ab}^{rs}\rangle \\ + \sum_{a<b<c,r<s<t}^{k,M-k} c_{abc}^{rst} |\Psi_{abc}^{rst}\rangle + \dots \quad (3.1) \end{aligned}$$

where we have once again made use of the naming convention outlined in Section 2.6.1. We also make reference to truncated-CI methods which allow only certain excitation levels relative to the HF wavefunction to be included in the wavefunction. For example, CISD and CISDT would include all excitation types up to doubles and triples, respectively.

3.3.2 Monte-Carlo Configuration Interaction

The MCCI algorithm (version 4) [5] builds upon an initial trial vector ($|\Psi_{ref}^{(0)}\rangle$), herein the converged closed-shell $|\Psi^{HF}\rangle$ but in general this may be a linear combination of x CSFs or SDs, through an iterative stochastic sampling procedure. From this reference space a random number of coupled CSFs ($N_{new}^{(1)}$) are generated, via single or double-excitations, and appended to $|\Psi_{ref}^{(0)}\rangle$, such that $|\Psi_{new}^{(1)}\rangle$, the first modification of the trial vector, takes the form of equation 3.2. This process is commonly referred to as branching the wavefunction. The specific iteration is provided in the superscript.

$$|\Psi_{new}^{(1)}\rangle = \sum_{q=1}^x c_q |\Psi_q\rangle + \sum_{p=x+1}^{x+N_{new}^{(1)}} c_p |\Psi_p\rangle = \sum_{r=1}^{x+N_{new}^{(1)}} c_r |\Psi_r\rangle \quad (3.2)$$

It should be noted that N_{new} is not a fixed parameter but instead differs between iterations. At early stages N_{new} is varied such that $|\Psi_{new}\rangle$ contains ~ 100 total

configurations but as the computation evolves N_{new} is taken to be \sim the same size as the relevant reference space therefore generating a trial wavefunction which is roughly twice the size of the specific reference space. Only configurations that match the spatial and spin symmetry of the desired wavefunction are included in $\{N_{new}\}$, reducing the potential space. As the same new configurations may be generated from different configurations in the reference space, the modified trial vector is checked for duplicates which are subsequently removed *via* the quick sort approach of Coe and Paterson [15].

The expansion coefficient of each CSF within $|\Psi_{new}^{(1)}\rangle$ can be determined through diagonalisation of the eigenvalue equation:

$$\mathbf{H}^{(1)} c^{(1)} = \mathbf{S}^{(1)} c^{(1)} E_{new}^{(1)} \quad (3.3)$$

where $\mathbf{H}^{(1)}$ and $\mathbf{S}^{(1)}$ are the Hamiltonian and overlap matrices respectively, $c^{(1)}$ is the coefficient vector and $E_{new}^{(1)}$ is the corresponding energy. This CSF overlap matrix is not diagonal as each CSF is generated *via* a projection method and a subsequent random walk through the spin path diagram, thus ensuring linear dependence. The diagonalisation algorithm implemented is that of Davidson, if only the lowest eigenvalue is of interest, however, if multiple states are required the Davidson-Liu methodology can be used. A c_{min} value is then introduced which allows only newly generated CSFs with a coefficient larger than this user-defined threshold to survive the iteration (i.e. $|c_p| \geq c_{min}$), else discarded. Every P_f iteration all CSFs present are subject to this pruning stage, referred to as a full-prune, and not solely those generated in the preceding branching stage as outlined in equation 3.4:

$$|\Psi_{new}^{(P_f t)}\rangle = \underbrace{|\Psi^{(P_f t-1)}\rangle + \sum_{k=N^{(P_f t-1)}+1}^{N^{(P_f t-1)}+N_{new}^{(P_f t)}} c_k |\Psi_k\rangle}_{\text{All Subject to Prune}} \quad (3.4)$$

where the subscript has been omitted to indicate CSFs that remained post-prune. It should be noted that a full prune is always performed on iteration 1 for both MCCI and sMCCI. However, this cycle is not included in any of the convergence check

procedure which follows. Thus, the number of CSFs present in $|\Psi^{(1)}\rangle$ will always be $\leq x + N_{new}^{(1)}$, and subsequently form the reference space for the following cycle, which in this example will be $|\Psi_{ref}^{(2)}\rangle$. This process of branching, diagonalisation and pruning is repeated until convergence of both the vector length ($conv.l$) and resulting energy ($conv.E$) has been achieved [9]. As per equation 3.5, if one allows c_{min} and the number of iterations to tend towards 0 and ∞ , respectively, the resulting wavefunction and energy would equate to that of FCI. This methodology would correspond to the standard algorithm with the exclusion of the pruning procedure.

$$\lim_{c_{min} \rightarrow 0, \text{iteration} \rightarrow \infty} \text{MCCI} \rightarrow \text{FCI} \quad (3.5)$$

The convergence check is initiated solely on iterations that follow a full-prune, which have the form $P_ft + 1$ where $t \in \mathbb{Z}^+$, and corresponds to the specific iteration the calculation is on. The stochastic nature of MCCI causes ΔQ_{P_ft+1} , which can either be the energetic or vector-length difference between iterations $P_ft + 1$ and $P_f(t-1) + 1$, to randomly fluctuate. As a result of this one does not test convergence directly from ΔQ_{P_ft+1} but instead from a moving average over L successive $P_ft + 1$ cycles. The equations below pertain to the energy convergence procedure.

$$\bar{E}_b = \frac{1}{L} \sum_{t=b+1-L}^b E_{new}^{(i=P_ft+1)} \quad (3.6)$$

The convergence check is fulfilled when $\bar{E}_b - \bar{E}_{b-1}$ for the last J differences satisfies equation (3.7):

$$\max_{b=t+1-J, t} |\bar{E}_b - \bar{E}_{b-1}| \leq E_{conv.thres.} \quad (3.7)$$

where $E_{conv.thres.}$ is the specific user-defined convergence criteria. Once converged, the wavefunction is subject to one normal and full-prune cycle ending with a final iteration in which no branching is performed, this final step is performed to obtain the energy corresponding to the fully pruned final system. Within the context of this thesis all calculations performed utilise L and J values of 3. For MCCI we perform a full-prune every 10 iterations, corresponding to a $P_f = 10$, therefore convergence can be achieved from iteration 61 and on-wards as there will be sufficient data to

test. A general schematic of the algorithm is given in Figure 3.2.

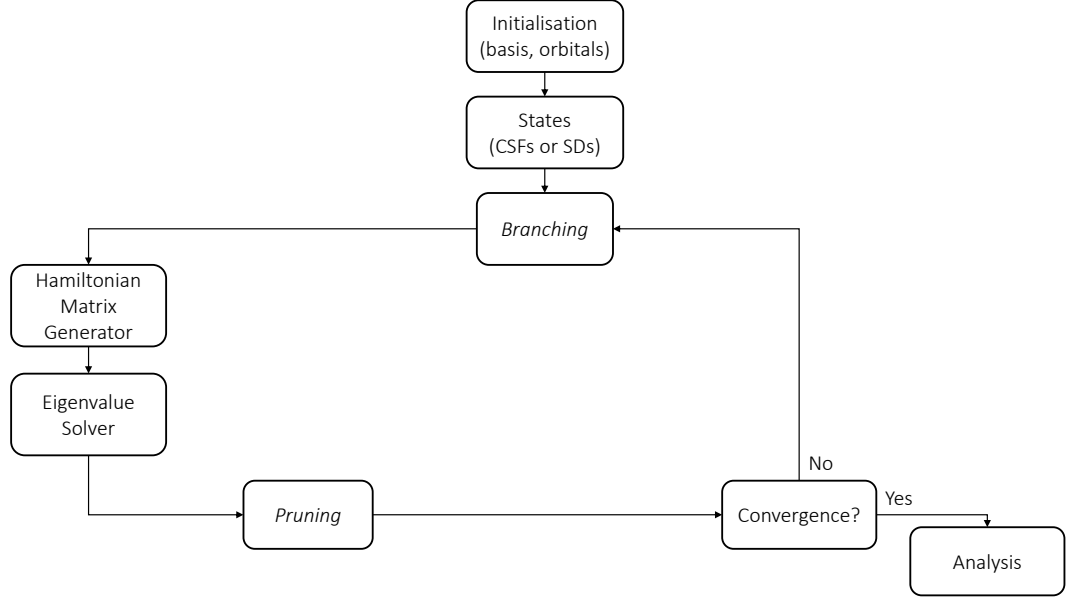


Figure 3.2: General overview of the MCCI algorithm.

The procedure outlined above was in respect to a computation running on a single node, but MCCI also has the option to be carried out in parallel across multiple processors (N_{proc}). Within this parallelised regime each processor would independently branch, diagonalise and prune a subset of $\sim \frac{N_{new}}{N_{proc}}$ configurations, subsequently sharing the surviving configurations amongst all other processors using MPI to generate the same reference space on each individual processor for the following iteration. All duplicates that remain after sharing the configurations would be removed.

3.3.3 Systematic-Monte Carlo Configuration Interaction

As outlined in the introductory section a truly systematic approach to MCCI would require consideration of N_{sd} , pruning as necessary and repeating this process for at least $\frac{n}{2}$ iterations. This could either be considering N_{sd} as one single entity, which would quickly suffer from the same drawbacks as FCI as the reference space increases, or by checking which set of configurations interact strongest with the reference space. However, for the latter approach the computations would quickly become computationally intractable due to the sheer amount of diagonalisations required

per iteration even for the smallest of configurational spaces and adding a small number of configurations. A possible way to circumvent this issue is to subdivide N_{sd} into random batches, considering each configuration in only one batch, and subjecting only the largest weighted configurations across all batches to the pruning stage. This methodology forms the basis of our proposed sMCCI approach.

As with MCCI the starting point is $|\Psi^{(0)}\rangle$, from which $N_{sd}^{(1)}$ is generated and randomly ordered, ensuring symmetry is preserved, and once again if any duplicates are present are removed using the approach given in [15]. The set of new configurations are then divided into separate batches based upon the user-defined i_{batch} parameter. This process generates $\frac{N_{sd}^{(1)}}{i_{batch}}$ independent batches, with the remainder forming a smaller one, and each are combined with the reference space. For each individual batch the coefficients are determined, via an analogous procedure to that in MCCI, with the program keeping track of the i_{add} configurations with the largest weighting across all batches. The largest weighted i_{add} configurations are stored and once again combined with the reference space. This final batch is then diagonalised and a full-prune performed. A full-prune is performed on each iteration as the entire potential interacting configurational landscape is considered, this would correspond to a $P_f = 1$, however, this can be varied if the user so requires. Thus, i_{add} defines an upper limit for the number of configurations that can be added in a single iteration. This process is repeated until the same convergence check as outlined in equation 3.6 and 3.7 is satisfied. As L and J are equal to 3 and we do not include the first iteration, one would expect the convergence check to begin on iteration 7. However, this current version of sMCCI begins checking for convergence on iteration 10.

The current bottleneck of sMCCI will thus be the stage at which approximately $\frac{N_{sd}}{i_{batch}}$ diagonalisations are to be performed, due to both the increasing reference space and larger potential excitation space. As diagonalisation of each batch can be performed independently one can increase the efficiency by parallelisation of this step. Through an MPI, the total number of batches are shared equally amongst the requested processors with one processor also receiving the aforementioned smaller batch. The algorithm designates a lead processor which is involved in the gen-

eration and distribution of the individual batches, the lead processor itself would also contain batches. After all diagonalisations have been performed each processor would send its best i_{add} configurations to the lead processor, which would in turn select the overall best i_{add} from this set. The lead processor would then diagonalise the final matrix and send the pruned wavefunction to each of the processors to guarantee all have the same reference space for the following iteration. The parallelised procedure is then repeated. This sharing procedure also ensures the reported results will be independent of the processor number, which cannot be guaranteed for the conventional MCCI approach. A detailed schematic of the parallel sMCCI algorithm is provided in Figure 3.3.

3.3.4 Pruned-Full Configuration Interaction

As a further comparison we wish to investigate the approach of systematically deconstructing the FCI wavefunction. We start from the normalised $|\Psi^{FCI}\rangle$ and remove configurations which have an absolute weighting lower than c_{min} , subsequently recalculating the energy within this reduced configurational subspace.

All FCI computations were performed with MOLPRO [16, 17], with truncated-CI computations performed with Gaussian 09 (Revision D.01) [18]. At each specific geometry the HF orbitals were re-optimised, within the one-electron basis, with the one and two-electron integrals attained from MOLPRO.

3.4 Results and Discussion

3.4.1 Neon

To initially calibrate the sMCCI approach we consider a single neon atom as described within a cc-pVTZ basis $[4s\ 3p\ 2d\ 1f]$, implementing the frozen-core approximation (FCA) for the lowest occupied molecular orbital (MO). This approximation ensures that the lowest energy MO will be doubly occupied in all configurations thereby reducing the potential configurational space. Neon is constrained to the D_{2h} point group with the ground state pertaining to A_g symmetry. The electronic

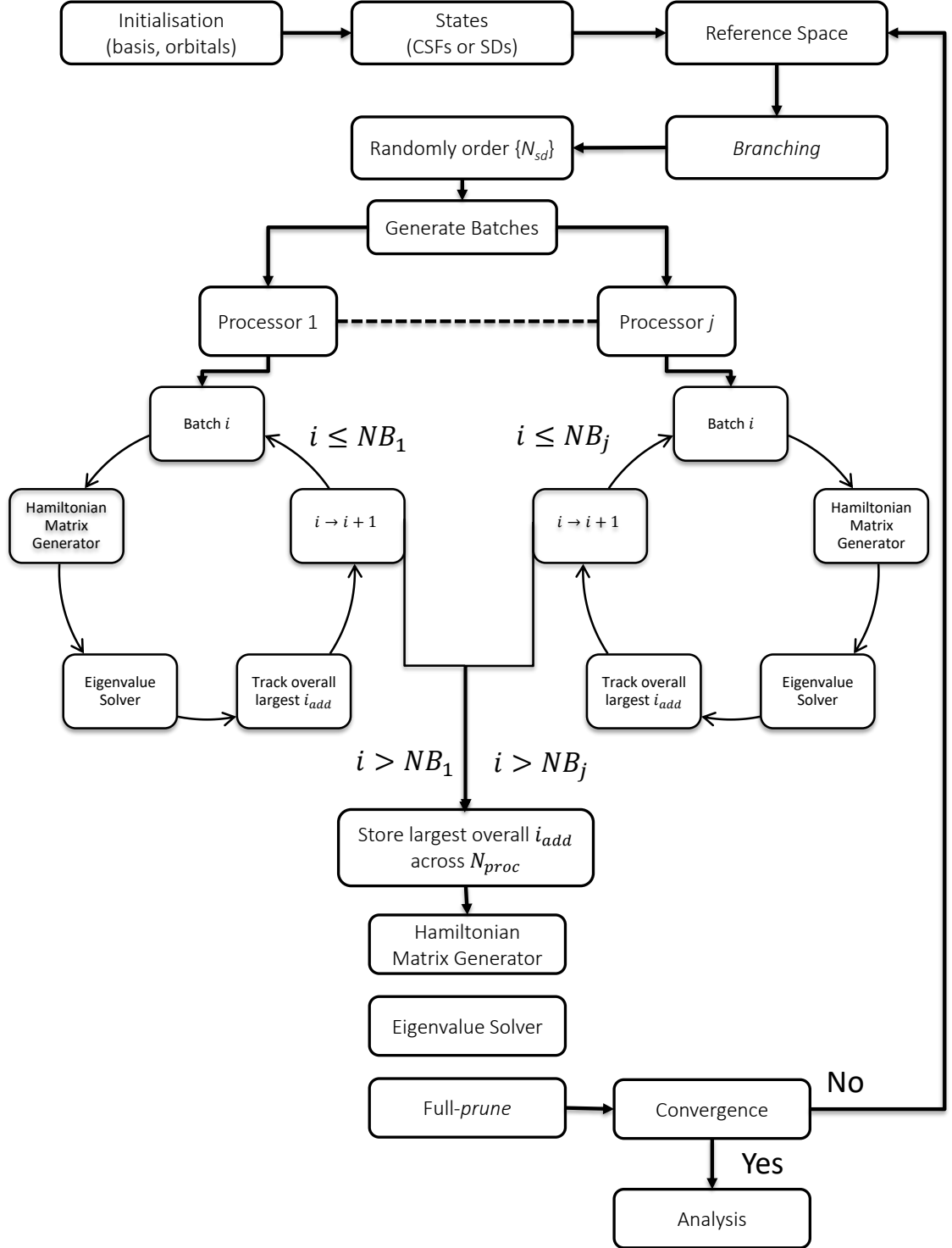


Figure 3.3: General overview of the parallel sMCCI algorithm, NB_1 and NB_j represent the number of batches on processor 1 and j respectively.

structure of neon should be sufficiently well described by $|\Psi^{HF}\rangle$, therefore the electron correlation can be thought of as purely dynamic in nature, giving a relatively straightforward single-reference system as a starting point. All calculations were performed across 8 processors of an Intel(R) Xeon(R) CPU X5660. The FCI energy of this system was found to be -128.802534 Hartree with $|\Psi^{FCI}\rangle$ containing 7.05×10^7 SDs, resulting in an $E^{corr.}$ of -169.849 kcal mol $^{-1}$. All energetic differences (ΔE) are given by the following:

$$\Delta E = E^{FCI} - E^{method} \quad (3.8)$$

with ΔE approaching 0 as the method captures more of $E^{corr.}$.

To begin, i_{batch} was varied from $10 \rightarrow 20000$ CSFs in various increments to observe the effect of altering the individual batch size, on both the resulting energy and CPU time, the i_{add} parameter was held fixed at 100 CSFs. The computation was allowed to run over 61 iterations with a c_{min} value of 10^{-4} , thus providing an upper limit of 6101 CSFs in the resultant $|\Psi^{sMCCI}\rangle$.

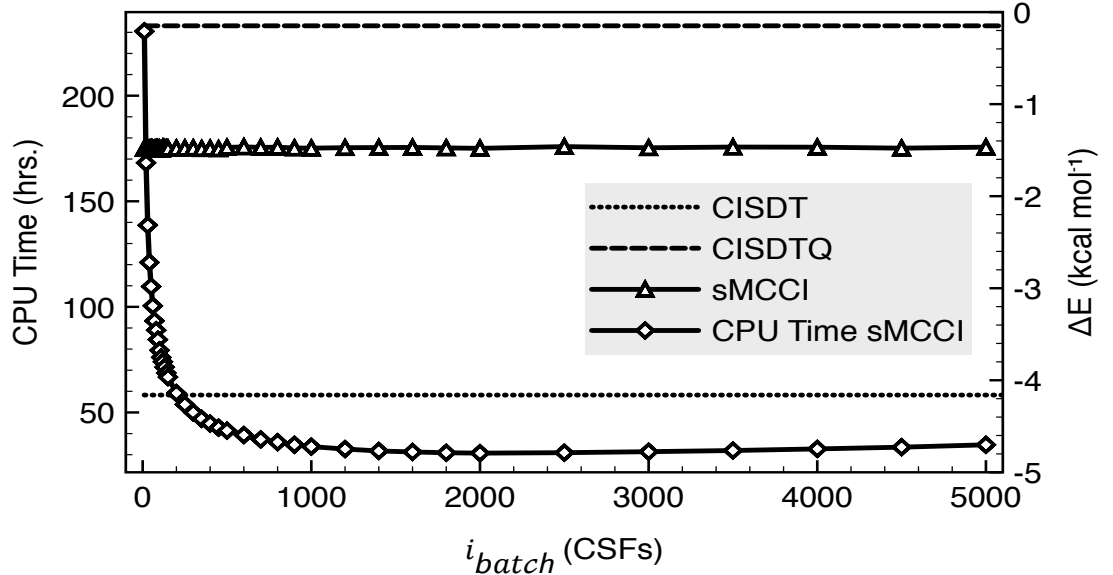


Figure 3.4: Varying i_{batch} for neon with a *cc-pVTZ* basis, $i_{add} = 100$ CSFs and $c_{min} = 10^{-4}$, computation was allowed to run over 61 iterations. The CPU Time *sMCCI* data set is plotted relative to the y_1 axis, with all other sets pertaining to y_2 . The CISDT and CISDTQ methods were also included for comparison.

For this system the batch size has no apparent effect on the resulting energy, as *sMCCI* captures 99.1 % of $E^{corr.}$ for all i_{batch} , with the $|\Psi^{sMCCI}\rangle$ containing on average (\bar{x}) 5658 CSFs. The standard deviation of the energy (σ_E) and CI vector

length (σ_l) was 7.25×10^{-3} kcal mol $^{-1}$ and 43 CSFs, respectively. sMCCI outperforms CISDT, energy lower by 2.685 kcal mol $^{-1}$, but not CISDTQ, as subsequent energy larger by 1.326 kcal mol $^{-1}$. However these truncated-CI methods contain orders of magnitude more configurations in the resulting wavefunctions. Despite no significant energetic dependence on i_{batch} , we do observe large variations in regards to the total CPU time. As the i_{batch} parameter is increased the CPU time drastically decreases reaching a minima for a value of 2000 CSFs, before steadily increasing (see Figure 3.4 and Table 3.1).

Table 3.1: *Resultant properties of varying i_{batch} for neon with a cc-pVTZ basis, $i_{add} = 100$ CSFs and $c_{min} = 10^{-4}$, computation was allowed to run over 61 iterations.*

i_{batch}	Energy (Hartree)	ΔE (kcal mol $^{-1}$)	CSFs	CPU Time (hrs.)
10	-128.800173	-1.481	5623	230.51
100	-128.800173	-1.481	5623	79.43
1000	-128.800179	-1.478	5637	33.84
2000	-128.800175	-1.480	5651	30.74
5000	-128.800196	-1.467	5724	34.68
10000	-128.800208	-1.460	5782	45.57
20000	-128.800210	-1.459	5791	71.48

We compare this computed i_{batch} value with the theoretical optimal value based on the scaling of the Davidson algorithm $O(\lambda X^2)$ [19], where X is the length of the trial vector and λ has upper limit of 30 and represents the number of Davidson vectors. We assume that sMCCI follows this scaling, and the various overheads such as removal of duplicates, and the creation and distribution of individual batches are negligible. We initially allow $B^{(\nu)} = \frac{N_{sd}^{(\nu)}}{i_{batch}^{(\nu)}}$ to represent the number of individual batches to be diagonalised, which we assume returns a value $\in \mathbb{Z}^+$, and each contain $N^{(\nu)} + i_{batch}^{(\nu)}$ configurations, where $N^{(\nu)}$ represents the number of configurations contained within the reference space of iteration ν . The time for a single iteration is thus given by equation 3.9.

$$\lambda(N^{(\nu)} + i_{batch}^{(\nu)})^2 B^{(\nu)} \quad (3.9)$$

Based on this the relative time upon going from iteration ν to $\nu + 1$ can be

represented by:

$$T = \frac{(N^{(\nu+1)} + i_{batch}^{(\nu+1)})^2 B^{(\nu+1)}}{(N^{(\nu)} + i_{batch}^{(\nu)})^2 B^{(\nu)}} \quad (3.10)$$

from which we can minimise with respect to $i_{batch}^{(\nu+1)}$ to generate the optimal parameter.

$$\frac{\partial T}{\partial i_{batch}^{(\nu+1)}} = \frac{N_{sd}^{(\nu+1)}}{B^{(\nu)}(N^{(\nu)} + i_{batch}^{(\nu)})^2} \left(1 - \frac{(N^{(\nu+1)})^2}{(i_{batch}^{(\nu+1)})^2} \right) = 0 \quad (3.11)$$

We observe that the optimum i_{batch} value is that which equals the number of configurations in the reference space, resulting in a different i_{batch} value for each iteration. This adaptive approach, using the same procedure and parameters outlined above, was found to take 32.2 CPU hrs., only slightly longer than an $i_{batch} = 2000$ CSFs. As the fixed i_{batch} of 2000 CSFs gave the quickest time we proceed with this value for the next part of the study.

We now turn our attention to the i_{add} parameter, holding i_{batch} fixed at 2000 CSFs, and once again allowing for 61 full-prune iterations with a c_{min} value of 10^{-4} . The i_{add} parameter was varied from $10 \rightarrow 1000$ CSFs, with larger values lowering the resulting energy more per iteration, whilst increasing the CPU time required to complete iteration 61 (see Table 3.2).

Table 3.2: *Resultant properties of varying i_{add} for neon with a cc-pVTZ basis, $i_{batch} = 2000$ CSFs and $c_{min.} = 10^{-4}$, computation was allowed to run over 61 iterations.*

i_{add}	Energy (Hartree)	ΔE (kcal mol ⁻¹)	CSFs	CPU Time (hrs.)
10	-128.793610	-5.600	610	1.49
100	-128.800179	-1.478	5654	30.92
200	-128.800408	-1.334	6415	59.80
300	-128.800429	-1.321	6496	71.14
500	-128.800488	-1.284	6730	82.75
1000	-128.800569	-1.233	7063	96.82

This is expected as i_{add} is the upper limit on the number of CSFs that can be added per iteration, therefore increasing the number of potential additions would lower the corresponding energy. However, for larger i_{add} values we also observe far greater deviations between the potential and computed vector lengths. This was due to convergence being achieved for an $i_{add} \geq 200$ CSFs well before the end of iteration 61, thus leading to numerous unneeded iterations (see Figure 3.5). The

discrepancy for an $i_{add} = 100$ CSFs is 447 CSFs, increasing to 53,938 CSFs for an $i_{add} = 1000$ CSFs. For an i_{add} of 10 CSFs, the energy is lowering by 1.31×10^{-1} kcal mol $^{-1}$ between iteration 60 and 61. As only ≤ 10 CSFs can be added per iteration the energy is only marginally improved, upon the completion of each cycle, therefore requiring considerably more iterations to reach convergence. We observe a similar effect for an i_{add} of 100 CSFs, albeit an order of magnitude lower (1.1×10^{-2} kcal mol $^{-1}$), when reducing the plotted energy range as shown in the graphical inset of Figure 3.5. As outlined previously for all other i_{add} values we observe convergence far before the 61st iteration, with larger i_{add} values reaching this in fewer cycles. The CPU time required to reach these iterations are also found to decrease with an increasing i_{add} : 9.47, 14.00, 19.20 and 29.75 CPU hours for an i_{add} of 1000, 500, 300 and 200 CSFs respectively. The energy change between iteration 60 and 61 for an $i_{add} = 1000$ CSFs was 1.8×10^{-4} kcal mol $^{-1}$, with the latter containing 3 additional CSFs.

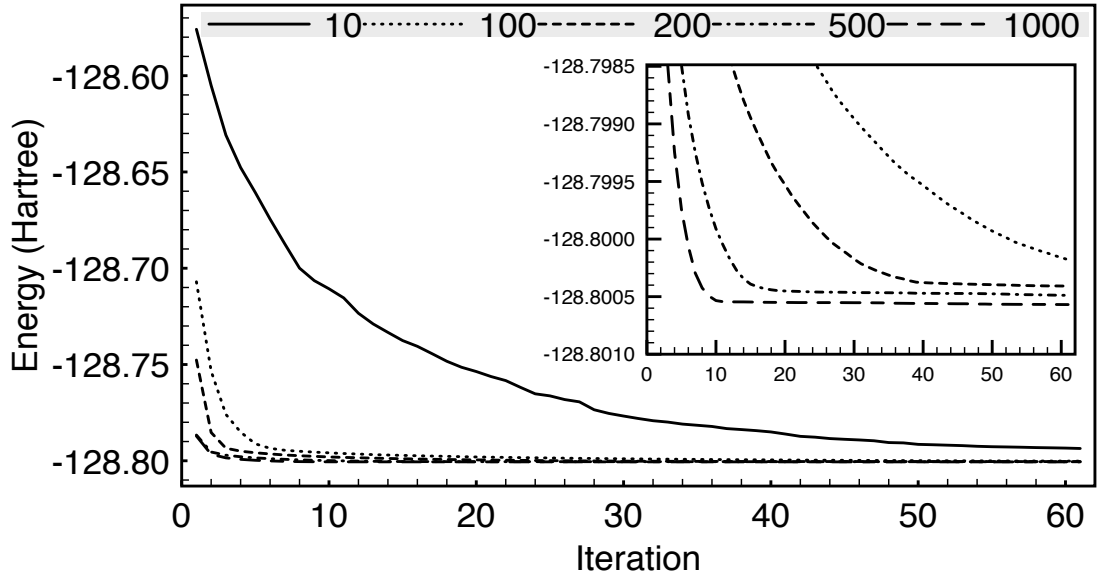


Figure 3.5: Varying i_{add} for neon with a cc-pVTZ basis, $i_{batch} = 2000$ CSFs and $c_{min} = 10^{-4}$, computation was allowed to run over 61 iterations. Inset: an enlarged view of the y_1 axis between $-128.7985 \rightarrow -128.8010$ Hartree.

Based on this, we propose i_{add} and i_{batch} values of 1000 and 2000 CSFs, respectively, implementing the convergence-check procedure outlined in Section 3.3.2, at early stages of the computation. All values of L and J are held fixed at 3 for sMCCI, with $P_f = 1$, therefore the check convergence should begin on iteration 7. However,

as mentioned previously we allow for at least 10 iterations. The $conv.E$ was varied from 10^{-3} to 10^{-4} Hartree with $conv.l$ held fixed at 100 CSFs, for all remaining sMCCI and MCCI computations $conv.l$ takes this value unless stated otherwise. The energy varied by less than 3.7×10^{-3} kcal mol $^{-1}$, both recovered 99.3 % of $E^{corr.}$, with the computations taking 9.45 and 14.62 hrs. respectively. Lowering the $conv.E$ threshold to 10^{-5} Hartree, once again provides no apparent energetic difference, 1.9×10^{-3} kcal mol $^{-1}$ with respect to 10^{-4} Hartree, only further raising the CPU time.

Table 3.3: *Resultant properties of varying $conv.E$ for neon with a cc-pVTZ basis, $i_{batch} = 2000$ CSFs, $i_{add} = 1000$ CSFs and $c_{min} = 10^{-4}$.*

$conv.E$ (Hartree)	Iteration	ΔE (kcal mol $^{-1}$)	CSFs	CPU Time (hrs.)
10^{-3}	11	-1.251	6903	9.45
10^{-4}	14	-1.247	6923	14.62
10^{-5}	17	-1.246	6941	19.79

We now compare our systematic approach to that of conventional MCCI, employing a $c_{min} = 10^{-4}$ and $conv.E = 10^{-3}$ Hartree. To maintain a level of consistency between the two approaches we begin the convergence check after at least 7 full prune iterations, corresponding to every 10^{th} iteration in MCCI and every iteration in sMCCI. A brief statistical analysis of the two methods was also employed in terms of \bar{x} and σ of ΔE , the corresponding vector length (l) and run time (t). We explore individual samples containing 5, 10 and 20 individual runs.

As shown in Table 3.4, the statistical properties regarding sMCCI are practically invariant for the various subsets, highlighting the high level of consistency between individual computations and thus all providing a good representation of the population statistics. For MCCI we observe statistical properties that vary to a greater extent between different subsets when compared to sMCCI (see Table 3.5), due to the random selection process. However, these variations are minimal with $\sigma_{\Delta E}$ varying by 3.8×10^{-2} and -2.2×10^{-2} kcal mol $^{-1}$ for successive increasing sample sizes of 5, 10 and 20. We therefore allow a sample size of 20 to represent the population for both sMCCI and MCCI.

The following comparison thus relates to the populated data. Despite containing

Table 3.4: *Resultant sMCCI properties of varying sample size for neon with a cc-pVTZ basis, $i_{batch} = 2000$ CSFs, $i_{add} = 1000$ CSFs and $c_{min} = 10^{-4}$. All energies are in terms of kcal mol $^{-1}$.*

Sample size	$\bar{x}_{\Delta E}$	$\sigma_{\Delta E}$	\bar{x}_l (CSFs)	σ_l (CSFs)	\bar{x}_t (sec.)	σ_t (sec.)
5	-1.252	10^{-3}	6897	9	4273.8	18.9
10	-1.252	10^{-3}	6899	7	4281.3	17.8
20	-1.252	10^{-3}	6900	6	4276.8	17.9

Table 3.5: *Resultant MCCI properties of varying sample size for neon with a cc-pVTZ basis and $c_{min} = 10^{-4}$. All energies are in terms of kcal mol $^{-1}$.*

Sample size	$\bar{x}_{\Delta E}$	$\sigma_{\Delta E}$	\bar{x}_l (CSFs)	σ_l (CSFs)	\bar{x}_t (sec.)	σ_t (sec.)
5	-1.697	1.98×10^{-1}	6914	53	486.4	37.0
10	-1.719	2.36×10^{-1}	6926	57	497.7	39.6
20	-1.711	2.14×10^{-1}	6932	61	500.5	49.0

32 less CSFs sMCCI captures 4.59×10^{-1} kcal mol $^{-1}$ more of $E^{corr.}$, indicating an increased compactness within the $|\Psi^{sMCCI}\rangle$. This can be attributed to sMCCI considering the entire single and double-excitation space at each iteration, therefore it is highly likely that, in this specific case, the 1000 most important CSFs are located at each step. As would be expected a systematic approach has a greater degree of consistency between individual runs, highlighted by a lower $\sigma_{\Delta E}$, σ_l and σ_t . However, this should not detract from a $\sigma_{\Delta E}$ of 2.14×10^{-1} kcal mol $^{-1}$ for MCCI as this still provides a consistent spread of values for a method that is entirely based upon a stochastic approach. In regards to the overall computational wall time sMCCI are a factor of 8.5 to that of MCCI, with values of 4276.8 and 500.5 sec., respectively. Therefore, for this specific system considering the fully interacting space results in a minimal energetic difference only drastically increasing the resulting wall time.

The parallelisation of both sMCCI and MCCI was then explored (see Figure 3.6), ranging from 8 to 72 processors. The following parameters were employed $c_{min} = 10^{-4}$ and $conv.E = 10^{-3}$ Hartree, once again subject to at least 7 full-prune iterations. At this current time the computational resources we have at our disposal contain nodes which have 12 processors each. Therefore, if we wish to use an $N_{proc} > 12$ we must utilise a multi-node algorithm which involves additional communication between all nodes and a pre-selected head node upon the completion of each cycle.

This would be expected to have a slight effect on the timings of individual runs when compared to a single node algorithm. The difference was investigated for an $N_{proc} = 12$, however, this only raised computations by 4 seconds raising no real issues. As the σ_t is far smaller than the relative timings of sMCCI, for an $N_{proc} = 8$, we compare only a single run of each at varying processor amounts. This is not the case for MCCI therefore we once again average each point over 20 individual runs.

For sMCCI increasing the number of available processors from 8 to 72 results in a wall time reduction of 78.8 %. In regards to MCCI this is far lower as a reduction of 26.0 % is observed. We observe very promising scaling factors upon changing from 8 to 36 processors for sMCCI, with the total wall time reducing by 68.8 %. However, this level of scaling is not observed for MCCI and we observe no benefit of going above 36 processors. As becomes apparent in the inset of Figure 3.6 it is entirely possible for fewer processor runs to result in faster computations, this is attributed to the small run time difference when increasing the processor number and the stochastic nature of the method. Across the run we did not see any points at which sMCCI outperforms MCCI, from a run time point of view, however, if a large enough N_{proc} is used this may in fact be possible. Despite this the removal of duplicates in N_{sd} would become the time consuming step. As outlined at the end of Section 3.3.2 within the parallelised MCCI regime each processor would independently branch, diagonalise and prune a subset of $\frac{N_{new}}{N_{proc}}$, therefore the resulting energy would have some dependence on the specific value of N_{proc} . This can be thought of as essentially a batch type equivalent in MCCI. This would not be the case for sMCCI as the sharing procedures insures no N_{proc} dependency.

If we are to compare the MCCI methodologies to that of p-FCI, we must transition from CSFs to SDs. When using SDs the resulting averaged sMCCI energy is 4.64×10^{-1} kcal mol⁻¹ larger than the CSF variant, with the former containing 2811 more configurations. The computational parameters of $c_{min} = 10^{-4}$ and $conv.E = 10^{-3}$ Hartree were used and again averaged over 20 runs. This is not surprising as CSFs are composed of SDs therefore one would expect a larger CI vector length when making use of the latter. The total wall time of the aforementioned

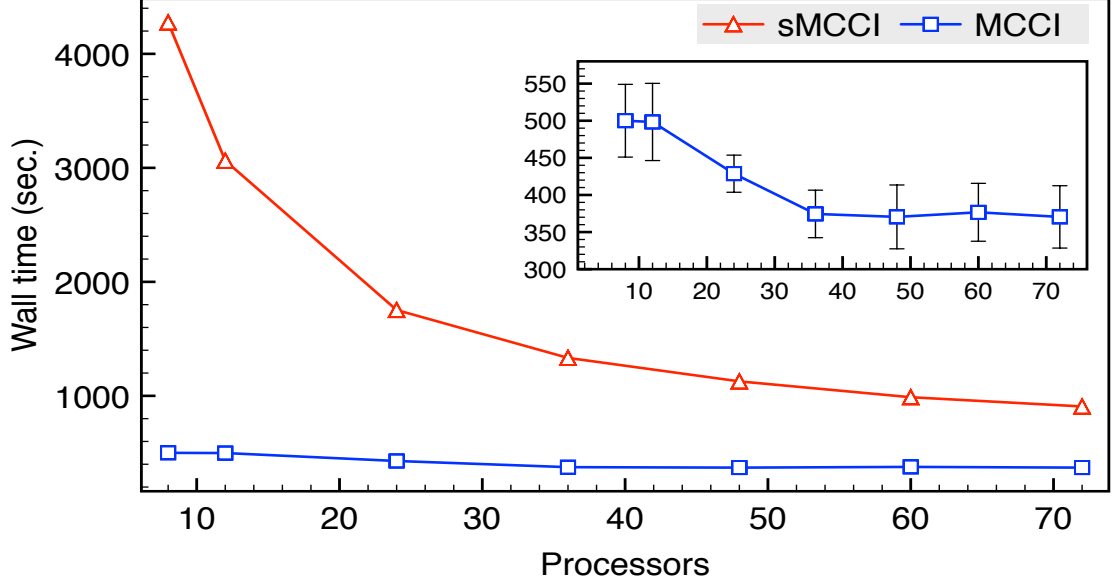


Figure 3.6: The *sMCCI* and *MCCI* wall time as a function of N_{proc} for neon within a *cc-pVTZ* basis, $c_{min} = 10^{-4}$, $i_{batch} = 2000$ CSFs, $i_{add} = 1000$ CSFs and $conv.E = 10^{-3}$ Hartree. Inset: an enlarged view of the y_1 axis between $300 \rightarrow 590$ seconds. The error bar relates to $\pm \sigma_t$.

computations also increased by 76.2 % upon this transition. In regards to MCCI, we observe a similar outcome as the energy from a SD approach is larger by 2.21×10^{-1} kcal mol $^{-1}$, containing 2338 more configurations. However, the total wall time was found to decrease by 20 % when using SDs. For SDs the energy differential between *sMCCI* and *cMCCI* is lowered to 2.15×10^{-1} kcal mol $^{-1}$, with the former now containing 441 more configurations.

Table 3.6: Resultant *MCCI* properties over 20 individual runs for neon with a *cc-pVTZ* basis, $i_{batch} = 2000$ SDs, $i_{add} = 1000$ SDs and $c_{min} = 10^{-4}$. All energies are in terms of kcal mol $^{-1}$.

Method	$\bar{x}_{\Delta E}$	σ_E	\bar{x}_l (SD)	σ_l (SD)	\bar{x}_t (sec.)	σ_t (sec.)
sMCCI	-1.716	10^{-4}	9711	2	7535.1	29.0
MCCI	-1.931	8.5×10^{-2}	9270	46	400.7	23.9

We now turn our attention to p-FCI, which for a $c_{min} = 10^{-4}$, contained 9679 SDs in $|\Psi^{p-FCI}\rangle$ with a resulting ΔE of -1.729 kcal mol $^{-1}$. This shows the high quality of both the systematic and conventional MCCI wavefunction, with the former actually resulting in a lower energy by -1.35×10^{-2} kcal mol $^{-1}$, as both are very close to the p-FCI. Another approach to compare wavefunctions is to explore the multi-reference (MR) character of a given system which can be quantified using the

following [10]:

$$MR = \sum_i |c_i|^2 - |c_i|^4 \quad (3.12)$$

where the sum is over all SDs contained within the wavefunction. As the coefficients are normalised ($\sum_i |c_i|^2 = 1$) wavefunctions containing a single SD would result in a MR character of 0, with this approaching 1 as the number of configurations increases. In addition to a similar energy across all the various approaches the MR character was 6.7×10^{-2} for all three methods validating the single-reference nature, with $|\Psi^{HF}\rangle$ representing 96.6 % of the wavefunction. The number of configurations of each substitution type present in the various wavefunctions, and their relative contribution, was then explored. For sMCCI and MCCI we take one single run and not an average as was done previously.

From a purely configurational standpoint all the wavefunctions are dominated by double, triple and quadruple excited configurations (see Figure 3.7). The MCCI and p-FCI wavefunctions also contain a very small number of sextuple excited configurations which are not observed in sMCCI. The major discrepancy between MCCI and the other two approaches arise when looking at the number of quadruple excited configurations as this approach contained 423 and 407 less when compared to sMCCI and p-FCI, respectively.

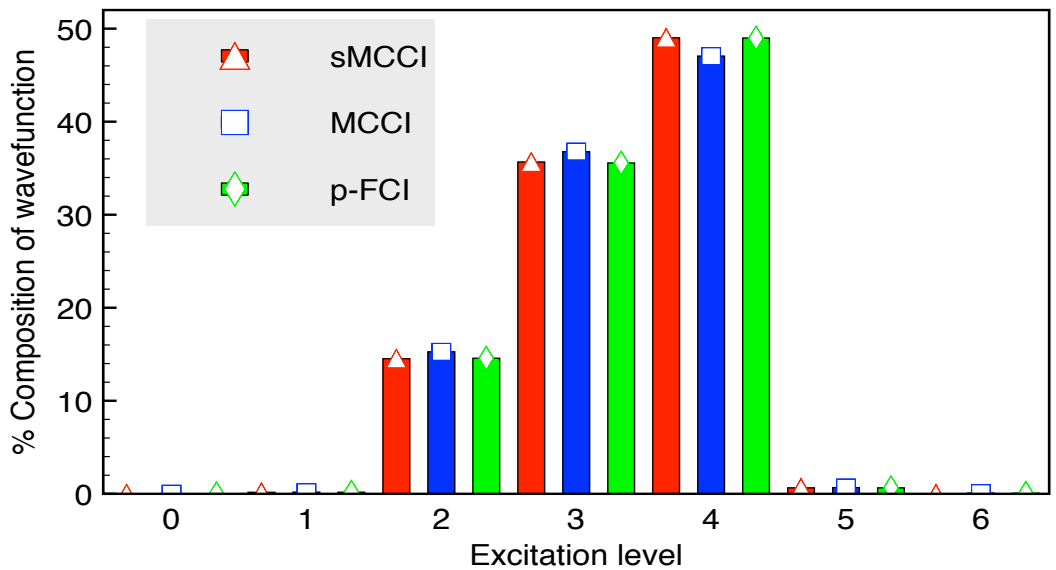


Figure 3.7: The % of configurations of each substitution level present in the various wavefunctions for neon with a cc-pVTZ, $i_{batch} = 2000$ SDs, $i_{add} = 1000$ SDs and $c_{min} = 10^{-4}$.

However, when looking at the total contribution of each substitution level the wavefunction is dominated by $|\Psi^{HF}\rangle$. This has been highlighted in Figure 3.8, where the y_1 axis represents the sum of absolute coefficients squared for each excitation level. Despite quadruple excitations composing of between 47 to 49 % of the wavefunctions, in terms of configuration amount, the total weighting of these are negligible, 4.0×10^{-2} % to be precise. After $|\Psi^{HF}\rangle$ the doubly excited configurations have the largest weighting with a value of 3.3 %. Therefore from a contribution standpoint the wavefunction is dominated by the HF wavefunction with some contribution from double-excited configurations.

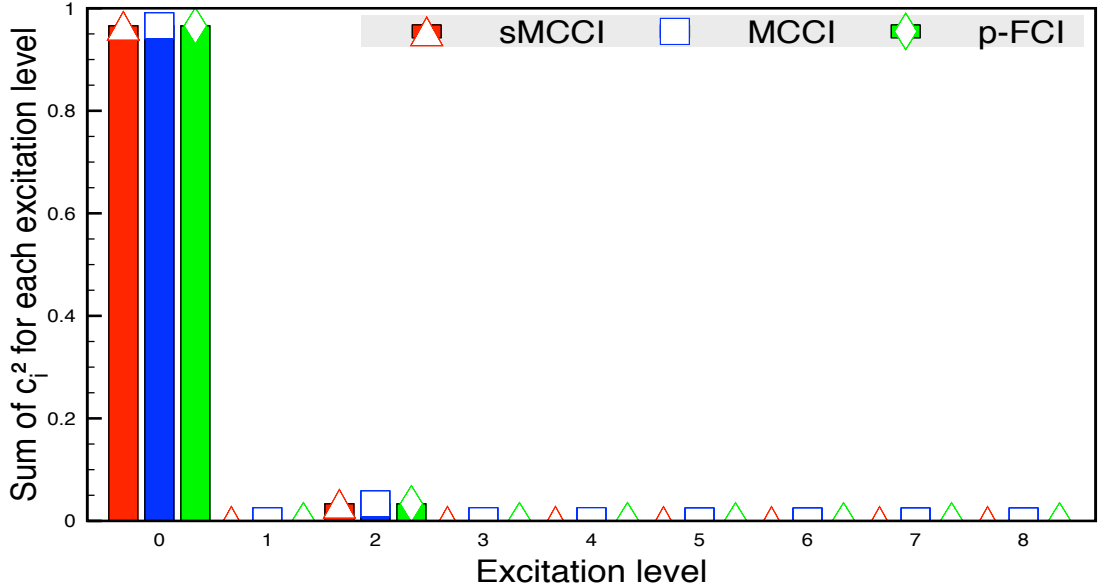


Figure 3.8: The sum of c_i^2 for each substitution level present in the various wavefunctions for Neon with a *cc-pVTZ*, $i_{batch} = 2000$ SDs, $i_{add} = 1000$ SDs and $c_{min} = 10^{-4}$.

We increase c_{min} to 10^{-3} and rerun a single computation for each of the three methods, a $conv.E = 10^{-3}$ was once again employed. The p-FCI wavefunction results in an energy of -128.790810 Hartree with a vector length of 1137 SDs. The sMCCI and MCCI energies are both higher by 1.97×10^{-1} and 5.81×10^{-1} kcal mol $^{-1}$, with the respective wavefunctions containing 1105 and 1120 SDs. Despite increasing c_{min} to 10^{-3} we still capture between 95.3 – 95.7 % of $E^{corr.}$. For this c_{min} no method includes quintuple excitations and above, with $|\Psi^{MCCI}\rangle$ containing the least amount of doubly excited configurations. The MR character was 6.2×10^{-2} for all approaches. Once again the composition of each wavefunction was very similar across the three methods (see Figure 3.9 and 3.10).

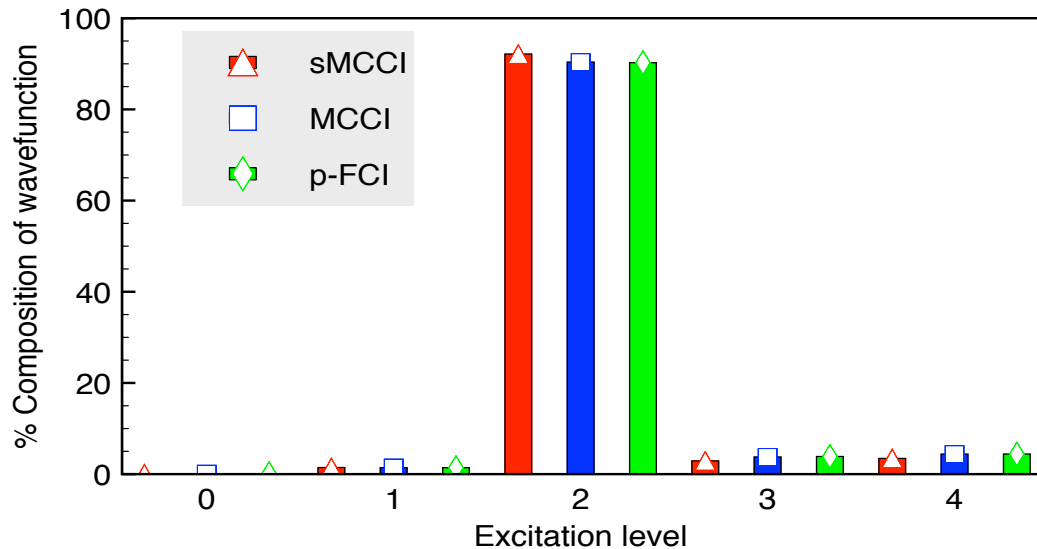


Figure 3.9: The % of configurations of each substitution level present in the various wavefunctions for neon with a *cc-pVTZ*, $i_{batch} = 2000$ SDs, $i_{add} = 1000$ SDs and $c_{min} = 10^{-3}$.

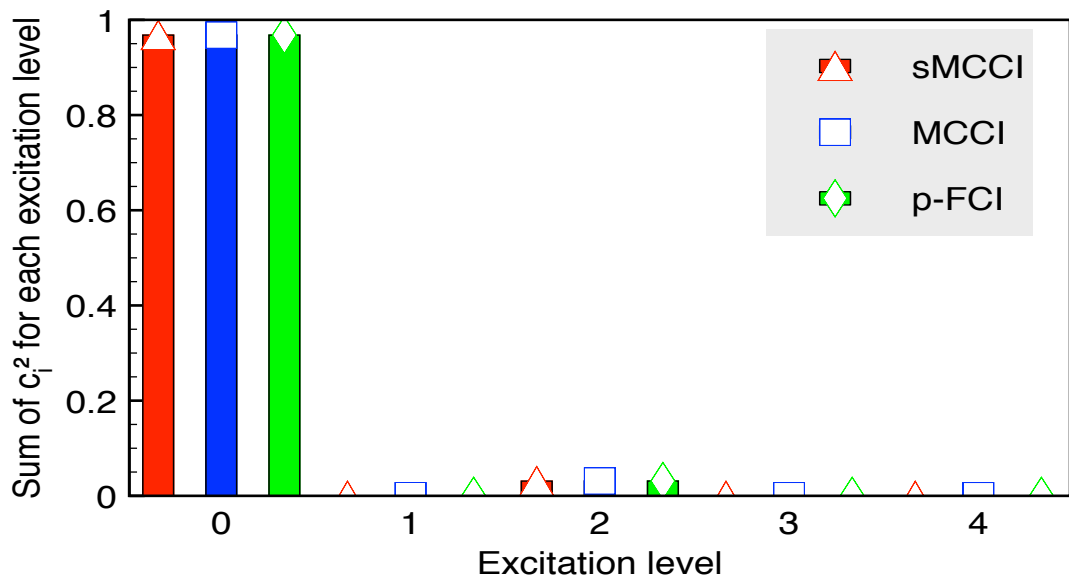


Figure 3.10: The sum of c_i^2 for each substitution level present in the various wavefunctions for neon with a *cc-pVTZ*, $i_{batch} = 2000$ SDs, $i_{add} = 1000$ SDs and $c_{min} = 10^{-3}$.

3.4.2 H₂O

We now turn our attention to the double-hydrogen dissociation of water with a cc-pVDZ [7s 4p 1d] basis, once again invoking the FCA for the lowest-energy MO. The distance between oxygen and hydrogen atoms (R_{OH}) were varied symmetrically from 1.0 to 4.6 Bohr, at 0.2 Bohr increments, with the HOH angle held constant at 104.5°, therefore maintaining C_{2v} symmetry throughout the entire PES. A previous study provides FCI energies which we will use for comparison [15]. Initially the same protocol as section 3.4.1 of varying i_{batch} and i_{add} was explored for an R_{OH} of 4.0 Bohr, allowing us to investigate this dependence on a system expected to have a great deal more MR character when compared to neon. The FCI energy for this separation is -75.932598 Hartree with $|\Psi^{FCI}\rangle$ containing 1.96×10^7 SDs, giving an $E_{corr.}$ of -250.841 kcal mol⁻¹. The batch size was varied from 0 to 2000 CSFs, using an $i_{add} = 100$ CSFs and $c_{min} = 10^{-4}$, see Table 3.7, which was shown to once again have no real energetic dependence only significantly effecting the CPU time.

Table 3.7: *Resultant properties of varying i_{batch} for H₂O ($R_{OH} = 4.0$ Bohr) with a cc-pVDZ basis, $i_{add} = 100$ CSFs and $c_{min.} = 10^{-4}$, computation was allowed to run over 61 iterations.*

i_{batch}	Energy (Hartree)	ΔE (kcal mol ⁻¹)	CSFs	CPU Time (hrs.)
10	-75.929600	-1.881	5998	372.21
100	-75.929599	-1.882	6004	115.79
1000	-75.929605	-1.878	6011	33.20
2000	-75.929598	-1.882	6013	26.85

Using this fixed $i_{batch} = 2000$ CSFs we vary the i_{add} parameter from 10 to 1000 CSFs (see Figure 3.11). The energy for an $i_{add} = 10$ CSFs was still lowering by 2.094×10^{-1} kcal mol⁻¹ between iteration 60 and 61. This difference lowered to 3.26×10^{-2} kcal mol⁻¹ for an $i_{add} = 100$ CSFs. This energy can once again be reached in fewer iterations and less CPU hours when using a larger i_{add} , analogous to the aforementioned neon situation.

Therefore once again we utilise an $i_{add} = 1000$ CSFs and implement the convergence check procedure on iteration 10. When examining $conv.E$ values of 10^{-3} and 10^{-4} Hartree we find an energy difference of 3.89×10^{-1} kcal mol⁻¹, with the CPU

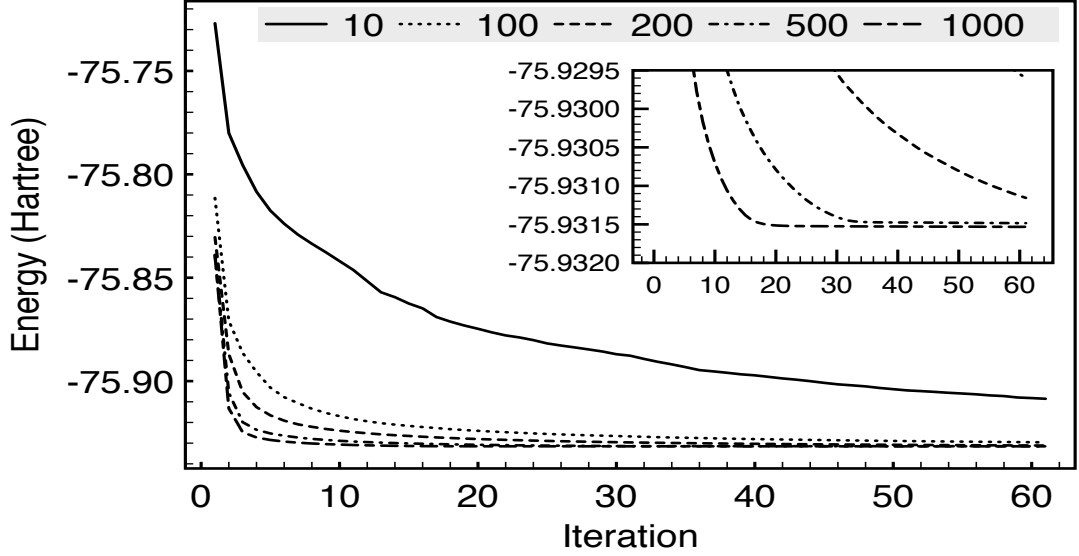


Figure 3.11: Varying i_{add} for H_2O ($R_{OH} = 4.0$ Bohr) with a cc-pVTZ basis, the core remained doubly occupied in all CSFs. Inset: an enlarged view of the y_1 axis between $-128.9295 \rightarrow -128.9320$ Hartree.

time of the latter a factor of 5.1 times that of the former. The respective wavefunctions for the convergence thresholds contained 10312 and 14901 configurations.

For the 4.0 Bohr R_{OH} system we also explored the statistical nature of MCCI and sMCCI over subsets of 5, 10 and 20 computations, a $conv.E = 10^{-3}$ Hartree, $c_{min} = 10^{-4}$, $i_{add} = 1000$ CSFs and $i_{batch} = 2000$ CSFs was used. Once again for the various subsets sMCCI show little variation (see Table 3.8).

Table 3.8: Statistical properties for various sample sizes of sMCCI computations for H_2O ($R_{OH} = 4.0$ Bohr), a $c_{min.} = 10^{-4}$, $conv.E = 10^{-3}$, $i_{add} = 1000$ CSFs and $i_{batch} = 2000$ CSFs.

Sample size	$\bar{x}_{\Delta E}$	$\sigma_{\Delta E}$	\bar{x}_l (CSFs)	σ_l (CSFs)	\bar{x}_t (sec.)	σ_t (sec.)
5	-1.068	6.7×10^{-4}	10310	6	4905.2	51.2
10	-1.068	6.2×10^{-4}	10311	5	4910.8	35.4
20	-1.068	8.8×10^{-4}	10312	7	4915.9	36.1

As shown in Table 3.9 for MCCI, the difference between $\sigma_{\Delta E}$ for a subset of 10 and 20 computations was 1.2×10^{-2} kcal mol $^{-1}$, similar to the neon counterpart despite containing 8789 more CSFs. As with the previous neon computations sMCCI shows a greater degree of consistency between individual runs when compared to MCCI. However, the resulting MCCI energy was found to be lower by 3.95×10^{-1} kcal mol $^{-1}$, containing 5409 more CSFs. The discrepancy in configurations can be

Table 3.9: *Statistical properties for various sample sizes of MCCI computations for H_2O ($R_{OH} = 4.0$ Bohr), $a_{c_{min.}} = 10^{-4}$, $conv.E = 10^{-3}$, $i_{add} = 1000$ CSFs and $i_{batch} = 2000$ CSFs*

Sample size	$\bar{x}_{\Delta E}$	$\sigma_{\Delta E}$	\bar{x}_l (CSFs)	σ_l (CSFs)	\bar{x}_t (sec.)	σ_t (sec.)
5	-0.665	5.6×10^{-3}	15732	46	3553.0	170.5
10	-0.664	6.6×10^{-3}	15736	35	3528.2	119.4
20	-0.673	1.9×10^{-2}	15721	75	3487.9	219.3

attributed to the varying N_{new} parameter in MCCI, and also starting the convergence procedure after 7 full prune iterations, equating to the 61st cycle in MCCI. As the reference space increases so does N_{new} , therefore the wavefunction can increase at a far superior rate for MCCI at large values, as sMCCI has an upper limit of adding 1000 configurations per iteration. Upon lowering $conv.E$ to 10^{-4} the MCCI energy varies by only 2.97×10^{-2} kcal mol⁻¹, far lower than the sMCCI difference. At a $conv.E$ of 10^{-4} Hartree both MCCI and sMCCI capture 99.7 of % $E_{corr.}$, with the latter containing 1013 less CSFs.

The scalability of both MCCI and sMCCI was then explored, for a $conv.E = 10^{-4}$ Hartree due to the significance discrepancy between the number of CSFs in the resulting $|\Psi^{MCCI}\rangle$ and $|\Psi^{sMCCI}\rangle$ for a threshold of 10^{-3} Hartree. We still observe a difference of 1013 CSFs for the lower convergence threshold, with $|\Psi^{sMCCI}\rangle$ once again the more compact of the two, which must be remembered when comparing wall times of the MCCI methods. We compare a single run at each varying processor amount with a c_{min} of 10^{-4} .

Upon increasing the number of processors, once again from 8 to 72, we find wall times that decrease by 78.2 and 18.7 % for sMCCI and MCCI respectively. When running on 8 processors the sMCCI computation is 403 % longer than the MCCI counterpart (24680 and 4905 seconds, respectively). If we then compare the wall time differential when utilising 72 processors, this significantly lowers as now sMCCI is only 35 % longer than the corresponding MCCI (5370 and 3987 seconds, respectively). For MCCI, once again due to the inherent randomness in MCCI we do not observe a smooth convergence when increasing the number of available processors, with a 72 processor run found to be slower by 369 sec. compared to a

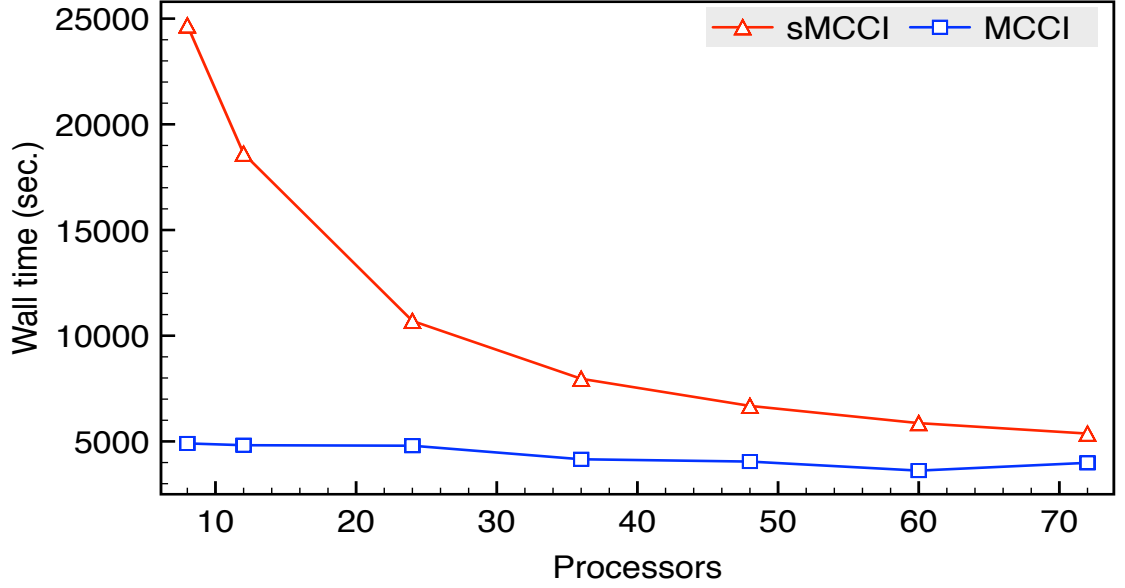


Figure 3.12: The *sMCCI* and *MCCI* wall time as a function of the number of processors for H_2O ($R_{OH} = 4.0$ Bohr) within a *cc-pVDZ* basis, $c_{min} = 10^{-4}$, $i_{batch} = 2000$ CSFs, $i_{add} = 1000$ CSFs and $conv.E = 10^{-4}$ Hartree.

computation utilising 60 processors.

We now turn our attention to the entire PES corresponding to the dissociation of both hydrogen atoms. In order to provide a quantitative account of the differences between the accuracy of each PES, we compare the nonparallelity error (NPE) and $\sigma_{\Delta E}$ across all points. The NPE is defined as follows:

$$NPE = \max|\Delta E| - \min|\Delta E| \quad (3.13)$$

for the two relevant points along the PES. This is due to only the curve shape being of importance and not the absolute energy values, if each point is shifted by a constant energy from the FCI potential relative quantities such as dissociation energies will still equal. The $\sigma_{\Delta E}$, as shown in equation 3.14, explicitly contains all points and not solely the difference between two points corresponding to the minimum and maximum error:

$$\sigma_{\Delta E} = \sqrt{\frac{1}{Q} \sum_{i=1}^Q (\Delta E_i - \bar{x}_{\Delta E})^2} \quad (3.14)$$

where Q represents each individual geometry considered in the PES and $\bar{x}_{\Delta E}$ is the average across all points. The NPE and $\sigma_{\Delta E}$ would thus equal 0 for a FCI curve. It

should be noted that these results are for single runs and not multiple runs as was the case earlier. The results for each separation considered are provided in Table 3.10, for a $c_{min} = 10^{-4}$ and $conv.E = 10^{-3}$ Hartree.

Table 3.10: ΔE and vector length pertaining to $|\Psi^{sMCCI}\rangle$ and $|\Psi^{MCCI}\rangle$ as a function of R_{OH} , $conv.E$ and c_{min} of 10^{-3} Hartree and 10^{-4} respectively.

R_{OH} (Bohr)	sMCCI		MCCI	
	ΔE (kcal mol $^{-1}$)	CSFs	ΔE (kcal mol $^{-1}$)	CSFs
1.00	-1.066	9645	-0.953	11092
1.20	-1.231	10148	-1.053	12965
1.40	-1.548	10389	-1.049	16329
1.60	-1.710	10491	-1.052	18332
1.80	-1.833	10563	-1.037	19847
2.00	-1.966	10551	-1.029	21120
2.20	-2.044	10542	-1.020	21821
2.40	-2.165	10562	-1.038	22621
2.60	-2.167	10543	-1.043	22498
2.80	-1.979	10551	-0.982	21384
3.00	-1.854	10550	-0.935	20722
3.20	-1.620	10501	-0.853	19328
3.40	-1.448	10465	-0.812	18182
3.60	-1.338	10445	-0.773	17622
3.80	-1.207	10410	-0.727	16653
4.00	-1.069	10301	-0.682	15623
4.20	-0.934	10260	-0.624	14906
4.40	-0.821	10179	-0.585	13912
4.60	-0.720	10117	-0.555	13079

For these parameters the MCCI energies are lower than the sMCCI counterparts. The maximum difference between the methods is 1.13 kcal mol $^{-1}$ corresponding to an R_{OH} of 2.40 Bohr. The NPE is found to be low for both MCCI and sMCCI with respective values of 4.976×10^{-1} and 1.447 kcal mol $^{-1}$, highlighting the good agreement with the FCI curve. In terms of $\sigma_{\Delta E}$ we observe lower values for MCCI when compared to sMCCI, 1.720×10^{-1} and 4.517×10^{-1} kcal mol $^{-1}$. This highlights the finding that not only is ΔE lower for all points but it varies to a far lesser extent when compared to the systematic approach.

Once again in order to perform the comparison with p-FCI must transition to SDs. We compare the results of a single computation at an $R_{OH} = 4.0$ Bohr with the following computational parameters $c_{min} = 10^{-4}$, $i_{add} = 1000$ SDs and $i_{batch} = 2000$

SDs at $conv.E$ values of 10^{-3} and 10^{-4} Hartree. All resulting energies from wavefunctions containing CSFs are found to be lower in energy than their SD counterparts. For the computations using SDs we observe the same general trend, as was found for CSFs, upon differing $conv.E$. However, the energy difference between sMCCI at these varying convergence values was larger at $1.317 \text{ kcal mol}^{-1}$. At a $conv.E = 10^{-4}$ Hartree sMCCI and MCCI have a ΔE of -1.070 and $-1.089 \text{ kcal mol}^{-1}$ respectively.

We now proceed with the method comparison using a $c_{min} = 10^{-3}$ and $conv.E = 10^{-3}$ Hartree. As shown in Figure 3.13 all methods are found to be in good agreement with the FCI curve, with the % $E^{corr.}$ recovered ranging between 94 to 98 %.

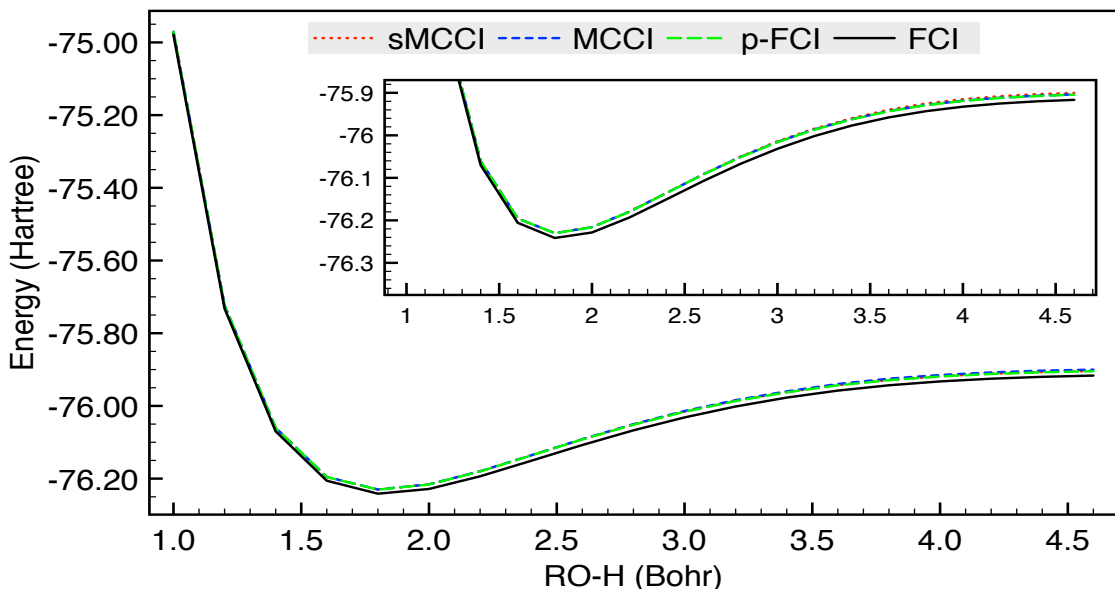


Figure 3.13: The PES for the double-hydrogen dissociation of H_2O for various methods. Graphical inset: The % of recovered $E^{corr.}$ as a function of R_{OH} for the various methods. The lowest energy MO was doubly occupied in all configurations and the H-O-H angle constrained to 104.5° .

The NPE is found to be $1.217 \text{ kcal mol}^{-1}$ lower for sMCCI when compared to MCCI with a $\sigma_{\Delta E}$ also lower by $5.49 \times 10^{-1} \text{ kcal mol}^{-1}$ (see Table 3.11). The most accurate PES is that approximated from a pruned FCI approach as the lowest NPE and $\sigma_{\Delta E}$ values are obtained. The p-FCI and sMCCI methods capture a similar % $E^{corr.}$ over the surface.

We now investigate the wavefunction composition of two points across the PES, corresponding to an $R_{OH} = 1.8$ and 4.0 Bohr (see Figure 3.14 and 3.15, respectively). At the equilibrium geometry the system is single reference with a MR character of 9.7×10^{-2} increasing to 7.2×10^{-1} for a separation of 4.0 Bohr. For an $R_{OH} = 1.8$

Table 3.11: *Various properties for each computational method, $c_{min} = 10^{-3}$ and $conv._E = 10^{-3}$ Hartree, all points of the PES were included.*

Method	NPE (kcal mol ⁻¹)	$\sigma_{\Delta E}$ (kcal mol ⁻¹)	$\bar{x}_{\%E_{corr.}}$	\bar{x}_l (SDs)
cMCCI	6.479	2.156	94.87	2074
sMCCI	5.262	1.607	95.32	2158
pruned-FCI	4.971	1.501	95.46	2291

Bohr the wavefunction is dominated by doubly excited configurations, between 90 to 92 %, with a small amount of quadruple excitations (Inset of Figure 3.14). In regards to the contribution of each excitation level, as the single reference nature suggests, the HF wavefunction dominates with a small contribution from doubly excited configurations.

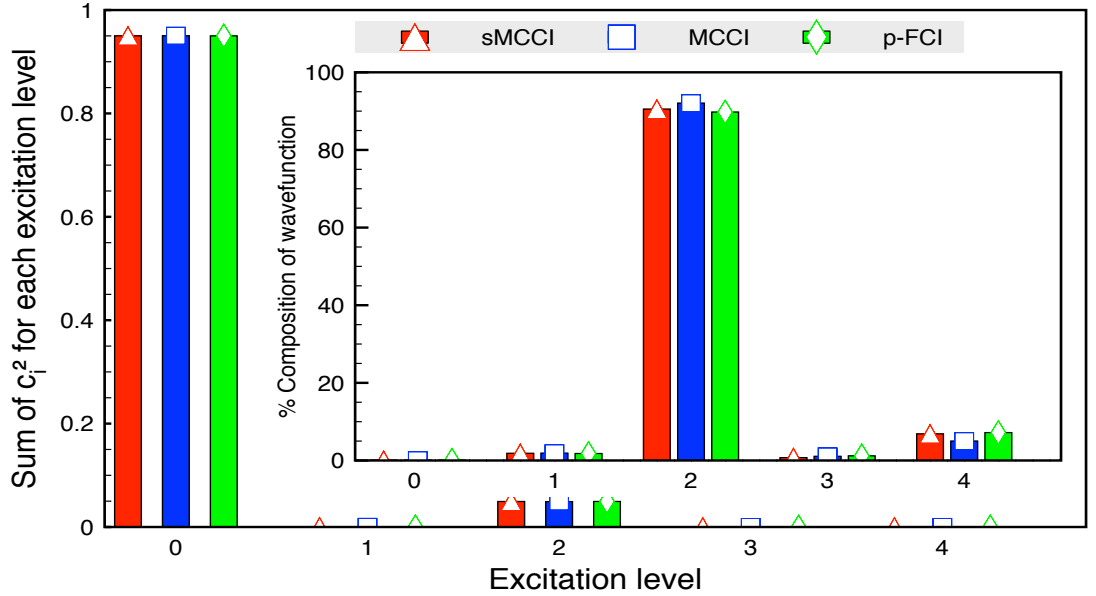


Figure 3.14: *The sum of c_i^2 for each substitution level present in the various wavefunctions for H_2O ($R_{OH} = 1.8$ Bohr) within a cc-pVDZ basis, $i_{batch} = 2000$ SDs, $i_{add} = 1000$ SDs and $c_{min} = 10^{-3}$. Inset: % composition of each wavefunction in terms of configurations.*

As shown in the inset of Figure 3.15, the composition for the highly multi-reference $R_{OH} = 4.0$ Bohr system differs significantly from an $R_{OH} = 1.8$ Bohr. This wavefunction contains up to sextuplet excited configurations in comparison to the limit of quadruple excitations for the equilibrium arrangement. In terms of relative importance the contribution of the HF wavefunction depletes from 95 %, for an $R_{OH} = 1.8$ Bohr, to 50 % for this stretched geometry. The contribution of the doubly excited configurations raises significantly, with a contribution of around

40 %. The contribution of singly, triply and quadruply excited configurations are also non-negligible. Therefore based on the above approach we observe no significant difference between the stochastic MCCI approach and the two systematic approaches of building up and down the wavefunctions.

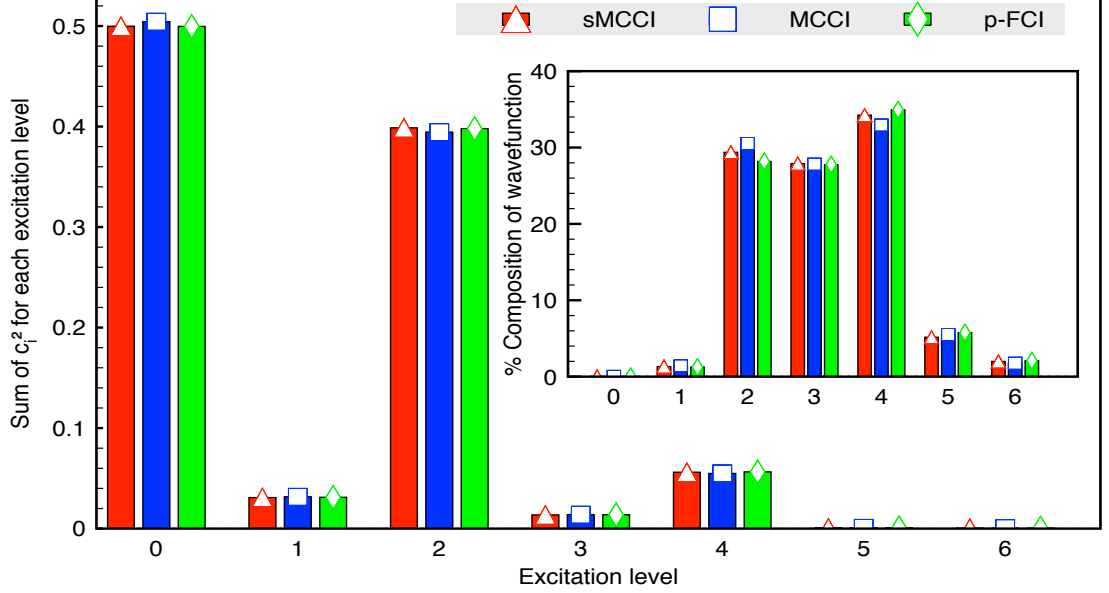


Figure 3.15: The sum of c_i^2 for each substitution level present in the various wavefunctions for H_2O ($R_{OH} = 4.0$ Bohr) within a cc-pVDZ basis, $i_{batch} = 2000$ SDs, $i_{add} = 1000$ SDs and $c_{min} = 10^{-3}$. Inset: % composition of each wavefunction in terms of configurations.

3.4.3 Carbon Monoxide

We now turn our attention to the determination of an excited state, specifically the first excited state of A_1 symmetry for carbon monoxide ($^1\Sigma^+$), within C_{2v} symmetry, and as described by a cc-pVDZ basis $[6s\ 4p\ 2d]$ with the two lowest energy MOs doubly occupied in all configurations. The excited state experimental bond length of 2.116 Bohr was used which gave a FCI energy of -113.055014 and -112.666416 Hartree. This corresponds to an excitation energy of 10.574 eV. To ensure wavefunction instability problems do not arise, which may become an issue if important ground state configurations are pruned in the excited state, all configurations contained within the A_1 ground state are present in the excited state wavefunctions. For a $c_{min} = 10^{-3}$, $conv.E = 10^{-3}$ Hartree, $i_{batch} = 2000$ CSFs and $i_{add} = 1000$ CSFs, the ground state MCCI and sMCCI wavefunctions contain 1770 and 1919

CSFs, with the latter 6.45×10^{-1} kcal mol $^{-1}$ lower in energy. In regards to the A_1 excited state the wavefunctions increase in size by a factor of 1.6 for MCCI and 1.5 for sMCCI. Once again the sMCCI is lower in energy by 4.06×10^{-1} kcal mol $^{-1}$. Both MCCI and sMCCI give respective excitation values of 10.668 and 10.658 eV, only overestimating this by quantity by less than one tenth of an eV when compared to FCI data. As the excited state wavefunctions contain significantly more configurations than their ground state counterparts we recompute the ground state energy in the space spanned by the excited state. This correcting approach gives MCCI and sMCCI excitation energies of 10.745 and 10.744 eV respectively, due to the lowering of the ground state energy from the increased configurational space. We conclude this excitation study by switching to SDs, allowing us to directly measure the MR character. We use computational parameters analogous to the CSFs study performed above. As was the case for neon and H₂O the SD wavefunctions are larger than the CSF variant, containing 3104 and 3168 SDs for MCCI and sMCCI respectively for the ground state wavefunction. The latter provided the lower energy of the two by 4.32×10^{-2} kcal mol $^{-1}$. In regards to the A_1 excited state both wavefunctions increase in size by a factor of 1.5, with sMCCI once again the lower of the two by 2.03×10^{-1} kcal mol $^{-1}$. We do not observe the same agreement with the excitation energy when implementing SDs as both methods deviate by > 1.6 eV. The MR character for the ground and excited state was shown to be 0.17 and 0.80, respectively, showing the extreme MR nature of the excited state. We then use the correcting regime outline above giving values of 9.039 and 9.045 eV for MCCI and sMCCI, respectively. The c_{min} parameter was lowered by an order of magnitude, lowering excitation energies by 1.73×10^{-1} and 1.77×10^{-1} . This lowering vastly increased the wavefunction size, with the corrected ground state energy resulting in excitation energies of 8.805 and 8.831 for MCCI and sMCCI respectively. Once again for this system we observe no apparent difference between the two MCCI methodologies. It should be noted that FCI on the excited state for this system was too computationally demanding therefore it was not possible to compare sMCCI and MCCI with p-FCI.

3.4.4 Chromium Dimer

The final system of interest herein is Cr_2 due to the inherently challenging electronic structure thereby producing an extremely difficult test case for the methods. We revert our attention to Figure 3.1 [10] which illustrates the PES corresponding to the internuclear separation of two chromium atoms, in the cc-pVDZ and cc-pVTZ basis, and using MCCI with a c_{min} of 2×10^{-4} and 5×10^{-4} for the former, and 2×10^{-4} for the latter. However, for the cc-pVTZ basis at a $c_{min} = 5 \times 10^{-4}$ and internuclear separation of 2.75 Å MCCI can get trapped in a local minimum of the configurational space providing an anomalous energy which is found to be larger than the corresponding cc-pVDZ energy, all other points of the surface satisfied cc-pVTZ < cc-pVDZ. This was attributed to the high multi-reference character and the substantial FCI space, which contains $\sim 10^{18}$ determinants. Therefore, we feel this is an appropriate point for further investigation using both MCCI and our systematic approach, as full consideration of the interacting space should reduce the chances of remaining in a local minimum.

Initially, a $c_{min} = 5 \times 10^{-4}$, $i_{batch} = 2000$ CSFs, $conv.E = 5 \times 10^{-4}$ Hartree, and $i_{add} = 100$ CSFs was used, all computations were performed on 12 processors with the lowest 18 MOs doubly occupied in all configurations. Despite not running until convergence was achieved, due to the interacting singles and doubles space exceeding the upper limit of 200 million configurations, the sMCCI approach reaches a lower energy than the standard MCCI methodology. This termination occurred on the 28th iteration in comparison to MCCI which normally converged on the 1044th iteration, with the resulting sMCCI wavefunction containing 92.53 % less configurations than MCCI with respective lengths of 2588 and 34629 CSFs. This once again emphasises the compact nature of the systematically obtained wavefunction. As shown in Figure 3.16, sMCCI reached the same energy as that of the converged MCCI result in only ~ 6 wall time hours. It should be remembered that a level of variation between individual MCCI runs would be expected, however, due to the wall time of 50 hours this was not feasible.

The i_{add} was then increased to 200 CSFs, all other computational parameters

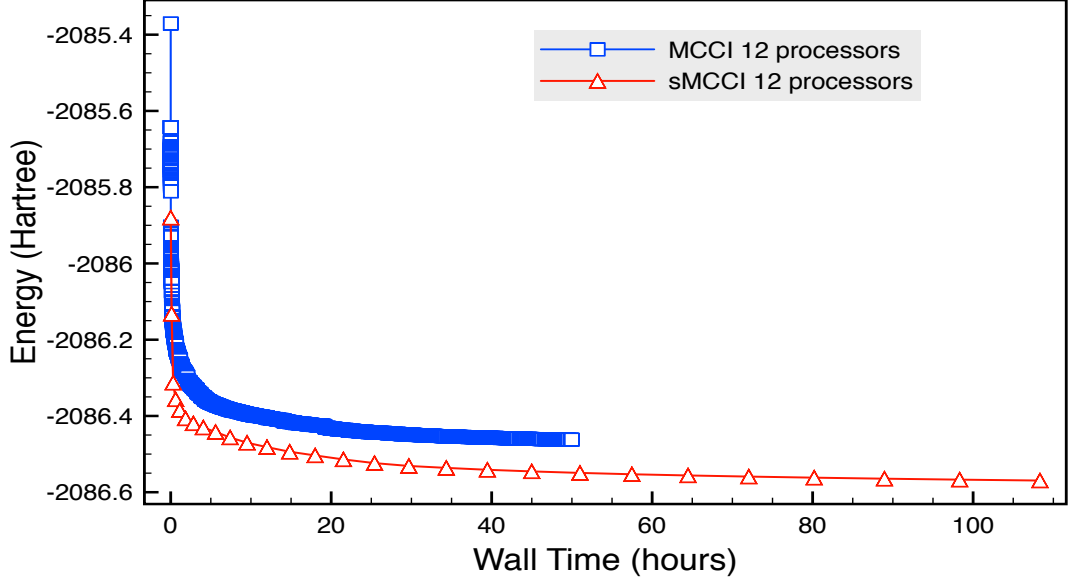


Figure 3.16: *Energy (Hartree) against time (hours) for MCCI and sMCCI 12 processor calculation of the chromium dimer at a bond length of 2.75 Å using CSFs, the cc-pVTZ basis with 18 frozen orbitals and a cutoff of $c_{min} = 5 \times 10^{-4}$.*

were analogous to that above, with the computations being performed on the EPSRC Tier-2 National HPC facilities (Cirrus) due to the greater number of processors and the increased available memory, thereby allowing the investigation of larger excitation spaces. For the following comparison we use 144 and 36 processors for sMCCI and MCCI, respectively. The sMCCI computation once again did not run until convergence was achieved, however, this was due to exceeding the wall time and not the excitation space, which peaked around 500 million CSFs. As the $i_{add} = 200$ CSFs computation was run on 136 more processors the wall time was lower than the $i_{add} = 100$ CSFs run. However, the converged MCCI energy with an $i_{add} = 200$ CSFs and run on 36 processors, was able to obtain a lower energy than the sMCCI equivalent. Despite running on a quarter of the number of processors MCCI was also found to result in a lower wall time (see Figure 3.17). The MCCI wavefunction at this larger i_{add} and processor number contained 33507 CSFs and converged on the 1113th iteration.

As we tend towards the processor limit we would favour a sMCCI approach due to the rapidly expanding interacting space, subject to the condition that the space could be stored in memory. Despite MCCI providing the highest energy, 12 processor run, it also provides the lowest energy overall, once again solidifying the stochastic

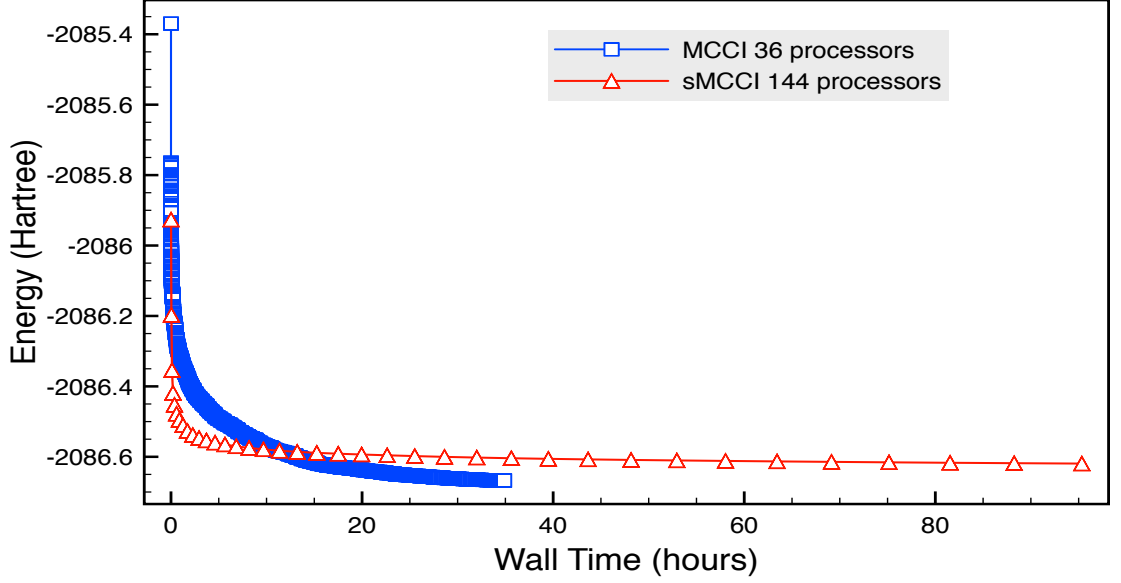


Figure 3.17: *Energy (Hartree) against time (hours) for MCCI and sMCCI using 36 and 144 processors respectively when applied to the chromium dimer at a bond length of 2.75 Å using CSFs, the cc-pVTZ basis with 18 frozen orbitals and a cutoff of $c_{min} = 5 \times 10^{-4}$.*

approach as this outperformed the systematic construction of the wavefunction. Therefore, we envisage a potential use of sMCCI in the validation of a single MCCI run or if multiple runs are required, as we can observe if a lower MCCI can be obtained by performing few iterations of the sMCCI approach.

3.5 Conclusion and Future Work

The stochastic Monte-Carlo configuration interaction (MCCI) approach was compared against two novel computationally tractable systematic regimes, in order to test the optimality of wavefunctions which augment a reference space with a random assortment of configurations. The first approach termed systematic-MCCI (sMCCI) involves the generation of the entire interacting space, which is randomised and subsequently reduced to smaller batches of i_{batch} size. The coefficient of each configuration within the batch is tested against the reference space and the overall i_{add} configurations with the largest weighting are stored. This final batch is once again combined with the reference space and diagonalised before being subject to a final selection criteria, this process is repeated iteratively until convergence is achieved. The second approach involves pruning the full configuration interaction

(FCI) wavefunction, this allows comparison of a method which initially considers all configurations and essentially deconstructs a wavefunction.

The approach of sMCCI was calibrated by a single neon atom in the cc-pVTZ basis. It was found that an i_{batch} and i_{add} of 2000 and 1000 CSFs, respectively, was found to be the most efficient and in line with our adaptive i_{batch} estimation, based upon the size of the wavefunction and the true scaling of the Davidson diagonalisation procedure. We observed enhanced scaling of the sMCCI algorithm when compared to MCCI, however, we did not observe systematic computations that were fast than their stochastic counterparts when considering up to 72 processors. The various approaches were then compared in terms of energy, length of converged CI vector and multi-reference character with all providing very similar properties. The wavefunction composition, in terms of number of configurations of each excitation level and relative contribution, was then explored. Once again all three methods perform similarly with the only discrepancy occurring with quadruple excitations, as MCCI contained ~ 400 CSFs less than the two systematic approaches.

We then turned our attention to the potential energy surface (PES) corresponding to the double-hydrogen dissociation in H_2O and described with a cc-pVDZ basis. This was chosen due to the varying degree of multi-reference character as the internuclear separation is altered. Prior to computing this PES the i_{batch} and i_{add} parameters were once again investigated for a separation of 4.0 Bohr. However, analogous results to the aforementioned neon system were obtained therefore we keep the i_{batch} and i_{add} equal to 2000 and 1000 CSFs, respectively. All three methods approximate the FCI PES to a similar accuracy, with pruned FCI giving the highest accuracy potential curved followed by sMCCI but there was no strong difference between the methods. For the equilibrium separation and 4.0 Bohr stretched system the wavefunction composition was essentially invariant between the methods, with a multi-reference character of 9.7×10^{-2} and 7.2×10^{-1} respectively.

The first A_1 excitation energy of carbon monoxide was then explored using both MCCI and sMCCI in a cc-pVDZ basis. Once again both methods perform similarly approximating this vertical transition energy to within < 0.1 eV of FCI data.

The study concludes with investigation of the chromium dimer at a particular challenging geometry, equal to an internuclear separation of 2.75 Å, in a cc-pVTZ basis and the 18 lowest energy molecular orbitals doubly occupied in all configurations. When using 12 processors, an absolute coefficient cutoff of 5×10^{-4} , $i_{add} = 100$ CSFs and $i_{batch} = 2000$ CSFs, the sMCCI resulted in a considerably lowering energy than the MCCI counterpart. However, upon increasing the number of processors to 36 MCCI resulted in the lowest energy overall, despite running sMCCI on 144 processors and increasing the i_{add} parameter to 200 CSFs.

Therefore we observe that the stochastic approach of building up the wavefunction gives sufficiently comparable energies and wavefunctions to methods that systematically consider the entire interacting space. This comparison was extended to single atomic energies, equilibrium and stretched geometries, and excited states. This gives us a clear indication that MCCI wavefunctions are reasonably close to optimal for the number of configurations used. The only observed anomaly to this was the 12 processor run for MCCI and sMCCI, where the latter had a considerably lowering energy and CI vector length. However, upon increasing the number of processors the MCCI provided the lowest energy overall.

Despite the enhanced scalability for sMCCI we were yet to observe converged computations that were faster than the corresponding MCCI run. However, large scale parallelisation may switch this ordering. At this moment in the development we are not suggesting that sMCCI replaces the stochastic approach but instead validates a single MCCI wavefunction thus giving indication when further runs are required. This was noticeable in the chromium dimer where sMCCI can be used relatively quickly to indicate if MCCI has become trapped in a local minimum configurational space, therefore requiring repeated runs to create a wavefunction with sufficient accuracy.

As the single and double space must be stored in available memory this limits the size of systems we can subject such a treatment to. Therefore, in the future we wish to explore potentially different ways to generate the interacting space and also the large scale parallelisation.

3.6 References

- [1] E. Rossi, G. L. Bendazzoli, S. Evangelisti, D. Maynau, *Chemical Physics Letters* **1999**, *310*, 530–536.
- [2] W. Helal, S. Evangelisti, T. Leininger, A. Monari, *Chemical Physics Letters* **2013**, *568-569*, 49–54.
- [3] J. C. Greer, *The Journal of Chemical Physics* **1995**, *103*, 1821–1828.
- [4] J. Greer, *Journal of Computational Physics* **1998**, *146*, 181–202.
- [5] L. Tong, M. Nolan, T. Cheng, J. Greer, *Computer Physics Communications* **2000**, *131*, 142–163.
- [6] J. P. Coe, D. J. Taylor, M. J. Paterson, *The Journal of Chemical Physics* **2012**, *137*, 194111.
- [7] A. Dutta, C. D. Sherrill, *The Journal of Chemical Physics* **2003**, *118*, 1610–1619.
- [8] M. L. Abrams, C. D. Sherrill, *The Journal of Physical Chemistry A* **2003**, *107*, 5611–5616.
- [9] W. Györffy, R. J. Bartlett, J. C. Greer, *The Journal of Chemical Physics* **2008**, *129*, 064103.
- [10] J. Coe, P. Murphy, M. Paterson, *Chemical Physics Letters* **2014**, *604*, 46–52.
- [11] B. Simard, M.-A. Lebeault-Dorget, A. Marijnissen, J. J. ter Meulen, *The Journal of Chemical Physics* **1998**, *108*, 9668–9674.
- [12] J. P. Coe, M. J. Paterson, *The Journal of Chemical Physics* **2013**, *139*, 154103.
- [13] P. Murphy, J. P. Coe, M. J. Paterson, *Journal of Computational Chemistry* **2018**, *39*, 319–327.
- [14] J. P. Coe, M. J. Paterson, *The Journal of Chemical Physics* **2014**, *141*, 124118.
- [15] J. P. Coe, M. J. Paterson, *The Journal of Chemical Physics* **2012**, *137*, 204108.

- [16] H.-J. Werner, P. J. Knowles, G. Knizia, F. R. Manby, M. Schütz, P. Celani, W. Györfy, D. Kats, T. Korona, R. Lindh, A. Mitrushenkov, G. Rauhut, K. R. Shamasundar, T. B. Adler, R. D. Amos, S. J. Bennie, A. Bernhardsson, A. Berning, D. L. Cooper, M. J. O. Deegan, A. J. Dobbyn, F. Eckert, E. Goll, C. Hampel, A. Hesselmann, G. Hetzer, T. Hrenar, G. Jansen, C. Köppl, S. J. R. Lee, Y. Liu, A. W. Lloyd, Q. Ma, R. A. Mata, A. J. May, S. J. McNicholas, W. Meyer, T. F. Miller III, M. E. Mura, A. Nicklass, D. P. O'Neill, P. Palmieri, D. Peng, K. Pflüger, R. Pitzer, M. Reiher, T. Shiozaki, H. Stoll, A. J. Stone, R. Tarroni, T. Thorsteinsson, M. Wang, M. Welborn, *MOLPRO, version 2019.2, a package of ab initio programs*, **2019**.
- [17] H.-J. Werner, P. J. Knowles, G. Knizia, F. R. Manby, M. Schötz, *Wiley Interdisciplinary Reviews: Computational Molecular Science* **2012**, 2, 242–253.
- [18] M. J. Frisch, G. W. Trucks, H. B. Schlegel, G. E. Scuseria, M. A. Robb, J. R. Cheeseman, G. Scalmani, V. Barone, G. A. Petersson, H. Nakatsuji, X. Li, M. Caricato, A. V. Marenich, J. Bloino, B. G. Janesko, R. Gomperts, B. Mennucci, H. P. Hratchian, J. V. Ortiz, A. F. Izmaylov, J. L. Sonnenberg, D. Williams-Young, F. Ding, F. Lipparini, F. Egidi, J. Goings, B. Peng, A. Petrone, T. Henderson, D. Ranasinghe, V. G. Zakrzewski, J. Gao, N. Rega, G. Zheng, W. Liang, M. Hada, M. Ehara, K. Toyota, R. Fukuda, J. Hasegawa, M. Ishida, T. Nakajima, Y. Honda, O. Kitao, H. Nakai, T. Vreven, K. Throssell, J. A. Montgomery, Jr., J. E. Peralta, F. Ogliaro, M. J. Bearpark, J. J. Heyd, E. N. Brothers, K. N. Kudin, V. N. Staroverov, T. A. Keith, R. Kobayashi, J. Normand, K. Raghavachari, A. P. Rendell, J. C. Burant, S. S. Iyengar, J. Tomasi, M. Cossi, J. M. Millam, M. Klene, C. Adamo, R. Cammi, J. W. Ochterski, R. L. Martin, K. Morokuma, O. Farkas, J. B. Foresman, D. J. Fox, *Gaussian 09 Revision D.01*, Gaussian Inc. Wallingford CT, **2016**.
- [19] D. Zuev, E. Vecharynski, C. Yang, N. Orms, A. I. Krylov, *Journal of Computational Chemistry* **2015**, 36, 273–284.

Chapter 4

Investigating a Series of Intramolecular Diels-Alder Reactions *via* High-Accuracy Thermochemical Analyses

4.1 Abstract

In this Chapter we present two studies on various intramolecular Diels-Alder reactions (IMD-A), in collaboration with the experimental Bebbington group at Mont-Clair State University, formerly of Heriot-Watt University. We utilise the high-accuracy quantum chemical composite method CBS/QB3 throughout. The first study involves incorporating a nitro group into the electron-rich furan acting as the diene, with the data discussed herein published in the Journal of Organic Chemistry [1] which will be cited if necessary. For the majority of systems it was found that furan nitration reduced activation barriers and raised exothermicities thus leading to more rapid reactions. This was attributed to positive charge stabilisation upon σ bond formation at the nitro bearing carbon. These reactions were found to proceed via an asynchronous transition state which was more apparent in the nitro case, thus facilitating the reaction with substituted dienophiles. The nature of the electron demand process was also probed for these nitrated systems and compared to their non-nitrated counterparts. The second study involved the investigation of hetero IMD-A substrates once again utilising the CBS/QB3 model. We investigate if structure-energy correlations exist in substrates that form two different σ bonds within the cycloaddition process, that had been found in homo bond formation IMD-A systems [2]. However, for the majority of systems studied herein we do not observe any strong correlations, with the exception of one substrate subset for which we observe a strong correlation between the transition state contraction and the retro Diels-Alder barrier.

4.2 Introduction

Pericyclic reactions have been the subject of many studies both experimentally [3–7] and computationally [8–18]. For a detailed description of various pericyclic processes such as electrocyclic and cycloaddition reactions, in both their photochemical and thermal variants, see [19]. All reactions attributed to the pericyclic family share a common characteristic; a concerted mechanism involving formation of a cyclic transition state with in-phase overlap of the necessary bonding orbitals.

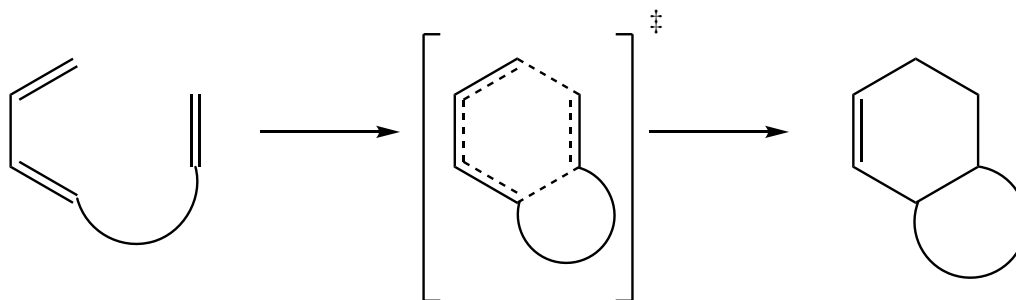


Figure 4.1: An overview of an arbitrary IMD-A reaction highlighting the cyclic transition state.

Within the context of this Chapter the particular pericyclic reactions that are of interest are those undertaking an intramolecular Diels-Alder (IMD-A) regime. The following notation when naming an IMD-A reaction is used throughout, diene/dienophile, to clearly identify the corresponding component within the molecule. We investigate two different classes of precursors, those involving furan/alkene moieties for which we present a detailed analysis of theory *vs.* experiment, and that of diene/aldehyde and unsaturated aldehyde/alkene substrates, which solely pertains to theoretical findings. These materials are of interest as their reactivity cannot be explained in a traditional Diels-Alder (D-A) sense through sole consideration of the frontier molecular orbitals (FMOs), as other factors, which will be discussed below, are shown to be more important in certain cases [20–23].

The first class of molecules we explore are those involving an aromatic diene, for which the diene moiety takes the form of a furan ring as this is found to be extremely sensitive to substituent effects. It should be noted that work regarding the use of furan as a dienophile has also been reported [24], however, herein it is solely employed as a diene, which becomes electron-poor upon incorporation

of a nitro group. A 2003 study by Crawford *et al.* [21] investigated the reaction rates for a series of substituted N-alkenyl-substituted furanyl amides, see Figure 4.2 for a specific example set. To note, the nomenclature employed herein uses **XA**, **XTS** and **XB** to represent the reactant, transition state and product pertaining to reaction **X** respectively. It was observed that upon halogenation of the furan, at position 5, reaction rates and associated yields increased dramatically. After 48 hours under reflux, the non-halogenated reaction generated a mixture of products, see last two structures of reaction set **1**, in corresponding yields of 40 and 48 %. For the halogenated reaction, under analogous reaction conditions, the entirety of the bromine precursor was converted to the corresponding cycloadduct. This is somewhat surprising as furan is employed as an electron-rich diene, reacting readily with electron-poor dienophiles. Therefore, it would be expected that the incorporation of an electron withdrawing group would hamper the viability of these reactions, or in some cases completely prevent said reactions taking place due to the removal of electron density from the diene. It was also found that dienophile substitution was tolerated to a much better degree, with once again higher yields and lower reaction times for the brominated system.

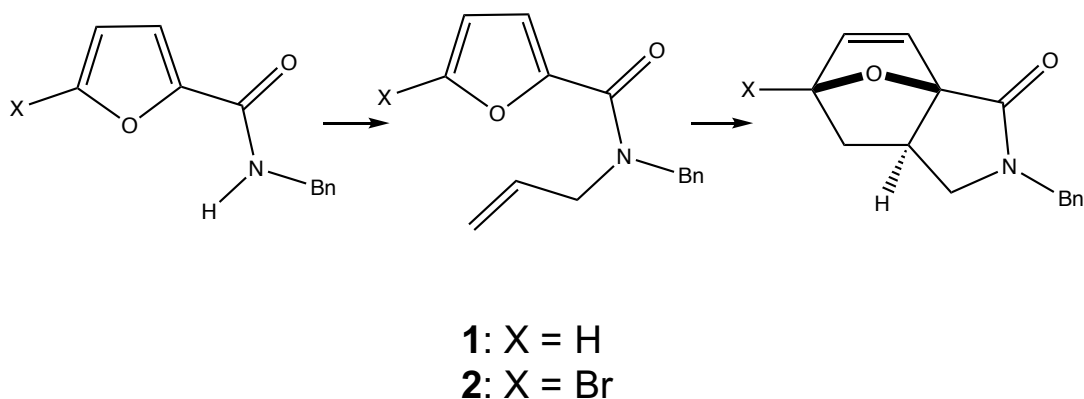


Figure 4.2: *Example set of reactions from published studies [21].*

A latter investigation by Pieniazek and Houk [22] employed the high accuracy composite quantum chemical method, CBS-QB3, to further probe the kinetic and thermodynamic D-A reaction pathways of both non-halogenated and halogenated furan species. An outline of this computational technique has already been provided in Section 2.12. This study was performed on 2-chlorofuran, 2-bromofuran and

2-fluorofuran/ethylene reactions. All enthalpy barriers and exothermicities were found to be lower by 2.1 to 3.4 and 4.9 to 8.7 kcal mol⁻¹, respectively, for these halogenated reactions when compared to the non substituted furan/ethylene system. It should be noted that for this study the two moieties were separate with no tether linking them, a normal intermolecular D-A reaction. In addition to more favourable reactions these findings also indicate the additional stabilisation observed within the halogenated species as the reaction proceeds i.e. greater stabilisation of the cycloadduct when compared to the transition state. For example the reaction of 2-chlorofuran/ethylene lowers barriers and exothermicities by 2.1 and 4.9 kcal mol⁻¹, respectively, thus highlighting the greater influence on the product. As the overall Gibbs free energy is approximately 0 for the furan/ethylene reaction, at 298.5 K, incorporating a halogen atom shifts this from an established equilibrated system to a spontaneous process in the forward direction, thereby allowing for greater product formation.

A follow up investigation by Padwa *et al.* [20] then explored this halogenation effect computationally in true IMD-A substrates, albeit now with Kohn-Sham density function theory (DFT), specifically using a B3LYP/6-31G(d) model. For these tethered precursors, upon bromination at position 5 of the furan ring activation barriers were found to decrease with exothermicities once again increasing. This thermodynamic and kinetic beneficial process has been assigned to the enhanced stabilisation of the partial positive charge, through hyperconjugation and σ -inductive effects, in both the transition state and resulting cycloadduct, as the halogenated carbon atom is now located in a more alkylated environment, as transitioning from a sp^2 to sp^3 hybridised carbon atom. The specific nature of the tether was also explored, using methylene and amide linkers, as was substitution at position 3 of the furan ring. The incorporation of a bromine atom at position 3 of the furan ring was once again found to enhance the subsequent reaction rates to a similar extent, however, for the amide tether steric interactions between the bromine and oxygen dominated, see the cycloadduct from reaction **2** for the amide linker.

A further investigation by Rae *et al.* [23] found that for a series of IMD-A sub-

strates, similar in structure to that of the aforementioned studies, chlorination of the dienophile significantly lowered the rate of reaction. The true role of FMOs in controlling the intramolecular reactions was also probed, with findings showing no correlation between FMO energies and reaction rates thus validating the claim that other factors may override FMO interactions. For the majority of substrates studied halogenation of the furan was found to have no effect on the nature of the important FMO interaction. If the important interaction is that of the highest occupied molecular orbital of the diene ($\text{HOMO}_{\text{diene}}$) and the lowest unoccupied molecular orbital of the dienophile ($\text{LUMO}_{\text{dienophile}}$) this is termed a normal electron demand process. The opposite would hold for an inverse electron demand procedure. The halogenation of the dienophile was also found to have no effect on the nature of FMO interactions for the majority of systems, although slightly altering the specific orbital energies. The steric bulk around the nitrogen was also explored by replacing the phenyl to a benzyl group, with the latter having a slightly higher forward reaction rate. Upon further inspection, it was also observed that the more exergonic reactions had earlier transition states when comparing distances of the corresponding carbon atoms in both the transition state and cycloadduct in accord with the Hammond postulate. Therefore, due to the early nature of the transition state there was a greater contraction in the newly forming σ bond lengths upon going from the transition state to the cycloadduct, termed herein as $\text{TS}_{\sigma\text{-con.}}$ and is outlined in equation 4.2. The transition states of these systems were further explored where it was observed that there was a strong structure-energy correlation [2]. This linear correlation between the $\text{TS}_{\sigma\text{-con.}}$ contraction and both the overall Gibbs free energy change and the retro D-A (rD-A) activation barrier was found for IMD-A substrates containing a variety of dienes and dienophiles. Surprisingly the correlation between $\text{TS}_{\sigma\text{-con.}}$ and the IMD-A activation barrier was found to be noticeably weaker. These correlations were also expected to hold for non-aromatic dienes. However, this correlation was not present in standard intermolecular D-A reactions.

In the first part of this study we initially investigate IMD-A reactions involving

a nitrated and non-nitrated furan as the diene moiety, due to the extreme electron withdrawing nature of the nitro group, to observe if effects mentioned previously in the regards to halogenation hold for these systems. Despite being the subject of previous studies direct comparison between the aforementioned furanyl systems has yet to be fully explored, as has subsequent substitution of the dienophile. Also to the best of our knowledge these systems have not been previously investigated using highly accurate thermochemical computational methods, therefore making prime candidates. Within this study we make a detailed comparison between these high accuracy theoretical models and experimental findings. In the second part we then extend this theoretical approach to the analysis of dienes and dienophiles containing a carbonyl group such as diene/aldehyde and unsaturated aldehyde/alkene substrates. These materials provide a synthetic pathway to functionalised dihydropyrans which are of importance particularly as intermediates in target synthesis [25]. We explore the overall energetics of such reactions, in which a heteroatom is explicitly included in the bond formation process, and also consider if structure-energy correlations hold for this class of materials.

4.3 Computational Details

4.3.1 Furan and Nitrofuran Dienes

All electronic structure computations were performed with Gaussian 09 (Revision D.01) [26] on the range of reactions given in Figure 4.3. Preliminary geometries were obtained *via* Kohn-Sham DFT [27, 28], B3LYP [29] functional with a split-valence double- ζ basis, 6-31G. The nature of each stationary point was confirmed by means of analytic Hessian computations, ensuring minima and transition states contained 0 and 1 imaginary vibrational modes, respectively. For reaction **7** an IRC computation following the forward and reverse displacement of the transition vector was undertaken thus ensuring the correct reaction pathway was modelled. We focused on this reaction as it is the only singly substituted dienophile therefore ensuring the *endo* and *exo* cycloadducts will be different. This was confirmed and

an analogous mode was observed for the rest of the systems thereby validating our reaction pathway.

The thermodynamic and kinetic pathway of the reactions was probed at both 298.15 and 383.00 K using a high accuracy complete basis set (CBS) model, the particular extrapolation procedure utilised was CBS-QB3 [30], a variant of the original CBS-Q model [31], as this method has been previously applied to similar systems [23] and has been shown to have a low mean average deviation, 1.1 kcal mol⁻¹ with respect to G2 test set, as outlined in Section 2.12 [32]. FMO energies were obtained from step one of the CBS-QB3 procedure, equating to the B3LYP functional with a split valence triple- ζ basis, 6-311G(2d,d,p). The FMOs relating to the dienophile were selected rationally. The HOMO orbital demonstrated significant amplitude of in-phase overlap of appropriate locally out-of-plane p orbitals on the ethylene segment. A similar approach was used to identify the LUMO, this time demonstrating an out-of-phase interaction. The identification of the HOMO/LUMO relating to the furan was straightforward, although the presence of the nitro substituent gave rise to a distinct difference in the observed LUMOs, with an extra nodal point at position three of the nitrofuran system when compared to the non-nitrated counterpart.

4.3.2 Carbonyl Dienes and Dienophiles

Initial geometries were once again obtained *via* DFT optimisations, B3LYP/6-31G, with a subsequent frequency computation, however, this time utilising Gaussian 16 (Revision A.03) [26]. Each individual reaction pathway was validated through an IRC computation on each transition state, thus linking the correct reactants to products through a high energy conformation. The reaction pathways outlined in Figure 4.7 were investigated at both 298.15 and 383.00 K, once again utilising the CBS-QB3 model.

4.4 Results and Discussion

4.4.1 Furan and Nitrofuran Dienes

Initially we explore some results provided by our experimental collaborators. In order to investigate the electronic effects we only incorporate the nitro group at position 5 of the furan ring ensuring no repulsive interactions will be prevalent. The tether linking the two moieties is also slightly different from the IMD-A substrates outlined in the Figure 4.2, containing an extra methylene bridge and also reversing the connection of the amide linker.

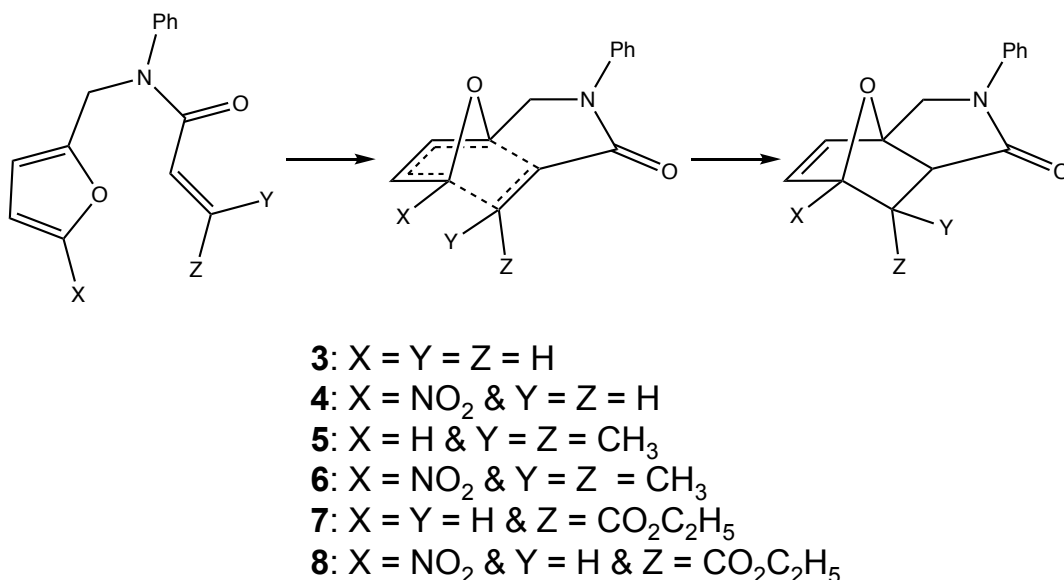
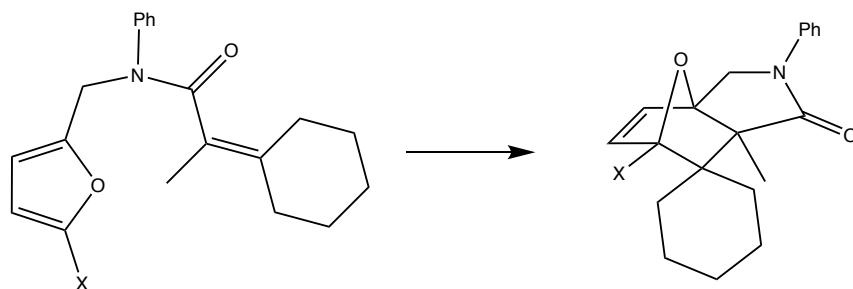


Figure 4.3: Various IMD-A substrates of interest within this study.

The reactions **4** and **6**, precursors containing a nitro group, were found to react faster than the corresponding non-nitrated systems, **3** and **5** respectively. This was highlighted by the % conversion at specific times in the reaction. For reaction **3** and **4** the conversion after 3 hours was 33 % and 49 % for the nitrated and non-nitrated cycloadduct respectively. At 24 hours this drastically increased to 93 and 100 %. In regards to reaction **5** after 2 hours the non-nitrated cycloadduct is not observed, however, a 40 % conversion is obtained for the nitrated counterpart. This highlights the inability of non-nitrated substrates to cope with even a simple di-methyl substitution of the dienophile. Despite not being of interest in our computational studies the conversion of **10A** to **10B**, see Figure 4.4, shows the highly substituted systems that can be obtained with nitrated furans thus highlighting the appeal of

such systems.



9: X = H

10: X = NO₂

Figure 4.4: *Experimental IMD-A reactions of interest [1].*

We now turn our attention to the theoretical approach in order to further explore the increased reaction rates and tolerance of dienophile substitution for the nitrated systems when compared to the non-substituted counterparts. We particularly focus on the possible increase in positive charge stabilisation of nitrated cycloadducts when compared to their precursors, *via* hyperconjugation effects as proposed by Padwa and Houk [20], and also the nature of resulting FMO interactions. The overall reaction enthalpy (ΔH_r) and free energy (ΔG_r) energetics, with associated barrier heights, ΔH_r^\ddagger and ΔG_r^\ddagger respectively, are given in Table 4.1 with the quantities each represents illustrated in Figure 4.5. For energetics pertaining to a rD-A regime this will be included in the subscript, i.e. the rD-A free energy activation barrier would be ΔG_{rD-A}^\ddagger . All reaction energetics provided herein are at 383 K as this best simulates the true reaction conditions, however, analogous results were obtained at 298 K.

Table 4.1: *Theoretically calculated reaction energetics at 383 K all values are in terms of kcal mol⁻¹.*

Reaction	ΔH_r^\ddagger	ΔG_r^\ddagger	ΔH_r	ΔG_r
3	17.0	22.2	-15.8	-9.5
4	15.5	21.1	-18.8	-12.5
5	19.9	26.4	-12.1	-4.0
6	15.6	22.4	-16.8	-8.1

Upon nitration, reactions **4** and **6** are found to be more exothermic and exergonic when compared to their non-nitrated analogues. The difference in exothermicity and exergonicity was 3 kcal mol⁻¹ for reaction **4**, which became more pronounced when

dealing with the di-methylated system as differences of 4.7 and 4.1 kcal mol⁻¹ were obtained respectively. The subsequent reaction barriers were also found to be lower for nitrated precursors. Once again, the differences were larger for the di-methylated reaction with ΔH_r^\ddagger and ΔG_r^\ddagger varying by 4.3 and 4 kcal mol⁻¹, in comparison to the hydrogen dienophile system as this was only 1.5 and 1.1 kcal mol⁻¹. This supports the experimental findings as **5B** is not observed within 2 hours, and only results in < 10 % conversion after 45 hours, which has the largest computed barriers and the lowest overall reaction energetics. For the unsubstituted dienophile, as was the case with the aforementioned halo-furans, we observe greater stabilisation for the nitrated compounds as the reaction proceeds *via* formation of the two σ bonds between the moieties. For this unsubstituted dienophile the exergonicity increases by 3 kcal mol⁻¹ with the free energy activation barrier reducing by 1.1 kcal mol⁻¹ when comparing the nitrated to non-nitrated reaction, see Figure 4.5. This leads to a larger rD-A barrier for reaction **4**, by 1.9 kcal mol⁻¹, therefore being less likely to revert back to the precursor. For the di-methylated dienophile the lowering of the free energy barrier and overall energy is the same at \approx 4 kcal mol⁻¹ leading to the same rD-A barrier for both reactions.

As mentioned in Section 4.2, FMO interactions are readily used to explain the reactivity of D-A reactions. If a normal electron demand process is followed the HOMO-LUMO gap (ΔE) will be lower when considering the HOMO_{diene} and LUMO_{dienophile}. If the opposite is true then this would be termed an inverse demand process. The ΔE relating to a normal (ΔE_{normal}) and inverse ($\Delta E_{inverse}$) electron demand process are outlined in Table 4.2 for the systems of interest. Also, for comparison we include values relating to the following intermolecular D-A model systems: **11** = furan/ethylene, **12** = furan/1,1-dimethylethylene, **13** = nitrofuran/ethylene and **14** = nitrofuran/1,1-dimethylethylene. These reactions also allowed us to identify the relevant HOMO/LUMO orbitals of the diene and dienophile for the intramolecular system.

As highlighted in the model reactions, **11** and **13**, upon diene nitration the electron demand clearly undergoes a complete reversal, with $\Delta E_{inverse}$ pertaining

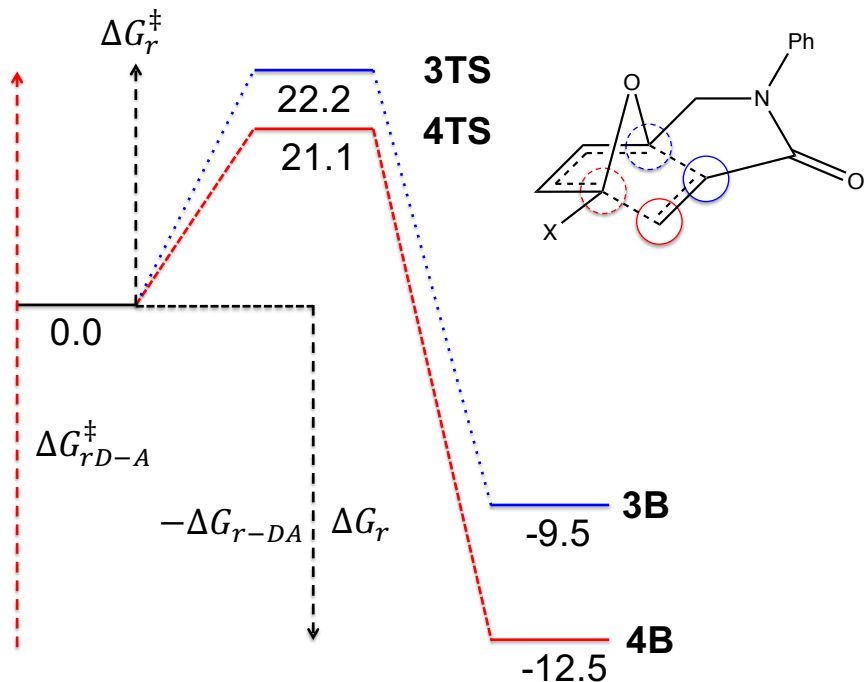


Figure 4.5: Relative free energies to the respective starting materials which are in terms of kcal mol^{-1} . The distance between the blue circles is denoted as TS_a where the carbon atom directly bound to the oxygen bridge is denoted as a_1 and the other as a_2 . A similar approach is used for the red circles, however, pertaining to TS_b . This nomenclature also holds for reactants and products.

Table 4.2: Normal and inverse electron demand energies for various reactions, computed at B3LYP/6-311G(2d,d,p).

Substrate	ΔE_{normal} (eV)	$\Delta E_{\text{inverse}}$ (eV)
3	5.3	8.1
4	6.0	4.9
5	5.3	7.1
6	6.0	4.9
11	6.5	7.7
12	6.9	7.0
13	7.7	4.9
14	8.0	4.1

to the nitro-substituted system also lower by 1.6 eV than ΔE_{normal} for **11**. When comparing reactions **12** and **14**, we once again observe a clear inverse demand for the nitro containing system, however, for the unsubstituted reaction the normal and inverse processes are much closer in energy, only a 0.1 eV difference in the two distinct gaps. In regards to the IMD-A reactions the nature of the electron demand is very clear. All nitrated substrates undergo an inverse electron demand process, with the opposite being true for the non-nitrated systems as they occur *via* a normal

regime, see Figure 4.6 for a visual comparison of the important FMOs for the four IMD-A substrates. If the reactivity of these species were to be truly described by ΔE , one would expect the largest difference to be for reaction **5**, with the lowest for **4**. However, ΔE_{normal} is found to be equal for **3** and **5** which supports the claim that other factors may override the FMO interactions, for **4** and **6** the $\Delta E_{inverse}$ is also found to be the same. If we solely consider **4A** this can be thought of as a polarity mismatched substrate as both the diene and dienophile would be electron deficient, the latter due to the conjugated carbonyl group. This switch in polarity lowers the FMO difference by 0.4 eV. The FMO difference for the di-methylated system also lowers by the same amount.

We now turn our attention to the transition state for each system to see if there pertains a connection between the increased substituent tolerance and the optimum arrangement. As outlined in Figure 4.5, we denote the bond involving the nitro bearing carbon as \mathbf{TS}_b , and the other as \mathbf{TS}_a with the explicit distances outlined in Table 4.3. The percentage difference ($\Delta\mathbf{TS}_{ba}$) is given as:

$$\frac{\mathbf{TS}_b - \mathbf{TS}_a}{\mathbf{TS}_a} \times 100 \quad (4.1)$$

where this quantity represents the difference of \mathbf{TS}_b and \mathbf{TS}_a relative to \mathbf{TS}_a . Thus the larger $\Delta\mathbf{TS}_{ba}$ the greater the asynchronicity between the two σ bonds.

Table 4.3: *Distance between carbon atoms involved in σ bond formation in the transition state.*

Transition State	\mathbf{TS}_a (Å)	\mathbf{TS}_b (Å)	$\Delta\mathbf{TS}_{ba}$
3	2.04	2.22	9
5	1.99	2.30	16
4	2.04	2.24	10
6	1.92	2.46	28

As both bonds are formed between carbon atoms one would expect a level of synchronicity between the two separate bond formations. However as per Table 4.3, we observe that all lengths are markedly different highlighting the asynchronous nature of the transition state. In all cases the length of \mathbf{TS}_b is far larger than that of \mathbf{TS}_a , with $\Delta\mathbf{TS}_{ba}$ ranging from 9 to 28 %. If we compare dienophiles containing

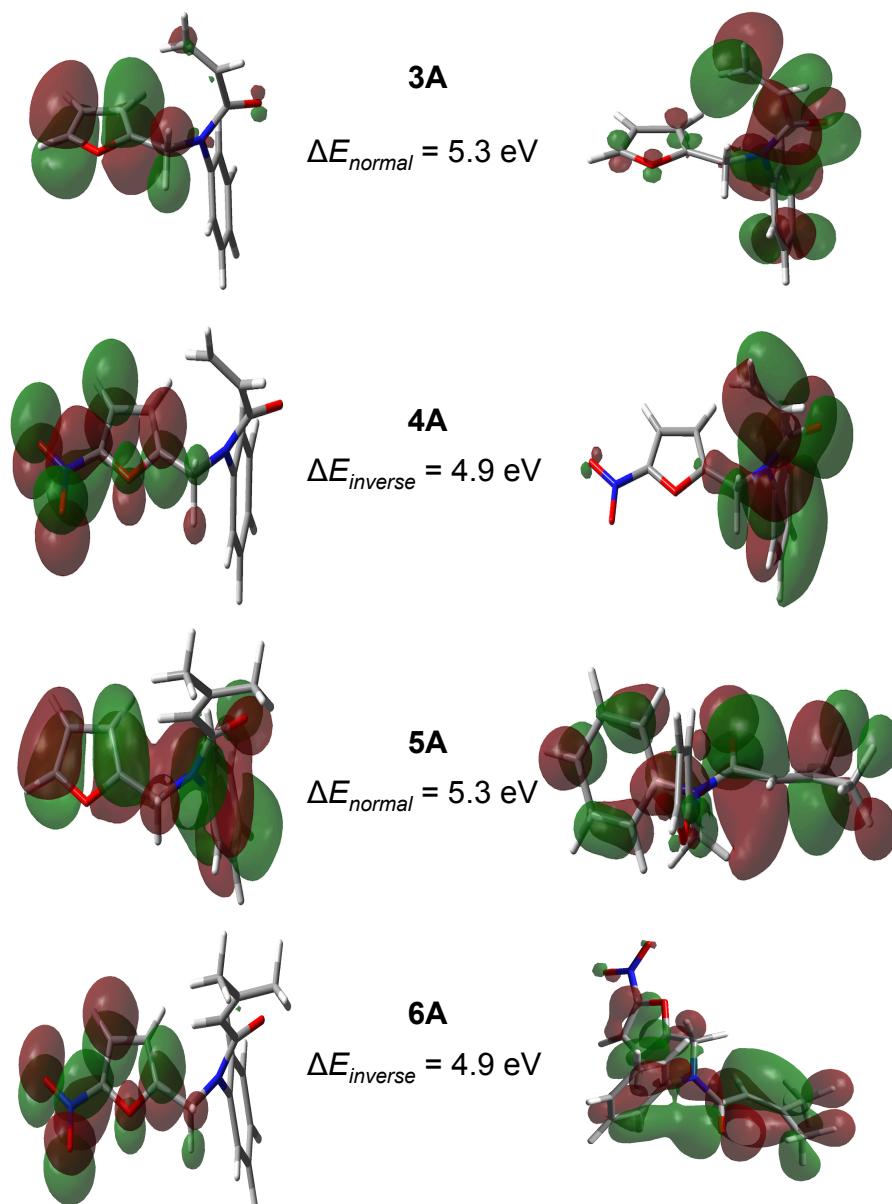


Figure 4.6: Important FMO interactions for various IMD-A substrates computed at B3LYP/6-311G(2d,d,p).

hydrogen atoms we observe that the length of TS_a and TS_b are very similar for the nitrated and non-nitrated systems, TS_a was actually found to be the same in both instances with TS_b deviating by only 0.02 Å. However, for the more sterically hindered di-methylated dienophile we observe a 12 % increase of the ΔTS_{ba} upon the incorporation of a nitro group into the diene, thus highlighting the larger difference between the length of TS_b when compared to TS_a for this system. The length of TS_a was found to decrease by 0.07 Å with TS_b increasing by 0.16 Å. For furan upon dienophile substitution ΔTS_{ba} increases by 7 %, however, for nitrofuran this drastically increases to 18 %. This highlights the asynchronous nature of the transition state, which is greater in the nitro cases indicating a degree of charge separation. It would be expected that there would be charge stabilisation of the partial positive charge on the nitro bearing carbon *via* transfer of electron density from the dienophile to diene which may be responsible for the larger TS_b length observed. This increased separation would thus explain the increased tolerance for dienophile substitution as steric interactions would be less important. For the non-nitrated system a similar transfer of electron density would not be expected, as the strong partial positive charge would not be observed, thereby the distance of TS_a and TS_b should be more equal indicating a more synchronous process when compared to the nitrated system. As the length of TS_b is smaller the steric interactions between the furan and substituted dienophile would become more prevalent reducing the substituent tolerance.

Experimentally it was then observed that upon incorporation of a $\text{CO}_2\text{C}_2\text{H}_5$ group into the dienophile the effect of nitration seen previously was not observed. As a result of this the reaction was also explored through CBS-QB3 computations the results of which are provided in Table 4.4. The incorporation of this substituent generates an extremely electron deficient dienophile, thus, **8A** can also be viewed as a polarity mismatched substrate. This would be more exaggerated than **4A** as the dienophile would be even more electron deficient due to being directly bonded to the electron withdrawing group. From experiment it was observed that the reaction involving furan could be performed at room temperature, however, for nitrofuran an

elevated temperature of 383 K was required. It should be noted that this reaction was still faster than all others within the study.

Table 4.4: *Theoretically calculated Gibbs reaction energetics at 383 K and in terms of kcal mol⁻¹. The difference in FMO energies are given in eV and for comparison we also include $\Delta\mathbf{TS}_{ba}$.*

Substrate	ΔG_r^\ddagger	ΔG_r	ΔE_{normal}	$\Delta E_{inverse}$	$\Delta\mathbf{TS}_{ba}$
7	17.9	-9.0	4.5	8.3	24
8	17.9	-11.0	5.1	5.9	22

The computed activation barriers are found to be the lowest thus supporting the experimental findings that these reactions are in accord with more rapid reactions. In this system it was also observed that both dienes undertake a normal electron demand process, with ΔE_{normal} for furan lower by 0.6 eV. The asynchronous nature of the transition state is also apparent, however, both are asynchronous to a similar degree.

4.4.2 Structure-Energy Correlations

As highlighted earlier we now switch our attention to IMD-A reactions which involve a diene or dienophile moiety which explicitly contains a carbonyl group. We further explore the work of Żurek *et al.* [2] to observe if this structure-energy correlation can be readily extended to hetero D-A substrates in which the same type of σ bonds are not formed. The set of reactions are outlined in Figure 4.7, which all involve the formation of one σ bond between carbon atoms and the other a σ bond between a carbon and oxygen atom. We also note that these systems contain non-aromatic dienes thus allowing us to explore this correlation for these types of materials. For comparison we also include the reactions of interest in Section 4.4.1, for these previously discussed systems it should be noted that upon nitration $\mathbf{TS}_{\sigma-con.}$ is found to be slightly higher, ranging from 0.3 to 0.8 %, thus validating that the more exergonic reactions have a slightly earlier transition state. The $\mathbf{TS}_{\sigma-con.}$ is given by the

following equation:

$$\mathbf{TS}_{\sigma_{con.}} = \frac{\frac{\mathbf{TS}_a - \mathbf{B}_a}{\mathbf{TS}_a} + \frac{\mathbf{TS}_b - \mathbf{B}_b}{\mathbf{TS}_b}}{2} \times 100 \quad (4.2)$$

where for the hetero IMD-A systems \mathbf{B}_a and \mathbf{B}_b represents the relevant bond lengths in the product which would be the carbon-oxygen and carbon-carbon distance respectively. Therefore, once again for larger $\mathbf{TS}_{\sigma_{con.}}$ values this would represent a larger contraction of the bond lengths upon converting from the transition state to product, and hence earlier transition states.

As the dienes are not as sterically locked, when compared to furan, it was observed that the cycloadduct produced in reaction **15** can be generated via two distinct transition states, **15TSZ** and **15TSE** where **Z** and **E** represents the specific configuration of the lower ethylene fragment of the diene-aldehyde substrate. As a result of this we initially explore this configurational dependence on the observed reaction energetics. All structures pertaining to the **E** configuration are found to be at least 2.2 kcal mol⁻¹ lower than those corresponding to the **Z** arrangement. For the enthalpy and Gibbs free energy we find that the barrier heights are essentially independent of the specific configuration employed, see Table 4.5 for explicit values once again at 383 K. From the overall reaction energetics we find that reactions involving the **Z** configuration are found to be more exothermic and exergonic by 2.07 and 2.52 kcal mol⁻¹ respectively.

Table 4.5: *Theoretically calculated reaction energetics for E and Z configurations based on reaction 15, at 383 K all values are in terms of kcal mol⁻¹.*

Conformer	ΔH_r^\ddagger	ΔH_r	ΔG_r^\ddagger	ΔG_r
Z	26.18	-20.97	32.81	-14.01
E	26.22	-18.90	33.24	-11.49

We proceed solely with the **E** configuration for the rest of the reactions provided in Figure 4.7 as this was the more chemically relevant structure due to the lower energy and we would not expect sufficient **E** to **Z** isomerisation. A Boltzmann analysis of these isomers highlights that if these were the only minima available the relative population would be $\approx 98:2$ % for **E:Z** respectively. The activation barriers,

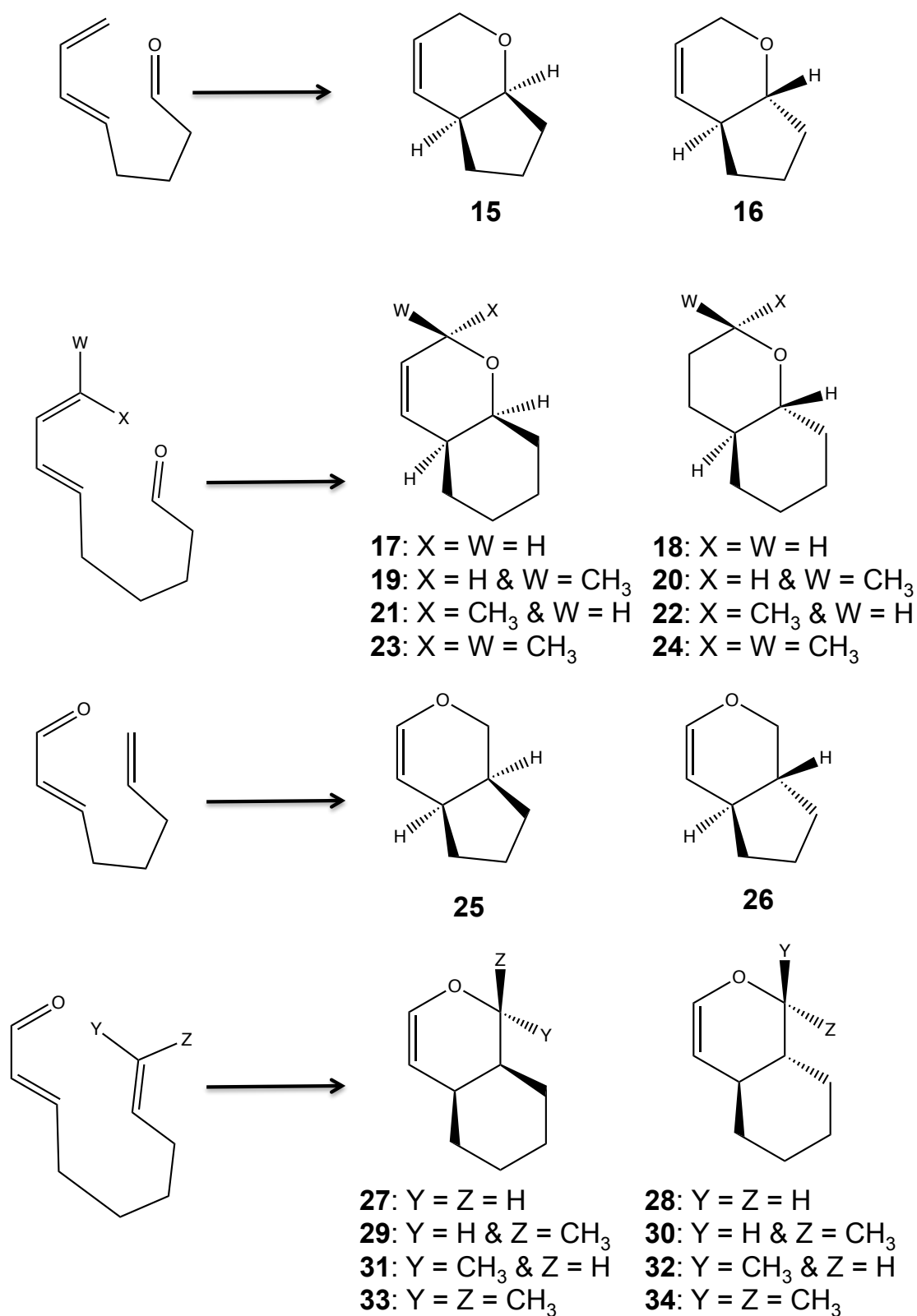


Figure 4.7: Various hetero IMD-A substrates of interest within this study.

overall reaction energetics and $\text{TS}_{\sigma\text{-con.}}$ contraction are given in Table 4.6. Once again all reactions are computed to be considerably exothermic and exergonic with $\text{TS}_{\sigma\text{-con.}}$ ranging from 26.08 to 29.00 %.

Table 4.6: *Theoretically calculated reaction energetics pertaining to the E configuration for the set of hetero IMD-A systems of interest at 383 K with all values in terms of kcal mol⁻¹. For comparison $\text{TS}_{\sigma\text{-con.}}$ has been included.*

Reaction	ΔH_r^\ddagger	ΔH_r	ΔG_r^\ddagger	ΔG_r	$\text{TS}_{\sigma\text{-con.}}$
15	26.22	-18.90	33.24	-11.49	26.93
16	26.14	-14.26	32.27	-7.43	26.08
17	28.56	-19.75	35.36	-11.92	27.72
18	25.07	-21.55	30.92	-14.48	27.19
19	25.32	-21.98	32.14	-13.73	27.48
20	22.19	-22.01	28.05	-14.59	27.02
21	30.10	-22.16	36.78	-14.20	28.23
22	27.31	-25.43	33.65	-17.62	27.84
23	27.36	-24.00	33.68	-15.72	27.95
24	24.62	-25.70	30.94	-17.45	27.63
25	27.16	-21.72	33.45	-14.20	27.36
26	25.43	-17.49	31.47	-10.45	27.06
27	26.18	-22.25	32.64	-14.43	27.39
28	28.16	-21.43	35.47	-13.00	27.84
29	23.94	-24.71	31.23	-16.21	27.88
30	25.87	-23.03	33.50	-13.80	28.12
31	25.72	-20.29	33.03	-11.66	28.16
32	24.68	-23.72	32.49	-14.72	28.40
33	23.62	-23.08	31.42	-13.51	28.55
34	22.93	-25.07	31.04	-15.22	29.00

The earliness of the transition state was explored *via* a Leffler equation which is provided in equation 4.3 [33]. This analysis shows that there should be a linear relationship between the overall Gibbs free energy and subsequent barrier, and as such a plot of ΔG_r^\ddagger *vs.* ΔG_r should provide α as the gradient of the slope. In this case α represents the similarity coefficient and is employed as a measure of the likeness between the transition state and the product compared with the initial substrate.

$$\Delta G_r^\ddagger = \alpha \Delta G_r \quad (4.3)$$

To explore this relationship, and for all analysis which follows, we split the IMD-A reactions into 2 different subsets, aromatic dienes which was the case for

the substrates in the previous discussion and those involving an explicit carbonyl group in the diene or dienophile, due to the varying nature of these reactions. The latter is further divided into those which contain a carbonyl atom in the diene or the dienophile, however, we do include a comparison of the entire carbonyl set in addition to these separated sets.

As shown in Figure 4.8 we do not observe a strong linear relationship between the Gibbs energetics for any of the reaction sets. The linear correlation is represented by R^2 , with the larger the magnitude of this value representing a stronger correlation between the properties of the data set. If we consider the furan systems R^2 is noticeably higher than the sets involving the carbonyl component. However, this correlation is still relatively weak. The R^2 for the carbonyl systems is essentially independent of the specific set employed, ranging from 0.0130 and 0.0435. The correlation between ΔG_r and ΔG_r^\ddagger for these IMD-A systems is far lower than that obtained by Żurek *et al.* [2] in their original study. It should be noted that for most of the molecules of interest within this thesis the $\mathbf{TS}_{\sigma\text{-}con.}$ is larger, with the exception of the furan systems, than in the literature study thus indicating an earlier transition state due to the larger contraction. For the furan system, based upon this weak correlation, we find an α value of 0.7965 thus indicating transition states that are appreciably product like. For the carbonyl systems this α value drastically lowers and as such is highly reactant like, however, it is clear that no correlation exists between these properties.

We then proceed to observe if there pertains a linear relationship between $\mathbf{TS}_{\sigma\text{-}con.}$ with both ΔG_r and ΔG_{rD-A}^\ddagger , see Figure 4.9 and 4.10 respectively. Also included is $\mathbf{TS}_{\sigma\text{-}con.}$ *vs.* ΔG_r^\ddagger which is illustrated in Figure 4.11.

For the above relationships the only strong correlation observed is in regards to the unsaturated aldehyde subset, with an R^2 of 0.90, for $\mathbf{TS}_{\sigma\text{-}con.}$ *vs.* ΔG_{rD-A}^\ddagger . The correlation for this reaction set decreases to 0.53 and 0.27 for $\mathbf{TS}_{\sigma\text{-}con.}$ *vs.* ΔG_r and $\mathbf{TS}_{\sigma\text{-}con.}$ *vs.* ΔG_r^\ddagger respectively. If we compare this to reactions involving a carbonyl dienophile, reactions **25** to **34**, the correlations are much weaker with R^2 having values of 0.04, 0.16 and 0.07 when expressed in the same order as above. This also

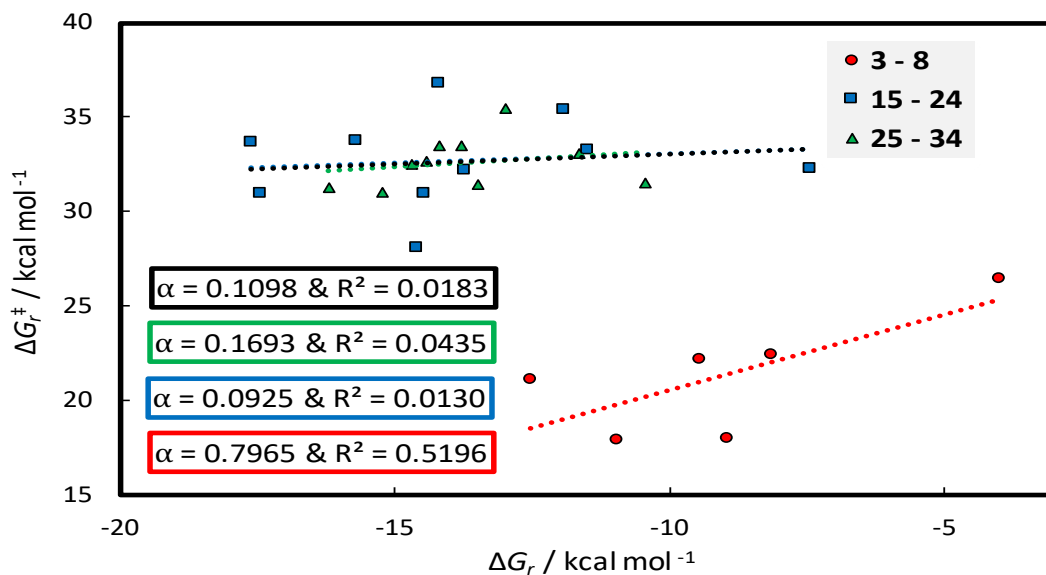


Figure 4.8: ΔG_r^\ddagger as a function of ΔG_r for various data sets of interest, with the inclusion of a linear best fit trendline for each data set. The black trend line represents the complete set of carbonyl containing dienes or dienophiles, with values reported computed at 383 K.

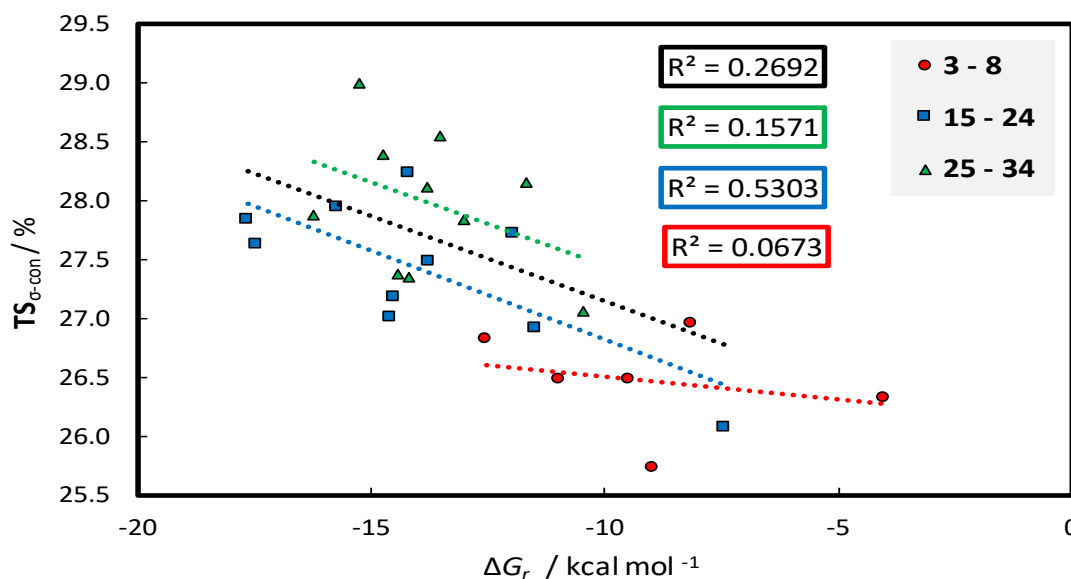


Figure 4.9: $\text{TS}_{\sigma\text{-con.}}$ as a function of ΔG_r for various data sets of interest, with the inclusion of a linear best fit trendline for each data set. The black trend line represents the complete set of carbonyl containing dienes or dienophiles, with values reported computed at 383 K.

highlights that the individual substrates are far less similar to each other than those involving a carbonyl diene cycloaddition. For the aromatic dienes we once again do not observe a strong correlation between any of the plotted data sets, only another weakly correlated data set, R^2 of 0.57, for $\text{TS}_{\sigma\text{-con.}}$ vs. ΔG_{rD-A}^\ddagger .

We further investigated the correlation, however, this time considering the σ

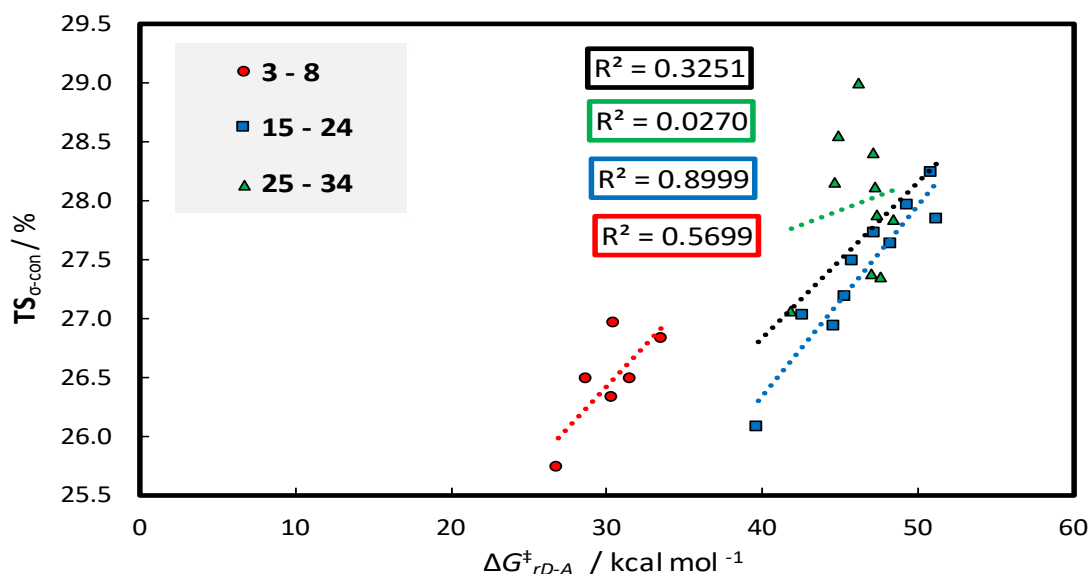


Figure 4.10: $\text{TS}_{\sigma\text{-con.}}$ as a function of $\Delta G_{rD-A}^{\ddagger}$ for various data sets of interest, with the inclusion of a linear best fit trendline for each data set. The black trend line represents the complete set of carbonyl containing dienes or dienophiles, with values reported computed at 383 K.

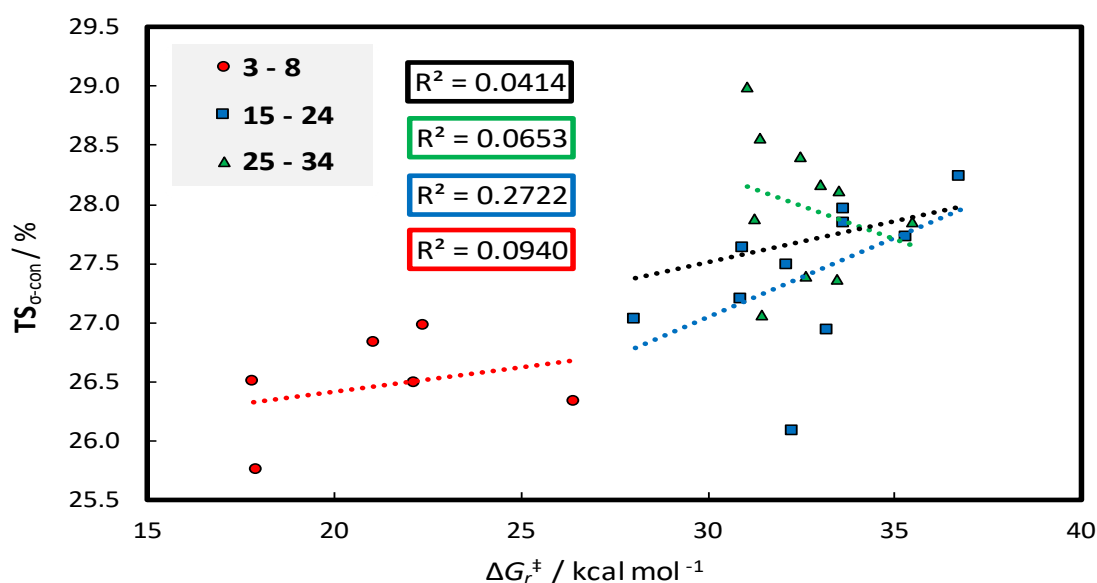


Figure 4.11: $\text{TS}_{\sigma\text{-con.}}$ as a function of ΔG_r^{\ddagger} for various data sets of interest, with the inclusion of a linear best fit trendline for each data set. The black trend line represents the complete set of carbonyl containing dienes or dienophiles, with values reported computed at 383 K.

bond between the carbon atoms and the σ bond between the carbon and oxygen atom in isolation. We do this solely for $\text{TS}_{\sigma\text{-con.}}$ vs. $\Delta G_{rD-A}^{\ddagger}$, see Figure 4.12 and 4.13 for data pertaining to carbon-oxygen and carbon-atoms distances respectively. The contraction of the carbon-oxygen distance is always larger than the corresponding carbon counterpart. However, we do not observe any strong correlations with R^2 of

reactions **15** to **24** for the combined set lowering dramatically upon this segregation of bond lengths.

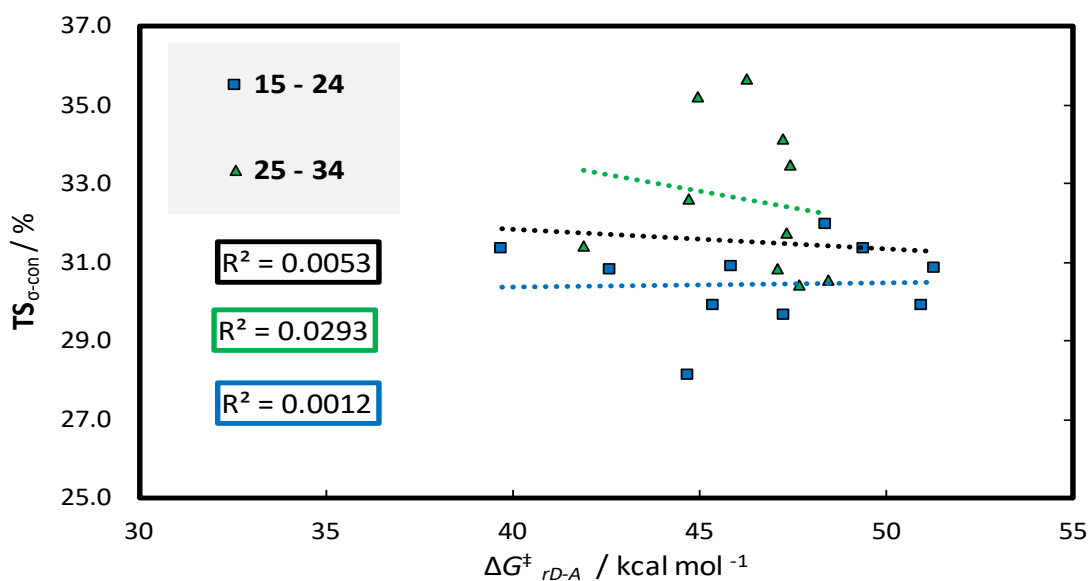


Figure 4.12: $\text{TS}_{\sigma\text{-con}}$ as a function of $\Delta G^{\ddagger}_{rD-A}$ for the carbon-oxygen distance only for the various data sets of interest, with the inclusion of a linear best fit trendline for each data set. The black trend line represents the complete set of carbonyl containing dienes or dienophiles, with values reported computed at 383 K.

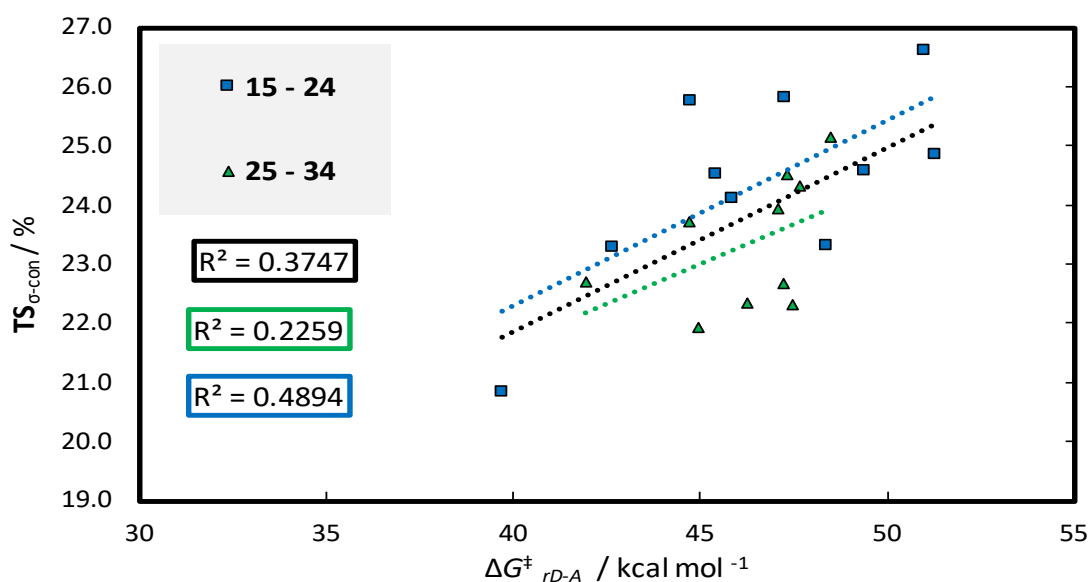


Figure 4.13: $\text{TS}_{\sigma\text{-con}}$ as a function of $\Delta G^{\ddagger}_{rD-A}$ for the carbon-carbon distance only for the various data sets of interest, with the inclusion of a linear best fit trendline for each data set. The black trend line represents the complete set of carbonyl containing dienes or dienophiles, with values reported computed at 383 K.

4.5 Conclusion

The effect of furan nitration and subsequent methylation of the dienophile was investigated using a high accuracy QM composite model, and compared to appropriate experimental data. For reactions **3** and **5** incorporating an electron withdrawing group into the diene was found to decrease reaction barriers and increase exothermicities contrary to simple chemical intuition. This was attributed to positive charge stabilisation of the nitro bearing carbon upon the transition from being sp^2 to sp^3 hybridised, thus in a more alkylated environment. For these reactions the electron demand completely reversed from a normal electron demand process to that of inverse in nature upon nitration. It was also found that there was greater asynchronicity between the bond forming σ carbon atoms in the nitrated systems which allowed dienophile substitution to be tolerated to a greater degree. However, the effect of nitration was not observed for the extremely polarity mismatched substrate, **10A**, with a normal electron demand process also being followed.

We then turned our attention to hetero IMD-A reactions to observe if a structure-energy correlation persisted in this class of materials, that was found to exist in other IMD-A systems. For the majority of carbonyl substrates we do not obtain a strong correlation between any properties. However, it was observed that for unsaturated aldehyde/alkene systems a strong correlation between $\mathbf{TS}_{\sigma-con.}$ and ΔG_{rD-A}^\ddagger existed. However, in order to explore this further we suspect a larger data set is required containing a variety of diene and dienophile substitutions for each cycloaddition.

4.6 References

- [1] T. Y. Cowie, M. Veguillas, R. L. Rae, M. Rougé, J. M. Żurek, A. W. Prentice, M. J. Paterson, M. W. P. Bebbington, *The Journal of Organic Chemistry* **2017**, *82*, 6656–6670.
- [2] J. M. Zurek, R. L. Rae, M. J. Paterson, M. W. P. Bebbington, *Molecules* **2014**, *19*, 15535–15545.
- [3] C. O. Kappe, S. S. Murphree, A. Padwa, *Tetrahedron* **1997**, *53*, 14179–14233.

- [4] W. Oppolzer, V. Snieckus, *Angewandte Chemie International Edition in English* **1978**, *17*, 476–486.
- [5] S. M. Lynch, S. K. Bur, A. Padwa, *Organic Letters* **2002**, *4*, 4643–4645.
- [6] P. Vogel, J. Cossy, J. Plumet, O. Arjona, *Tetrahedron* **1999**, *55*, 13521–13642.
- [7] G. Pohnert, W. Boland, *Tetrahedron* **1997**, *53*, 13681–13694.
- [8] J. E. Carpenter, C. P. Sosa, *Journal of Molecular Structure* **1994**, *311*, 325–330.
- [9] D. C. Spellmeyer, K. N. Houk, *Journal of the American Chemical Society* **1988**, *110*, 3412–3416.
- [10] O. Wiest, D. C. Montiel, K. N. Houk, *The Journal of Physical Chemistry A* **1997**, *101*, 8378–8388.
- [11] V. Guner, K. S. Khuong, A. G. Leach, P. S. Lee, M. D. Bartberger, K. N. Houk, *The Journal of Physical Chemistry A* **2003**, *107*, 11445–11459.
- [12] M. J. S. Dewar, C. Jie, *Accounts of Chemical Research* **1992**, *25*, 537–543.
- [13] J.-C. Lizardo-Huerta, B. Sirjean, P.-A. Glaude, R. Fournet, *Proceedings of the Combustion Institute* **2017**, *36*, 569–576.
- [14] A. B. Kacka, R. A. Jasinski, *Heteroatom Chemistry* **2016**, *27*, 279–289.
- [15] V. A. Guner, K. S. Khuong, K. N. Houk, A. Chuma, P. Pulay, *The Journal of Physical Chemistry A* **2004**, *108*, 2959–2965.
- [16] S. Grimme, C. Mueck-Lichtenfeld, E.-U. Wuerthwein, A. W. Ehlers, T. P. M. Goumans, K. Lammertsma, *The Journal of Physical Chemistry A* **2006**, *110*, 2583–2586.
- [17] D. H. Ess, A. E. Hayden, F.-G. Klaerner, K. N. Houk, *The Journal of Organic Chemistry* **2008**, *73*, 7586–7592.
- [18] K. S. Khuong, C. M. Beaudry, D. Trauner, K. N. Houk, *Journal of the American Chemical Society* **2005**, *127*, 3688–3689.
- [19] S. Kumar, V. Kumar, S. Singh in *Pericyclic Reactions*, (Eds.: S. Kumar, V. Kumar, S. Singh), Academic Press, **2016**, pp. 1–321.

- [20] A. Padwa, K. R. Crawford, C. S. Straub, S. N. Pieniazek, K. N. Houk, *The Journal of Organic Chemistry* **2006**, *71*, 5432–5439.
- [21] K. R. Crawford, S. K. Bur, C. S. Straub, A. Padwa, *Organic Letters* **2003**, *5*, 3337–3340.
- [22] S. N. Pieniazek, K. N. Houk, *Angewandte Chemie International Edition* **2006**, *45*, 1442–1445.
- [23] R. L. Rae, J. M. Zurek, M. J. Paterson, M. W. P. Bebbington, *Organic and Biomolecular Chemistry* **2013**, *11*, 7946–7952.
- [24] C.-H. Chen, P. D. Rao, C.-C. Liao, *Journal of the American Chemical Society* **1998**, *120*, 13254–13255.
- [25] S. M. Weinreb in *Comprehensive Organic Synthesis*, (Eds.: B. M. Trost, I. Fleming), Pergamon, Oxford, **1991**, pp. 401–449.
- [26] M. J. Frisch, G. W. Trucks, H. B. Schlegel, G. E. Scuseria, M. A. Robb, J. R. Cheeseman, G. Scalmani, V. Barone, G. A. Petersson, H. Nakatsuji, X. Li, M. Caricato, A. V. Marenich, J. Bloino, B. G. Janesko, R. Gomperts, B. Mennucci, H. P. Hratchian, J. V. Ortiz, A. F. Izmaylov, J. L. Sonnenberg, D. Williams-Young, F. Ding, F. Lipparini, F. Egidi, J. Goings, B. Peng, A. Petrone, T. Henderson, D. Ranasinghe, V. G. Zakrzewski, J. Gao, N. Rega, G. Zheng, W. Liang, M. Hada, M. Ehara, K. Toyota, R. Fukuda, J. Hasegawa, M. Ishida, T. Nakajima, Y. Honda, O. Kitao, H. Nakai, T. Vreven, K. Throssell, J. A. Montgomery, Jr., J. E. Peralta, F. Ogliaro, M. J. Bearpark, J. J. Heyd, E. N. Brothers, K. N. Kudin, V. N. Staroverov, T. A. Keith, R. Kobayashi, J. Normand, K. Raghavachari, A. P. Rendell, J. C. Burant, S. S. Iyengar, J. Tomasi, M. Cossi, J. M. Millam, M. Klene, C. Adamo, R. Cammi, J. W. Ochterski, R. L. Martin, K. Morokuma, O. Farkas, J. B. Foresman, D. J. Fox, *Gaussian 09 Revision D.01 and Gaussian 16 Revision A.03*, Gaussian Inc. Wallingford CT, **2016**.
- [27] P. Hohenberg, W. Kohn, *Physical Review* **1964**, *136*, B864–B871.
- [28] W. Kohn, L. J. Sham, *Physical Review* **1965**, *140*, A1133–A1138.

- [29] P. J. Stephens, F. J. Devlin, C. F. Chabalowski, M. J. Frisch, *The Journal of Physical Chemistry* **1994**, *98*, 11623–11627.
- [30] J. A. Montgomery, M. J. Frisch, J. W. Ochterski, G. A. Petersson, *The Journal of Chemical Physics* **2000**, *112*, 6532–6542.
- [31] J. W. Ochterski, G. A. Petersson, J. A. Montgomery, *The Journal of Chemical Physics* **1996**, *104*, 2598–2619.
- [32] F. Jensen, *Introduction to Computational Chemistry*, John Wiley & Sons Ltd., West Sussex, England, **1999**.
- [33] A. Williams, *Free Energy Relationships in Organic and Bio-Organic Chemistry*, The Royal Society of Chemistry, **2003**, pp. X001–X004.

Chapter 5

Ionisation Potential of Organic π -Conjugated Materials: A Comparison Between Experiment and Theory

5.1 Abstract

In this chapter we utilise Kohn-Sham density functional theory to investigate the vertical ionisation potential of various π -conjugated systems that are of interest within the field of organic optoelectronics. The work presented herein was performed in collaboration with Professor Ian Galbraith, of Heriot-Watt University, the experimental organic semiconductor optoelectronic group, of the University of St Andrews consisting of Susanna Challinger, Professor Ifor Samuel and Professor Graham Turnbull, and Professor Ian Baikie of KP Technology Ltd. Initially the exchange-correlation functional, basis set and external environment was benchmarked against recent experimental findings for which MN15/6-31G(d) in conjunction with an implicit solvent model provides the best combination in terms of accuracy and computational expense. We observe good agreement between experiment and the simple single molecular computations, within 100 meV of the experimental uncertainty range, for all known amorphous materials with larger deviations when there is a degree of ordering within the thin-film environment, which is the case for P3HT and PTB7. To investigate the effect of ordering on the IP for these systems we explore a simple π -stacked system, enclosed once again in an implicit solvent. This ordering was found to profoundly lower the IP pertaining to P3HT, now with a deviation to the upper experimental limit of 30 meV. We also extend this single molecular comparison to the optical gap each material.

5.2 Introduction

There has been a recent surge of interest in photovoltaic devices, and optoelectronic devices in general, employing organic π -conjugated systems as the active materials [1–4] deviating from conventional silicon based models. These organic systems exude numerous benefits over their inorganic counterparts such as lower device fabrication costs, as they are based on the most abundant chemical elements on earth and are not subjected to high temperatures hereby increasing the scope of potential substrates as no longer a need for thermal robustness, and also effective light absorbing agents therefore requiring less active material. Despite having numerous advantages we are yet to observe power conversion efficiencies (PCEs) that exceed silicon based systems, with significantly less known about their charge generation and transport mechanism. In 1975 the largest observed PCE was 0.001 % increasing to 5.5 % over the following 30 years [5]. This limit currently resides around 9 % based on recent studies [6, 7]. These organic solar cells (OSCs) consist of a bulk-heterojunction (BHJ) layer which is composed of an electron donor (D) material, normally a π -conjugated organic polymer or small molecule, and that of electron accepting (A) properties, which usually takes the form of a fullerene derivative. The most widely studied BHJ is a D-A blend of poly-3-hexylthiophene (P3HT) and 6,6-phenyl-C61-butyric acid methyl ester (PC₆₁BM) with observed PCEs of 4 to 5 % [6, 8]. Other donor materials such as MEH-PPV and PTB7 homopolymers are widely studied, with various copolymers such as fluorene-benzothiadiazole and fluorene-PFB also having significant interest in OSCs [9] (see Figure 5.6 for the chemical structures of such polymers).

The optoelectronic properties of organic systems are inherently tied to the conjugated backbone of the material. The overlap of p orbitals from adjacent sp^2 hybridised carbon atoms, or various heteroatoms such as oxygen, nitrogen and sulphur, generates a delocalised π system over the entire backbone determining the nature of the highest occupied and lowest unoccupied molecular orbital, HOMO and LUMO, respectively. The subsequent overlap of these frontier molecular orbitals (FMOs) between neighbouring organic small molecules or polymers influences

the intermolecular transfer integrals which relates to the charge mobility of the material [10]. In crystalline inorganic materials mobilities are on the order of 10^2 to 10^3 $\text{cm}^2 \text{V}^{-1} \text{s}^{-1}$ in comparison to organic systems which are found to be lower at > 1 $\text{cm}^2 \text{V}^{-1} \text{s}^{-1}$. For amorphous, highly disordered, organic materials this substantially lowers to between 10^{-6} and 10^{-3} $\text{cm}^2 \text{V}^{-1} \text{s}^{-1}$ [11].

The mechanism within an OSC begins with photon absorption by the donor material, for which the photon must have an energy larger than the optical gap (Δ_0) for this electronic excitation to take place. The generation of free-charge carriers within an organic regime involves the dissociation of a strongly bound electron-hole pair, termed an exciton, on the electron donor *via* electron-transfer from D to A at an appropriate interface. However, this process is not sharply defined and can also occur through an exciton energy-transfer from D to A and subsequent hole-transfer from A back to D, with both processes resulting in the formation of the same final state (see Figure 5.1) [10]. This process is not as complicated for inorganic systems as the coulomb interaction between the hole and electron, corresponding to the exciton binding energy, is far weaker and can spontaneously dissociate at thermal energies around room temperature.

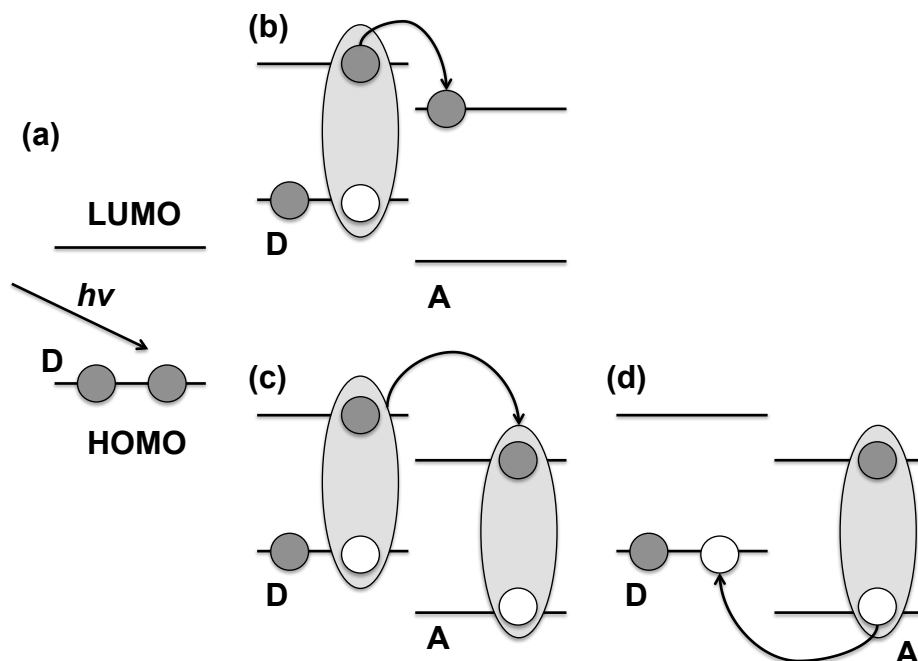


Figure 5.1: *Generation and dissociation of an exciton in organic π -conjugated materials. (a) photon absorption with energy larger than the optical gap, (b) exciton dissociation by electron-transfer from D to A, (c) energy-transfer process from D to A and (d) hole-transfer from A to D. Adapted from [5].*

These free-charges would then hop from adjacent molecules until they reach the relevant terminal electrodes thus generating a current. Optimisation of each step within this charge generation procedure is required to reach optimal device performance as various factors such as exciton recombination, due to the location of an interface outwith the maximum excitonic diffusion length which is usually 5 to 10 nm with a layer thickness of 100 to 200 nm required for sufficient light absorption, and the individual morphologies of D and A materials, to ensure sufficient charge carrier movement, may hinder this charge generation process [12].

If we solely consider the electron-transfer approach, as outlined in Figure 5.1(b), to bring about exciton dissociation at the D-A interface the LUMO energy of A must be offset, with respect to the LUMO on D, by an energy corresponding to at least the exciton binding energy. The typical binding energy for singlet excitons is normally between 0.3–0.5 eV, increasing for triplet species as a result of the exchange interaction between the individual charged entities [12]. This has been shown in terms of an energy level diagram in Figure 5.2. The optical gap of each material has been shown in black, where this represents the minimum energy required to generate a bound exciton. The fundamental gap between the two materials is highlighted in red, the energy difference between the HOMO of D and LUMO of A, and is proportional to the maximum voltage that may be supplied by the device. The overall efficiency of the device is a combination of this cross-linked band gap and the offset of corresponding energy levels, provided that the donor optical gap is < 3 eV [8] to overlap sufficiently with the visible region of the solar spectrum.

As these organic π -conjugated materials have extremely complex morphologies, unlike the highly ordered inorganic materials, one must initially explore the aforementioned properties on a molecular level to have any real chance of understanding the interplay between successive molecules in the thin-film bulk material, and thus optimise device performance. In this study we solely focus on a range of electron donors (see Figure 5.6) that are either of current or potential use in OSCs. As expressed earlier in Subsection 2.3.2 within Hartree-Fock theory the HOMO energy level can be equated to the minimum amount of energy required to remove an elec-

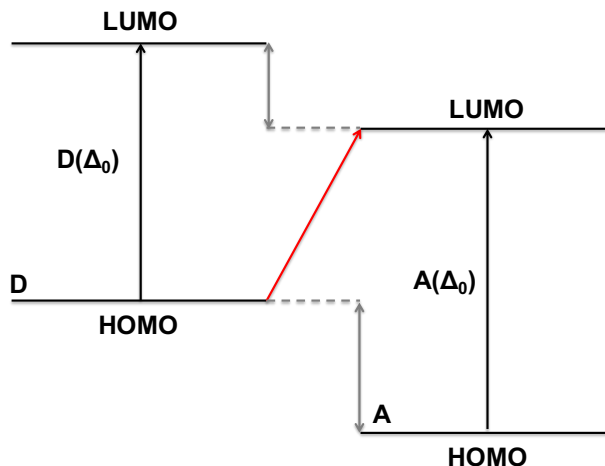


Figure 5.2: *FMOs and associated transitions pertaining to organic materials. Adapted from [8].*

tron from the system, ionisation potential (IP), with the same holding true for the LUMO, however, this time pertaining to the electron affinity (EA) of the system. This allows one to express the maximum afforded voltage as the difference between the IP(D) and EA(A) [10].

Herein we draw comparison between current state of the art photoelectron spectroscopy and that attained *via* a computational based treatment. This tandem approach allows one to investigate the relationship between molecular conformations, of a finite oligomer length, and the exuded ionisation potential as reliable and accurate determination of this quantity is crucial to further our understanding of donor materials. As the thin-films contain oligomers with a length that equates to the polymer limit we can then investigate to which degree these relatively straightforward computations model the complex environment exhibited in the organic film.

At this moment in time the gold standard of computational techniques is coupled cluster theory containing explicit single and double corrections, with triples estimated by a perturbative approach, CCSD(T). This post-HF method has been outlined earlier in Subsection 2.6.4. A study by Krause *et al.* [13] has used this approach to benchmark the vertical IP for various small molecules and atoms, in conjunction with a polarised triple- ζ basis (def 2-TZVPP). The work by Richard *et al.* [14] also used CCSD(T) to compute IPs and EAs of small organic systems, containing fewer than 20 heavy atoms, that are also of interest in organic optoelec-

tronics. An extrapolation to the complete basis set limit, for the convergent basis set series aug-cc-pVXZ where $X = D, T, \dots$, was also implemented due to the finite representation of each MO within the basis.

However, these aforementioned methods can only be readily applied to the smallest of chemical systems due to the inherent unfavourable scaling of M^7 , where M represents the number of basis functions. For this approach doubling the basis functions would result in a theoretical calculation time of $\times 128$ that of the reduced basis function computation. These already time consuming methods would then be computationally unfeasible for the lengths of oligomers considered herein. Therefore, in order to investigate oligomers of appreciable length, whilst still maintaining a sufficient level of accuracy, one may use Kohn-Sham (KS) density functional theory (DFT) [15, 16]. This method formally scales as M^4 and can be readily applied in the determination of ionisation potentials.

The ionisation potential can be approximated in two fairly simple regimes from DFT calculations. The first is a difference in energies between the N and $(N - 1)$ -electron systems, where N represents the number of electrons in the systems. If both share the same geometry this is referred to as a vertical process, and adiabatic, if both have been fully optimised for their respective charges. The second is a DFT alternative to the Hartree-Fock Koopmans' theorem based approach relating the IP to the negative energy of the HOMO eigenvalue. In conjunction with the frozen orbital approximation the physical nature of the KS orbitals have also been questioned, and thus the validity of representing such quantities, as these orbitals were initially introduced to represent the electron density of a fictitious set of non-interacting electrons. A 2007 study by Zhang *et al.* [17] explored this orbital based approach for a range of small molecules, employing a range of different exchange-correlation functionals ($E_{xc}[\rho]$). However, all were found to deviate by ≥ 0.7 eV, with some deviating by up to 4 eV.

Within this study we explore both approaches as approximations to the IP and compare with recent experimental findings. The ultimate aim is to keep the computational protocol as cheap as possible to allow investigation of oligomers with a

considerable length, whilst still providing comparable results to the experimental study. We also extend this comparison to the optical gap of the material.

5.3 Photoemission Spectroscopy

We now briefly explore the underlying principles of an experimental technique which allows determination of the IP of a chemical system, photoemission spectroscopy (PS). This technique is based upon the photoelectric effect proposed by Einstein in 1905, which was one of the initial driving forces in the development of quantum mechanics. Upon photoexcitation of the material through photon absorption, which is governed by the incident light frequency (ν_i), a photoelectron is ejected with a maximum kinetic energy (K_{max}) given by:

$$K_{max} = h\nu_i - \Phi = h(\nu_i - \nu_0) \quad (5.1)$$

where Φ is the material’s work function and equals the minimum energy required to remove an electron, and is therefore proportional to the threshold frequency (ν_0). For the photoelectric effect to occur $\nu_i > \nu_0$, with the increasing difference corresponding to an increase in the electron’s kinetic energy. Therefore, analysis of the photoelectron’s kinetic energy distribution will thus allow one to infer detail pertaining to the energy levels of the ionised system [18]. The photon energy used to induce the photoelectric effect is commonly in the ultraviolet region of the electromagnetic spectrum, ranging from ~ 3 to 20 eV. The electron analyser and detector will then capture the kinetic energy of each photoelectron, and the relative number of each sharing the same kinetic energy respectively.

5.4 Computational Details

All computations were performed using Gaussian 16 (Revision A.03) [19] both in a solvated environment, through inclusion of an implicit polarisable continuum model (PCM) [20, 21], employing the integral equation formalism (IEF) [22–24], and in

the gas-phase. All ground state geometries were fully optimised in their specific environment. For small oligomers the stationary points were characterised as minima as no imaginary eigenvalues were observed upon diagonalisation of the Hessian matrix. For larger oligomers we do not compute this vibrational analysis due to memory issues, however, these systems were built in a strategic approach from fully optimised minima structures. The optical gap was computed via time-dependent DFT (TD-DFT) [25] at the optimised ground state geometry.

5.5 Results and Discussion

5.5.1 Experimental Data

Before introducing any theoretical values we initially provide the experimental findings, both in terms of devised methodology and result interpretation. All experiments were performed by our external collaborators at the University of St. Andrews and KP Technology Ltd and thus only a brief overview will ensue.

All measurements were performed with the recently developed APSO4 system, a combination of ambient pressure PS and Kelvin probe microscopy, to predict the material's absolute Φ . A generic overview of the experimental setup is outlined in Figure 5.3.

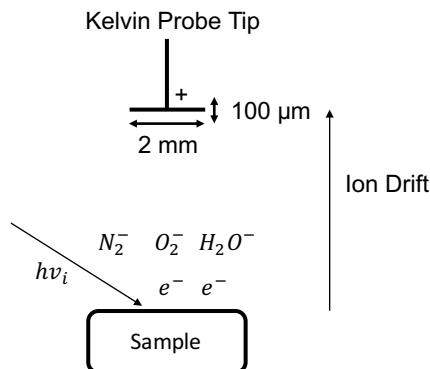


Figure 5.3: *Schematic of experimental setup. Ions generated by collisions of atmospheric molecules and photoelectrons drift to the vibrating 2 mm Kelvin probe tip.*

From a tunable UV light source the incident photon energy is scanned from 6.9 to 4.1 eV. The generated photoelectrons, subject to the frequency condition outlined in Section 5.3, then collide with atmospheric N_2 , O_2 and H_2O molecules subsequently

resulting in anion formation. Despite information of the electron's kinetic energy being lost due to inelastic scattering processes, with the aforementioned atmospheric particles, the overall charge is conserved. For each photon energy the positively charged kelvin probe detector, set at a bias of +10 V, measures the resulting ion current [26]. The more photoelectrons generated the stronger the current and *vice versa*, with no current observed if the incident frequency condition is not fulfilled. The photoelectron yield (*PEY*) for a specific photon energy, close to the ionisation threshold, is attained from the following:

$$PEY = A(h\nu_i - \Phi)^3 \quad (5.2)$$

where A is a constant for yield [27]. Therefore, from a Fowler's analysis based approach for semiconductors, plotting the cuberoot of the *PEY* as a function of photon energy, and extrapolating to the baseline gives Φ [28]. The experimental results for the polymers of interest are provided in Figure 5.4, for fluorene specific oligomer lengths were also studied, see Figure 5.5.

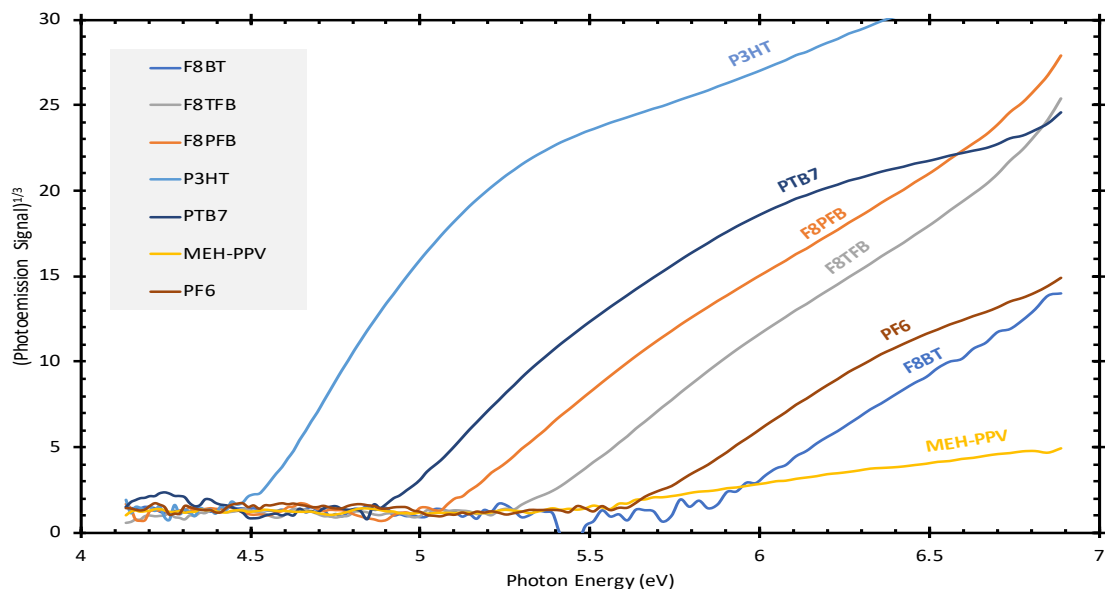


Figure 5.4: *Cube root of the photoelectron yield as a function of photon energy for the molecules of interest.*

As shown in Figure 5.4 and 5.5 all the π -conjugated materials of interest have a measured IP of between 4.5 to 5.9 eV, see Table 5.3 for a full comparison. All materials also show a linear response up to a photon energy of 500 meV past the

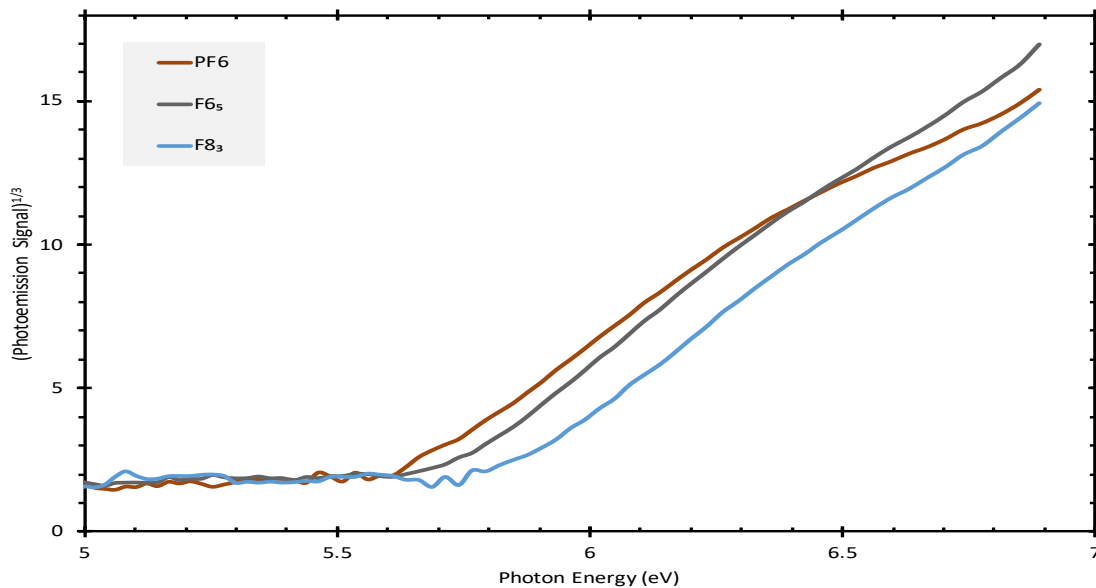


Figure 5.5: *Cube root of the photoelectron yield as a function of photon energy for a fluorene trimer and pentamer, the polymer has once again been included for comparison.*

photoemission threshold, with F8PFB, F8TFB, F8BT, MEH-PPV and the smaller fluorene oligomers showing a linear response over the entire range of photon energies considered. For PF6, P3HT and PTB7 as the photon energy increases the gradient of the slope decreases, this occurs at approximately 6.4, 5.2 and 5.5 eV respectively.

The absorption spectra, results of which are discussed in Subsection 5.5.5, were attained from a CARY 300 UV-Vis spectrometer for a wavelength range of 190 to 800 nm.

5.5.2 Initial DFT Benchmarking

As outlined previously ionisation potentials may be calculated from electronic structure methods with particular interest in electron density based approaches, KS-DFT, as this methodology can be applied to systems of far larger size than established post-HF methods. As outlined in Section 2.7, chemical properties determined from DFT are highly susceptible to the specific approximations used within $E_{xc}[\rho]$, and as such any study should commence with a suitable calibration.

Initially, a solvent-phase calibration was performed comparing both the vertical ionisation potential (E^{IP}) and a Koopmans' theorem (ϵ) based approach, albeit within the framework of DFT, to that of recent experimental findings. Herein, E^{IP}

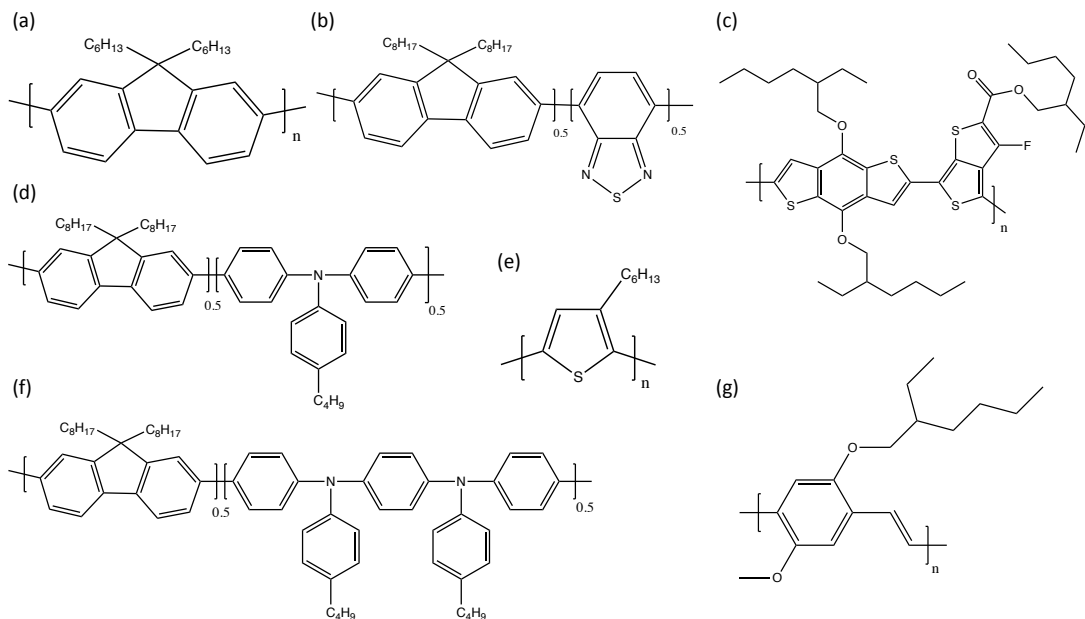


Figure 5.6: The molecules of interest within this study: (a) poly-F6 (PF6), (b) F8BT, (c) poly-TB7 (PTB7), (d) F8TFB, (e) poly-3HT (P3HT), (f) F8PFB and (g) MEH poly-PV (MEH-PPV).

is calculated by the energy difference between the mono-cation radical ($E^{\bullet+}$) and neutral state (E^0), with the nuclear framework of both pertaining to the optimised neutral arrangement.

The experimental results pertain to thin films in which oligomer lengths tend towards the polymer limit, with the exception of the smaller fluorene materials. However, in a computational sense this is impracticable and as such we must use oligomers of finite length denoted as n , for example a F6 dimer would be represented as F6₂. We therefore incorporate further degrees of freedom between direct comparison between theory and experiment due to the insufficient description of the molecule, however, we expect this to be of minimal importance as an oligomer length, for which the IP had shown convergence at were used.

The functionals tested were B3LYP [29, 30], CAM-B3LYP [31], MN15 [32] and PBEPBE [33, 34], in the first instance with the standard Pople 6-31G(d) one-electron basis set, on model systems of F6₇ and F8BT₅ (see Figure 5.7). The functionals were chosen as they utilise different approximations to the exchange-correlation functional, which are hybrid, range-separated hybrid, meta-hybrid and pure generalised gradient approximation (GGA) respectively. We neglect the use of double-hybrid

methods as we expect these to be too computationally demanding for the systems of interest herein. In both systems to reduce the computational expense we replace the alkyl chains with hydrogen atoms, as the addition of these groups are primarily for solubility purposes [35] and would be expected to have little effect on resulting electronic properties. The F8BT₅ oligomer was also fluorene capped at both ends. An implicit PCM solvent having a dielectric permittivity of ~ 3 was selected as this matched the experimental thin film closely.

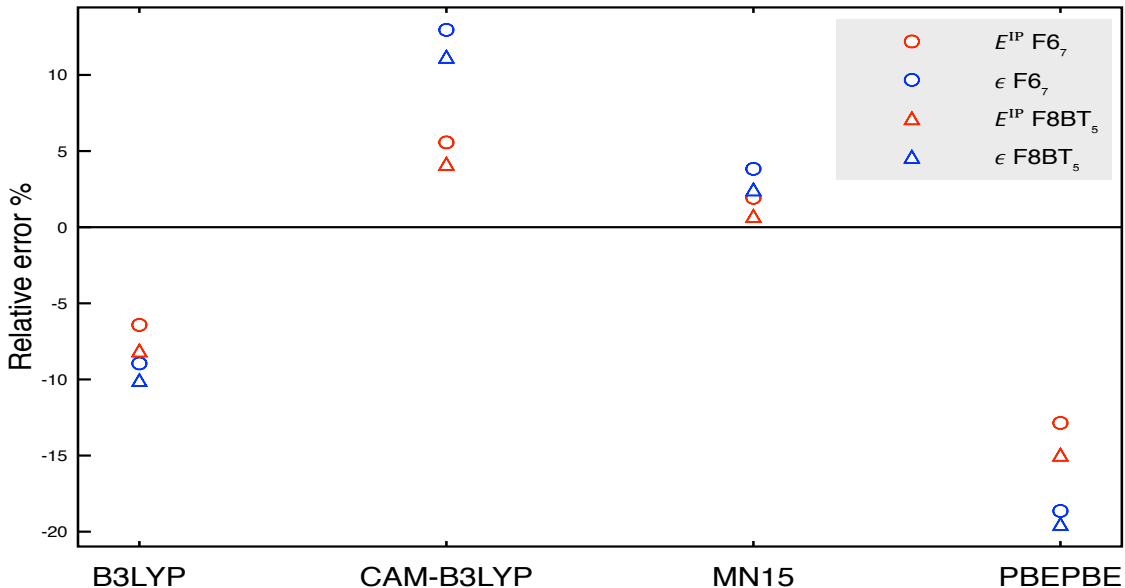


Figure 5.7: Percentage difference, with respect to experimental value, of E^{IP} and ϵ , as a function of $E_{xc}[\rho]$ for both F6₇ and F8BT₅. All values computed using 6-31G(d), with an implicit solvent model.

The experimental E^{IP} for PF6 and F8BT is found to be 5.64 ± 0.05 and 5.85 ± 0.05 eV, respectively. As highlighted in Figure 5.7, the best agreement for both F6₇ and F8BT₅ is with the MN15 functional. For E^{IP} the deviation of F6₇ and F8BT₅ is 1.9 % and 0.7 % corresponding to absolute errors of 0.109 and 0.043 eV respectively. The relative error of ϵ is higher with deviations of 3.8 % and 2.5%. All other functionals either under, B3LYP and PBEPBE, or overestimate, CAM-B3LYP, to a considerably larger extent. It should be noted that all functionals compliment the experimental trend for the ordering of E^{IP} , i.e. F8BT₅ > F6₇.

To further validate our theoretical approach we now compute E^{IP} in the gas-phase for MN15/6-31G(d). To clarify the distinction between solvated and gas-phase values we explicitly state GAS in the subscript otherwise pertaining to solvent

data. Upon removal of the implicit solvent model, we observe $E_{\text{GAS}}^{\text{IP}}$ that deviate to a significantly greater extent with experiment than their solvated counterparts. For F6₇ and F8BT₅ we now find relative errors of 10.1 and 7.3 % resulting in absolute deviations to experiment of 0.568 and 0.427 eV respectively. If we consider F6₇, the solvation energy of the neutral ground state is -0.363 eV, whereas the corresponding solvation energy of the mono-cation is -0.822 eV, highlighting the greater influence of the solvent on the charged system. Therefore, the difference in ionisation potentials between the two environments can be attributed to the additional stabilisation of the cation in the solvent environment. We find analogous results for F8BT₅ with a lower additional stabilisation of 0.384 eV. The ϵ values, however, differ to a far lesser extent due to the small geometrical deviation in the optimised neutral structures in the two environments. An overview of this brief comparison is given in Table 5.1.

Table 5.1: *Percentage difference, with respect to experimental value, of E^{IP} and ϵ , as a function of external molecular environment for both F6₇ and F8BT₅. All values computed using the MN15 functional employing a 6-31G(d) basis set.*

Molecule	E^{IP}	ϵ	$E_{\text{GAS}}^{\text{IP}}$	ϵ_{GAS}
F6 ₇	1.93	3.83	10.07	2.64
F8BT ₅	0.74	2.48	7.30	1.32

In order to further support the use of an implicit solvent model we now make a second comparison to published experimental $E_{\text{GAS}}^{\text{IP}}$ taken from the National Institute of Standards and Technology (NIST) for a range of simple π -conjugated systems. As can be seen from Table 5.2, we observe far better agreement between $E_{\text{GAS}}^{\text{IP}}$ and the literature values, compared to E^{IP} , when using MN15/6-31G(d). Clearly, one would expect this logical agreement as there would be no reason to include a continuum dielectric constant when comparing to the experimental findings. This comparison is merely to show that implementation of a solvating model considerably worsens the agreement between the ionisation potentials and the published gas-phase findings. These studies show the importance, and also give confidence in our methodology, of including a dielectric screening to approximate the environment in the organic thin-films. For benzene and 2,3'-bithiophene using the SMD implicit

solvent model [36] worsened the deviation between theory and experiment by 0.2 and 0.1 eV respectively, therefore we solely use the IEFPCM continuum model.

Table 5.2: *Comparison of ionisation potentials, including and excluding an implicit dielectric model, to that of experimental gas-phase measurements where ΔE represents the difference between theory and experiment. All values computed at MN15/6-31G(d) and in terms of eV.*

Molecule	$E_{\text{GAS}}^{\text{IP}}$	E^{IP}	Exp. $E_{\text{GAS}}^{\text{IP}}$	$\Delta E_{\text{GAS}}^{\text{IP}}$	ΔE^{IP}
thiophene [37]	9.27	7.27	8.85	0.42	-1.58
2,2'-bithiophene [38]	7.52	6.28	7.83	-0.31	-1.55
3,3'-bithiophene [38]	7.80	6.54	7.99	-0.19	-1.45
2,3'-bithiophene [38]	7.66	6.41	7.91	-0.25	-1.50
fluorene [39]	7.64	6.49	7.91	-0.27	-1.42
styrene [40]	8.18	6.85	8.46	-0.29	-1.62
benzene [41]	9.10	7.62	9.24	-0.14	-1.62

We now briefly explore the basis set influence on E^{IP} for F6₇ and F8BT₅. The following basis sets were used 6-31G(d), 6-31G(d,p), 6-31+G(d,p) and 6-311+G(d,p). Upon inclusion of p functions on all hydrogen atoms in a split valence double- ζ basis E^{IP} was found to differ by 2 and 1 meV for F6₇ and F8BT₅, respectively. We observe no apparent benefit from this inclusion, therefore, we omit 6-31G(d,p) from a computational efficiency viewpoint. For F6₇ the split valence double- ζ basis set with diffuse and polarisation functions considerably worsens the agreement to experiment, with an error of 5.7 %. This error is only increased when going to the split valence triple- ζ basis set. A similar finding is observed for 6-31+G(d,p) and 6-311+G(d,p) for F8BT₅ with errors of 4.4 and 5.5 %. This is not too surprising as the electronic density of the mono-cation should be more localised rendering these added basis functions somewhat redundant. For both systems ϵ behaves in an analogous fashion for the variation of basis sets. This has been outlined in Figure 5.8.

In summary, the relatively cheap, in computational terms, protocol of MN15/6-31G(d) including an implicit PCM potential has been found to accurately reproduce the measured ionisation potentials of both PF6 and F8BT, as we are within the experimental uncertainty limit for F8BT and only 59 meV from the upper uncertainty limit of PF6. We apply this model chemistry to the remaining π -conjugated systems

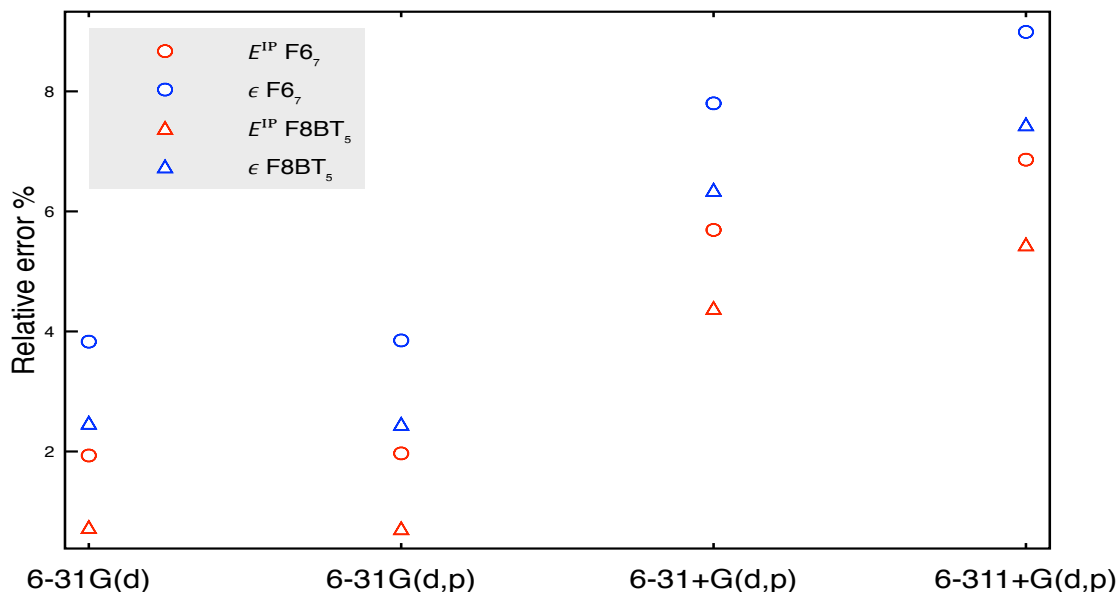


Figure 5.8: Percentage difference, with respect to experimental value, of E^{IP} and ϵ , as a function of basis set for both $F6_7$ and $F8BT_5$. All values computed using the MN15 functional, with an implicit solvent model.

of interest shown previously in Figure 5.6.

5.5.3 Material Comparison

For $F6_3$ the influence of hexyl chains on E^{IP} was briefly explored. The inclusion of hexyl chains was found to lower E^{IP} by 37 meV, thus having a small influence on electronic properties despite drastically increasing the number of basis functions as the polymer length becomes larger. The addition of each hexyl chain adds 108 basis functions when compared to a single hydrogen atom. Therefore for the material comparison we invoke this side chain adjustment in the computational chemical structure. In regards to P3HT we initially follow the same protocol by replacing the hexyl chains with a hydrogen atom. In all other copolymers the alkyl chains pertaining to the fluorene subunits were once again replaced with a hydrogen atom with all other alkyl chains truncated to that of a methyl group. For the remaining MEH-PPV system the alkyl chain was once again replaced with a methyl group, with the specific oligomer capped at the end with the appropriate phenyl group.

As can be seen in Table 5.3 we observe good agreement, within ~ 100 meV of the experiment uncertainty range, for the theoretically computed ionisation potentials with exception of P3HT and PTB7 systems, as respective deviations of 0.79 and 0.64

Table 5.3: Comparison between theory and experimentally determined E^{IP} for the systems of interest where $\Delta\epsilon$ is the difference between the Koopmans based approach and experiment. The theoretical Δ_0 has also been included. All values computed at MN15/6-31G(d) with implicit solvent and in terms of eV.

Molecule	n	Exp. E^{IP}	E^{IP}	ϵ	ΔE^{IP}	$\Delta\epsilon$	Δ_0
F8BT	5	5.85 ± 0.05	5.89	6.00	0.04	0.15	2.853
F8TFB	4	5.31 ± 0.05	5.40	5.52	0.09	0.21	3.396
F8PFB	3	5.08 ± 0.05	5.19	5.36	0.11	0.21	3.403
P3HT	10	4.51 ± 0.05	5.35	5.49	0.84	0.98	2.461
PTB7	6	4.92 ± 0.05	5.61	5.74	0.69	0.82	2.218
MEH-PPV	8	5.40 ± 0.10	5.59	5.71	0.19	0.31	2.745
PF6	8	5.64 ± 0.05	5.74	5.89	0.10	0.25	3.469

eV from the upper bound experimental limit were obtained. Once again ϵ values all deviate to a larger extent, validating the two-step approach used when determining E^{IP} . If we initially disregard P3HT and PTB7, the ordering of E^{IP} for the various materials compliments that of experiment: F8BT > PF6 > MEH-PPV > F8TFB > F8PFB. The aforementioned discrepancies, and possible solutions to this, will be explored in Subsection 5.5.6.

5.5.4 Ionisation Potential as a Function of F6 Oligomer Length

The influence of n on E^{IP} was then explored for F6, both experimentally $n = 3, 5$ and computationally $n = 1, 2, 3, 5, 7, 8$, as shown in Figure 5.9.

In terms of the theoretical E^{IP} we observe clear convergence to a value of ~ 5.744 eV as n increases, with E^{IP} varying by 5 meV upon changing from $n = 7$ to 8. The agreement between ionisation potentials is found to be better for smaller oligomer lengths, $n = 3$ and 5, as both fall within the experimental uncertainty range. As n tends towards the polymer limit we find a converged theoretical E^{IP} that lies above the true experimental value to a greater extent. However, this value only deviates with respect to the upper experimental error by 54 meV giving a rather good representation. Once again ϵ is found to further overestimate the ionisation potential when compared with the two-step approach.

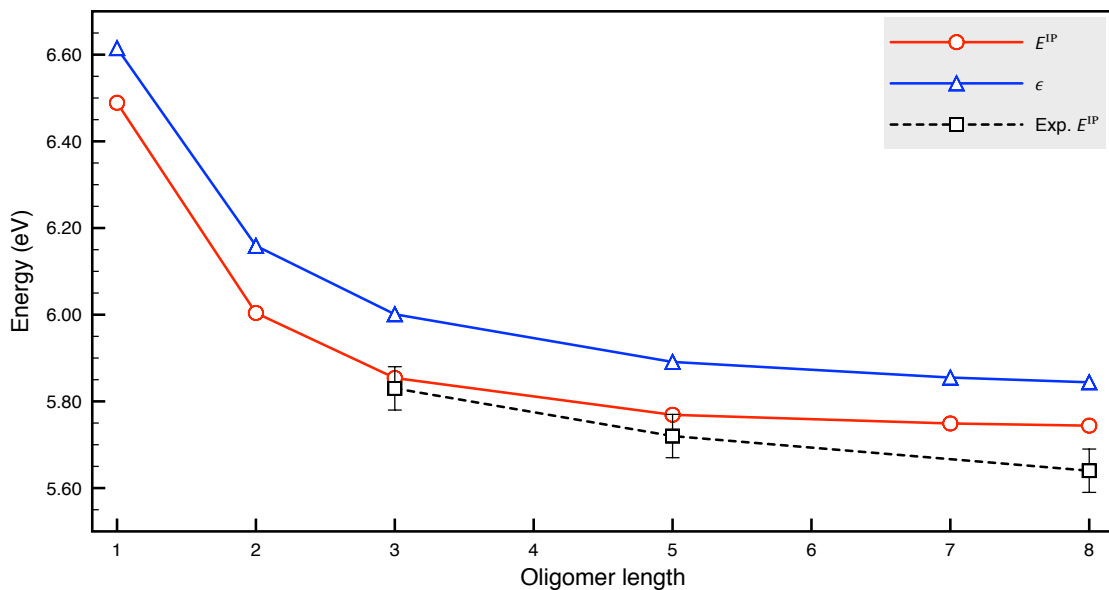


Figure 5.9: E^{IP} and ϵ as a function of F6 oligomer length. All theoretical values computed at MN15/6-31G(d) with implicit solvent. For the experimental data set we equate $n = 8$ to the polymer limit and include the relevant error bars of ± 0.05 eV.

5.5.5 Excited State Analysis

We now extend this cheap computational protocol to the determination of the optical gap of the π -conjugated materials. We acknowledge that the aforementioned functional may not be optimal, however, this serves solely as a corollary from the good agreement with the ground state properties and as such we wish to investigate how well this applies to the determination of excited states. As outlined in the Introduction the optical gap refers to the minimum energy to generate a bound exciton. To determine this quantity we use TD-DFT and equate this gap to the first transition with a non-zero oscillator strength. The results for the single molecule systems are provided earlier in Table 5.3, and an illustrative comparison between theory and experiment is provided in Figure 5.10. Once again we solely consider the vertical electronic transition due to the large discrepancy of the timescales of electron and nuclear motion. The addition of the implicit solvent within a vertical TD-DFT computation represents a non-equilibrated process. Within this approach only the electrostatic interactions between the solvent and solute are optimised. As the electron density changes upon photoexcitation this polarises the solvent, which in turn polarises the solute. The cavity shape in this case is constrained to that of

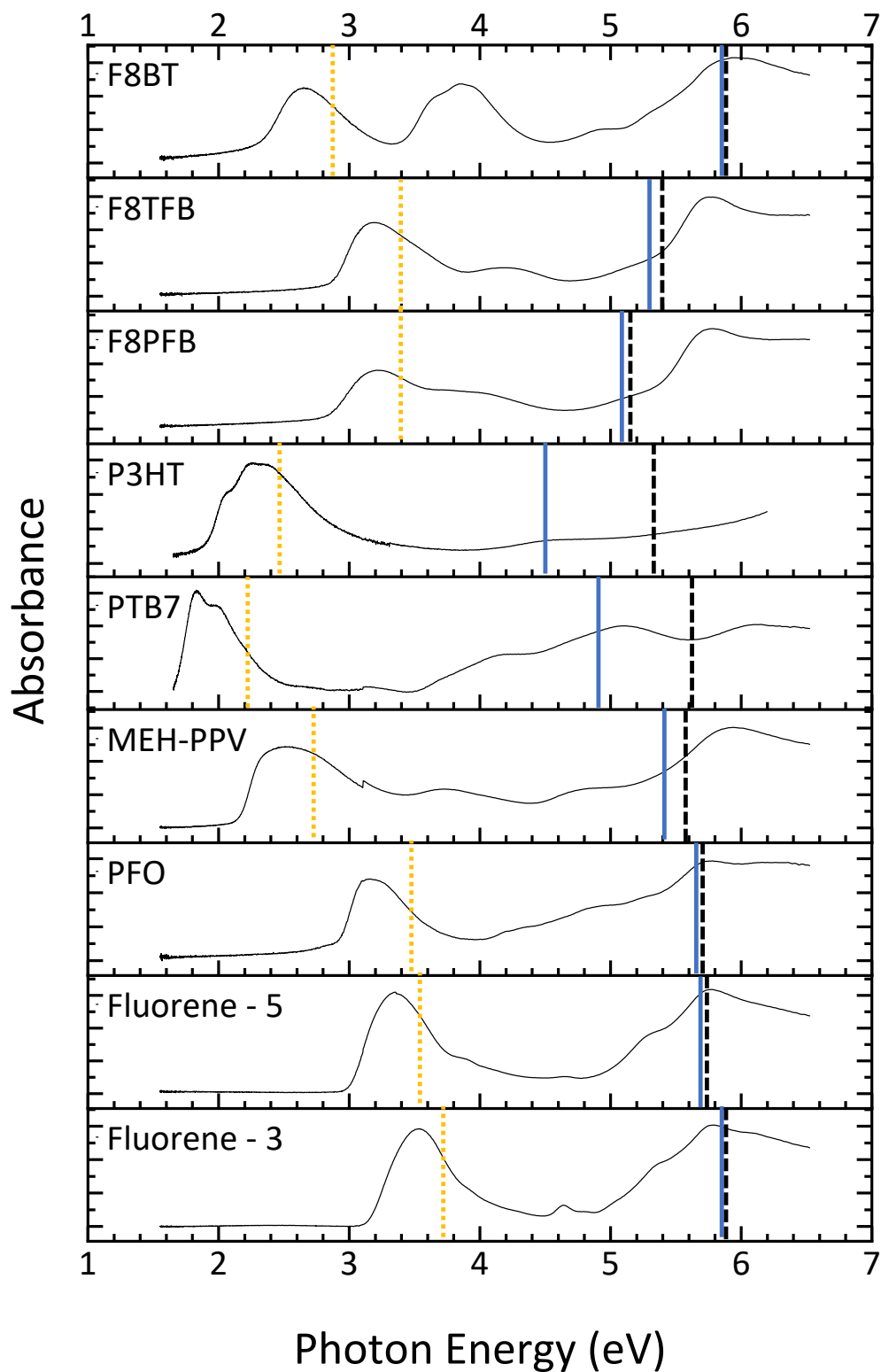


Figure 5.10: The experimental absorbance measurement for F8BT, F8TFB, F8PFB, P3HT, PTB7, MEH-PPV, PF6, F6₅ and F6₃. The E^{IP} obtained from theory and experiment are marked by the dashed black and solid blue line respectively. The theoretical Δ_0 is also included for comparison, dashed yellow line.

the optimal ground state.

From the experimental results all absorbance spectra show an increase at photon energies > 5 eV, as we tend towards the ionisation thresholds for most materials. For F6₃, F6₅, PF6 and F8BT the ionisation energy also corresponds to the maximum absorbance of the material. For F8PFB and F8TFB the maximum absorbance is located at larger energies than IP, in comparison to P3HT and PTB7 which have a maximum absorbance in the visible region of the electro-magnetic spectrum.

For all materials the theoretical optical gap, in all cases the $S_0 \rightarrow S_1$ transition energy, was located at larger values than that of experimental findings. This deviation between theory and experiment is around 0.2 to 0.5 eV for the range of materials considered. Once again for the materials the relative ordering of Δ_0 matches the experimental trend, despite no exchange-correlation functional benchmark for the excitation energies. It should also be noted that P3HT and PTB7 once again show the largest deviations when compared to experiment. If we solely consider the varying oligomer lengths of fluorene we observe a small decrease in Δ_0 as the length of the conjugated backbone increases, which is to be expected and would ultimately converge as the polymer length tends towards ∞ . The absorption profiles of F8TFB and F8PFB are also strikingly similar, both containing a maximum absorbance around 5.6 eV and a smaller absorbance peak at a lower photon energy of 3.2 eV. The theoretical Δ_0 are also practically the same for these materials at a value of 3.4 eV.

5.5.6 Crystalline Materials

We now revert our attention to the aforementioned anomalous P3HT and PTB7 cases. It has been shown that these materials exhibit some degree of ordering within the bulk environment [42–44], which would be likely to influence the resulting IP. This is consistent with the fact that we achieved lower deviations with isolated thiophene containing small molecules in the gas-phase as shown in Table 2. No intermolecular interactions arising from stacking is accounted for within the aforementioned calculations as these are based on entirely on single molecules of a

specific oligomer length. If we consider P3HT it has been shown that there is a clear IP/HOMO dependence based on the polymeric ordering, as 98 % semi-crystalline regioregular P3HT has an IP of 4.5 eV increasing by 0.3 eV when the same material has crystalline packing [42]. A study by Tsoi *et al.* [43] also observed a correlation between the experimental HOMO energy and the regioregularity of P3HT, as the regioregular arrangement forms a semi-crystalline arrangement and is found to have a lower HOMO energy than the regiorandom, amorphous structure.

As shown above we observe large discrepancies between the experimental and theoretical ionisation potentials for both P3HT and PTB7. The relative errors with respect to experiment are 18.5 and 14.1 %, corresponding to absolute errors of 0.835 and 0.692 eV. We initially explore P3HT due to the larger deviations despite being a relatively straightforward homopolymer. It should also be noted that PTB7 has always been a particularly challenging case to model with any degree of accuracy.

The first approach was to reestablish the alkyl side chains as previous calculations by Wildman *et al.* [45] have shown that the minimum dihedral angle for a thiophene dimer is highly sensitive to the inclusion and subsequent length of the side chain employed. This was attributed to the closeness of the alkyl side chain with the central dihedral creating a repulsive steric interaction between them, and thus influencing the equilibrium intermonomer dihedral. This steric interaction is not present in fluorene oligomers and as such the central intermonomer dihedral remains constant under variation of side chain substituents [45].

The E^{IP} as a function of oligomer length was computed for thiophene systems containing methyl (CH_3) or hexyl (C_6H_{13}) side chains, for comparison we also include the hydrogen (H) substituted system used in Subsection 5.5.3. The results of this are provided in Table 5.4.

For a dimer system the intermonomer dihedral (S-C-C-S) changes rather significantly from 15.6° to 24.0° and 27.3° when incorporating CH_3 and C_6H_{13} side chains, respectively. To note a dihedral of 0° would correspond to a trans-arrangement within the general polymer naming convention. The presence of side chains lowers E^{IP} by ~ 0.2 eV for the range of oligomers considered, with no noticeable

Table 5.4: E^{IP} as a function of thiophene oligomer length with the indicated side chains. All values computed at MN15/6-31G(d) with implicit solvent and in terms of eV.

n	Side Chain			Exp.
	H	CH ₃	C ₆ H ₁₃	
2	6.285	6.135	6.116	4.51 ± 0.05
4	5.648	5.447	5.427	
6	5.452	5.235	5.244	
10	5.345	5.188	5.163	

difference in regards to whether CH₃ or C₆H₁₃ side chains are used. Despite this inclusion we are still 0.653 eV from the experimental value, 0.603 eV from the upper uncertainty limit, even for $n = 10$. As a precaution the $E_{xc}[\rho]$ dependence on a 3HT₄ was explored for B3LYP and CAM-B3LYP. However, as expected the best agreement is still with MN15 as the aforementioned functionals differ with respect to experiment by 0.942 and 1.427 eV, respectively, with the equivalent MN15 system differing by 0.917 eV.

To investigate the effect of packing we initially model a system containing two tetramer units which are π -stacked along the molecular axis, essentially generating a parallel arrangement as outlined in Figure 5.11(a). However, it must be noted that rigorous modelling of the crystalline environment is out with the scope of this study, therefore we only proceed with a brief comparison to show the plausibility that ordering within the material could be responsible for the large discrepancies obtained.

For the time being the side chains have once again been replaced with a single hydrogen atom. As one would expect dispersion interactions between the oligomers to be of importance we attain the optimised geometry by means of B3LYP/6-31G(d) containing the GD3BJ empirical correction [46] as this functional performed more similarly to MN15. From this geometry subsequent energies were computed at MN15/6-31G(d). Within this approach E^{IP} was lowered to 5.314 eV from a single molecular system value of 5.648 eV. To note, the MN15 optimised system gave an E^{IP} of 5.352 eV thus highlighting the small difference in the geometries obtained from the different functionals. However to include dispersion in the optimisation

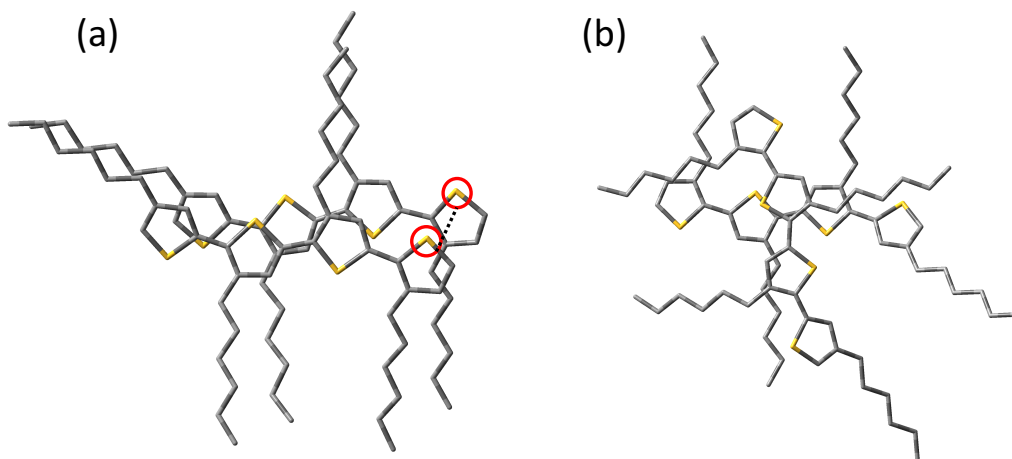


Figure 5.11: *Orientation of π -stacked systems with (a) representing the parallel and (b) perpendicular arrangement. All geometries obtained at B3LYP/6-31G(d) with GD3BJ empirical dispersion and within an implicit PCM environment. The red circles represents the coordinate varied within the scan.*

procedure we continue to use B3LYP to generate the relaxed geometry. Upon re-inclusion of C_6H_{13} side chains E^{IP} lowers to 5.118 eV. This shows the substantial lowering of E^{IP} when comparing the single and parallel π -stacked systems. The absolute lowering upon stacking for a thiophene tetramer is 0.334 and 0.309 eV for H and C_6H_{13} substituted systems respectively. We also explore another ordering orientation in which the single units are perpendicular to one another, illustrated in Figure 5.11(b). For the C_6H_{13} side chain system this arrangement gave an E^{IP} of 5.246 eV, 0.128 eV greater than the parallel arrangement.

Table 5.5: *E^{IP} as a function of the orientation of two π -stacked tetramer thiophene units containing C_6H_{13} side chains. All energy values computed at MN15/6-31G(d) with implicit solvent and in terms of eV, geometries obtained at B3LYP/6-31G(d) with GD3BJ empirical dispersion.*

Orientation	E^{IP}	ΔE^{IP}
Parallel	5.118	0.608
Perpendicular	5.258	0.736

To validate the optimised intermolecular separation for the parallel arrangement, taken to be the distance between the highlighted sulphur atoms as outlined in Figure 5.11, was varied from 3 to 4.5 Å in increments of 0.1 Å. As shown below in Figure 5.12 the lowest energy of E^0 and $E^{\bullet+}$ is obtained for an internuclear separation of

3.8 Å, providing an E^{IP} of 5.119 eV. This equates well to the optimised internuclear separation of 3.778 Å.

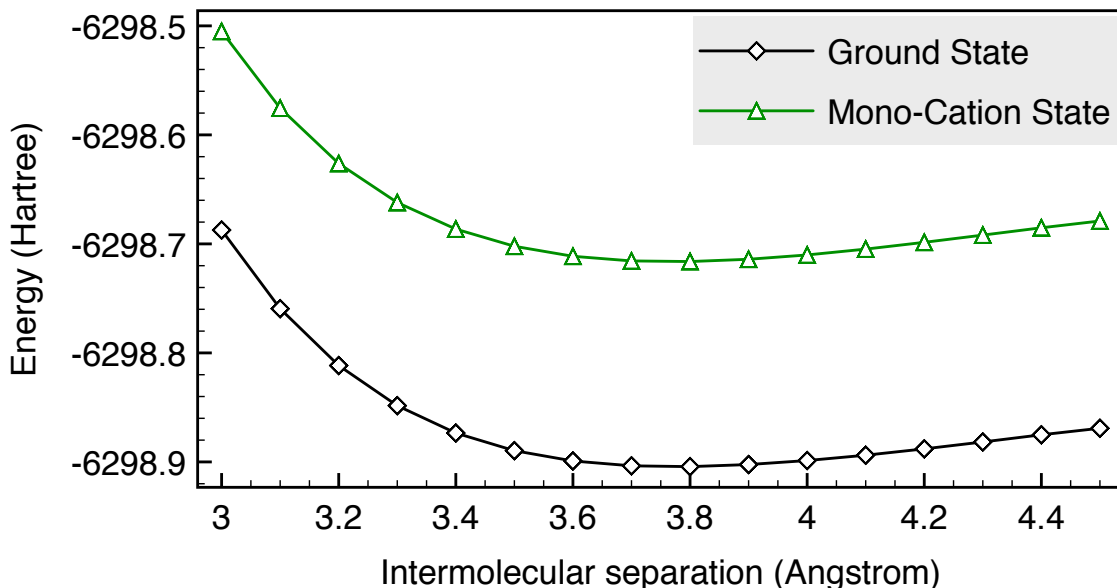


Figure 5.12: *Energy (Hartree) as a function of intermolecular separation (Å) for the parallel π -stacked $3HT_4$.*

As outlined in Table 5.5 we still obtain deviations > 0.6 eV with respect to the experimental value, despite the incorporation of a second interacting molecular unit. However, we are only dealing with small oligomer lengths for the stacked systems, $n = 4$, and as such would still expect E^{IP} to lower as n increases. For the associated single molecule thiophene approach, provided earlier in Table 5.4, the E^{IP} lowers by 0.264 eV when increasing the oligomer length from $n = 4$ to 10 for the hexyl side chain system.

For the π -stacked system we thus increase the length of the oligomer to $n = 10$ for the parallel arrangement only, as this nuclear framework was 0.555 eV lower in energy and provided the lowest E^{IP} when compared to the perpendicular arrangement. As the side chain effect is essentially the same for CH_3 and C_6H_{13} , < 20 meV for the range of thiophene oligomers tested, we implement the former from a purely computational viewpoint as the 20 hexyl groups would drastically increase the computational cost for this size of system. For this set-up E^{IP} lowered to 4.589 eV, providing a value close to the experimental finding of 4.51 ± 0.05 eV.

The effect of stacking was also investigated for the TB7_3 system. The single molecule E^{IP} for TB7_3 was found to be 5.632 eV. However the incorporation of a

second unit only lowers the E^{IP} by 0.122 and 0.146 eV for the parallel and perpendicular arrangement respectively. This lowering is far less significant than observed previously for the 3HT systems. This highlights the complexity within PTB7 to model the thin-film with any real accuracy and thus more sophisticated models must be undertaken.

5.6 Conclusion

The ionisation potential obtained from a computationally cheap protocol was compared to recent experimental findings. This protocol involved modelling a single molecular unit encompassed in a polarisable continuum, matching the dielectric of the thin-film. This simplified comparison between theory and experiment provided a good agreement for all materials known to be amorphous in the thin-film, within 100 meV from the upper experimental limit. However, if molecular ordering is prevalent in the thin-film there was found to be a large discrepancy between the two methods as was the case with P3HT and PTB7. We briefly explored the effect of ordering on the ionisation potential for P3HT, by which the incorporation of an interacting second molecular unit gave an ionisation potential that was extremely close to that of experimental. The PTB7 system was found to be more challenging and despite the inclusion of the second molecule deviations upwards of 0.5 eV still persist. The optical gap was also determined based on the single molecule model, for which the relevant ordering of this transition was found to be in good agreement with experiment.

5.7 References

- [1] X. Guo, M. Baumgarten, K. Müllen, *Progress in Polymer Science* **2013**, *38*, Topical issue on Conductive Polymers, 1832–1908.
- [2] G. Luo, X. Ren, S. Zhang, H. Wu, W. C. H. Choy, Z. He, Y. Cao, *Small* **2016**, *12*, 1547–1571.

- [3] C. Dyer-Smith, J. Nelson in *Practical Handbook of Photovoltaics (Second Edition)*, (Eds.: A. McEvoy, T. Markvart, L. Castañer), Academic Press, Boston, **2012**, pp. 543–569.
- [4] N. Tessler in *Encyclopedia of Materials: Science and Technology*, (Eds.: K. J. Buschow, R. W. Cahn, M. C. Flemings, B. Ilshner, E. J. Kramer, S. Mahajan, P. Veyssi re), Elsevier, Oxford, **2001**, pp. 4486–4490.
- [5] C. Solanki, *Solar Photovoltaics: Fundamentals, Technologies And Applications*, PHI Learning, **2015**.
- [6] S.-H. Liao, H.-J. Jhuo, Y.-S. Cheng, S.-A. Chen, *Advanced Materials* **2013**, *25*, 4766–4771.
- [7] C. Liu, C. Yi, K. Wang, Y. Yang, R. S. Bhatta, M. Tsige, S. Xiao, X. Gong, *ACS Applied Materials & Interfaces* **2015**, *7*, 4928–4935.
- [8] G. Dennler, M. C. Scharber, C. J. Brabec, *Advanced Materials* **2009**, *21*, 1323–1338.
- [9] A. Facchetti, *Materials Today* **2013**, *16*, 123–132.
- [10] B. Kippelen, J.-L. Br das, *Energy & Environmental Science* **2009**, *2*, 251–261.
- [11] V. Coropceanu, J. Cornil, D. A. da Silva Filho, Y. Olivier, R. Silbey, J.-L. Br das, *Chemical Reviews* **2007**, *107*, 926–952.
- [12] O. V. Mikhnenko, P. W. M. Blom, T.-Q. Nguyen, *Energy & Environmental Science* **2015**, *8*, 1867–1888.
- [13] K. Krause, M. E. Harding, W. Klopper, *Molecular Physics* **2015**, *113*, 1952–1960.
- [14] R. M. Richard, M. S. Marshall, O. Dolgounitcheva, J. V. Ortiz, J.-L. Br das, N. Marom, C. D. Sherrill, *Journal of Chemical Theory and Computation* **2016**, *12*, 595–604.
- [15] P. Hohenberg, W. Kohn, *Physical Review* **1964**, *136*, B864–B871.
- [16] W. Kohn, L. J. Sham, *Physical Review* **1965**, *140*, A1133–A1138.

- [17] G. Zhang, C. B. Musgrave, *The Journal of Physical Chemistry A* **2007**, *111*, 1554–1561.
- [18] J. Holmes in *Encyclopedia of Spectroscopy and Spectrometry*, (Ed.: J. C. Lindon), Elsevier, Oxford, **1999**, p. 1831.
- [19] M. J. Frisch, G. W. Trucks, H. B. Schlegel, G. E. Scuseria, M. A. Robb, J. R. Cheeseman, G. Scalmani, V. Barone, G. A. Petersson, H. Nakatsuji, X. Li, M. Caricato, A. V. Marenich, J. Bloino, B. G. Janesko, R. Gomperts, B. Mennucci, H. P. Hratchian, J. V. Ortiz, A. F. Izmaylov, J. L. Sonnenberg, D. Williams-Young, F. Ding, F. Lipparini, F. Egidi, J. Goings, B. Peng, A. Petrone, T. Henderson, D. Ranasinghe, V. G. Zakrzewski, J. Gao, N. Rega, G. Zheng, W. Liang, M. Hada, M. Ehara, K. Toyota, R. Fukuda, J. Hasegawa, M. Ishida, T. Nakajima, Y. Honda, O. Kitao, H. Nakai, T. Vreven, K. Throssell, J. A. Montgomery, Jr., J. E. Peralta, F. Ogliaro, M. J. Bearpark, J. J. Heyd, E. N. Brothers, K. N. Kudin, V. N. Staroverov, T. A. Keith, R. Kobayashi, J. Normand, K. Raghavachari, A. P. Rendell, J. C. Burant, S. S. Iyengar, J. Tomasi, M. Cossi, J. M. Millam, M. Klene, C. Adamo, R. Cammi, J. W. Ochterski, R. L. Martin, K. Morokuma, O. Farkas, J. B. Foresman, D. J. Fox, *Gaussian 16 Revision A.03*, Gaussian Inc. Wallingford CT, **2016**.
- [20] S. Miertus, E. Scrocco, J. Tomasi, *Chemical Physics* **1981**, *55*, 117–129.
- [21] R. Cammi, J. Tomasi, *Journal of Computational Chemistry* **1995**, *16*, 1449–1458.
- [22] E. Cancès, B. Mennucci, *Journal of Mathematical Chemistry* **1998**, *23*, 309–326.
- [23] E. Cancès, B. Mennucci, J. Tomasi, *The Journal of Chemical Physics* **1997**, *107*, 3032–3041.
- [24] B. Mennucci, E. Cancès, J. Tomasi, *The Journal of Physical Chemistry B* **1997**, *101*, 10506–10517.
- [25] E. Runge, E. K. U. Gross, *Physical Review Letters* **1984**, *52*, 997–1000.

- [26] I. D. Baikie, A. C. Grain, J. Sutherland, J. Law, *Applied Surface Science* **2014**, *323*, 45–53.
- [27] J. Pankove, *Optical processes in semiconductors*, Dover Publications, Inc., New York, USA, **1975**.
- [28] I. D. Baikie, A. Grain, J. Sutherland, J. Law, *physica status solidi c* **2015**, *12*, 259–262.
- [29] A. D. Becke, *The Journal of Chemical Physics* **1993**, *98*, 1372–1377.
- [30] C. Lee, W. Yang, R. G. Parr, *Physical Review B* **1988**, *37*, 785–789.
- [31] T. Yanai, D. P. Tew, N. C. Handy, *Chemical Physics Letters* **2004**, *393*, 51–57.
- [32] H. S. Yu, X. He, S. L. Li, D. G. Truhlar, *Chemical Science* **2016**, *7*, 5032–5051.
- [33] J. P. Perdew, K. Burke, M. Ernzerhof, *Physical Review Letters* **1996**, *77*, 3865–3868.
- [34] J. P. Perdew, K. Burke, M. Ernzerhof, *Physical Review Letters* **1997**, *78*, 1396–1396.
- [35] S. Inoue, H. Minemawari, J. Tsutsumi, M. Chikamatsu, T. Yamada, S. Horiuchi, M. Tanaka, R. Kumai, M. Yoneya, T. Hasegawa, *Chemistry of Materials* **2015**, *27*, 3809–3812.
- [36] A. V. Marenich, C. J. Cramer, D. G. Truhlar, *The Journal of Physical Chemistry B* **2009**, *113*, 6378–6396.
- [37] L. Klasinc, A. Sabljia, G. Kluge, J. Rieger, M. Scholz, *Journal of the Chemical Society, Perkin Transactions 2* **1982**, 539–543.
- [38] A. Kraak, H. Wynberg, *Tetrahedron* **1968**, *24*, 3881–3885.
- [39] B. Ruscic, B. Kovac, L. Klasine, H. Gusten, *Zeitschrift für Naturforschung* **1978**, *33a*, 1006–1012.
- [40] J. M. Dyke, H. Ozeki, M. Takahashi, M. C. R. Cockett, K. Kimura, *The Journal of Chemical Physics* **1992**, *97*, 8926–8933.
- [41] L. A. Chewter, M. Sander, K. Muller Dethlefs, E. W. Schlag, *The Journal of Chemical Physics* **1987**, *86*, 4737–4744.

- [42] M. Baghgar, M. D. Barnes, *ACS Nano* **2015**, *9*, 7105–7112.
- [43] W. C. Tsoi, S. J. Spencer, L. Yang, A. M. Ballantyne, P. G. Nicholson, A. Turnbull, A. G. Shard, C. E. Murphy, D. D. C. Bradley, J. Nelson, J.-S. Kim, *Macromolecules* **2011**, *44*, 2944–2952.
- [44] V. Savikhin, L. K. Jagadamma, L. J. Purvis, I. Robertson, S. D. Oosterhout, C. J. Douglas, I. D. Samuel, M. F. Toney, *iScience* **2018**, *2*, 182–192.
- [45] J. Wildman, P. Repiscak, M. J. Paterson, I. Galbraith, *Journal of Chemical Theory and Computation* **2016**, *12*, 3813–3824.
- [46] S. Grimme, S. Ehrlich, L. Goerigk, *Journal of Computational Chemistry* **2011**, *32*, 1456–1465.

Chapter 6

Quantum Mechanical Analyses of Molecular Dynamics of π -conjugated Materials

6.1 Abstract

In this chapter we explore one of the first set of molecular dynamics simulations on organic π -conjugated materials employing a newly parameterised force-field for these types of systems. This was performed in collaboration with Professor Ian Galbraith and Dr. Jack Wildman. The generated ensembles were then transferred to individual input files to be used with Gaussian 09, and each configuration was subject to a computation using density functional theory. This combined approach allowed not only exploration of the configurational landscape but also of the resulting electronic properties of each frame within the simulation, which is not routinely performed in literature. The self consistent field energy, ionisation potential, optical gap and magnitude of the dipole moment was explored across the ensembles and compared to normal unimodal data distributions. For energetic properties it was clear that good agreement to the ensemble average was found for far reduced sample sizes. However, for the magnitude of the dipole moment in fluorene systems we did not observe this good agreement for lower subsets.

6.2 Introduction

As mentioned previously in Chapter 5 organic π -conjugated materials have been of current interest as the active material in optoelectronic devices, with the hope of ultimately replacing inorganic materials [1–8]. However, we are yet to observe power conversion efficiencies (PCEs) in organic photovoltaics (OPVs) that rival their inorganic counterparts [5, 6, 9]. This shortcoming has been attributed to the high degree of disorder within organic materials and thus the insufficient transfer of charge between adjacent molecules [10]. This is in comparison to highly ordered silicon based networks. However, other factor such as material defects, thus trapping the charge, and also the inability of the exciton to reach a donor-acceptor interface as it is entirely possible they are located further than the typical exciton diffusion length, which is between 5–10 nm for singlet excitons, would also contribute to the lowering of the PCE [10, 11]. The chemical properties, on a single molecular level such as the optical absorption (Δ_0) or ionisation potential (IP), would also be expected to vary significantly due to the inherent flexibility of the polymeric system.

In order to fully understand the interplay between organic π -conjugated units in a thin film, and thus provide a means to explore the relationship with the exuded PCEs, one must first explore the structural landscape of an individual unit. A common approach to investigate the scope of potential configurations available to a system is through molecular dynamics (MD) simulations. As the accuracy of these MD simulations are inherently reliant on the force-fields used to describe the bonded and non-bonded terms, previously outlined in Section 2.13.1, this has limited the application of such a technique to organic π -conjugated materials due to the lack of readily available force-fields. This was due to MD simulations being primarily used within the biochemical community to describe protein dynamics [12–15], which would be out with the scope of even the most basic electronic structure theory approach due to the drastically large system sizes. Despite these already available force-fields containing terms which would be transferable to organic π -conjugated materials, it would be expected that parametrisation of various terms would have to be carried out.

A recent study by Wildman *et al.* [16] sought to fill this void in available force-fields by developing a general parameterisation scheme for organic π -conjugated materials, one of the first approaches to do so, that may be of interest in organic optoelectronics, a brief review of which follows. This study was based upon two model systems of fluorene and thiophene at varying oligomer lengths herein denoted as F_x and T_x , respectively, where x represents the chain length. These materials in their side chain containing form are outlined in Figure 6.1. The OPLS force-field [17–23] was used as a starting point, as for F_1 and T_1 systems all terms would be expected to be sufficiently well described and thus directly transferable. Therefore, increasing to F_2 and T_2 would only require investigation of the bonding terms linking the two monomers and the resulting atomic charges. However, the terms pertaining to inter-molecular bond lengths and angles would also be expected to be well described by the monomeric OPLS force-field therefore they were omitted from the parameterisation regime. As benchmarking requires the use of high-accuracy methods, and as such is the limiting factor for systems above a certain size, it is of interest to observe if less sophisticated approaches can generate similar findings. This was explored for the dihedral energy profile of T_2 in which it was found that using CAM-B3LYP [24] with a 6-31G(d) basis for geometries, and a larger cc-pVTZ basis for subsequent energies was found to provide an analogous potential energy surface (PES) to that computed with energies of CCSD(T) quality extrapolated to the complete basis set (CBS) limit, with associated geometries obtained with MP2/aug-cc-pVTZ [25]. As these molecules usually contain side-chains to aid in the solubility process [26], the dependence on the dihedral PES for this inclusion was also explored. The PES for F_2 was invariant under side-chain addition. However, this was not the case for T_2 due to the closeness of the side-chain to the dihedral creating a steric repulsion. This steric repulsion would already be accounted for within the force-field, from the transferred non-bonded terms, therefore the approach was then to create an alternative thiophene system for which the alkyl chain was further away from the central dihedral thus omitting this steric repulsion and allowing it rely on purely an electronic effect. After this alteration it was found that the side-chains made very little

contribution, leading to the conclusion that for a force-field dihedral PES side chains are not required. In regards to the partial charges these were computed *via* the electron density at CAM-B3LYP/cc-pVTZ , once again with geometries obtained at CAM-B3LYP/6-31G(d). In order for the partial charges to be fully transferable to any oligomer length the partial charges corresponding to the central unit and the sum of partial charges corresponding to the end units must equal 0, respectively. As the end units can have net charges that do not total 0 one must explore various oligomer lengths until this condition is satisfied. These charges were found to converge sufficiently quick upon changing the oligomer length, however, an additional problem was identified for systems that did show an end-end reflection symmetry. This is observed within 3-hexylthiophene (3HT) oligomers as one of the alkyl chains will point inwards to the central intermolecular chain whereas the other will point outwards creating an asymmetry in the charge distribution. In order to bypass this each end unit must have a combination of the two appropriate units, so that the non-zero charge distributions essentially cancel one another. However for varying side chain lengths there was found to be no simple way of making this process more general and as such one should compute this for the length required.

The object of this study is to explore one of the first set of molecular dynamics simulations employing this recently parameterised force-field on various oligomer lengths of 9,9-dioctyl fluorene (F8) and 3HT, see Figure 6.1. From these MD simulated configurations we then transfer them to a format to allow one to subject them to an electronic structure analysis. We provide an examination of the SCF energy, ionisation potential, Δ_0 and magnitude of the dipole moment across the configurational landscape, and provide an early statistical analysis comparing to normal unimodal data distributions.

6.3 Computational Details

6.3.1 Molecular Dynamics Simulation

All molecular dynamics (MD) simulations were performed through GROMACS version 4.6.5 [27, 28] employing a recently parametrised force-field [16]. Simulations were undertaken for dimer, tetramer and octamer systems of both 3HT and F8 encompassed in a cubic box of chloroform, with a solvent to box distance of 0.7 nm in all cases excluding the dimer systems which was modified to 1.2 nm, ensuring non-covalent self interaction between periodic images was of no issue. The preliminary state of the system was generated by means of an initial steepest-descent energy minimisation procedure, restricted NVT and NPT equilibration, 500 ps of run time for each process with thermal and pressure coupling at 273.15 K and 1.01325 bar respectively, and lastly 10 ns of further NPT equilibration, now with the solute constraints lifted.

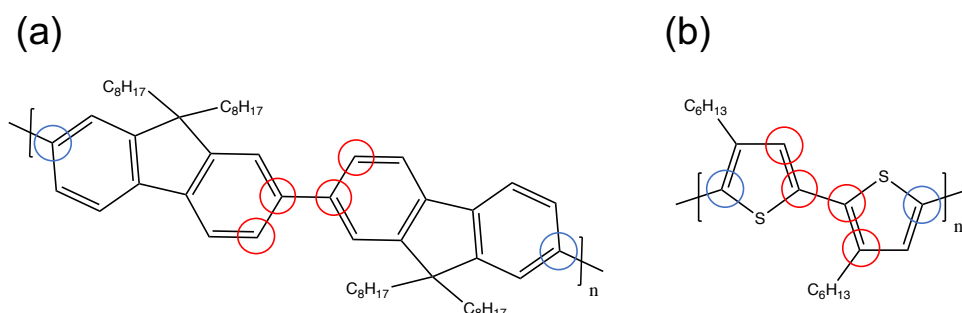


Figure 6.1: The molecular structure of F8 and 3HT where $n = 1, 2$ and 4 for the dimer, tetramer and octamer respectively. The red and blue circles represent the central dihedral and end-to-end lengths of importance, respectively.

6.3.2 Molecular Dynamics Post Processing

As the process of transferring configurations between classical and quantum mechanical packages, for example from GROMACS to Gaussian, is no trivial process we briefly pause to outline the protocol and highlight various scripts used herein. It should be noted that the scripts used build upon previous interface programs and were developed by our collaborators Wildman and Galbraith [29].

From an MD simulation the Gromacs generated production*.xtc files are con-

verted and compiled into one protein data bank (pdb) formatted file using the TrjCatConv.sh, where * represents any of the individual files. This script is a two step approach for which the initial trjcat script compiles each production*.xtc into one single overall production_final.xtc file therefore containing the entire trajectory. The subsequent trjconv script then converts this trajectory into the appropriate pdb format. This script also ensures only the coordinates pertaining to the solute remain. As input the TrjCatConv.sh script requires an addition file, termed an index file with a .ndx extension, for which each line is a successive \mathbb{Z}^+ ranging from 1 to Y where Y represents the number of atoms in the molecule. For the electronic structure computations the hexyl and octyl side chains were removed and replaced with a methyl group to reduce the computational expense. This was achieved *via* the following process. Firstly, a new index file which completely ignores the side chains is required. This side chain removed index file is generated by the GenerateNDX_NoSC.sh script, which relies on four various input files. The first is the standard topology file for the fully side chain containing system, with the second being a single lined text file providing the integer values of the first and last atom to be removed on the beginning monomeric unit only. This has been outlined in Figure 6.2, where Cs₁ and Hs₁₁ represent the first carbon of the side chain and the first hydrogen of this carbon atom, respectively. Therefore, this text file would include the \mathbb{Z}^+ corresponding to Hs₂₁ and Hs₆₃. The third and fourth input parameters are single integer values representing the oligomer length and the number of atoms in a monomer, excluding the end hydrogen atoms, respectively. This side chain removed .ndx file is then used as input for the TrjCatConv.sh script, generating the appropriate .pdb file. The final step is thus converting the combined .pdb file to the appropriate individual .com files to allow them to be used as input in Gaussian 09. This is performed using a SideChainAdjustment.sh script, which involves additional data processing *via* a SideChainAdjustment.py python script. The input required at this point is the number of atoms in the removed side chain molecule. In addition to this a text file is also required with each line containing the integer of the carbon for which the side chain was appended to, in our specific example this would be Cs₁,

and that of the carbon which is to be replaced with a hydrogen atom, Cs₂. This would thus generate a set of suitable .com input files for which the sidechain has been reduced to a methyl group. The route section of the individual .com files can also be altered by editing the SideChainAdjustment.sh script, or *via* a simple sed LINUX command.

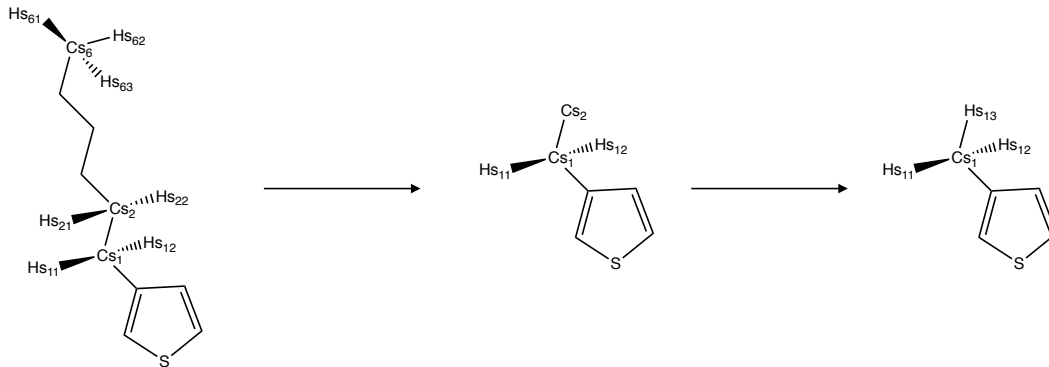


Figure 6.2: *Brief overview of the side chain removal process highlighting particularly carbons referenced in the text. Only important atoms to this procedure are defined all others are implied.*

As will be explored in the proceeding text we make reference to the central dihedral angle for the dimer system, the particularly dihedral is outlined in Figure 6.1. This is obtained through a Dihedral.sh script which utilises a Dihedral.py script. This script computes the dihedral (ϕ) by the following relation:

$$\cos(\phi) = -\frac{\vec{n}_a \cdot \vec{n}_b}{|\vec{n}_a||\vec{n}_b|} \quad (6.1)$$

where \vec{n}_a and \vec{n}_b are vectors normal to each plane created by two of the red circles on one monomer and the bonded carbon, and $|\vec{n}_a|$ represents the vector magnitude [30]. We also make reference to the end-to-end length which is given by the following standard equation:

$$\sqrt{(x_a - x_b)^2 + (y_a - y_b)^2 + (z_a - z_b)^2} \quad (6.2)$$

where x_a , y_a and z_a are the 3 spatial coordinates of the appropriate atom a , the same would hold for b . The specific atoms used to construct this length is provided by the blue circles in Figure 6.1.

6.3.3 Electronic Structure Computations

All electronic density based quantum chemical computations were performed in the gas phase through Gaussian 09 (Revision D.01) [31]. The CAM-B3LYP [24] functional was utilised in all single-point computations undertaken, in conjunction with a polarised double zeta basis set (cc-pVDZ). All excited state calculations were performed with time-dependent density functional theory [32] utilising the B3LYP [33, 34] functional with a 6-31G basis set. This functional has been previously shown to perform well for optical properties of fluorene [35, 36], and was further shown to provide accurate values pertaining to thiophene [30]. The inclusion of polarisation functions on heavy atoms changes Δ_0 for fluorene by ≈ 0.07 eV, thus validating the 6-31G approach in terms of accuracy and computational cost [30]. As all individual computations were self-contained and independent from one another we could run them in parallel and mass submit through a suitable bash submission script. An extraction script based on the grep and awk LINUX commands was also utilised to generate the raw data used in the proceeding Section.

6.4 Results and Discussion

6.4.1 Auto-Correlation and Sampling Protocol

A crucial parameter that ought to be investigated is the correlation between adjacent configurations of a given sampling interval (τ_s) for various properties of interest. This is calculated *via* an auto-correlation function as follows:

$$A(\tau_s) = \frac{\sum_{t=1}^{C-1} P(t)P(t + \tau_s)}{\sum_{t=1}^C [P(t)]^2}; P(t) = x(t) - \bar{x}_{ens.}(t) \quad (6.3)$$

where $x(t)$ is the property at t , $\bar{x}_{ens.}$ is ensemble average and C is the number of configurations within this ensemble, all of which are separated by τ_s . Despite being outwith the scope of this thesis the auto-correlation function was thoroughly explored for 3HT₁₆ in terms of the energy, end-to-end length, bond angle and dihedral angle, see Figure 6.3 for this plot [30]. The energy was found to converge

as low as $\tau_s \approx 1$ ps whereas the correlation between the conformation properties persisted up to a $\tau_s \approx 40$ ps. This was to be expected as the simulation contains thousands of atoms, from both solute and solvent, with the energy being a random sum of contributions from each.

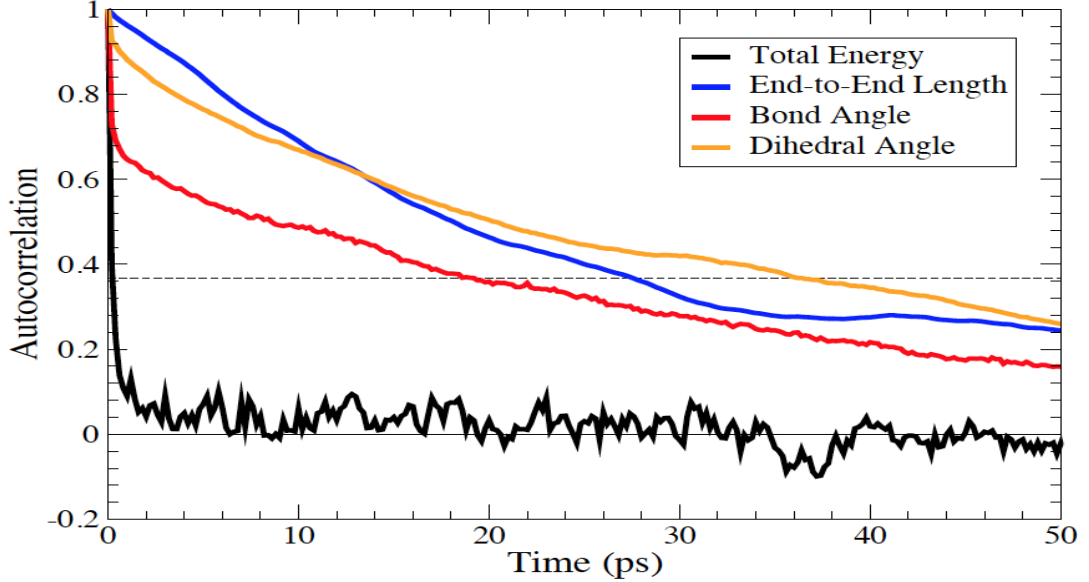


Figure 6.3: The auto-correlation function at corresponding τ_s values for various properties of $3HT_{16}$. The property is said to be uncorrelated at τ_s when the auto-correlation function is lower than e^{-1} , which is represented by the dashed black line [30].

Therefore to avoid over and under-sampling of the MD simulation a $\tau_s = 10$ ps was employed as this would be a reasonable compromise. This would result in 10001 configurations, based upon the total run time of 100 ns, however, this ensemble was further reduced to 1001 and 2001 configurations for F8 and T6 respectively, corresponding to a τ_s of 100 and 50 ps. This was a result of the appeared convergence of the intermonomer dihedral distribution, illustrated in Figure 6.4, for these reduced $3HT_2$ and $F8_2$ configurational sets. For both $F8_2$ and $3HT_2$ the auto-correlation for the reduced ensembles, therefore equating to the corresponding τ_s , was investigated for both the SCF energy, intermolecular dihedral and end-to-end length, with all having a value lower than e^{-1} . In the case of $F8_2$ we did not use the explicit dihedral but instead a planar deviation measurement, which involved scaling all the dihedral angles that were greater than 90° by $180 - \phi$. The auto-correlation function was also computed for the SCF energy and the end-to-end length of the $F8_8$ and $3HT_8$ systems. For both systems the energy was uncorrelated, however, in regards

to the end-to-end length a slight correlation was present with auto-correlation values of 0.63 and 0.65 for F8₈ and 3HT₈ respectively.

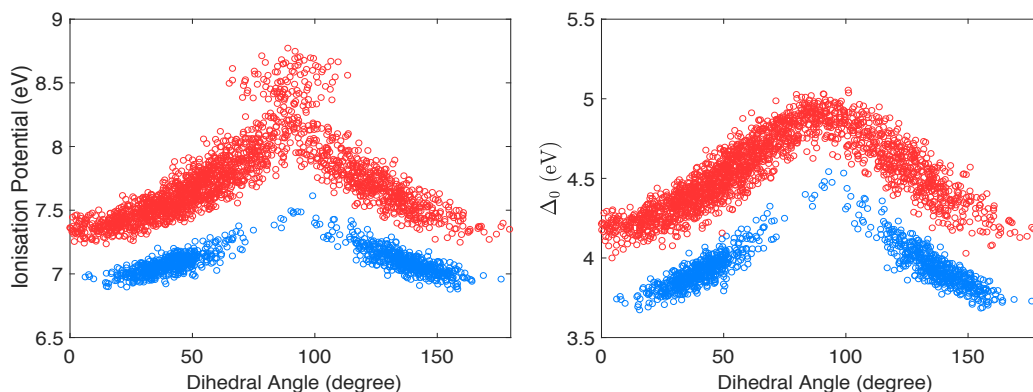


Figure 6.4: A plot of (a) Ionisation Potential and (b) Optical Absorption as a function of dihedral angle for F8₂ (blue) and T6₂ (red) respectively. Ionisation potentials were computed at CAM-B3LYP/cc-pVDZ and Δ_0 at B3LYP/6-31G.

As discussed in Section 6.2 using geometries obtained *via* CAM-B3LYP/6-31G(d) and a subsequent SCF computation at CAM-B3LYP/cc-pVTZ was found to be in very good agreement with that obtained from very computationally intensive computations of geometries and energies at MP2/aug-cc-pVTZ and CCSD(T)/CBS, respectively [16, 25]. This agreement was explored for the PES corresponding to the intermonomer dihedral rotation for T₂, with a maximum error of $< 1 \text{ kJ mol}^{-1}$, corresponding to $\approx 0.24 \text{ kcal mol}^{-1}$, well within chemical accuracy and the errors inherent to DFT methods. To reduce the computational expense we reduced the basis set of the SCF energy computation to cc-pVDZ, with deviations of 0.3 kJ mol^{-1} with respect to the larger basis set. This was also extended to F₂ systems for which this deviation was slightly larger at 0.9 kJ mol^{-1} . The PES surface for both materials at the varying basis sets is illustrated in Figure 6.5.

6.4.2 Self Consistent Field Energy

We now turn our attention to a more statistical analysis of various ensemble properties determined *via* electronic structure theory computation on each extracted

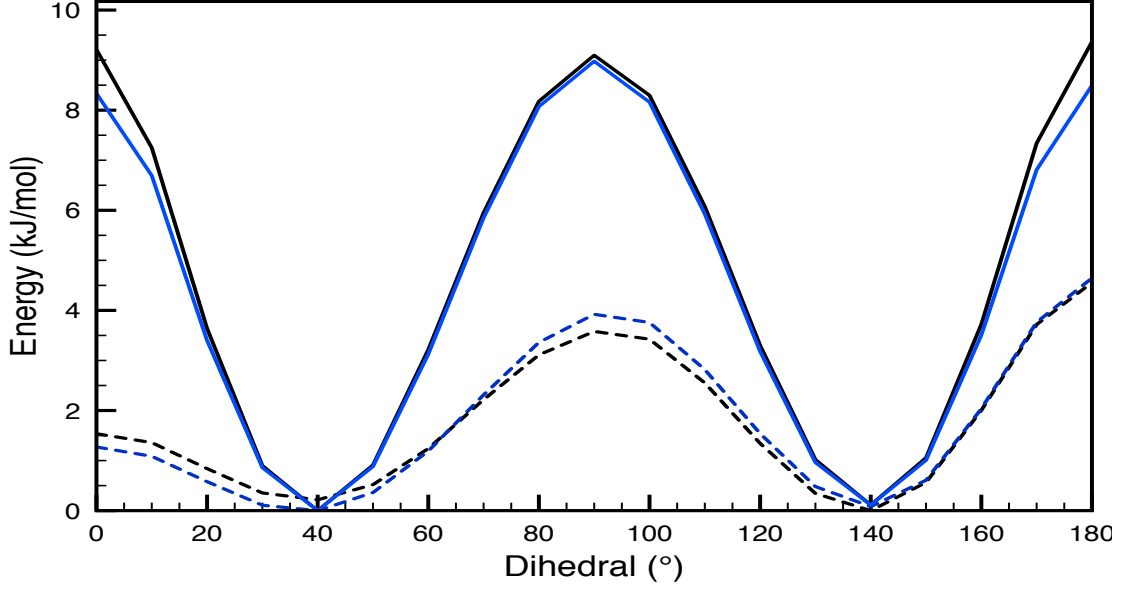


Figure 6.5: The PES corresponding to a relaxed dihedral scan at CAM-B3LYP with a cc-pVTZ (black) and cc-pVTZ (blue). The solid and dashed lines relate to F8₂ and 3HT₂, respectively.

configuration. The first property of the ensemble we investigate is the converged electronic self consistent field (SCF) energy. The raw data has been outlined in Figure 6.6(a) and (b) for the F8₂ and 3HT₂ systems, respectively. As shown we observe a fairly equilibrated distribution which was also observed for the tetramer and octamer variants of both systems. For the ensemble statistics we use the following population definitions, as implemented in MATLAB 2019b [37], for the mean ($\bar{x}_{ens.}$), standard deviation ($\sigma_{ens.}$), skewness ($\gamma_{ens.}$) and kurtosis ($\beta_{ens.}$):

$$\bar{x}_{ens.} = \frac{1}{N} \sum_{i=1}^N x_i \quad (6.4)$$

$$\sigma_{ens.} = \sqrt{\frac{1}{N} \sum_{i=1}^N |x_i - \bar{x}_{ens.}|^2} \quad (6.5)$$

$$\gamma_{ens.} = \frac{\frac{1}{N} \sum_{i=1}^N (x_i - \bar{x}_{ens.})^3}{\sigma_{ens.}^3} \quad (6.6)$$

$$\beta_{ens.} = \frac{\frac{1}{N} \sum_{i=1}^N (x_i - \bar{x}_{ens.})^4}{\left(\sum_{i=1}^N (x_i - \bar{x}_{ens.})^2 \right)^2} - 3 \quad (6.7)$$

where x_i is the specific property of configuration i . The mean and standard deviation have been used previously, for example in Section 3.4.1 when comparing various subsets of MCCI and our systematic variation. However, we also introduce two new statistical measurements in this analysis. The skewness, or third central moment of the distribution, is a measurement of the asymmetry of a data set around the mean. The skewness for a unimodal normal distribution is 0, corresponding to a completely symmetric data set. For $\gamma < 0$ the data set has a longer tail to the left, subsequently ensuring that the majority of data points are condensed at the right portion of the data set, the opposite is true for $\gamma > 0$ values. The kurtosis, or fourth central moment of the distribution, is another quantity which allows one to explore the shape of a distribution. This quantity is a measurement of the outliers contained within a data set, which for a normal unimodal distribution is equal to 3. Therefore, it is common practice to scale the kurtosis to observe the shape differences relative to a normal distribution. A positive kurtosis value indicates that the data set has more outliers than a normal distribution, and *vice versa* for a negative kurtosis.

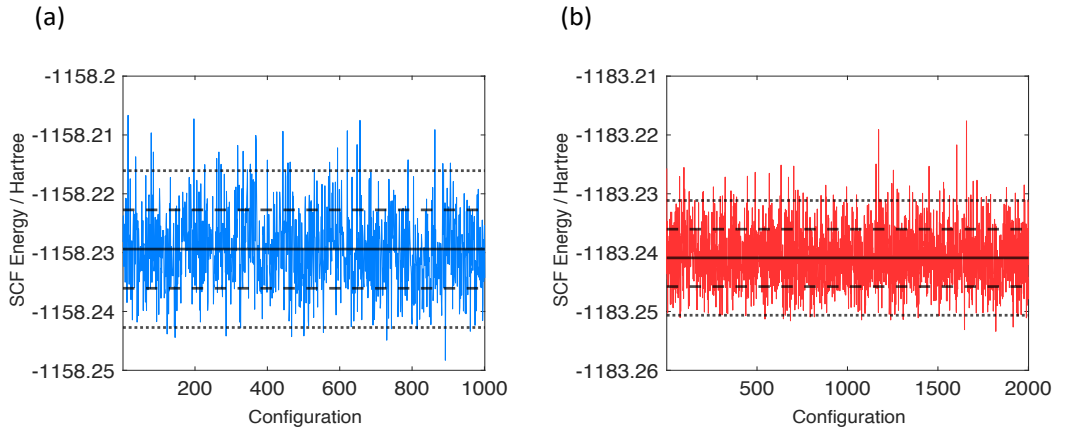


Figure 6.6: *SCF energy (Hartree) for each successive configuration in the MD simulation for (a) F8₂ and (b) 3HT₂. The $\bar{x}_{ens.}$ is represented by the solid black line with the dashed and dotted lines representing $\bar{x}_{ens.} \pm \sigma_{ens.}$ and $\bar{x}_{ens.} \pm 2\sigma_{ens.}$, respectively.*

As per Table 6.1 and the associated histogram in Figure 6.7 we observe that each data set is very similar to a normal unimodal distribution, computed from the ensemble mean and standard deviation. This is highlighted by the small positive

skewness and kurtosis value for data set.

Table 6.1: *Various ensemble statistics pertaining to the SCF energy for the systems of interest.*

System	Range (Hartree)	$\bar{x}_{ens.}$ (Hartree)	$\sigma_{ens.}$ (Hartree)	$\gamma_{ens.}$	$\beta_{ens.}$
F8 ₂	0.041633	-1158.229398	0.006663	0.314791	0.126011
F8 ₄	0.065251	-2315.276379	0.009658	0.240185	0.050619
F8 ₈	0.100111	-4629.368913	0.013748	0.187358	0.321810
3HT ₂	0.035772	-1183.2408913	0.004875	0.471776	0.392163
3HT ₄	0.046593	-2365.298248	0.006806	0.349569	0.093248
3HT ₈	0.071742	-4729.111320	0.010054	0.197685	-0.055278

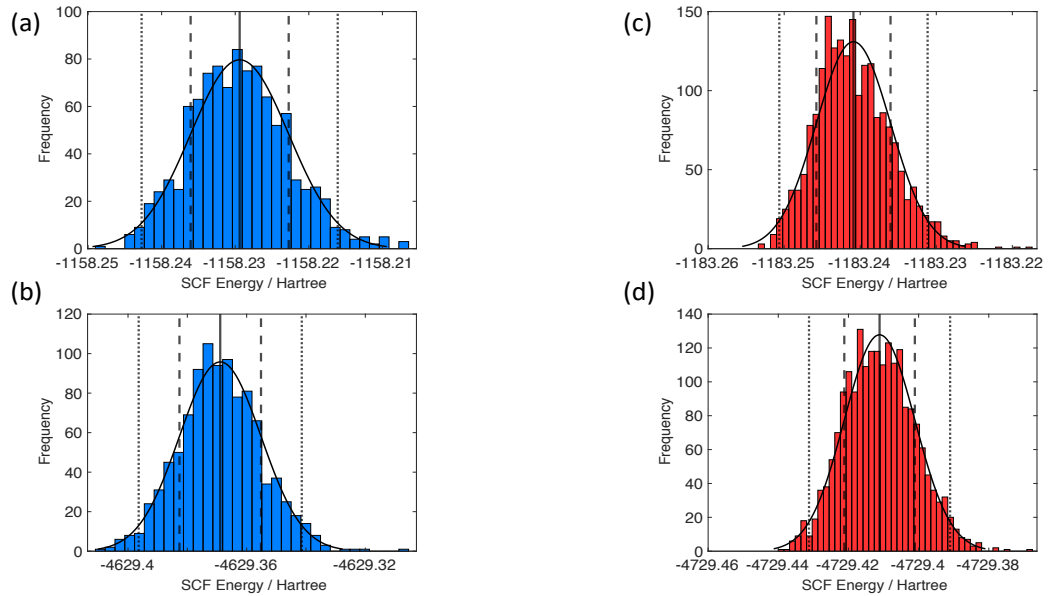


Figure 6.7: *Histogram of SCF energy for (a) F8₂, (b) F8₈, (c) 3HT₂ and (d) 3HT₈ ensembles. The black solid curve represents a normal unimodal distribution based on the $\bar{x}_{ens.}$ and $\sigma_{ens.}$. The black vertical line represents $\bar{x}_{ens.}$ with the dashed and dotted lines representing $\bar{x}_{ens.} \pm \sigma_{ens.}$ and $\bar{x}_{ens.} \pm 2\sigma_{ens.}$ respectively.*

The number of configurations for which we observe a convergence to the ensemble mean was then explored. This allowed us to investigate how many configurations were required to give a sufficient representation of the ensemble mean. The following approach was undertaken:

$$\bar{X}_i = \frac{\frac{1}{i} \sum_{j=1}^i x_j - \bar{x}_{ens.}}{\bar{x}_{ens.}} \quad (6.8)$$

where i will take each \mathbb{Z} value between 1 and 1001 for systems of fluorene, and 1 and 2001 for that of thiophene. For example, an $i = 3$ would represent the relevant

difference of the average SCF energy of the first i configurations to that of the ensemble. This average convergence procedure for the various systems is illustrated in Figure 6.8.

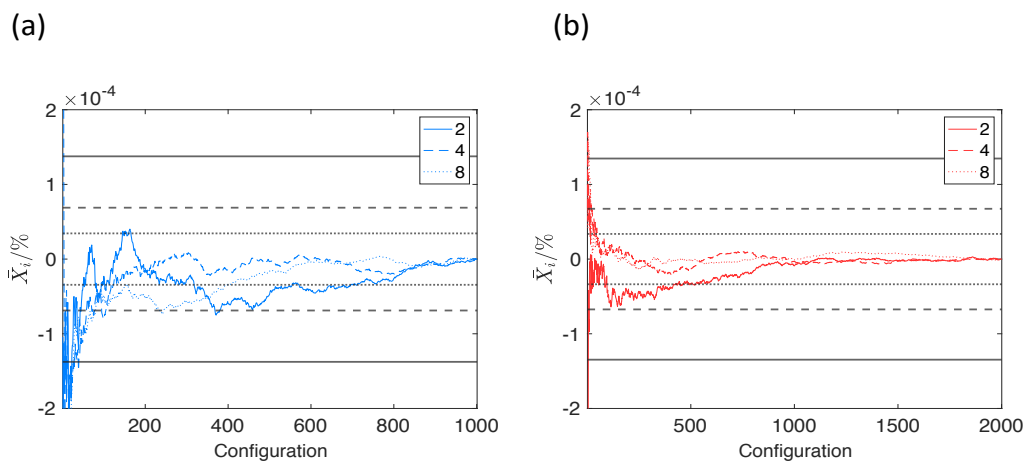


Figure 6.8: \bar{X}_i (%) pertaining to the SCF energy for (a) fluorene and (b) thiophene oligomers of interest. The solid, dashed and dotted black lines represents a \bar{X}_i (%) equal to 1 kcal mol⁻¹ for the appropriate dimer, tetramer and octamer systems, respectively.

As shown above for all oligomer lengths we start to observe convergence at around 800 configurations, it is clear that going above 1000 configurations for thiophene has no effect on the energy convergence. In regards to 3HT₈ we observe convergence far earlier at ≈ 500 configurations. However, the magnitude of the scale must be remembered as the upper and lower limits correspond to a difference of $\pm 2 \times 10^{-4}$ %. Therefore, to each of the plots we have added the % of \bar{X}_i that would correspond to a ± 1 kcal mol⁻¹ difference of the specific ensemble. For the fluorene oligomers by ≈ 400 configurations all data sets are within this reduced energy range. However, for the thiophene systems all are within ± 1 kcal mol⁻¹ for practically all sizes of \bar{X}_i out with the initial fluctuation for configurations at the beginning of the simulation.

6.4.3 Vertical Ionisation Potential

The next property we investigate is the vertical ionisation potential of the aforementioned ensembles, due to the importance in organic π -conjugated materials and also

the clear dependence on the molecular framework. The ionisation potential for the configurational landscape of F8₂ and F8₈, and the corresponding 3HT counterparts are outlined in Figure 6.9(a) and (b), respectively, and once again an equilibrated spread of data points is observed. The ensemble statistics for the various systems are provided in Table 6.2. The IP range was found to decrease in a step-wise fashion for the fluorene systems only, with respective values of 0.734, 0.601 and 0.400 eV for successive larger oligomer lengths. This was not the case for thiophene systems as range values of 1.537, 1.650 and 1.069 eV were obtained respectively. However, for both materials $\bar{x}_{ens.}$ was found to obey this step-wise diminishing pattern. As the determination of the ionisation potential involves the ground state SCF energy the above statistics will be inherently included.

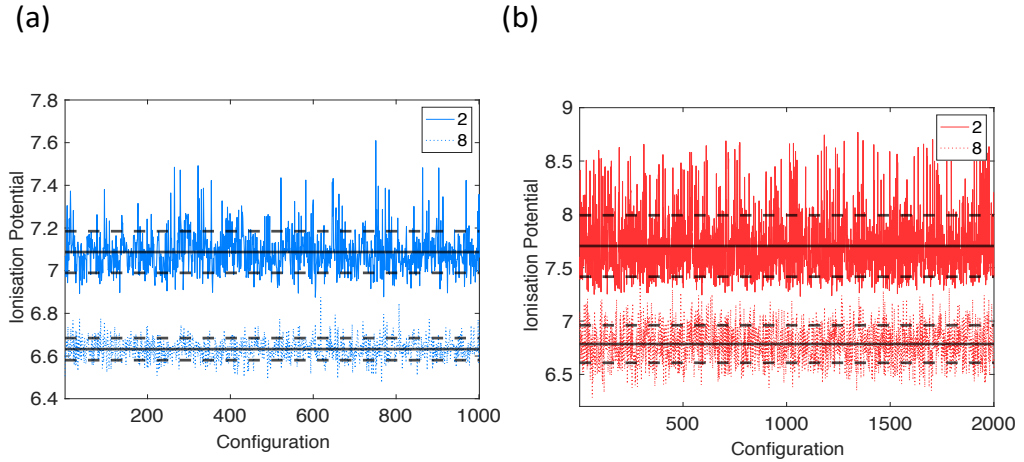


Figure 6.9: Ionisation potential for each successive configuration in the MD simulation for (a) F8_{2/8} and (b) 3HT_{2/8}. The $\bar{x}_{ens.}$ is represented by the solid black line with the dashed line representing $\bar{x}_{ens.} \pm \sigma_{ens.}$. The y-axis is in terms of eV.

Table 6.2: Various ensemble statistics pertaining to the ionisation potential for the systems of interest.

System	Range (eV)	$\bar{x}_{ens.}$ (eV)	$\sigma_{ens.}$ (eV)	$\gamma_{ens.}$	$\beta_{ens.}$
F8 ₂	0.734157	7.087365	0.097594	1.131263	2.443665
F8 ₄	0.601359	6.765818	0.077474	0.512711	0.728794
F8 ₈	0.399581	6.632331	0.051790	0.259834	0.568594
3HT ₂	1.536883	7.703714	0.287819	1.194793	1.472648
3HT ₄	1.650267	7.066011	0.225623	0.641980	0.993865
3HT ₈	1.068511	6.784771	0.175767	0.144580	-0.354520

As outlined in Table 6.2 and Figure 6.10 as we increase the oligomer lengths the likeness to a unimodal normal distribution strengthens. For $F8_2$ and $3HT_2$ we observe distributions that are positively skewed to a considerable extent, this can be clearly observed in the relevant histograms for example in Figure 6.10(c), for this we also observe a small grouping of data points centered at ≈ 8.5 eV which also decreases the likeness to a Gaussian distribution. As we increase this oligomer length the skewness and kurtosis both decrease, with the octamer giving a strong representation of a unimodal distribution.

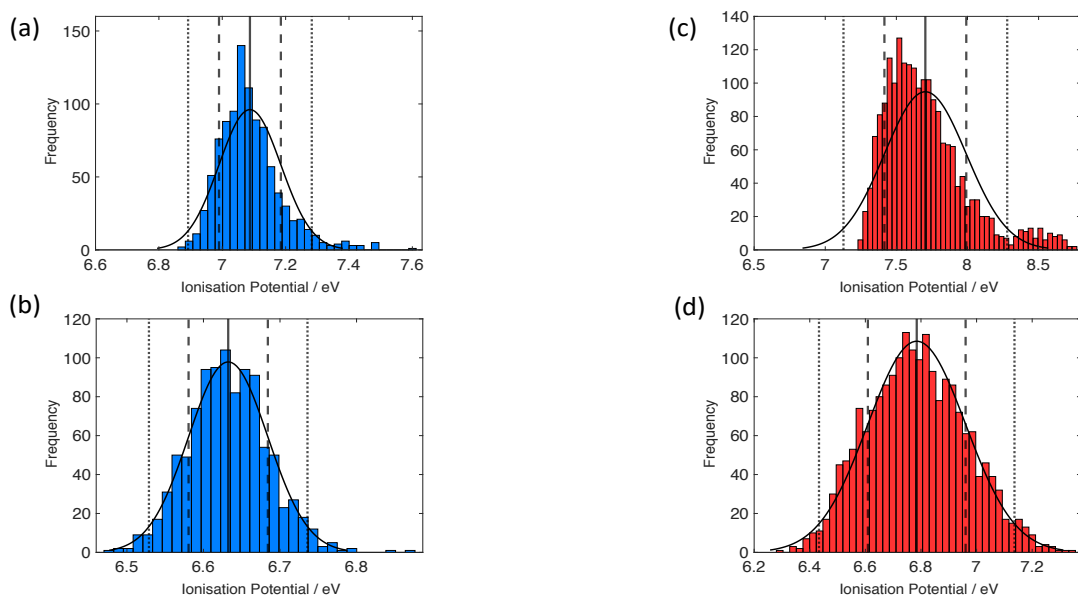


Figure 6.10: Histogram of ionisation potential for (a) $F8_2$, (b) $F8_8$, (c) $3HT_2$ and (d) $3HT_8$ ensembles. The black solid curve represents a normal unimodal distribution based on the $\bar{x}_{ens.}$ and $\sigma_{ens.}$. The black vertical line represents \bar{x}_i with the dashed and dotted lines representing $\bar{x}_{ens.} \pm \sigma_{ens.}$ and $\bar{x}_{ens.} \pm 2\sigma_{ens.}$ respectively.

The convergence average was once again explored in a similar fashion to Section 6.4.2. All the fluorene oligomers show convergence by ≈ 700 configurations, with this at a slighting larger configuration amount of ≈ 1000 configurations for thiophene oligomers. However, for the octamer chain length of each system we observe an earlier convergence of the ionisation potential at ≈ 400 and ≈ 650 configurations, respectively. Once again \bar{X}_i for each successive i is within ± 1 kcal mol $^{-1}$ for practically all the points considered out with the initial fluctuation. Also, the $3HT_4$ systems approaches this ± 1 kcal mol $^{-1}$ limit at ≈ 300 configurations before steadily decreasing to convergence.

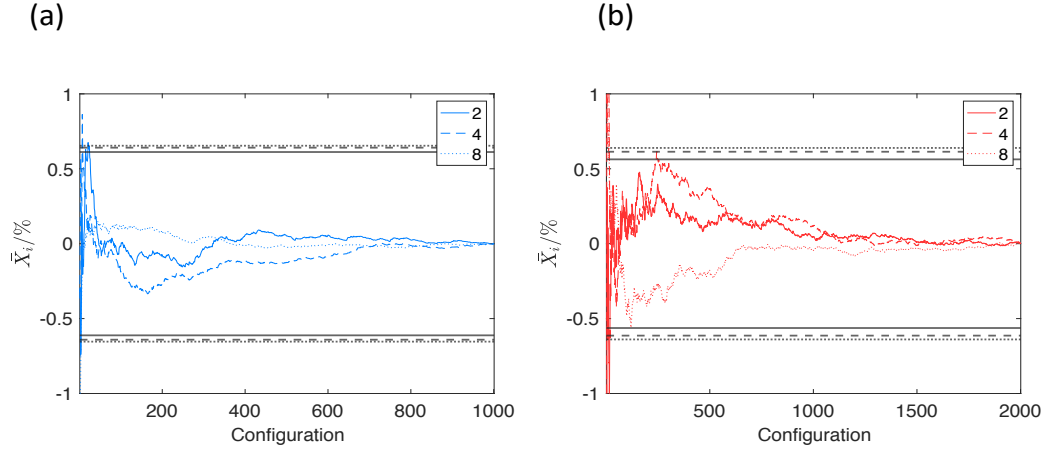


Figure 6.11: \bar{X}_i (%) pertaining to the ionisation potential for (a) fluorene and (b) thiophene oligomers of interest. The solid, dashed and dotted black lines represents an \bar{X}_i (%) equal to 1 kcal mol⁻¹ for the appropriate dimer, tetramer and octamer systems, respectively.

6.4.4 Optical Transition Gap

We now turn our attention to the Δ_0 gap for the various systems of interest. Once again we solely focus on the vertical transition energy which is computed *via* time-dependent DFT. The raw data is outlined in Figure 6.12 with the familiar equilibrated spread of data points observed. Once again, upon increasing the conjugation length the ensemble mean is found to decrease, transitioning from 3.93 to 3.29 eV for PF8₂ to PF₈. For 3HT the $\bar{x}_{ens.}$ goes from 4.53 to 3.37 eV. This is to be expected as the conjugation length of the molecular backbone increases.

Table 6.3: Various ensemble statistics pertaining to the Δ_0 for the systems of interest.

System	Range (eV)	$\bar{x}_{ens.}$ (eV)	$\sigma_{ens.}$ (eV)	$\gamma_{ens.}$	$\beta_{ens.}$
F8 ₂	0.8686	3.9306	0.1293	1.2188	2.5198
F8 ₄	0.8777	3.4704	0.1135	0.7101	1.1111
F8 ₈	0.7038	3.2851	0.0866	0.4556	0.7077
3HT ₂	1.0544	4.5299	0.2233	0.1068	-0.9136
3HT ₄	1.5677	3.7595	0.2750	0.3293	-0.2410
3HT ₈	1.4057	3.3692	0.2407	0.1803	-0.2985

As observed in Table 6.3 and Figure 6.13 we once again observe a better agreement to a normal unimodal distribution upon increasing the conjugated backbone

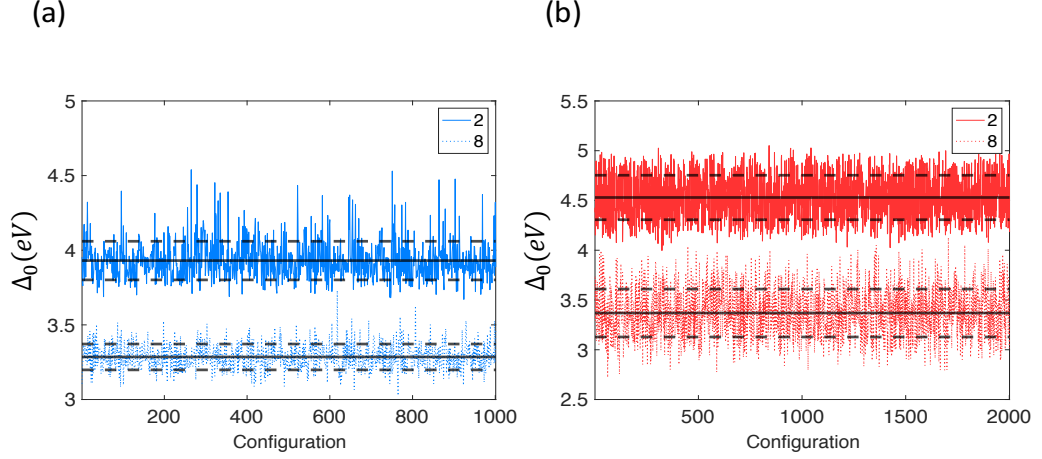


Figure 6.12: Δ_0 (eV) for each successive configuration in the MD simulation for (a) $F8_{2/8}$ and (b) $3HT_{2/8}$. The $\bar{x}_{ens.}$ is represented by the solid black line with the dashed line representing $\bar{x}_{ens.} \pm \sigma_{ens.}$.

length, however, we do not observe an apparent different between $3HT_4$ and $3HT_8$. As per Figure 6.13(a) the $F8_2$ data set is noticeably skewed to the right. The distribution of $3HT_2$ is also particularly striking, see Figure 6.13(c), as we do not observe one clear peak but a near spread of data points between $\pm 1 \sigma_{ens.}$ of $\bar{x}_{ens.}$

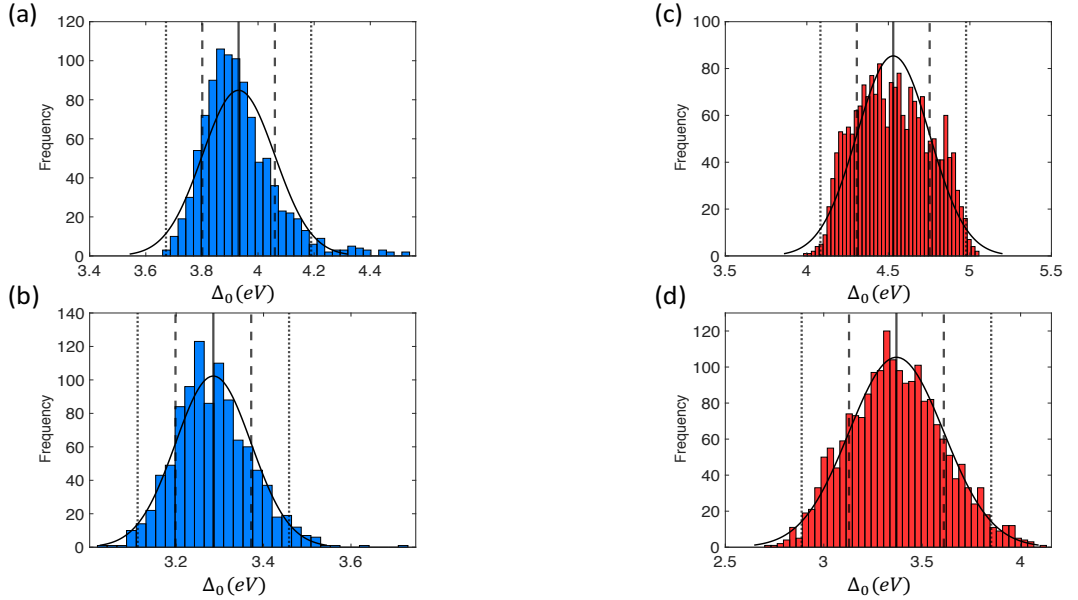


Figure 6.13: Histogram of Δ_0 for (a) $F8_2$, (b) $F8_8$, (c) $3HT_2$ and (d) $3HT_8$ ensembles. The black solid curve represents a normal unimodal distribution based on the $\bar{x}_{ens.}$ and $\sigma_{ens.}$. The black vertical line represents $\bar{x}_{ens.}$ with the dashed and dotted lines representing $\bar{x}_{ens.} \pm \sigma_{ens.}$ and $\bar{x}_{ens.} \pm 2\sigma_{ens.}$ respectively.

The convergence of the average was once again investigated, see Figure 6.14.

This plot was very similar to the ionisation potential equivalent provided previously in Figure 6.11. For fluorene we observe convergence for all oligomer lengths at ≈ 700 configurations, which for thiophene was found to be a little more at ≈ 1200 configurations. Once again the F8₈ was found to reach convergence earlier at ≈ 400 configurations with the thiophene alternative reaching this at ≈ 600 configurations. This early convergence was also found for the 3HT₂ at ≈ 500 configurations. For all the oligomer lengths pertaining to fluorene we are within ± 1 kcal mol⁻¹ from $\bar{x}_{ens.}$, however, for thiophene, specifically the tetramer and octamer oligomers, we observe a fluctuation outwith these limits until ≈ 550 configurations.

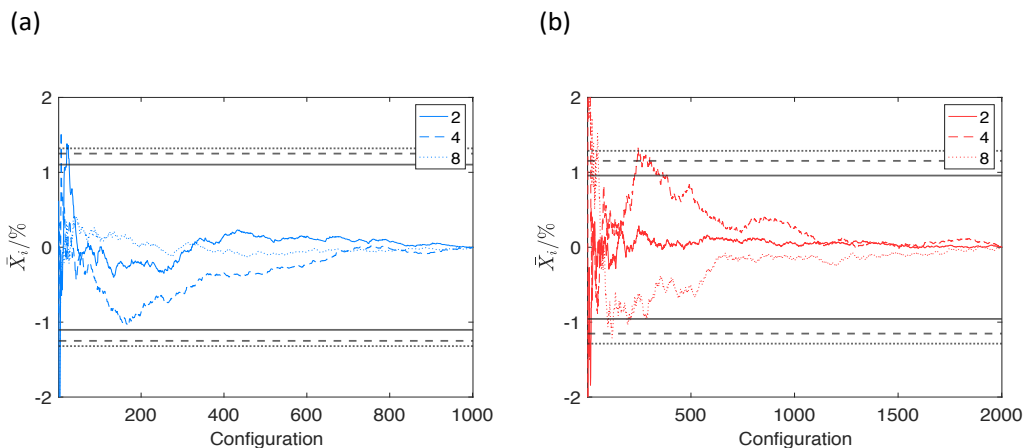


Figure 6.14: \bar{X}_i (%) pertaining to the Δ_0 for (a) fluorene and (b) thiophene oligomers of interest. The solid, dashed and dotted black lines represents an \bar{X}_i (%) equal to 1 kcal mol⁻¹ for the appropriate dimer, tetramer and octamer systems, respectively.

6.4.5 Magnitude of the Dipole Moment

We now turn our attention to a non-energetic property of the ensembles, specifically the magnitude of the dipole moment. It is clear from the plot of the raw data for F8₂ we do not observe the equilibrated spread of values obtained previously, see Figure 6.15. Instead the property equilibrates and then a considerable fluctuation occurs, once again establishing an equilibrium and continuing within this regime.

As was to be expected increasing the oligomer length was found to increase the $\bar{x}_{ens.}$ for each of the two systems. Increasing the oligomer length was also found to

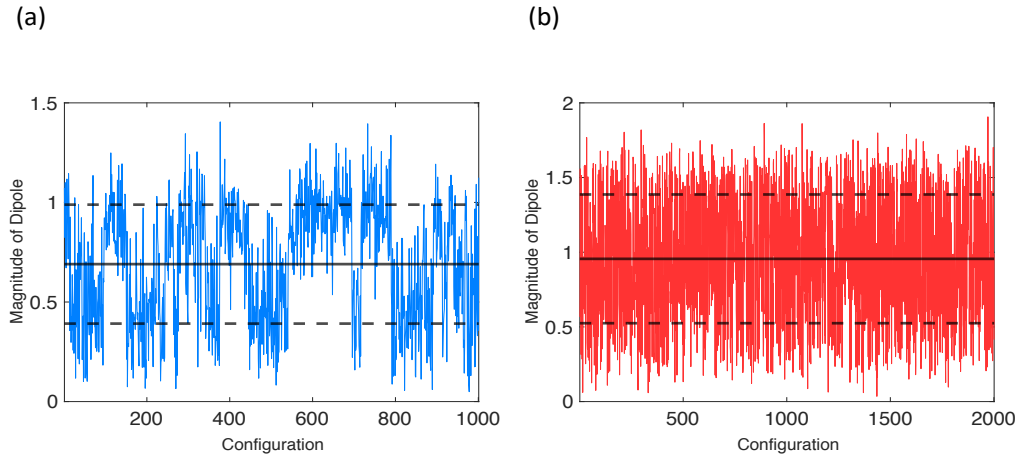


Figure 6.15: *Magnitude of the dipole moment for each successive configuration in the MD simulation for (a) $F8_{2/8}$ and (b) $3HT_{2/8}$. The $\bar{x}_{ens.}$ is represented by the solid black line with the dashed line representing $\bar{x}_{ens.} \pm \sigma_{ens.}$. The y-axis is in terms of Debye.*

Table 6.4: *Various ensemble statistics pertaining to the magnitude of the dipole moment for the systems of interest.*

System	Range (Debye)	$\bar{x}_{ens.}$ (Debye)	$\sigma_{ens.}$ (Debye)	$\gamma_{ens.}$	$\beta_{ens.}$
$F8_2$	1.3549	0.6903	0.2987	-0.1778	-0.9796
$F8_4$	2.0493	0.9839	0.4253	0.2205	-0.5111
$F8_8$	2.2933	1.1267	0.4746	0.3932	-0.3521
$3HT_2$	1.8714	0.9557	0.4310	-0.0408	-1.0897
$3HT_4$	3.0026	1.3034	0.5156	0.2373	-0.3293
$3HT_8$	3.9215	1.7417	0.6409	0.2229	-0.2489

provide subsets that were closer to a normal unimodal distribution. If we further investigate the $F8_2$ histogram, see Figure 6.16, it is essentially a bimodal distribution, with the peaks occurring at dipole magnitudes corresponding to $x_{ens.} \pm \sigma_{ens.}$. In regards to the $3HT_2$ histogram the spread of data points is fairly constant across the range of $x_{ens.} \pm \sigma$.

We then turn our attention to the convergence of the average for these various systems. As per Figure 6.17 we do not observe a clear convergence to $\bar{x}_{ens.}$ for the fluorene systems. However, for thiophene we observe a convergence by ≈ 1000 configurations. For $F8_4$, despite averaging over 800 configurations we approximate a value that is $\approx 10\%$ lower than the ensemble mean.

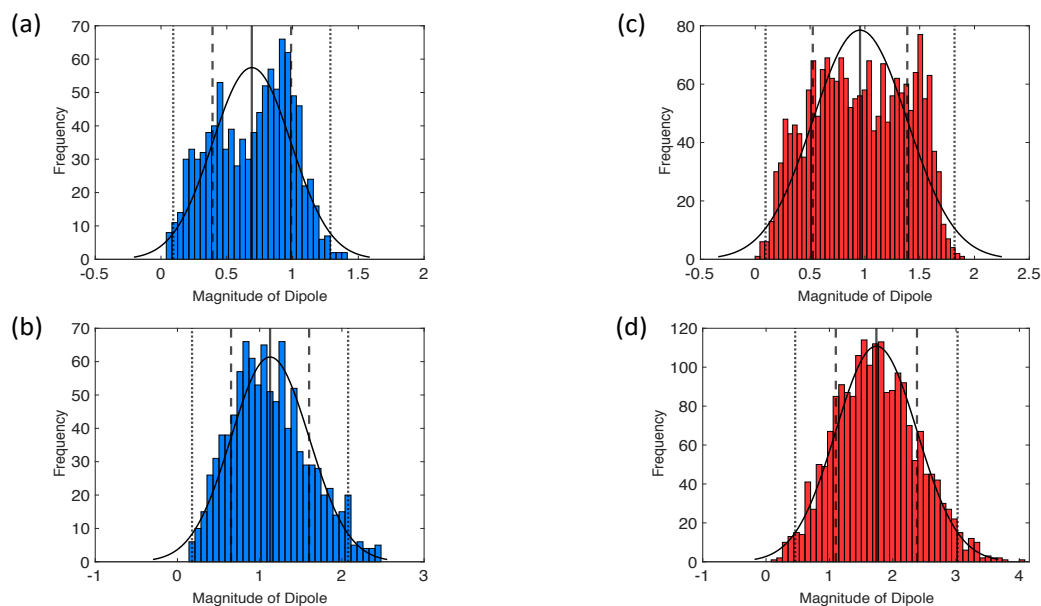


Figure 6.16: Histogram of the magnitude of the dipole moment for (a) $F8_2$, (b) $F8_8$, (c) $3HT_2$ and (d) $3HT_8$ ensembles. The black solid curve represents a normal unimodal distribution based on the $\bar{x}_{ens.}$ and $\sigma_{ens.}$. The black vertical line represents $\bar{x}_{ens.}$ with the dashed and dotted lines representing $\bar{x}_{ens.} \pm \sigma_{ens.}$ and $\bar{x}_{ens.} \pm 2\sigma_{ens.}$ respectively. The x-axis is in terms of Debye.

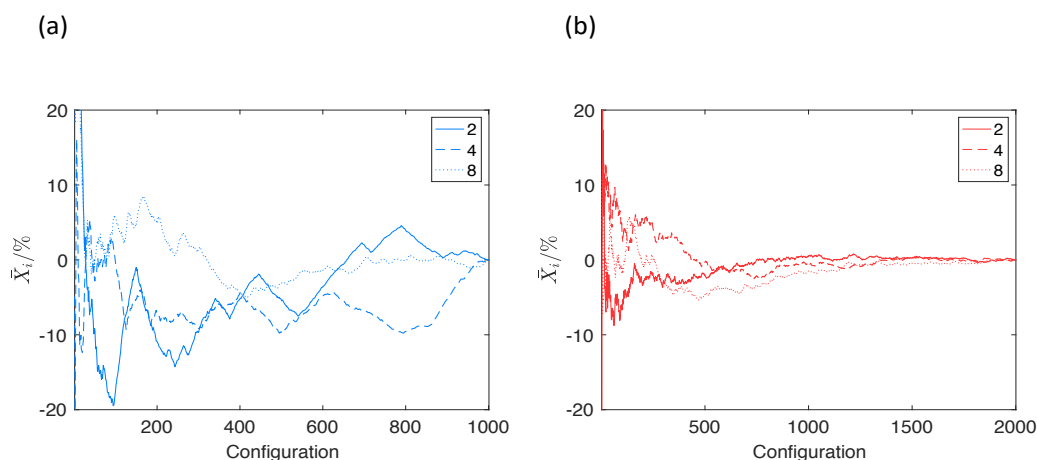


Figure 6.17: \bar{X}_i (%) pertaining to magnitude of the dipole moment for (a) fluorene and (b) thiophene oligomers of interest.

6.5 Conclusion

The configurational landscape of organic π -conjugated materials that are of interest in organic photovoltaic devices was explored *via* molecular dynamics simulations employing a recently parameterised force-field. This configurational landscape was then transferred to a suitable format to allow an electronic structure based treat-

ment, and a brief statistical analysis of various properties was undertaken. It was observed for energetic based properties in order approximate the property to within ± 1 kcal mol⁻¹ one could use subsets far lower than the 1001 and 2001 employed herein. This is also observed for the thiophene oligomers in terms of the magnitude of the dipole moment, however, for fluorene we do not see this steady convergence even at our ensemble limits.

It would also be of interest in future work to perform these simulations on other organic π -conjugated materials, such as those provided in Figure 5.6. This would allow one to test the force-fields on not only homopolymers but those of alternating monomers, and thus explore the resulting ensemble properties.

6.6 References

- [1] X. Guo, M. Baumgarten, K. Müllen, *Progress in Polymer Science* **2013**, *38*, Topical issue on Conductive Polymers, 1832–1908.
- [2] G. Luo, X. Ren, S. Zhang, H. Wu, W. C. H. Choy, Z. He, Y. Cao, *Small* **2016**, *12*, 1547–1571.
- [3] C. Dyer-Smith, J. Nelson in *Practical Handbook of Photovoltaics (Second Edition)*, (Eds.: A. McEvoy, T. Markvart, L. Castañer), Academic Press, Boston, **2012**, pp. 543–569.
- [4] N. Tessler in *Encyclopedia of Materials: Science and Technology*, (Eds.: K. J. Buschow, R. W. Cahn, M. C. Flemings, B. Ilshner, E. J. Kramer, S. Mahajan, P. Veyssi re), Elsevier, Oxford, **2001**, pp. 4486–4490.
- [5] S.-H. Liao, H.-J. Jhuo, Y.-S. Cheng, S.-A. Chen, *Advanced Materials* **2013**, *25*, 4766–4771.
- [6] C. Liu, C. Yi, K. Wang, Y. Yang, R. S. Bhatta, M. Tsige, S. Xiao, X. Gong, *ACS Applied Materials & Interfaces* **2015**, *7*, 4928–4935.
- [7] G. Dennler, M. C. Scharber, C. J. Brabec, *Advanced Materials* **2009**, *21*, 1323–1338.
- [8] A. Facchetti, *Materials Today* **2013**, *16*, 123–132.

- [9] C. Solanki, *Solar Photovoltaics: Fundamentals, Technologies And Applications*, PHI Learning, **2015**.
- [10] B. Kippelen, J.-L. Brédas, *Energy & Environmental Science* **2009**, *2*, 251–261.
- [11] O. V. Mikhnenko, P. W. M. Blom, T.-Q. Nguyen, *Energy & Environmental Science* **2015**, *8*, 1867–1888.
- [12] E. G. Marklund, J. L. Benesch, *Current Opinion in Structural Biology* **2019**, *54*, 50–58.
- [13] N. Trbovic, B. Kim, R. A. Friesner, A. G. Palmer III, *Proteins: Structure Function and Bioinformatics* **2008**, *71*, 684–694.
- [14] M. Orozco, *Chemical Society Reviews* **2014**, *43*, 5051–5066.
- [15] M. O. A. Hospital, J.R. Goni, J. Gelpi, *Advances and Applications in Bioinformatics and Chemistry* **2015**, *8*, 37–47.
- [16] J. Wildman, P. Repiscak, M. J. Paterson, I. Galbraith, *Journal of Chemical Theory and Computation* **2016**, *12*, 3813–3824.
- [17] W. L. Jorgensen, D. S. Maxwell, J. Tirado-Rives, *Journal of the American Chemical Society* **1996**, *118*, 11225–11236.
- [18] W. L. Jorgensen, N. A. McDonald, *Journal of Molecular Structure: THEOCHEM* **1998**, *424*, A Faithful Couple: Qualitative and Quantitative Understanding of Chemistry, 145–155.
- [19] N. A. McDonald, W. L. Jorgensen, *The Journal of Physical Chemistry B* **1998**, *102*, 8049–8059.
- [20] R. C. Rizzo, W. L. Jorgensen, *Journal of the American Chemical Society* **1999**, *121*, 4827–4836.
- [21] M. L. P. Price, D. Ostrovsky, W. L. Jorgensen, *Journal of Computational Chemistry* **2001**, *22*, 1340–1352.
- [22] E. K. Watkins, W. L. Jorgensen, *The Journal of Physical Chemistry A* **2001**, *105*, 4118–4125.

- [23] G. A. Kaminski, R. A. Friesner, J. Tirado-Rives, W. L. Jorgensen, *The Journal of Physical Chemistry B* **2001**, *105*, 6474–6487.
- [24] T. Yanai, D. P. Tew, N. C. Handy, *Chemical Physics Letters* **2004**, *393*, 51–57.
- [25] J. W. G. Bloom, S. E. Wheeler, *Journal of Chemical Theory and Computation* **2014**, *10*, PMID: 26588510, 3647–3655.
- [26] S. Inoue, H. Minemawari, J. Tsutsumi, M. Chikamatsu, T. Yamada, S. Horiuchi, M. Tanaka, R. Kumai, M. Yoneya, T. Hasegawa, *Chemistry of Materials* **2015**, *27*, 3809–3812.
- [27] D. Van Der Spoel, E. Lindahl, B. Hess, G. Groenhof, A. E. Mark, H. J. C. Berendsen, *Journal of Computational Chemistry* **2005**, *26*, 1701–1718.
- [28] D. V. D. S. B. Hess, C. Kutzner, E. Lindahl, *Journal of Chemical Theory and Computation* **2008**, *4*, 435–447.
- [29] J. Wildman, I. Galbraith, *Private Communication*.
- [30] J. Wildman, PhD thesis, Heriot-Watt University, **2017**.
- [31] M. J. Frisch, G. W. Trucks, H. B. Schlegel, G. E. Scuseria, M. A. Robb, J. R. Cheeseman, G. Scalmani, V. Barone, G. A. Petersson, H. Nakatsuji, X. Li, M. Caricato, A. V. Marenich, J. Bloino, B. G. Janesko, R. Gomperts, B. Mennucci, H. P. Hratchian, J. V. Ortiz, A. F. Izmaylov, J. L. Sonnenberg, D. Williams-Young, F. Ding, F. Lipparini, F. Egidi, J. Goings, B. Peng, A. Petrone, T. Henderson, D. Ranasinghe, V. G. Zakrzewski, J. Gao, N. Rega, G. Zheng, W. Liang, M. Hada, M. Ehara, K. Toyota, R. Fukuda, J. Hasegawa, M. Ishida, T. Nakajima, Y. Honda, O. Kitao, H. Nakai, T. Vreven, K. Throssell, J. A. Montgomery, Jr., J. E. Peralta, F. Ogliaro, M. J. Bearpark, J. J. Heyd, E. N. Brothers, K. N. Kudin, V. N. Staroverov, T. A. Keith, R. Kobayashi, J. Normand, K. Raghavachari, A. P. Rendell, J. C. Burant, S. S. Iyengar, J. Tomasi, M. Cossi, J. M. Millam, M. Klene, C. Adamo, R. Cammi, J. W. Ochterski, R. L. Martin, K. Morokuma, O. Farkas, J. B. Foresman, D. J. Fox, *Gaussian 09 Revision D.01*, Gaussian Inc. Wallingford CT, **2016**.
- [32] E. Runge, E. K. U. Gross, *Physical Review Letters* **1984**, *52*, 997–1000.

- [33] A. D. Becke, *The Journal of Chemical Physics* **1993**, *98*, 1372–1377.
- [34] C. Lee, W. Yang, R. G. Parr, *Physical Review B* **1988**, *37*, 785–789.
- [35] S. Schumacher, A. Ruseckas, N. A. Montgomery, P. J. Skabara, A. L. Kanibolotsky, M. J. Paterson, I. Galbraith, G. A. Turnbull, I. D. W. Samuel, *The Journal of Chemical Physics* **2009**, *131*, 154906.
- [36] N. A. Montgomery, J.-C. Denis, S. Schumacher, A. Ruseckas, P. J. Skabara, A. Kanibolotsky, M. J. Paterson, I. Galbraith, G. A. Turnbull, I. D. W. Samuel, *The Journal of Physical Chemistry A* **2011**, *115*, 2913–2919.
- [37] MATLAB version R2019b, The Mathworks, Inc., Natick, Massachusetts, **2019**.

Chapter 7

Conclusions and Future Work

To conclude this thesis we briefly review the overarching findings of each Chapter indicating possible follow up studies that may be of future interest.

7.1 Conclusions and Future Work

Within this thesis a range of computational techniques were employed to investigate chemical systems exhibiting a varying degree of complexity, whether that be in terms of geometries or electronic structure. The black box technique of Monte Carlo configuration interaction (MCCI), which involves iteratively building up the wavefunction through stochastic additions to the current reference space, remaining in the wavefunction only if their coefficient is greater than a user-defined threshold, was systematically modified to test the optimality of such generated wavefunctions. This systematic modification allowed consideration of the entire interacting space *via* the reduction of this space to smaller batches, with the potential to add the largest weighted configurations across all batches. A comparison to the MCCI methods was also made for full configuration interaction, and a pruned alternative. For neon, within a cc-pVTZ basis there was no apparent difference between the methods as all recovered 99 % of the correlation and displayed a very similar wavefunction composition. The next system we explored was the potential energy surface (PES) corresponding to the double-hydrogen dissociation in H_2O . Once again it was observed that the stochastic wavefunctions were very similar to those generated by a systematic regime, with a very similar non-parallelity error across the PES. The wavefunction composition was also explored for two particular points along the PES surface, one that was single and the other highly multi-reference in nature, corresponding to a separation of 1.8 and 4.0 Bohr respectively. The wavefunction for the approximated methods for the aforementioned points were very similar, once again validating the optimal nature of the stochastic MCCI wavefunction. The comparison was then extended to the approximation of the first A_1 excitation energy, for which both MCCI approaches were within 0.1 eV of the FCI calculated energy despite vastly reduced wavefunctions. The pruned FCI approach was computationally too demanding for comparison to this excitation energy. The final system explored was a particularly challenging point of the Cr_2 PES, corresponding to a separation of 2.75 Å, for which it was observed that the stochastic MCCI approach resulted in the lowest energy across all runs considered. Despite, the enhanced scalability we

were yet to observe systematic computations that were faster than their stochastic counterparts. Also, for systematic computations the potential excitation space for each iteration had to be stored in available memory this therefore limits the size of systems that can be studied using this approach. Therefore two avenues of future work is to explore the large scale parallelisation and also alternative ways to generate the vast interacting space.

The next study involved the thermochemical and kinetic analysis of two sets of intramolecular Diels-Alder reactions (IMD-A) using a high accuracy composite method, CBS-QB3. The first involved the incorporation of a nitro group into the furan in-conjunction with substitution of the dienophile. It was observed, both experimentally and theoretically, that despite generating an electron deficient diene the nitro substituted reactions were found to be more exergonic, with a reduction in the activation barrier. This was attributed to a greater stabilisation of the partial positive charge on the nitro bearing carbon upon following this reaction pathway. The nature of the important frontier molecular orbital interactions were also explored for which upon nitration the systems went from a normal to an inverse electron demand process. The nitrated systems were also found to tolerate dienophile substitution to a greater degree, which was attributed to the greater asynchronicity in the nitrated systems for the σ bond formation process. The distance between the nitro bearing carbon and the substituted dienophile in this transition state was found to be increased when comparing with the non-substituted system, thus tolerating substitution to a better degree. The only exception to this nitration effect was observed when an extremely electron withdrawing, $\text{CO}_2\text{C}_2\text{H}_5$, was incorporated into the dienophile. This however generates an extremely polarity mismatched substrate, as both the diene and dienophile are electron deficient. The second part of this study involved the study of hetero IMD-A reactions to investigate if there was a structure-energy correlation that exists in normal IMD-A substrates. However, for the majority of systems studies herein we did not observe strong correlations, with the exception of the unsaturated aldehyde/ethylene IMD-A reaction for which we observe strong correlation between the transition state contraction and the retro

Diels-Alder barrier. However, to investigate this structure-energy correlation further a larger representative set of related substituted diene and dienophiles are required.

We then turned our attention to a density functional theory approach to compute the ionisation potential of various organic π -conjugated materials that have potential use as organic donors in photovoltaic devices. We initially compare the experimental ionisation potential attained from the organic thin film to a simple computational approach of a single oligomer encompassed in a implicit solvent model. This simple approach was found to provide considerable agreement for all materials for which there was no ordering in the thin film, within 100 meV of the experimental uncertainty range. However, if stacking is important within the molecular environment this must be accounted for. The influence of stacking was then investigated for which it was found to have a substitution effect on the ionisation potential computed for P3HT. For the single molecule computations the optical gap was also computed with considerably good agreement between theory and experimental despite no benchmarking of the exchange-correlation for the excited state.

The thesis concludes with molecular dynamics simulations on two organic π -conjugated systems of varying oligomer lengths employing a recently developed force-field. A brief statistical analysis of the ensembles was undertaken for various relevant properties obtained from electronic structure computations. It was observed that the energetic properties converged within ± 1 kcal mol⁻¹ of the ensemble mean for reduced subsets relatively quickly when compared to a structural based property. A future avenue of potential work is to undertake simulations on various copolymers, such as those outlined in Chapter 6, employing this new force-field and exploring them once again with electronic structure methods.